

General Disclaimer

One or more of the Following Statements may affect this Document

- This document has been reproduced from the best copy furnished by the organizational source. It is being released in the interest of making available as much information as possible.
- This document may contain data, which exceeds the sheet parameters. It was furnished in this condition by the organizational source and is the best copy available.
- This document may contain tone-on-tone or color graphs, charts and/or pictures, which have been reproduced in black and white.
- This document is paginated as submitted by the original source.
- Portions of this document are not fully legible due to the historical nature of some of the material. However, it is the best reproduction available from the original submission.

REPORT NO. CASD-NAS-75-015
CONTRACT NAS 8-28201

(NASA-CR-143870) DESIGN, FABRICATION, AND
TEST OF A GRAPHITE/EPOXY METERING SHELL
(GEMS) Final Report, Jun. 1973 - Apr. 1975
(General Dynamics/Convair) 187 p HC \$7.00

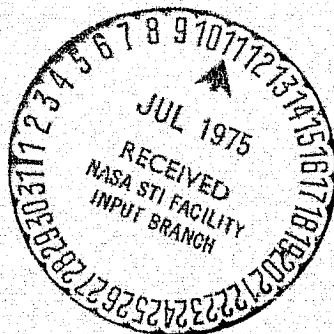
N75-26414

Unclas

CSSL 11D G3/39 26603

DESIGN, FABRICATION, AND TEST OF A GRAPHITE/EPOXY METERING SHELL (GEMS)

FINAL REPORT
June 1973 to April 1975



GENERAL DYNAMICS
Convair Division

FOREWORD

The Graphite/Epoxy Metering Shell (GEMS) program was accomplished under contract to the National Aeronautics and Space Administration, George C. Marshall Space Flight Center. The contracting officers representative was Mr. Carl Loy.

The program was conducted in San Diego, California by the Composite Structures Group of General Dynamics Convair Division. This group was under the direction of Mr. J. D. Forest. Mr. J. Prunty was the program manager.

The following Convair personnel contributed to this report:

Mr. J. Prunty	Composite Structures Programs
Mr. H. McCutchen	Structures Analysis
Mr. R. S. Wilson	Structures Analysis
Mr. J. Ramsey	Structures Analysis
Mr. D. R. Linsenmann	Structures Analysis
Mr. M. Varlas	Materials and Processes
Mr. R. G. Huntington	Structural Dynamics
Mr. G. E. Pynchon	Physical Properties Laboratory
Mr. R. L. Pleasant	Thermodynamics
Mr. D. A. Nirchl	Structures Test Laboratory
Mr. W. D. Bowers	Structures Test Laboratory
Mr. D. B. Page	Structures Test Laboratory

In addition, the following personnel made significant contributions in the areas indicated:

Mr. A. E. Gloyer	Structures Design
Mr. J. Hertz	Fabrication
Mr. C. Podvin	Laser Measurement Systems
Mr. M. D. Campbell	CTE Measurement
Mr. N. J. Brown	Tool Design
Mr. R. C. Christopher	Fabrication
Mr. G. L. Olson	Fabrication
Mr. J. L. Winger	Quality Assurance

Approved by:

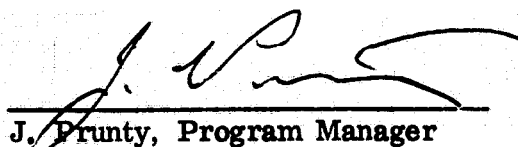

J. Prunty, Program Manager

TABLE OF CONTENTS

<u>Section</u>	<u>Page</u>
1 INTRODUCTION	1-1
2 PRELIMINARY DESIGN	2-1
2.1 EVALUATION OF FULL-SCALE DATA	2-1
2.1.1 Dimensional Stability	2-1
2.1.2 Decoupling Concepts	2-3
2.1.3 Minimum CTE Concepts	2-4
2.1.4 Conclusions From Full-Scale Studies	2-5
2.2 SUBSCALE STUDIES	2-5
2.3 SELECTION OF LAMINATE SCALE	2-6
2.4 CONCLUSIONS OF PHASE II	2-7
2.4.1 General	2-7
2.4.2 Metering Structure/SSM Interface	2-8
3 DESIGN AND ANALYSIS	3-1
3.1 DESIGN	3-1
3.1.1 Initial Material Selection	3-1
3.1.2 Alternate Resin Candidates	3-1
3.1.3 Fiber Candidates	3-1
3.1.4 HM-S/X-30 and Modmor I/X-30 Data	3-2
3.1.5 Adhesive System	3-3
3.1.6 Metering Shell Structural Arrangement	3-3
3.2 ANALYSIS	3-11
3.2.1 Design Criteria	3-11
3.2.2 Laminate Selection	3-16
3.2.3 Structural Analysis	3-27
4 FABRICATION PROGRAM	4-1
4.1 COMPONENT FABRICATION	4-1
4.1.1 General Layup and Cure Procedures	4-1
4.1.2 Trimming and Machining	4-3
4.1.3 Problem Areas	4-3
4.1.4 Shell Skins and Splice Straps	4-3
4.1.5 Bolt Ring Segments	4-5
4.1.6 "T" Ring Segments	4-8
4.1.7 "I" Ring Segments	4-11
4.1.8 Ring Splice Angles and Straps	4-13
4.1.9 Hub Channel Rings	4-16

TABLE OF CONTENTS, Contd

<u>Section</u>		<u>Page</u>
	4.1.10 Hub Skins and Splice Straps	4-17
	4.1.11 Support Tees and Angles	4-18
	4.1.12 Spider Legs	4-19
	4.1.13 Other Details	4-22
	4.2 SUBASSEMBLIES	4-22
	4.3 FINAL ASSEMBLIES	4-23
5	TEST PROGRAM	5-1
	5.1 STATIC TEST	5-1
	5.1.1 Summary	5-1
	5.1.2 Test Specimen	5-1
	5.1.3 Test Setup	5-1
	5.1.4 Test Conditions and Procedures	5-6
	5.1.5 Test Results	5-6
	5.1.6 Correlation of Strain Gauge Results with Analytical Predictions	5-39
	5.2 DYNAMIC TEST	5-42
	5.2.1 Test Setup and Conditions	5-42
	5.2.2 Instrumentation	5-42
	5.2.3 Test Results	5-42
	5.2.4 Analysis of Results	5-46
	5.3 THERMAL VACUUM TEST	5-49
	5.3.1 Test Description	5-49
	5.3.2 Instrumentation	5-51
	5.3.3 Test History	5-53
	5.3.4 Test Results	5-57
	5.3.5 Structural Analysis	5-69
6	CONCLUSIONS AND RECOMMENDATIONS	6-1
	6.1 CONCLUSIONS	6-1
	6.2 RECOMMENDATIONS	6-1

LIST OF FIGURES

<u>Figure</u>	<u>Page</u>
1-1 LST Configuration	1-2
2-1 Three-Point SSM Attachment	2-3
2-2 Athermalized Truss Concept, Graphite-Epoxy	2-5
2-3 Half-Scale Metering Truss, GEMS Program	2-6
2-4 Half-Scale Metering Shell, GEMS Program	2-7
3.1-1 GEMS Assembly	3-4
3.1-2 Longitudinal Splice	3-5
3.1-3 Cross Section, Forward Ring	3-6
3.1-4 Cross Section, Intermediate Ring	3-7
3.1-5 Field Splice and Attachment to LST Main Ring	3-8
3.1-6 Secondary Mirror Support	3-9
3.2-1 Longitudinal Lamina Properties	3-14
3.2-2 Transverse Lamina Properties	3-14
3.2-3 Shear Properties	3-14
3.2-4 Ply Orientation Versus CTE	3-17
3.2-5 Symmetric Field Joint Finite Element Model	3-18
3.2-6 Forward Ring	3-20
3.2-7 Forward Ring Athermalization Study	3-22
3.2-8 Cross Section, Intermediate Ring	3-23
3.2-9 Field Splice and Attachment to LST Main Ring	3-24
3.2-10 Spider Leg Laminate Orientation	3-26
3.2-11 Effect of Variations of CTE of $[0_3/\pm 45.5/90]_s$ on Longitudinal CTE of Secondary Mirror	3-26
3.2-12 Cantilever Bending of Continuously Mounted Shell	3-31
3.2-13 Resultant Loading of a Curved I Beam	3-34
3.2-14 Detailed View of I Section Flange	3-34
3.2-15 Detailed View of Web Flange	3-34

LIST OF FIGURES, Contd

<u>Figure</u>		<u>Page</u>
3.2-16	Finite Element Model of Secondary Mirror Support	3-39
3.2-17	Point Loading of Secondary Mirror Support Rings	3-39
3.2-18	Secondary Mirror Support Ring	3-41
3.2-19	Spider Beam-Torque Box Shear Clips	3-44
3.2-20	Shear Loading in T-Shear Clips	3-44
3.2-21	T-Shear Clip Effective Side Shear	3-45
3.2-22	Spider Attach Flange	3-46
3.2-23	Field Joint Attach Flange	3-50
4-1	GEMS Program Fabrication Sequence	4-2
4-2	Layup of Shell Skin 4-Ply Module	4-4
4-3	Aluminum Skin Tool and 4-Ply Module	4-4
4-4	Illustration of Shell Skin Prepared for Cure	4-6
4-5	Layup of Bolt Ring Segment	4-6
4-6	Bolt Ring Bagged for Autoclave Cure	4-7
4-7	Cured Bolt Rings and Tooling	4-8
4-8	"T" Ring Segment Layup	4-9
4-9	Inverted "T" Ring Bagged for Autoclave Cure	4-10
4-10	Layup Configuration for the I-Ring Segments	4-12
4-11	I-Ring Segments Bagged for Autoclave Cure	4-12
4-12	Cured Splice Angles on Steel Tool	4-13
4-13	Flat Layup and Kit Extraction	4-14
4-14	Splice Angles	4-14
4-15	Splice Straps	4-15
4-16	Flat Panel	4-15
4-17	Hub Channel Ring Layup	4-16
4-18	Bagging Schematic for Hub Skins and Splice Straps	4-18

LIST OF FIGURES, Contd

<u>Figure</u>	<u>Page</u>
4-19	Layup Module for Angles and Tee's 4-19
4-20	Modmor I/X-30 Angles Layup 4-20
4-21	Modmor I/X-30, 24-Ply T 4-20
4-22	Modmor I/X-30 T Angle Layup 4-21
4-23	GEMS Secondary Mirror Support Subassembly 4-23
4-24	Final Assembly Fixture 4-24
4-25	Secondary Mirror Spider Support Banded In-Place 4-25
4-26	GEMS Assembly Before Instrumentation 4-26
5.1-1	Test Setup 5-2
5.1-2	Loading Cylinder Installations 5-4
5.1-3	GEMS Strain Gage Locations 5-5
5.2-1	Accelerometer Locations and Accelerometer Sign Convention 5-43
5.3-1	GEMS in Thermal Vacuum Test 5-50
5.3.2-1	Thermocouple Locations 5-51
5.3.2-2	Schematic of Hewlett-Packard Laser Measurement System 5-52
5.3.2-3	Laser/Optical Assembly 5-52
5.3.4-1	GEMS Test Conditions 5-58
5.3.4-2	GEMS Uniform Temperature Cycles 5-60
5.3.4-3	GEMS Uniform Temperature Cycles 5-60
5.3.4-4	Uniform Temperature Cycles 5-61
5.3.4-5	Uniform Temperature Cycles 5-61
5.3.4-6	Forward Shell Cycles 5-64
5.3.4-7	Forward Shell Cycles 5-64
5.3.4-8	Midshell Cycles 5-65
5.3.4-9	Midshell Cycles 5-65

LIST OF FIGURES, Contd

<u>Figure</u>	<u>Page</u>
5.3.4-10 Aft Shell Cycles	5-67
5.3.4-11 Aft Shell Cycles	5-67
5.3.5-1 Shell Model Program Elements	5-70
5.3.5-2 Secondary Mirror Support Structure Elements	5-71
5.3.5-3 Front Ring/Secondary Mirror Support Joint	5-72
5.3.5-4 Forward Ring Model	5-73
5.3.5-5 Intermediate Splice Model	5-74
5.3.5-6 Shell Segments	5-75
5.3.5-7 Aft Spider Model Axial View (Graphics)	5-76
5.3.5-8 Aft Spider Leg (Graphics)	5-76
5.3.5-9 Field Splice	5-76
5.3.5-10 Field Splice Model	5-77
5.3.5-11 GEMS Analytical Model UTC	5-78
5.3.5-12 GEMS Analytical Model SPTC	5-79
5.3.5-13 GEMS Analytical Model MSTC 0 = CAL	5-80
5.3.5-14 GEMS Analytical Model ASTC 0 = CAL	5-81
5.3.5-15 GEMS Analytical Model Optimization* = CAL	5-82
5.3.5-16 Graphite/Epoxy Section Temperature Response to Thermal Vacuum Test Heating	5-84
5.3.5-17 Graphite/Epoxy Section Temperature Response to Predicted Flight Heating Conditions	5-85

LIST OF TABLES

<u>Table</u>	<u>Page</u>
2-1 Thermal Movement of Secondary Mirror, Full-Scale LST	2-2
2-2 Effects on Thermal Movement of Decoupling or Material Changes	2-4
3-2.1 Payload Bay Load Factors	3-12
3-2.2 Test Results, Tensile Moduli of 12-ply Unidirectional Modmor I/X-30	3-13
3-2.3 Test Results, Poisson's Ratio and Shear Modulus for 12-ply Unidirectional Modmor I/X-30	3-13
3-2.4 Unidirectional CTE, 12-ply Modmor I/X-30	3-13
3-2.5 Material Design Allowables	3-15
3-2.6 GEMS Modmor I/X-30 Material Properties	3-18
3-2.7 Effect of Zero CTE Laminate Orientation in Spider Legs on Secondary Mirror	3-26
3-2.8 Shell Load Intensities	3-28
I-V Deflection and Strain Data for the Axial Load Test Runs	5-7
VI-X Deflection and Strain Data for the Side Load Test Runs	5-18
5-1 Summary of Predicted and Measured Stresses	5-41
5-2 Modal Data	5-44
5-3 Damping Coefficient	5-45
5.3.4-1 Thermocouple Groups - Thermocouple Locations by Number are shown in Figure 5.3.2-1	5-59
5.3.4-2 Despace, Uniform Temperature Cycles	5-62
5.3.4-3 Forward Shell Cycle Deltas	5-63

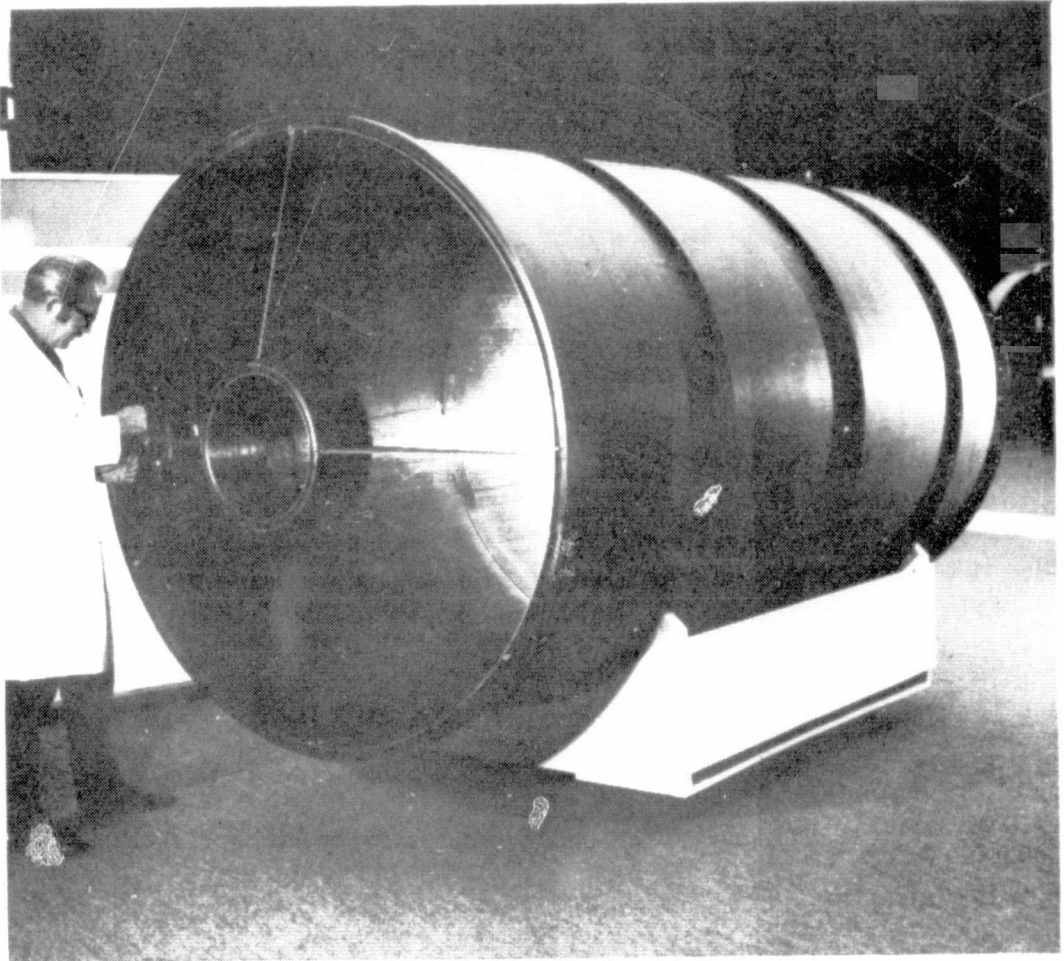
ABSTRACT

The subject of this report is a program to design, fabricate and test a dimensionally stable metering structure in support of the Large Space Telescope (LST) program.

Graphite/epoxy was the material selected as the only viable candidate material which can meet the stringent thermal expansion criteria of the LST.

Preliminary studies led to the selection of the structural shell concept for development in this program. A metering shell was designed with emphasis on dimensional stability in conjunction with low cost. This structure was then fabricated in graphite/epoxy without significant problems.

Thermal expansion test coupons extracted from the layups of the skin panels indicated the attainment of a Coefficient of Thermal Expansion (CTE) of 0.0666 micrometers/ $m^{\circ}K$ (0.037 microinches/ $in^{\circ}F$). Subsequent thermal vacuum chamber tests on the complete metering shell demonstrated an expansion of the 2.95 meters (116 inches) overall length of 0.27 micrometers/ $^{\circ}K$ (6 microinches/ $^{\circ}F$). Static and dynamics tests, which demonstrated adequacy with respect to limit loads and stiffness were also accomplished.



ORIGINAL PAGE IS
OF POOR QUALITY

SUMMARY

The Graphite-Epoxy Metering Shell Program (GEMS) was conducted by Convair Division, San Diego, for NASA Marshall Space Flight Center under Contract NAS8-28201. The objective of the program was to demonstrate the dimensional stability and structural integrity of a graphite-epoxy structure as applied to the metering structure of the Large Space Telescope (LST). This was achieved by the design, fabrication, and test of a half-scale metering structure. The program started with a preliminary design phase in June 1973 and culminated with the completion of thermal vacuum testing in December 1974.

In the preliminary design phase, a comparison was made between the shell concept and the alternative truss concept for the metering structure. This was accomplished by an evaluation of the results of parallel studies of full-scale structure for the LST. Thermal distortion, dynamic response, design aspects, material selection, cost, and weight were investigated. The evaluation of the data led to the following conclusions:

- . The shell and truss concepts can both be designed to comply with the dimensional stability criteria.
- . The metering structure must be isolated from the large thermally induced distortions in the uninsulated aluminum subsystems module and micrometeoroid shield shells.
- . Control of, or compensation for, scatter in the attained values of the coefficient of thermal expansion (CTE) is essential for compliance with the required dimensional stability.
- . Both concepts can meet the stiffness requirements.
- . The truss is best with respect to weight.
- . The shell is best with respect to cost.

In addition to the evaluation of the full-scale studies, an investigation was made to determine the appropriate scale for the GEMS program. This was determined to be one-half scale in overall dimensions but full scale with respect to laminate thickness on the basis of:

- a. Validity of thermal-vacuum test results due to the use of full-scale laminates in the half-scale model.

- b. Valid development of full-scale fabrication techniques due to the use of full-scale laminates.
- c. Minimized program costs due to savings in material, fabrication, and test costs.

On the basis of these findings, it was decided to proceed with the design of a one-half scale metering shell of the dimensions shown in Figure 1. The overall geometry for this purpose was the one shown in the final report of the LST Phase A study.

The criteria for dimensional stability selected for the GEMS were the stringent criteria published in the LST Phase A report. These are typified by the key criterion on which the GEMS program was focused. This required that the despace between the secondary and the primary mirrors be held within 2 micrometers (80 microinches) for a uniform temperature change of 5.55C (10F) through the metering structure. One-half of this dimensional change was applicable as the criterion for the half-scale GEMS

The material system finally selected featured Modmor I, a high modulus fiber which is very suitable for the design of unidirectional zero CTE laminates. MSFC and Convair cooperated in parallel testing of the selected X-30 epoxy to qualify this material for outgassing characteristics. This material was selected on the basis of the availability of a data base on material characteristics, very satisfactory fabrication experience, and, most importantly, freedom from microcracking. The latter phenomenon severely degrades thermal expansion characteristics.

Design of the GEMS was accomplished primarily on the basis of two dominant criteria, dimensional stability and minimum cost. Low cost tooling design was developed in conjunction with design of each component and the basic part planning was accomplished by the designer to assure compatibility of the design with fabrication techniques.

Fabrication of the GEMS was completed without significant problems. The low cost tooling and fabrication techniques produced high quality parts, particularly with respect to dimensional tolerances. The accuracy of the ply orientation, which affects the attainable near zero CTE, was easily maintained to within a small fraction of a degree across the large skin panels. Assembly was particularly easily accomplished since the use of overlaying butt straps at the splices of the 12 skin panels eliminated the need for precision fits at these interfaces. The proven techniques are directly applicable to the full scale metering structure, and no difficulties in scaleup are anticipated.

After fabrication, the GEMS was subjected to static, dynamic, and thermal/vacuum testing. The philosophy adopted in this program was to emphasize the crucial thermal expansion tests in the thermal vacuum chamber. Only minimal static and dynamic testing were performed since the metering shell is not critical with respect to strength and stiffness.

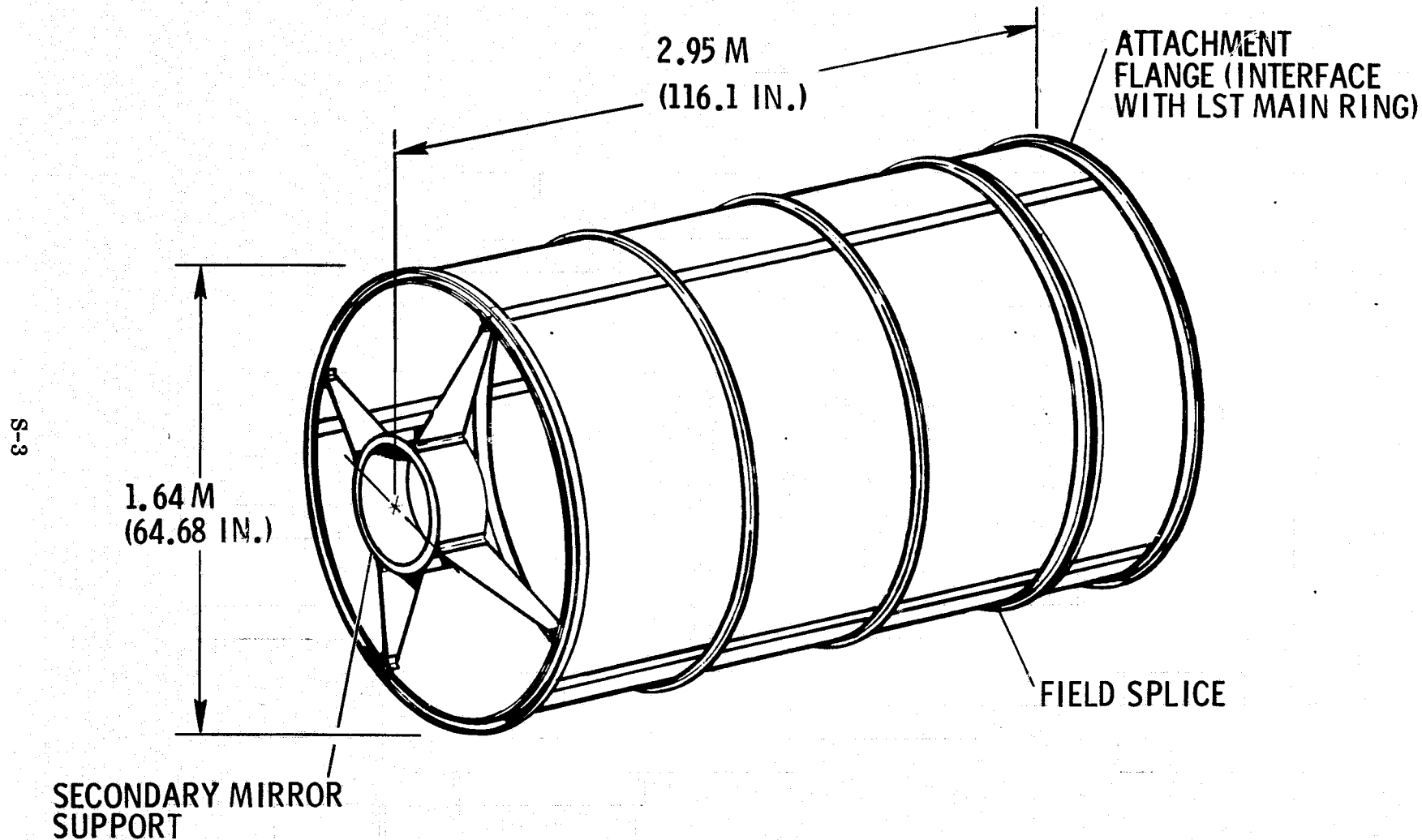


Figure 1. Half-Scale LST Metering Shell

In the static test an axial load was first applied to the hub of the secondary mirror support structure. This induced the limit stress condition in the potentially critical spider leg to hub ring attachments. In the second test condition a radial load was applied at the forward end of the shell to induce limit tensile load intensities in the aft attachment flange and limit compressive load intensities in the shell skin. This test was accomplished without problems. A simple dynamic test was accomplished in the static test fixture. This low cost expediency gave rise to a problem in that some motion occurred in the base of the test fixture. Fortunately, sufficient accelerometers were located on the base to permit an analysis of this effect. This analysis indicated a fixed base first mode frequency of 38 Hz for the half geometrical scale, one-quarter mass scale GEMS assembly or an equivalent 19 Hz for the full-scale LST metering shell. This value exceeds the requirement of 15 Hz of the LST Phase A report and further improvement could be made by reducing the bolt spacing from the current average of approximately 15 cm (6 in.) in the field splice and aft attachment flange.

The thermal expansion tests were performed in the Livermore thermal vacuum chamber at Convair. It was anticipated that the crucial problem in this test would involve the measurement of the very low thermal strains to the required degree of accuracy on a large specimen under the relevant test conditions. Several measurement systems were investigated. The basic laser interferometer was abandoned because of the possibility of measurement errors caused by the thermal expansion of the optical elements which would need to be located inside the thermal vacuum chamber. The Extended Fizeau System avoids this problem since only plane mirrors are required within the chamber. This system was not adopted due to the need to develop a suitable fringe counter and recording system. The Plane Mirror Dilatometer adaptation of the Hewlett Packard laser measurement system does not involve the problems pertinent to the interferometer or the Fizeau system. The system is fully developed and does not require the location of sensitive optical elements in the varying thermal environment. The concern about the feasibility of using this system was that, prior to the GEMS application, the equipment had been used only in a benign environment, and only for measurements over very short distances. It was anticipated that serious problems would be encountered in maintaining alignment of the system with a large specimen, in measurement noise due to vibration, and in measurement errors due to expansion of the optical elements which were essentially exposed to an outdoor environment. In fact, no difficulties were encountered with this application of the Plane Mirror Dilatometer and measurements were readily obtained to a resolution for 0.013 micrometer (0.5 microinch).

During the test, 13 valid cycles were obtained varying the uniform temperature of the shell skin between -73C (-100F) and -29C (-20F). For a test condition involving the measurement of submicrometer strains in the 2.95 meter length of the GEMS structure, the general characteristics of the cyclic data plots were remarkably consistent and repeatable. At the start of these cycles the overall expansion of the GEMS was 1.88 micrometers/5.55C (75 microinches/10F). This improved to a value of 1.52

micrometers/5.55C (60 microinches/10F) at the last cycle. This improvement appears to be characteristic of graphite-epoxy and has been noted in coupon type testing. Test coupons are now precycled ten times between -73C (-100F) and 52C (125F).

The demonstrated dimensional stability of the GEMS, 1.52 micrometers/5.55C approached the goal of 1.00 micrometer/5.55C, and the test value attained indicates impressive stability which may well meet the actual requirements of the LST if the temperature change in the metering structure during a period of observation is less than 5.55C (10F).

An important consideration is that the characteristics of the despace plots appear to indicate that the test conditions were unduly severe. A temperature variation of 44.4C (80F) was used in the test to enhance the measurement of the small thermal strains. The period for each cycle was limited to approximately 80 minutes, the time required to obtain the temperature differential and to assure stabilization of the shell skin temperature at each end point. This situation resulted in a test rate of temperature change approximately 200 times the rate expected in the flight condition. Under this condition of high radiant heating, the negative expansion shell skin responded very rapidly, while the bulk temperature of the heavier positive expansion elements such as the field splice lagged significantly. In this out-of-phase condition, the thermal strains in the negative expansion skin were additive to the strains in the positive expansion elements at a point where the strains in these elements are peaking out, a phenomena which is clearly seen in the plotter test data. This additive effect applies to both the peaks and valleys of the thermal strain plots. In contrast to this, the skin thermal strains would be subtractive in the nearly in-phase condition applicable to the flight case. Thus the performance of the GEMS is probably significantly better than the 1.52 micrometers/5.55C indicated by the test results.

SECTION 1

INTRODUCTION

The Large Space Telescope (LST) is being developed by the NASA for launch into earth orbit by the Space Shuttle. This instrument, at the time of the GEMS design, was a three-meter-aperture-diameter, Cassegrainian reflecting telescope.

The GEMS program is concerned with the metering structure for the LST. In the Phase A Reference Configuration shown in Figure 1-1, this was designed to hold the alignment of the secondary mirror relative to the primary mirror. The secondary mirror is provided with an adjustment capability to correct the alignment immediately prior to any period of observation. Following this adjustment, the metering structure must maintain this alignment within extremely close tolerances throughout the period of observation. This period may be as much as 10 hours, and may occur following a reorientation of the telescope, such as from parallel orientation to normal to the solar radiation. Significant temperature changes and temperature gradients occur in the metering structure under these conditions, even though the structure is insulated on both sides. To enhance the performance of the telescope, the desired goal is to maintain the specified close tolerances on the secondary-to-primary mirror alignment through these temperature changes during the period of observation. The specified tolerances are:

Despace	=	±2 micrometers
Decenter	=	±10 micrometers
Tilt	=	±4.9 microradians

The attainment of such stringent alignment requires the use of a structural material that exhibits a coefficient of thermal expansion (CTE) close to zero. Metallics are effectively ruled out by this requirement. Titanium, a frequent choice for a low-expansion metallic, has a CTE of $7.2 \mu\epsilon/^{\circ}\text{K}$. This value would give a despace effect of approximately 42 micrometers on the 5.9-meter length of the metering structure for a change of only 1°K , obviously at least an order of magnitude too large. Invar, a 36% nickel alloy, is unique for a metallic in displaying a CTE of $0.54/^{\circ}\text{K}$ in the relevant temperature range. Invar would therefore give a despace of approximately 3 micrometers for 1°K . This is still too large, since the predictions of temperature changes are as high as 5°K or more. In addition, Invar violates an LST requirement prohibiting the use of magnetic materials.

Obviously, the dimensional stability requirements of the LST are best met by the adoption of a material that can give a CTE of zero. Graphite/epoxy is the only viable candidate in this important respect. The ply orientation of this laminated material can be selected to give a CTE of nominally zero. The material has been well proven in

LARGE SPACE TELESCOPE (LST) MSFC Reference Configuration

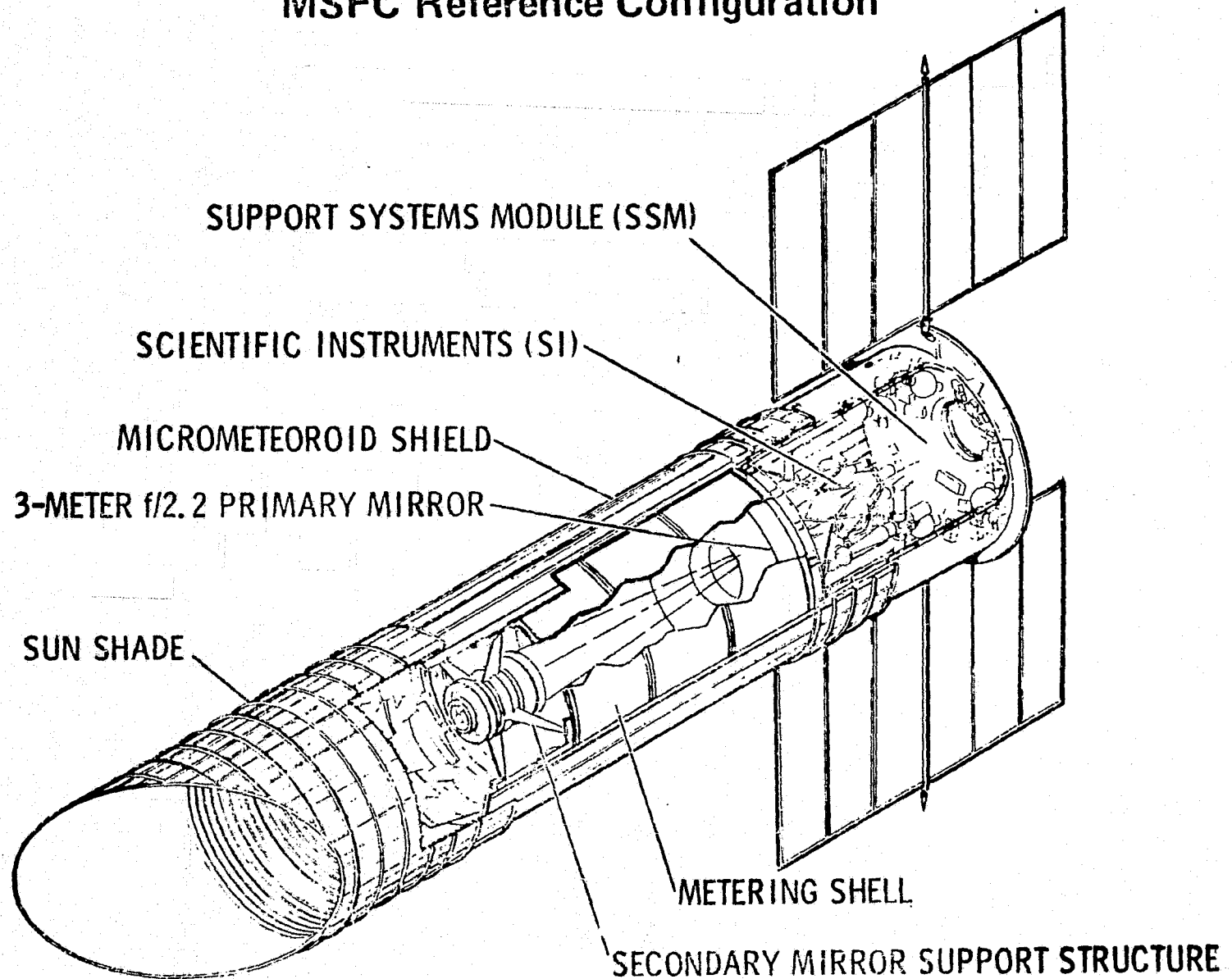


Figure 1-1. LST Configuration.

other structural applications, and some suitable varieties such as HM-S/X-904 and HM-S/X-30 have been qualified by outgassing tests to meet contamination control requirements.

The purpose of the GEMS program was to develop a graphite/epoxy metering structure for the LST application. This was accomplished by the design, fabrication, and test of such a structure. The program involved four phases.

- Phase II — Optical Structure Preliminary Design
- Phase III — Detail Design, Analysis, Material Processing, Component Test, and Quality Control
- Phase IV — Fabrication and Instrumentation
- Phase V — Test Evaluation and Delivery

Phase I was not part of the GEMS program, but consisted of an earlier development of polyimide composites for a different application.

Phase II of the program was started in June 1973 and the test program of Phase V was completed in December 1974. Two major delays occurred during the program. First, at the end of Phase II, production of the selected X-904 epoxy system was terminated for ecological reasons. This required the qualification of an alternative system, X-30, to the outgassing standards of 50M02442 "ATM Material Control for Contamination due to Outgassing." This was successfully accomplished in cooperation with MSFC. Following material procurement, the fabrication of the GEMS was accomplished within the originally scheduled time span. After completion of the static and dynamic tests, a further delay was caused by uncertainties with respect to the feasibility of measuring strains in the submicrometer range under the conditions of the thermal vacuum test. Due largely to the cooperation of MSFC, this problem was successfully resolved.

The major objectives of the preliminary design phase were (1) to select a concept for the purpose of this program from the competing metering shell and metering truss concepts, and (2) select a suitable scale for fabrication and test. The shell was selected since estimates made at that time indicated least cost for this concept. One-half scale was selected to minimize program costs and since this size is adequate to demonstrate performance and to develop fabrication techniques.

On this basis, a half-scale metering shell was designed using the geometry of the metering structure of the LST Phase A Reference Configuration shown in Figure 1-1. This geometry and size were pertinent to the 3 meter diameter LST which was under consideration at that time. The resulting half-scale metering shell is shown in Figure 1. A feature of importance which was adopted is the use of full-scale composite laminates in the half-scale structure. This was necessary to obtain true half-scale response to the thermal environment, to develop laminates directly applicable to the full-scale LST, and to develop fabrication techniques which could be readily scaled up to full size.

The primary objective of the program was then to demonstrate that a low cost metering shell could meet the dimensional stability requirements of the Large Space Telescope. In line with this objective the goal of meeting the full-scale LST stability criteria was established: These criteria applied with a structural temperature differential of 5.55°K (10°F), and for the half-scale version were translated to:

Despace	=	± 1 micrometer (39.37 microinches)
Decenter	=	± 5 micrometers (196.9 microinches)
Tilt	=	± 4.9 microradians (1 arc second)

The value of the tilt criterion was tentatively maintained as the same as for the full-scale LST. This was because it was considered that bowing of the shell structure would be the major contribution to tilt, and in this case due to geometrical similarity this value would be independent of scale. The temperature differential could be applied as a uniform temperature change, a longitudinal gradient, or a circumferential gradient. Under these conditions, the despace value of ± 1 micrometers was theoretically determined to be the most critical criterion. Prior to fabrication of the shell the thermal expansion of the selected laminates was experimentally verified to be within the range consistent with the overall stability requirements.

The goal of low cost was attained by focusing attention in design on simple component geometries, simple fabrication and assembly techniques and low cost concepts for the associated tooling.

SECTION 2

PRELIMINARY DESIGN

2.1 EVALUATION OF FULL-SCALE DATA

This phase of the program performed preliminary design studies and assembled comparative data on the two candidate concepts for the metering structure of the large space telescope (LST). This led to the selection of one concept, the shell, for the purpose of this program. Studies were also accomplished to determine the most suitable scale for the metering structure. This was determined to be half-scale on the basis of low program costs, valid representation of full-scale characteristics, realistic development of full-scale laminates, and low technical risk.

The structural concept and material system for the scale model was, of course, selected on the basis of the results of studies on the full-scale LST. These studies were performed under a parallel company-funded program on the overall LST system. A substantial part of the Phase II task in the contractual effort involved the assessment of the full-scale LST data to facilitate the selection of the structural concept and a material system for the scale model.

2.1.1 DIMENSIONAL STABILITY. Given acceptable non-contaminating characteristics, the most critical consideration with respect to the metering structure involves the stringent requirements for dimensional stability. In the parallel company-funded studies, Convair has developed a Nastran model of the complete LST structure including the subsystems module (SSM) and micrometeoroid shield (MMS). This model has been found to be essential for meaningful analysis of dimensional stability in view of the large distortions that the uninsulated aluminum SSM and MMS transmit to the metering structure. The model has been exercised frequently and selected results are presented here to aid in the comparison between the truss and the shell concepts in the critical area of dimensional stability.

The comparative performance with respect to compliance with dimensional stability criteria for the truss and shell concepts are compared. The basis of the analysis is a period of observation for the LST shortly following a reorientation of the instrument, which causes a change in structural temperatures. The secondary mirror is adjusted immediately prior to observation but is subsequently displaced due to a thermal gradient change around the circumference of the metering shell of 0, +1.1, +0.2, and -0.06°F at 90-degree arc intervals. The values of the thermal coefficient of expansion (CTE) used in the analysis were 0.05μ in/in °F and 0.07μ in/in °F for the truss longitudinally. Two observations are pertinent at this point: 1) other analyses based on different operational requirements indicate that the temperature changes may be

increased by as much as a factor of 10, and 2) the attainment of this low value of CTE requires the development of techniques to control or compensate for the effects of scatter. Current indications are that scatter in the CTE of graphite epoxy may be approximately plus or minus three times the absolute values assumed in the analysis. Techniques for compensating for scatter are under investigation and are described later on in this report.

The movements of the secondary mirror relative to primary mirror are shown in Table 2-1 for each of the two metering structure concepts. The contributions of the MMS and SSM are shown in addition to that of the metering structure to produce the totals given. These contributions are due to the transmission through the aft end of the metering structure of large distortion effects from the aluminum MMS and SSM. (These figures do not exactly summate to the totals shown since they are extracted from the analysis as vectors in varying directions.)

Table 2-1. Thermal Movement of Secondary Mirror, Full-Scale LST

CONCEPT	DUE TO	SECONDARY MIRROR MOVEMENTS		
		DECENTER (μm)	TILT ($\mu\text{ RAD}$)	DEFOCUS (μm)
TRUSS (GRAPHITE/EPOXY)	MMS	64.9	16.9	-0.7
	SSM	20.8	5.0	-1.2
	TRUSS	0.72	0.14	+0.2
	TOTAL	85.2	21.8	-1.7
SHELL (GRAPHITE/EPOXY)	MMS	45.0	12.9	-0.4
	SSM	16.2	4.3	-0.8
	SHELL	0.45	0.08	+0.1
	TOTAL	56.6	17.1	-1.1
ALLOWABLE (PER PHASE A REPORT)		± 10.0	4.90	± 2.0

Obviously, the totals for decenter and tilt do not comply with requirements in either the truss or the shell. If the effects of the MMS and SSM can be eliminated, however, the figure indicates that both concepts comply with the allowable movements. This would apparently be true even if the temperature changes were an order of magnitude higher than used in the analysis. To achieve the required level of stability necessitates consideration of methods of decoupling the SSM and MMS from the metering structure and techniques for control of the CTE. These considerations have been addressed for both the truss and the shell concept and are described in the following section.

2.1.2 DECOUPLING CONCEPTS. One feasible approach to "decoupling" the SSM and MMS is a three-point attachment of the SSM to the bulkhead while the metering structure is still continuously attached to the bulkhead. This is illustrated in Figure 2-1. This allows the SSM and MMS to distort independently of the metering structure since a three-point attachment is statically determinate. This concept requires the addition of a ring frame to the SSM to replace the "decoupled" bulkhead. The support points of the LST from the orbiter are then located at this ring frame. This approach will also require local reinforcement of the metering structure in the vicinity of the three hard points to meet the stiffness requirement of a fixed-base, natural frequency of 15 Hz minimum. This is probably not a penalty, since analysis has shown that even in the case of the continuously attached SSM, high local load intensities are induced into the metering structure due to the proximity of the main LST/orbiter attachments.

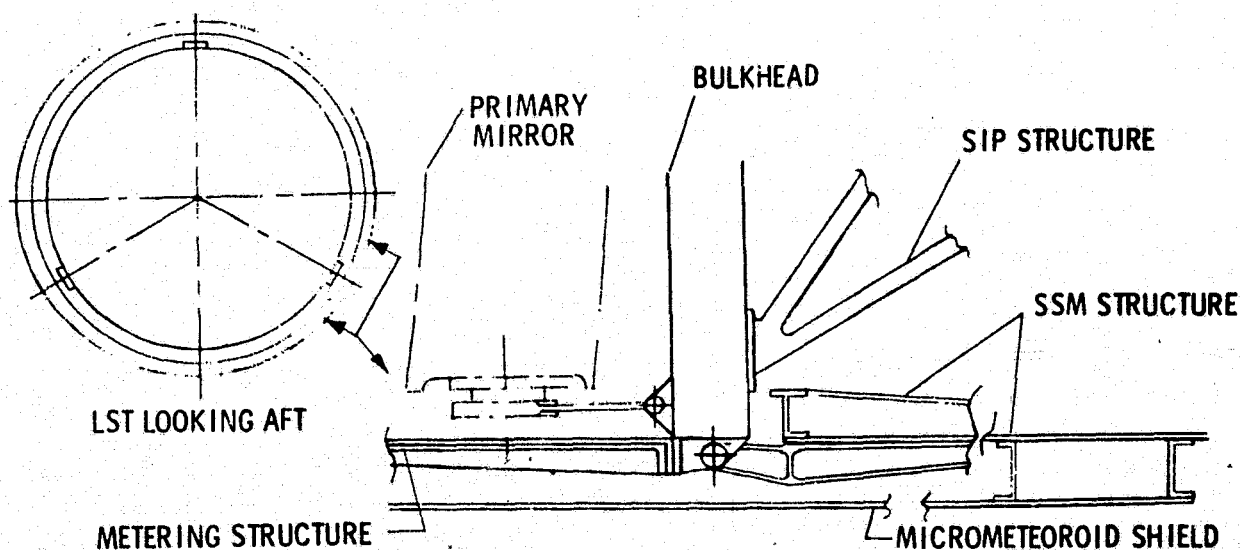


Figure 2-1. Three-Point SSM Attachment

In another decoupling concept the three components of the optical system, the metering structure, the primary mirror support, and the scientific instrument structure (SIS) are connected by links to a single pivot point at each of three points around the circumference of the bulkhead. This approach tends to minimize the alignment problem throughout the optical structure but may have other problems due to the complexities involved in the intermeshed linkage, particularly in view of the extreme precision fits that will be required.

Another approach to the problem of coupled distortion effects is to minimize them by changing the material of the MMS and SSM to graphite-epoxy to reduce the distortions by employing a material with a low coefficient of expansion. The basic shell structures using this material will be more expensive than aluminum shells, but this may be offset by the costs of the linkages and load distribution structures required in the two concepts previously discussed.

Table 2-2 presents preliminary results of analysis for these concepts. The requirements are met in all three modes for the concepts previously discussed. A fourth possibility, graphite-epoxy for the MMS alone, is added to show that this is a potential solution.

Table 2-2. Effects on Thermal Movement of Decoupling or Material Changes

CONCEPT	DECENTER (μ m)	TILT (μ RAD.)	DEFOCUS (μ m)
COMMON 3-POINT	0.82 ✓	0.02 ✓	0.03 ✓
3-POINT SSM	0.45 ✓	0.08 ✓	0.12 ✓
G/E MMS & SSM	5.15 ✓	0.42 ✓	0.30 ✓
G/E MMS	12.10	1.82 ✓	0.20 ✓
ALLOWABLE	± 10.0	4.90	± 2.0

The conclusion from this study is that coupling effects can be sufficiently alleviated to allow either metering structure concept, truss or shell, to meet dimensional stability requirements provided the low coefficients of thermal expansion used in the analysis can be attained. In the event that scatter in the value of this property cannot be adequately controlled, techniques for compensation for this effect are feasible for both truss and the shell concept, and are described in the remainder of this section.

2.1.3 MINIMUM CTE CONCEPTS. In the case of the truss-type metering structure, the "Athermalized Concept" offers an attractive means of attaining very low nominal values of effective coefficient of expansion. In this concept of a "tubular" truss structure, the rings are designed such that the expansion/contraction of the ring compensates for the expansion/contraction of the column as shown in Figure 2-2. The ratio of coefficients of expansion shown is a nominal value for the current LST. Considerable

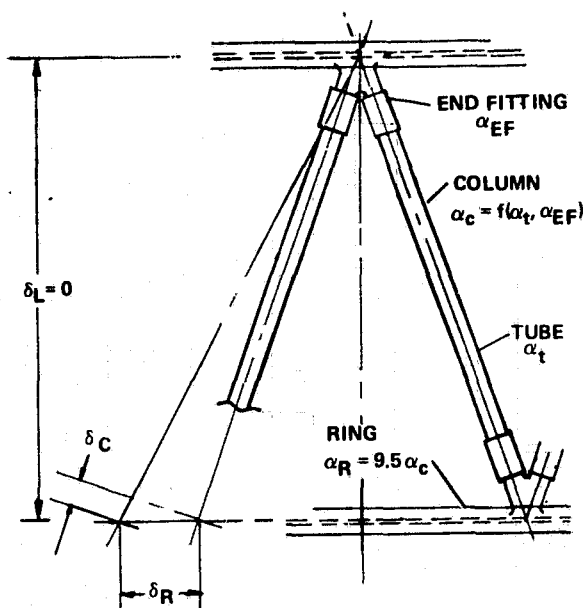


Figure 2-2. Athermalized Truss Concept, Graphite-Epoxy

variation will occur with geometry variations and with temperature differentials between the frame and column. As previously discussed the performance of this concept is extremely susceptible to the effects of scatter in the value of the CTE. A feasible approach to compensating for this would be to employ tubes and end fittings with opposing expansion characteristics. These components could then be tested to obtain "as-built" coefficients of expansion and the position of the fitting/tube splice adjusted to obtain the required effective CTE for the strut assembly.

In the case of the shell concept, a method of tuning graphite-epoxy structures to obtain very low values of CTE has been successfully demonstrated under a parallel IRAD program. This approach consists of de-

signing a component with a negative CTE, testing it to obtain the true CTE, and bonding on aluminum (positive CTE) strips to obtain an effective $CTE \rightarrow 0$. This approach could be applied to the shell-type metering structure by adding strips in line with the primary and secondary mirror attachment points to control the CTE in these critical locations.

2.1.4 CONCLUSIONS FROM FULL-SCALE STUDIES. It was concluded that by use of methods such as described here that both the truss and the shell concepts can meet the dimensional stability requirements. Neither is strength critical and both meet stiffness requirements, 19-Hz fixed-base natural frequency for the truss and 26-Hz for the shell — versus the requirement of 15 Hz. From the technical standpoint, the data indicated there is little to choose between the two concepts. The shell is heavier but weight is not currently critical. Estimates at that time indicated the shell to be the least costly. The estimates are not quoted here since subsequent design improvements in the truss have invalidated the original estimate of the cost differential.

2.2 SUBSCALE STUDIES

In parallel with the assessment of the full-scale data, both the truss and the shell concepts were studied to determine the appropriate reduced scale and configuration. The truss concept shown in Figure 2-3 was studied to determine the validity of a half-scale representation of the metering truss. This included analysis of the scaled details. Half-scale was considered to be the minimum scale at this time since the one-inch-diameter tubes applicable to this scale have been successfully manufactured.

The 1-1/2-inch high ring cross section is almost identical to that used for rings successfully fabricated and spliced by Convair for the OV-1 adapter. Analysis has been performed on the half-scale end fittings and these were shown to be feasible.

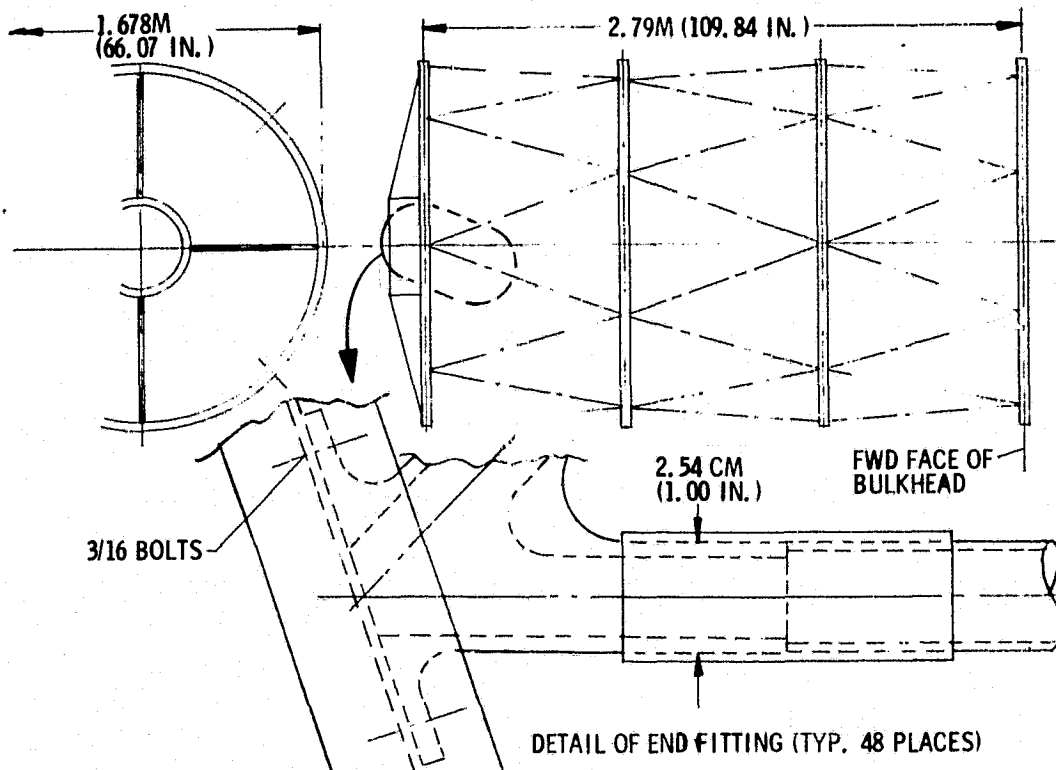


Figure 2-3. Half-Scale Metering Truss, GEMS Program

Similar design and analytical efforts have also been performed on a half-scale shell structure shown in Figure 2-4 with the same conclusions as the truss. This concept is described in more detail in Section 3.

2.3 SELECTION OF LAMINATE SCALE

A critical question arose with respect to scale models of composite structures. "Should the laminate be scaled in thickness?" This question was addressed and the conclusion was that the full-scale laminate should be used if possible. The alternative scaled laminate involves either a compromise in the number of plies, or in the ply thickness. Either of these compromises result in a difference in properties compared to those of the full-scale material.

Studies indicated that there are no geometrical or fabrication problems involved in the use of full-scale laminates on the half-scale structure. This approach was therefore adopted since:

- a. The full-scale laminate is truly representative of the full-scale LST material with respect to both fabrication and characterization.

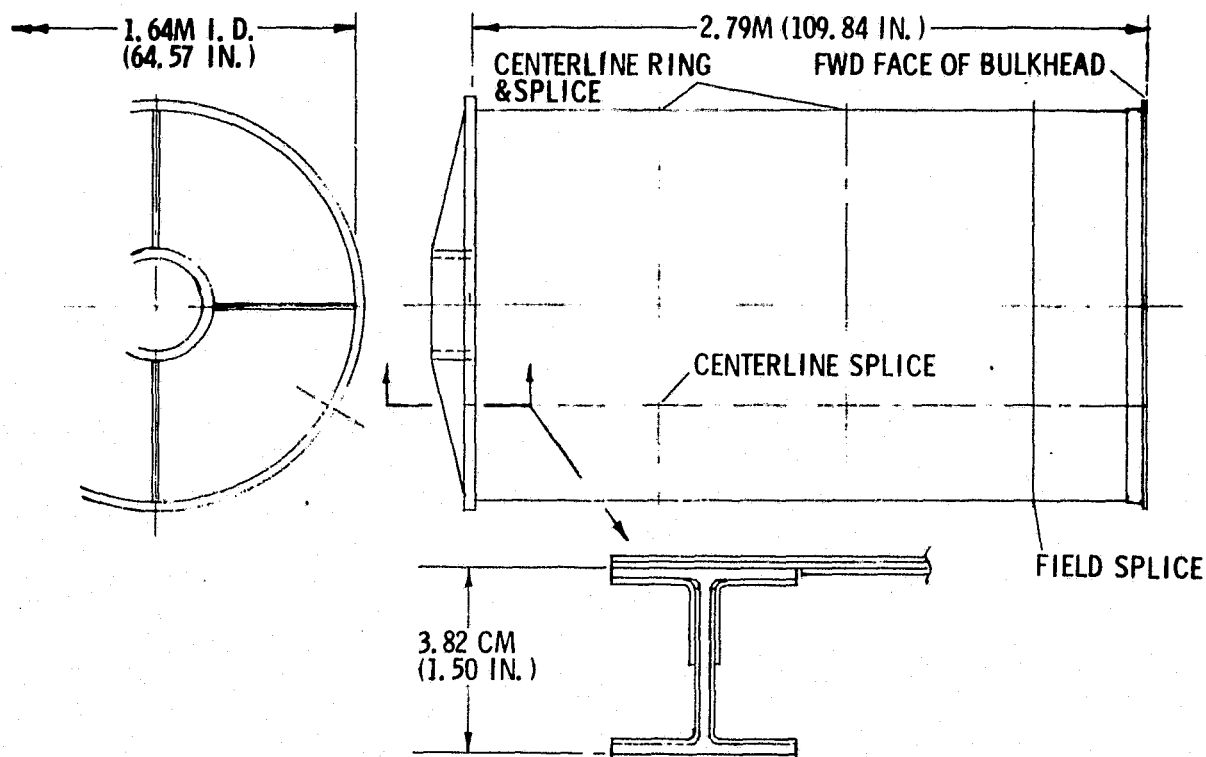


Figure 2-4. Half-Scale Metering Shell, GEMS Program

- b. Valid responses will be obtained in thermal vacuum testing.
- c. Valid limit load testing can be conducted by inducing the correct full-scale load intensities with the application of twice the truly scaled external loads.
- d. Dynamic tests will fulfill the essential requirement of verifying the method of analysis and determining the structural damping factor.

2.4 CONCLUSIONS OF PHASE II

2.4.1 GENERAL. As a result of the Phase II studies, Convair recommended that a scale of one-half size be adopted for this program. With respect to the choice between the truss and the shell concept, the study results indicated that both are acceptable from the standpoint of performance. There may be differences in development requirements associated with the attainment of close tolerances on coefficients of thermal expansion, but these differences cannot be determined without further development. In view of this situation, the estimated lower cost of the shell was considered the dominant factor. On this basis, the shell concept was adopted for the purposes of this program. In conjunction with this, the full-scale laminate was also adopted on the basis of the considerations discussed in Section 2.3.

2.4.2 METERING STRUCTURE/SSM INTERFACE. There are at least five candidate concepts for this interface — the baseline concept, and the four concepts presented in Section 2.1.2 as approaches to alleviating structural distortions.

At the close of Phase II, it was not possible to make a selection of one of these concepts without the considerable schedule slippage that would be required to perform the necessary trade studies and obtain agreement on the selection. The problem presented by this situation was that some local reinforcement at the aft end of the shell may be required, but at locations which differ depending on the interface concept selected. However, the local reinforcement is not expected to present significant problems in view of the following:

- a. Peak point load in the metering structure for a three-point attachment is only 2450 pounds ultimate.
- b. Dynamic analysis showed a natural frequency with a longeron at each of the three points of 22.7 Hz versus the requirement of 15 Hz.

In view of these considerations it was decided to proceed with design using a continuous bolted flange interface of the metering structure to the LST main ring with the assumption of a fixed base condition. A subscale structure designed on this basis was considered adequate to meet the objectives of the program in proving out the overall concept of the graphite-epoxy metering structure in view of the apparently nominal nature of the local reinforcement that may eventually be required. Furthermore, the section of the metering shell aft of the field splice can be modified or rebuilt in the event of a future requirement to test the effect of the selected interface.

SECTION 3

DESIGN AND ANALYSIS

3.1 DESIGN

3.1.1 INITIAL MATERIAL SELECTION. At the initiation of detail design, a serious problem arose in connection with material procurement. The material system selected for the program in concurrence with NASA MSFC was HM-S/X-904 or Modmor I/X-904. This selection was made on the basis of proven compatibility with the space environment, particularly with respect to acceptable outgassing characteristics, thermal expansion characteristics, resistance to microcracking, and the availability of an adequate design data base. At this point we were notified by the vendor of the basic resin used in X-904 epoxy that production had been terminated. In this situation it seemed unlikely that X-904 would be available in the future for application to the LST; consequently, the use of X-904 in an LST development program was deemed unacceptable.

In cooperation with NASA MSFC, other candidates were reviewed and tests were performed to select a suitable alternative.

3.1.2 ALTERNATE RESIN CANDIDATES. Candidate resin system to replace the selected X-904 formulation were Whittaker's 5208, American Cyanamid's BP-907, Hercules' 3501, Fiberite's X-30 (505), and Shell's Epon-1031 in the X-904 formulation. Convair is evaluating several of these systems under an existing independent research and development (IRAD) program. The Epon-1031 was dropped from consideration for the GEMS program because there was insufficient time to fully evaluate its equivalency to the old X-904 formulation. The other resin systems are or have been used extensively on other programs although very little of the data is available on the two candidate fibers (HM-S and Modmor I). The X-30 system was selected for the GEMS program on the basis of acceptable outgassing characteristics, the availability of extensive data with the candidate fibers, and proven resistance of the resin to microcracking when used as the matrix for high-modulus reinforced composites.

3.1.3 FIBER CANDIDATES. Thermal expansion requirements have dictated the need for a high-modulus fiber reinforcement. The two fibers selected for consideration on the GEMS program were the Hercules' or Courtauld's HM-S and the Morganite Modmor I. The fibers are considered equivalent and interchangeable. Convair's design analysis dictates a fiber modulus of 57 ± 2 msi. Morganite had made Modmor I in the past in the 57- to 59-msi modulus range. Convair therefore placed an order with Fiberite for Modmor I/X-30.

3.1.4 HM-S/X-30 AND MODMOR I/X-30 DATA

3.1.4.1 Outgassing Tests. Specimens of HM-S/X-30, postcured at 275 and 350°F respectively, were submitted by Convair to NASA MSFC for outgassing tests. The panels were tested per the ATM requirements and successfully passed the acceptance criteria as described in NASA MSFC Document 40M51264.

In addition, extensive outgassing tests have been performed at Convair on HM-S/X-30. Convair's facility consists of an ultra-clean vacuum system using a carbon-vane roughing pump and an ion high-vacuum pump capable of ultimate pressures lower than 10^{-7} torr. Measurements are usually made at pressures below 10^{-6} torr. Specimen temperature can be as high as 200°F; collector surfaces including a quartz crystal microbalance (QCM) and optical surfaces are held at 75°F. A General Electric partial-pressure analyzer employs a mass spectrometer to identify outgassing or residual gas products and can detect pressures as low as 10^{-14} torr. A QCM measures the mass of condensable outgassing product and is capable of detecting 3.5×10^{-9} gm/cm². The third capability of the apparatus is in-site reflectivity measurements at two wavelengths, 1848 Å and 1236 Å, of optical surfaces on which outgassing products may condense. Degradation of optical surfaces due to outgassing can thus be determined.

Convair recently completed a 226-hour exposure test (0/±30/±60/90)_s layup of HM-S/X-30 with the following parameters: pressure less than 2.3×10^{-7} torr, specimen temperature of 140°F, QCM temperature of 76 to 81°F, and collecting mirror temperature of 72 to 81°F. Mirror reflectivity changes were as follows:

1848 Å		1236 Å	
<u>Specular</u>	<u>Diffuse</u>	<u>Specular</u>	<u>Diffuse</u>
1.9%	2.2%	1.9%	0%

As specular reflectivity decreases, the diffuse reflectivity theoretically increases (or absorption takes place). The accuracy of Convair's reflectivity measurement is estimated to be 2%; consequently, within this uncertainty no degradation of the optical surface was detected. There was only a 1 Hz change in the QCM frequency. Since there is a resolution of 1 Hz with this instrument, at most 3.5×10^{-9} gm/cm² was deposited on the QCM which is located four inches from the specimen. The initial and final weights of the specimen were 21.0937 and 21.0931 grams, respectively. Since the accuracy of the weight measurement is determined by the absorption of moisture during weighing, this makes the fourth decimal place uncertain. It is therefore concluded that there was no change in weight of the specimen. The mass spectrometer detected no outgassing masses above 43 AMU.

3.1.4.2 Properties Test Data. Convair has extensive mechanical and physical properties data on the Fiberite X-30 epoxy resin with various high-modulus fibers; i.e., HM-S, Modmor I, GY-70 and Thermal 75. Very extensive thermal property data has been generated by Convair under Air Force Contract F33615-72-C-1388, "Advanced Composite Missile and Space Design Data." This data includes effects of resin systems, composite layup, resin content, microcracks, etc., on composite thermal expansion. Under this program, the X-30 system was selected for the continued production and evaluation of mirror substrates because of its ease in processing and resistance to microcracking.

The effects of water on Modmor I/X-30 has been evaluated by Fiberite Corporation under Navy Contract, shows no adverse effects for the intended application.

3.1.5 ADHESIVE SYSTEM. Hysol's EA-934 Epoxy is selected as the adhesive system for the skin splices, the attachment of rings and field splice segments to the skin, the joint of elements of the secondary mirror support, and all other secondary bonding applications. This system is selected primarily on the basis of acceptable outgassing characteristics and the availability of an extensive data base. The EA-934 adhesive has been tested at -320° F.

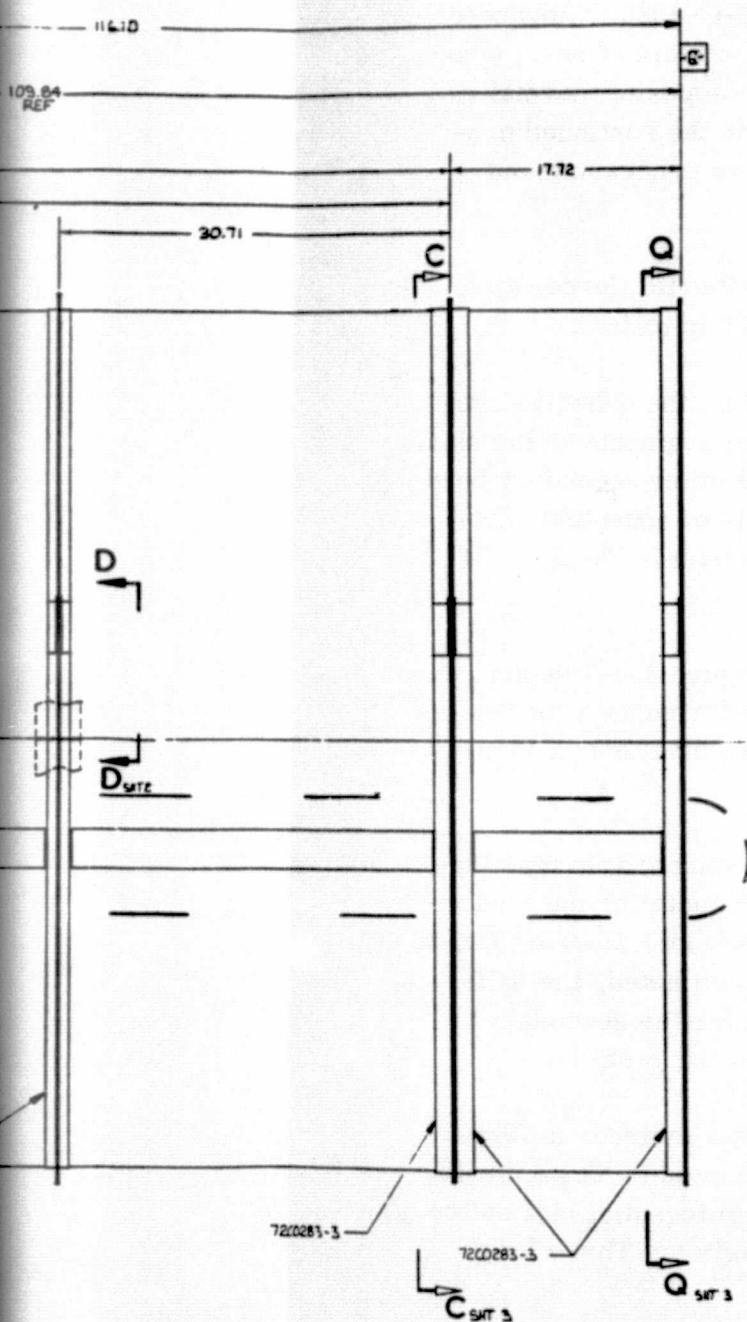
3.1.6 METERING SHELL STRUCTURAL ARRANGEMENT. Figure 3.1-1 depicts the structural arrangement, the overall geometry of which is in conformance with the geometry of the metering truss shown in the Large Space Telescope Phase A Final Report.

The structural concept employed is of the ring-supported, semi-monocoque type featuring a monolithic unstiffened skin, the stability of which is adequate for the load intensities applicable to the LST. The structure utilizes graphite/epoxy Modmor I/X-30 throughout, except for the adhesives and fasteners. As previously noted, the half-scale structure employs full-scale laminate thicknesses except for the secondary mirror support legs. It is described in more detail in the following sections.


3.1.6.1 Monocoque Skin. The skin of the metering shell forms a cylinder 2.79m (109.84 in.) long and 1.64m (64.56 in.) in diameter. It is fabricated in 12 segments consistent with the proposed full-scale metering shell. A circumferential butt splice occurs at each of the two intermediate frames and at the field splice. Three longitudinal butt splices are provided at 120-degree arc intervals.

The dominant design criteria for the skin are:

- a. Longitudinal coefficient of expansion (CTE) = 0.
- b. Shell stability of the full-scale shell under shear and compression.



NOTES:

- 1.0 LOCATE INDICATED SPLICE STRIPS SUCH THAT THE GAPS AT EACH END, AS NOTED, ARE EQUAL WITHIN .03.
- 1.1 LOCATE 72C0263-2 & -7 SO THAT THE TWO LOCATING DIMENSIONS MEET THE FOLLOWING CRITERIA:
 - A. BE EQUAL TO EACH OTHER WITHIN .03.
 - B. BE EQUAL TO OR GREATER THAN .01.
- 1.2 LOCATE THE INDICATED SKIN SEGMENTS SUCH THAT THE TWO GAPS ARE EQUAL WITHIN .03.
- 1.3 ALL SPLICES, FITTINGS, SKINS, FRAMES, & ASSYS ARE BONDED (UNLESS NOTED OTHERWISE ON F/D) WITH O-00096-52 EPOXY. APPLY EPOXY PER O-79129-14.
- 1.4 APPLY PRESSURE ACROSS ALL BOND LINES DURING CURE
- 1.5 TORQUE FASTENERS PER O-70058.
- 1.6  INDICATES CRITICAL INSPECTION

AR	O-00096-52	EPOXY
59	MS21044H3	NUT
102	AN360PD10L	WASHER
8	AN360PD10	WASHER
4	AN3607A	BOLT
16	AN3606A	BOLT
39	AN3605A	BOLT
3	72C0283-3	FRAME
2	72C0283-2	FRAME
1	72C0283-1	FRAME
4	72C0282-2	NTACH FITTING
4	72C0282-1	NTACH FITTING
1	72C0281-1	STRUCTURE
3	72C0263-6	SPLICE
5	-7	
5	-6	
6	-5	
9	-4	
6	-3	
3	-2	
5	72C0263-1	SKIN
8	-2	WASHERS MP AN360PD10; SEE SHIT 3
ASSY OF SECONDARY MIRROR SUPPORT		
-1	PART NO	DESCRIPTION SPECIFICATIONS: NOTES: ETC.
PARTS LIST		
ASSY DASH NO		
PRELIMINARY DESIGN DRAWING		
GRAPHITE EPOXY METERING SHELL (GEMS) ASSEMBLY		
GENERAL DYNAMICS		
14170		
72C0280		
MAY 14 1964		
SAN DIEGO, CALIFORNIA		

FOLDOUT FRAME

2

These lead to the selection of a ply layup that must:

- a. Exhibit a nominal CTE = 0.
- b. Exhibit low sensitivity of CTE to manufacturing variation in ply orientation.
- c. Be symmetrical to avoid distortion during cure.
- d. Equal ≈ 0.06 inch in thickness to meet the stability requirement.

The selected laminate that meets these requirements is $(0_3/\pm 45.5/90)_S$ using twelve 0.005-inch plies to give a thickness of 0.06 inch.

The longitudinal edges of the skins are joined by a butt splice arrangement which features inner and outer splice straps, as shown in Figure 3.1-2. The splice straps are bonded with room temperature cure-epoxy adhesive EA 934. The splice straps are the same thickness and layup as the skins to minimize cost by permitting the layup and cure of the straps in one segment with the associated skin panels.

3.1.6.2 Secondary Mirror Support Ring. This ring is located at the forward end of the metering shell. Its primary function is to distribute the loads from the legs of the secondary mirror support structure into the monocoque skin. It must also provide adequate stiffness to assure that the natural frequencies of any in-place dynamic

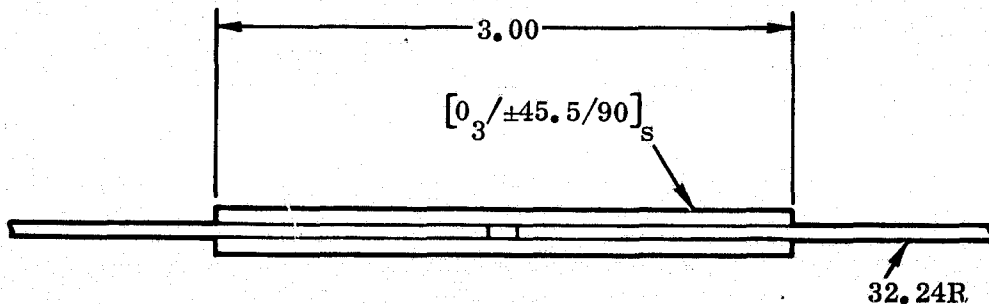


Figure 3.1-2. Longitudinal Splice

response modes at this station are acceptable. An I-section, shown in Figure 3.1-3, has been selected to meet this requirements on the basis of adequate strength and stiffness for minimum material and layup costs.

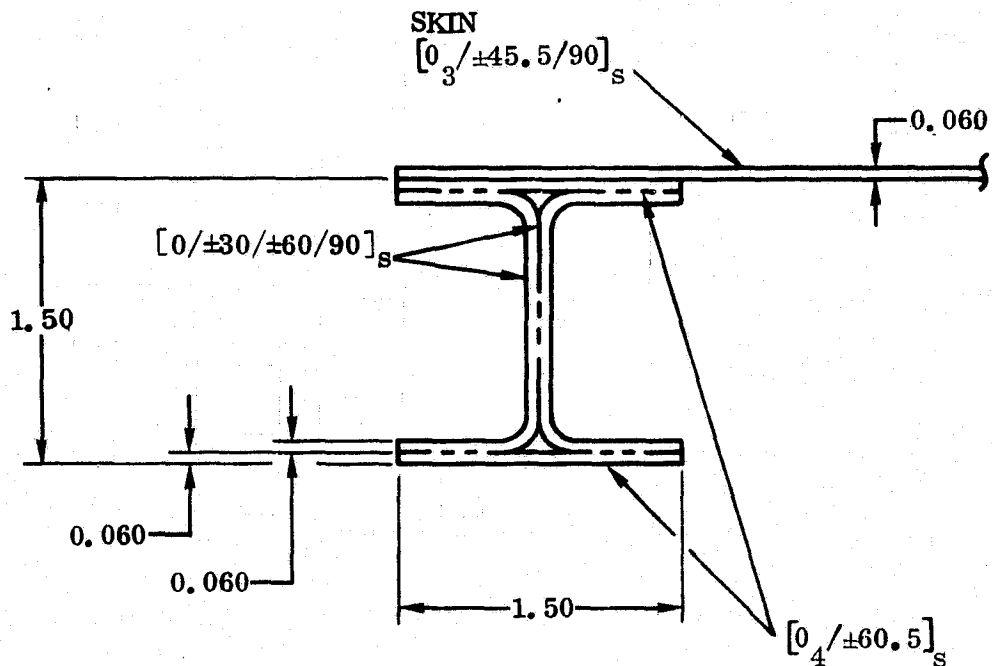


Figure 3.1-3. Cross Section, Forward Ring

The most important design criterion for this ring in conjunction with the effective skin is that a nominal overall coefficient of expansion of zero should be provided to minimize the decenter of the secondary mirror due to asymmetric heating. The attainment of this is complicated by the anisotropic nature of a zero CTE laminate. It would be extremely difficult and expensive to lay up this type of laminate around the circumference of a frame by varying the ply angular orientation to maintain the correct relationship relative to the local tangency. The adopted solution to this problem is to use a pseudo-isotropic layup with a positive CTE for the two channel sections shown in Figure 3.1-3, and an anisotropic negative CTE layup for the two cap strips. The layups selected to accomplish this are shown in Figure 3.1-3.

3.1.6.3 Intermediate Rings. These occur at two stations consistent with the full-scale LST arrangement. The primary function of the intermediate rings is to maintain the shape of the shell to ensure overall stability. Each ring also provides the outer strap of a circumferential skin splice. The skin splice arrangement is completed by the provision of an internal circumferential strap. The approach to the design of these rings is the same as the approach proposed for the LST to reduce costs. A T-section is used for the cross section, as shown in Figure 3.1-4. The proportions of the cross section are selected to allow the use of the same tooling as for the forward ring. The ply orientations are the same as for the skin to avoid the development of different layup techniques and to assure compatibility with the skin expansion.

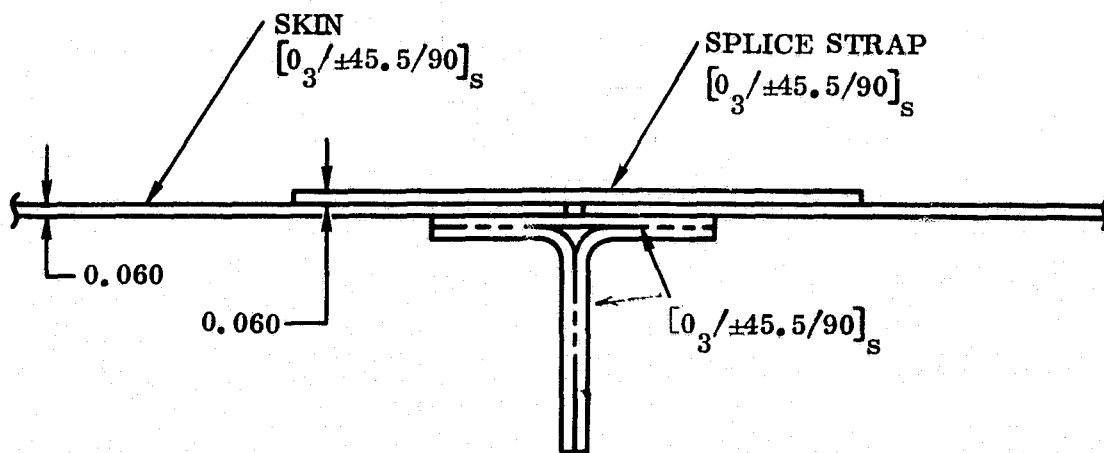


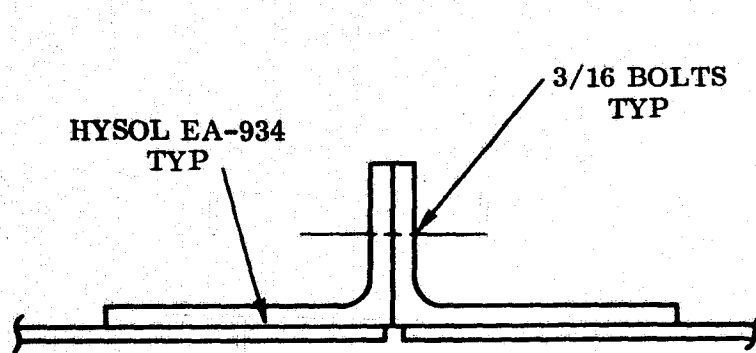
Figure 3.1-4. Cross Section, Intermediate Ring

The size of the ring segments and the location and arrangement of the splices are similar to those described for the secondary mirror support ring.

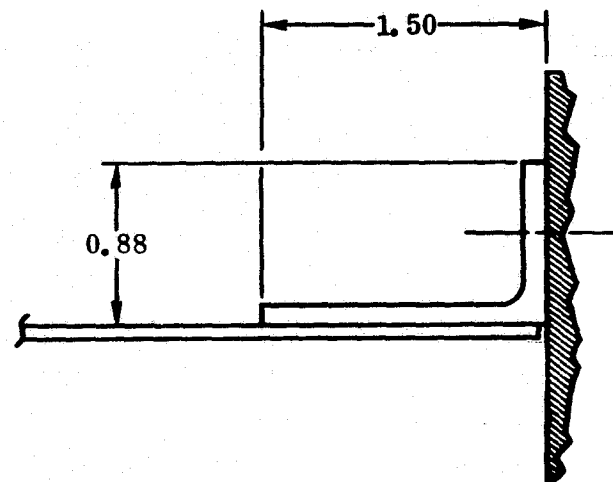
3.1.6.4 Skin Splices. The circumferential skin splices have been described in conjunction with the intermediate rings in Section 3.1.2.3. Three longitudinal splices occur at 120-degree arc intervals. The skins are butted and joined by internal and external splice strips bonded with room temperature curing Hysol EA-934. The splice straps and also the circumferential splice straps described in Section 3.1.2.3 use the same laminate $(0_3/\pm 45.5/90)_s$ as the basic skin. This design minimizes tooling and layup costs by allowing the straps to be layed up with the skin and subsequently cut from the cured panels.

3.1.6.5 Field Splices and Attachment of LST Main Ring. To minimize costs, the components used for these two items are identical. The detail arrangement of both is shown in Figure 3.1-5. The design is, of course, based on the more highly loaded attachment to the LST main ring. The peak loading in this case, however, is only 67 lb/in. ultimate. In this situation the dominant criterion for bolt selection arises from the requirement for non-magnetic properties. In this case, the prime material candidates were aluminum, titanium, and corrosion-resistant steel, A-286 CRES. All of these materials were under consideration for the full-scale LST. For the half-scale metering shell, A-286 CRES was selected on the basis of availability and since there was cause for concern due to the possibility of failure of 3/16-inch-diameter aluminum bolts due to overtightening.

3.1.6.6 Secondary Mirror Support Structure. This structure consists of a cylindrical hub on the optical axis of the telescope, supported from the forward ring of the



FIELD SPLICE



MAIN RING ATTACHMENT

Figure 3.1-5. Field Splice and Attachment to LST Main Ring

shell by four radial legs. It is shown in Figure 3.1-6. The hub consists of two concentric cylindrical skins attached at each end to a channel section frame to form a closed box section. The secondary mirror is attached via system of alignment actuators to the forward face of the hub. Continuity of the bending structure across the hub is provided by differential/bending in the two end rings. The significant design criteria for the secondary mirror support structure are:

- a. The attainment of $CTE \rightarrow 0$ to minimize decenter and tilt due to non-uniform temperature distributions across the structure, and despace due to temperature variations.
- b. Minimized projected frontal area to minimize obscuration.
- c. Adequate lateral stiffness in the legs for the first bending mode of the legs and for rotational response of the mass at the hub.

The last two criteria cause the selection of a solid-plank type cross section for the legs to achieve the required stiffness with minimum frontal area. To meet the first criterion requires a ply orientation similar to the skin, which used $(0_3/\pm 45.5/90)_S$. This is an excellent layup since the CTE is relatively insensitive to manufacturing variations in the ply orientation. However, the thickness of the full-scale secondary mirror support leg is expected to be in the neighborhood of 0.5 inch, a dimension

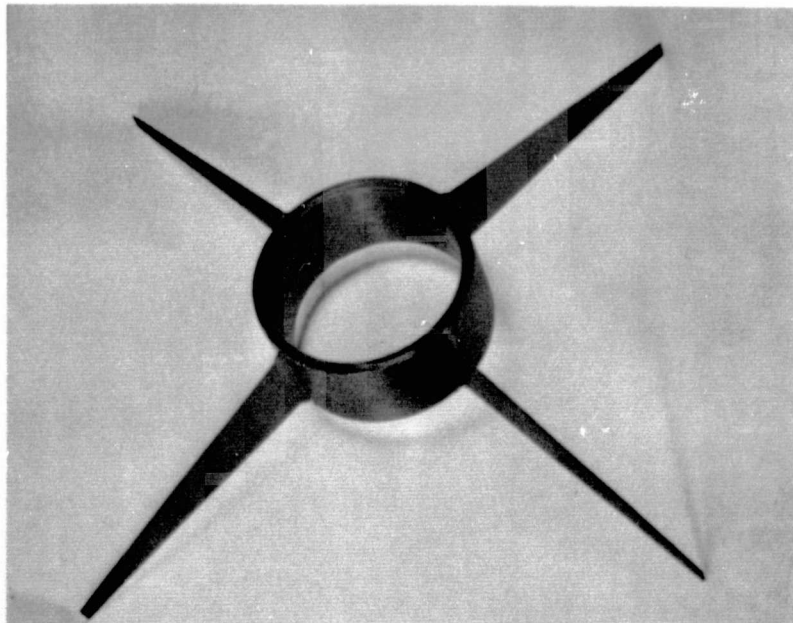


Figure 3.1-6. Secondary Mirror Support

determined by stiffness requirements. Since the legs are not strength critical, in contrast with the approach taken on the GEMS structural generally, half-scale thickness for the half-scale component was adopted. This approach effected a significant saving in material and layup costs of these thick components, while still simulating full-scale fabrication techniques and assuring the correct dimensional response to temperature variations.

3.2 ANALYSIS

3.2.1 DESIGN CRITERIA

3.2.1.1 Dimensional Stability. The GEMS structure is designed to give an effective coefficient of thermal expansion of nominally zero in the applicable orbital temperature range. Within the constraints of minimum CTE data scatter, stiffness and strength, the ply orientation is such that sensitivity to small perturbations about the exact layup is minimized. Generally, the approach was to maximize dimensional stability. The design objective is to maintain the following alignment criteria in the GEMS structure for the most severe temperature changes in the observational environment.

Despace = ± 1.0 micrometer (39.37 microinches)

Decenter = ± 5.0 micrometers (196.85 microinches)

Tilt = 4.9 microradians (1.0 arc second)

These values are scaled for the half-scale structure from the full-scale LST criteria:

Despace = ± 2.0 micrometers (78.74 microinches)

Decenter = ± 10.0 micrometers (393.7 microinches)

Tilt = 4.9 microradians (1.0 arc second)

3.2.1.2 Load Factors. Full scale load factors as stated in Reference 2.2.1 are presented in Table 3-2.1.

3.2.1.3 Factor of Safety. The ultimate factor of safety applied to limit loads shall be 1.75. This value is adopted since it would permit the static testing of the full-scale LST flight article to 1.4 times limit load, thereby reducing program costs by the elimination of a static test article.

3.2.1.4 Material Properties and Design Allowables. The laminate material system selected was Modmor I/X-30. Considerations determining selection were high modulus, adequate strength, reliability, workability and availability. Tables 3-2.2, 3-2.3, and 3-2.4 present test data generated from panels fabricated with the Modmor I/X-30 prepreg as received. Where data was missing, existing data on HM-S/X-30 was used. Figures 3.2-1, 3.2-2 and 3.2-3, present typical stress-strain curves for HM-S/X-30 based on test data generated at GD/CD (Reference 3.2.2). HM-S/X-30 values are sufficiently close to Modmor/X-30 values as to warrant their use in completing the material properties design space. Table 3-2.5 presents a composite summary of material design allowables for the system.

Table 3-2.1 Payload Bay Load Factors

Condition*	X_o	Y_o	Z_o
Liftoff**	-1.7 ±0.6	±0.3	-0.8 -0.2
High Q Boost	-1.9	±0.2	+0.2 -0.5
Booster End Burn	-3.0 ±0.3	±0.2	-0.4
Orbiter End Burn	-3.0 ±0.3	±0.2	-0.5
Space Operations	-0.2 +0.1	±0.1	±0.1
Entry	±0.25	±0.5	+3.0 -1.0
Subsonic Maneuvering	±0.25	±0.5	+2.5 -1.0
Landing and Braking	±1.5	±1.5	+2.5
Crash†	+9.0 -1.5	±1.5 ±1.5	+4.5 -2.0

*Positive X, Y, Z directions equal aft, right, and up. Load factor carries the sign of the externally applied load (as applied to the shuttle payload).

**The factors include dynamic transient load factors at lift off.

† Crash load factors are ultimate and only used to design payload support fittings. All other load factors are limit. Crash load factors are for the nominal payload of 65,000 pounds. The specified crash load factors shall act separately.

Table 3-2.2. Test Results, Tensile Moduli of 12-ply Unidirectional Modmor I/X-30

PANEL IDENTIFICATION	MODULUS (10 ⁶ PSI)	
	LONGITUDINAL*	TRANSVERSE*
T4	29.8	1.32
T5	27.4	1.17
T6	27.3	1.20
3X	28.6	—
4X	28.6	—
T7	26.8	—
T8	26.2	—
T9	30.1	1.16
T11	30.2	1.22
T12	29.0	1.19
T14	28.6	1.23
AVERAGE	28.4	1.21

*AVERAGE OF THREE SPECIMENS/PANEL

Table 3-2.3. Test Results, Poisson's Ratio and Shear Modulus for 12-ply Unidirectional Modmor I/X-30

PANEL	POISSON'S* RATIO	TUBE	SHEAR MODULUS (10 ⁶ PSI)
T4	0.30	1	0.89
T5	0.22	2	0.78
T6	0.24	3	0.90
3X	0.29	4	0.83
4X	0.33	5	0.76
T7	0.26	6	0.91
T8	0.30		
T9	0.28		
T10R	0.23		
AVERAGE	0.27	AVERAGE	0.85

*AVERAGE OF THREE SPECIMENS/PANELS

Table 3-2.4. Unidirectional CTE, 12-ply Modmor I/X-30

LONGITUDINAL		
PANEL	m/m °K	IN./IN. °F
T4	-0.72	-0.40
T5	-0.58	-0.32
T6	-0.52	-0.29
T7	-0.29	-0.16
T8	-0.40	-0.22
T9	-0.49	-0.27
T10A	-0.54	-0.30
T10R	-0.65	-0.36
T11	-0.65	-0.36
T12	-0.63	-0.35
T13	-0.49	-0.27
T14	-0.59	-0.33

TRAVERSE		
PANEL	m/m °K	IN./IN. °F
T4	24.1	+13.4
T5	24.8	+13.8
T6	25.2	+14.0
T9	24.8	+13.8
T10R	25.6	+14.1
T11	24.7	+13.7
T12	25.7	+14.3
T13	25.6	+14.2
T14	26.8	+14.9

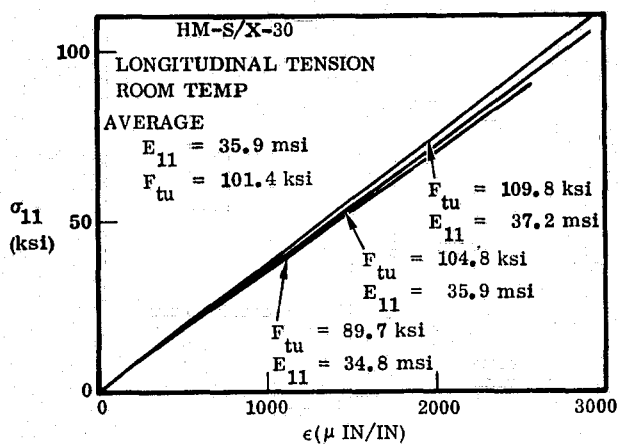


Figure 3.2-1. Longitudinal Lamina Properties

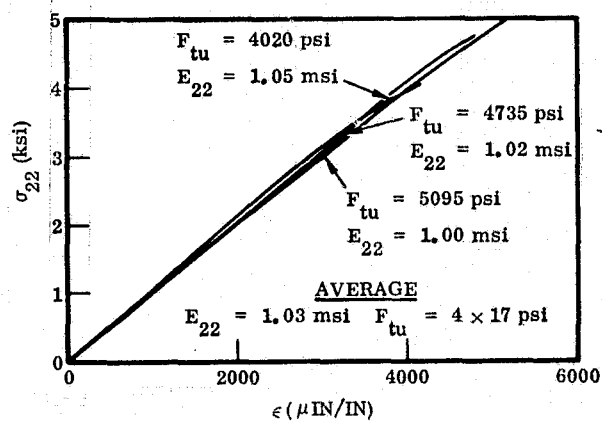


Figure 3.2-2. Transverse Lamina Properties

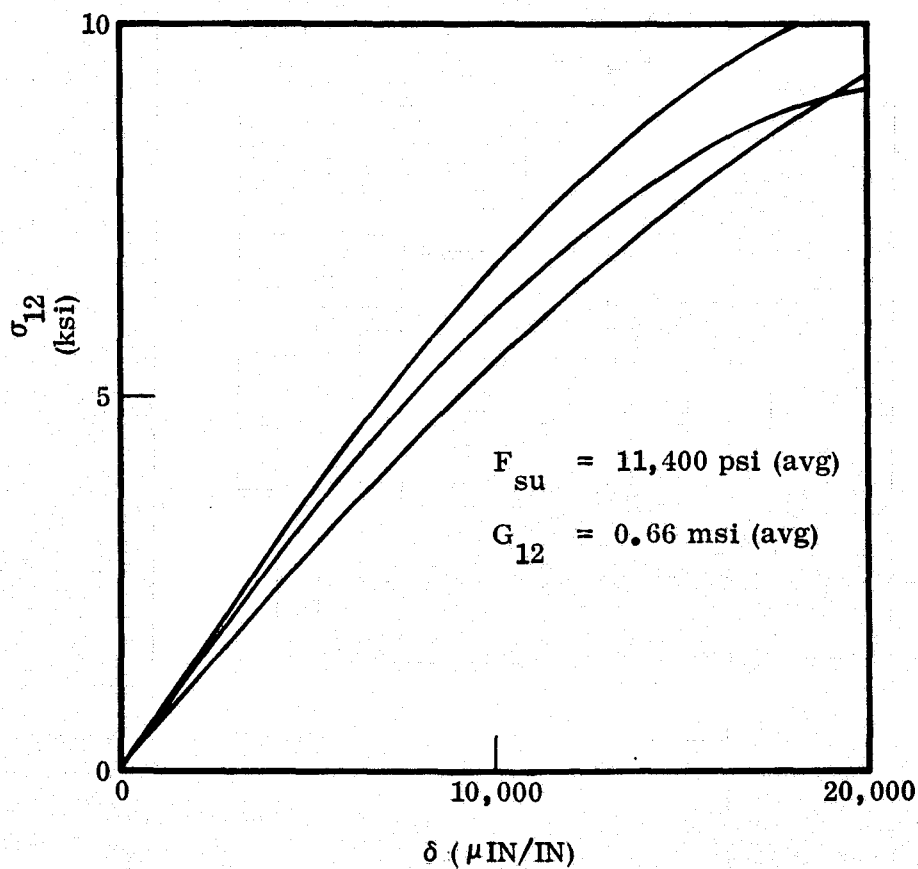


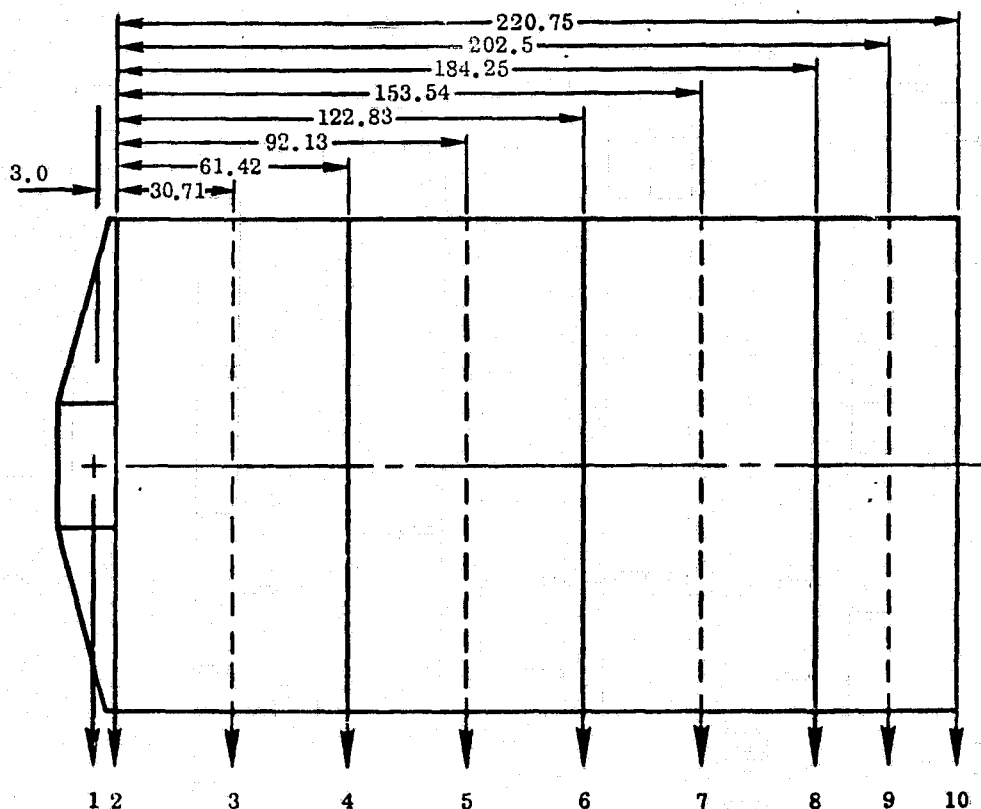
Figure 3.2-3. Shear Properties

Table 3-2.5 Material Design Allowables

F_{tu} (ksi)		$\epsilon_{tu} \times 10^6$	
L	89.7	L	2580
T	4.02	T	4080
F_{cu} (ksi)		$\epsilon_{cu} \times 10^6$	
L	89.7	L	2580
T	—	T	—
$F_{su LT}$ (ksi)	11.44	$\gamma_{LT} \times 10^6$	>22,000
E (msi)		$\alpha(\mu\epsilon/Fo)$	
L	28.4*	L	-.33*
T	1.21*	T	14.9*
G_{LT} (msi)	.85*		
ν_{LT}	.27*		

*Modmor I/X-30 average test results

3.2.1.5 Mass Properties (complete model, full-scale). The following mass properties were input to the finite element model for the purpose of the internal loads analysis.



STATION	1	2	3	4	5	6	7	8	9	10
MASS-LB	224.0	51.84	51.12	67.68	51.12	67.68	51.12	55.92	30.48	28.8

TOTAL MASS = 679.76 LB

3.2.2 LAMINATE SELECTION. Three key structural components strongly influence the thermal dimensional stability: 1. shell structure; 2. forward ring; 3. secondary mirror support structure. A design relying on thermal insensitivity rather than compensation was selected on the basis of minimum number of design variables with attending heightened reliability. Thermal insensitivity was achieved by selecting lamina orientations that produce zero coefficient of thermal expansion (CTE) along the metering axis. Selection criteria for the candidate laminates was: 1. design weight; 2. adequate stiffness and strength; 3. minimum sensitivity to small perturbations about the design orientation.

Parameter studies utilized a laminate analysis program that calculates laminate properties from the stacking sequence and orientation of the lamina. Preliminary

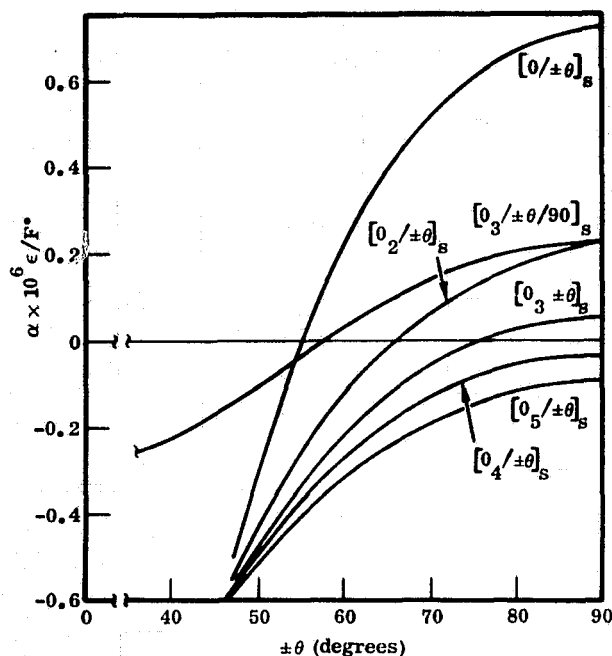


Figure 3.2-4. Ply Orientation Versus CTE

analysis considered laminate families such as depicted in Figure 3.2-4. Several specific laminates satisfy the zero CTE requirement. It is desirable, however, to select the laminate with least sensitivity to small variations in the crossply angle (i.e., least slope near zero CTE). Of the laminates considered, $[0_3/\pm\theta/90]_S$ and $[0_3/\pm\theta]_S$ were most promising. These laminates are .06 and .05 inch thick respectively. Stability considerations (Section 3.2.4.1) forced the selection of the thicker laminate, $[0_3/\pm\theta/90]_S$. Based on the preliminary material data, the orientation for zero CTE was $[0_3/\pm 57.5/90]_S$. Material testing demonstrated lower uni-directional modulus than initially anticipated. The new material data input resulted in shifting the optimum layup to $[0_3/\pm 45.5/90]_S$. The properties of this laminate are listed in Table 3-2.6.

Shell Dimensional Stability

In addition to the zero CTE laminates utilized in the skins, the shell structures also has three rings (excluding the forward ring) and a field joint. The field joint and aft attachment ring are composed of curved flanges that require separate consideration since free expansion through the thickness of the flanges is significant. It is necessary to fully characterize the thermal expansion through the thickness of the flange which has a high coefficient of thermal expansion, and the interaction of this expansion with surrounding structure. To characterize these interactions, a finite element model was developed (Figure 3.2-5). For the material system under consideration (Modmor I/X-30) each curved flange will displace (Reference 3.2.3)

$$\Delta L/F^\circ = -1.25 \times 10^{-7} \text{ in/F}^\circ \quad (1)$$

The field joint is composed of two such curved flanges and the aft attachment ring, one. Thus the field joint and the aft attachment ring together contribute

$$\Delta L/F^\circ = -3.75 \times 10^{-7} \text{ in/F}^\circ \quad (2)$$

Excluding the forward ring and four inches of the shell bonded to the ring, the effective length of the shell is 101.38 inches. Thus, the effective CTE of the shell becomes

$$\text{CTE} = \frac{-3.75 \times 10^{-7} \text{ in/F}^\circ}{101.38 \text{ in}} = -.0037 \times 10^{-6} \text{ in/in-F}^\circ \quad (3)$$

The actual CTE of the shell alone including data correction, is $-.00539 \times 10^{-6}$ in/in-F°. The corrected CTE for the shell plus becomes

$$\begin{aligned} \text{CTE} &= -.00539 \times .00539 \times 10^{-6} - .0037 \times 10^{-6} \\ &= -.00909 \times 10^{-6} \text{ in/in-F}^\circ \end{aligned} \quad (4)$$

Table 3-2.6. GEMS Modmor I/X-30 Material Properties

	1	2
E_x	16.4×10^6 psi	13.788×10^6 psi
E_y	7.88×10^6 psi	
ν_{xy}	.298	
ν_{yx}	.143	
G_{xy}	2.99×10^6 psi	
α_x	$-0.037 \mu\text{in/in F}$	$-0.147 \mu\text{in/in F}$
α_y	$1.19 \mu\text{in/in F}$	
ρ	.06 pci	.06 pci
t	.06 in.	.12 in.

1. $[0_s / \pm 45.5/90]_{S(x)}$ applies to shell skins, intermediate rings, light baffles (if integral), aft attachment ring, spider legs (x is radial, spider hub (x is circumferential)).
2. Applies to Fwd I ring (x is circumferential).

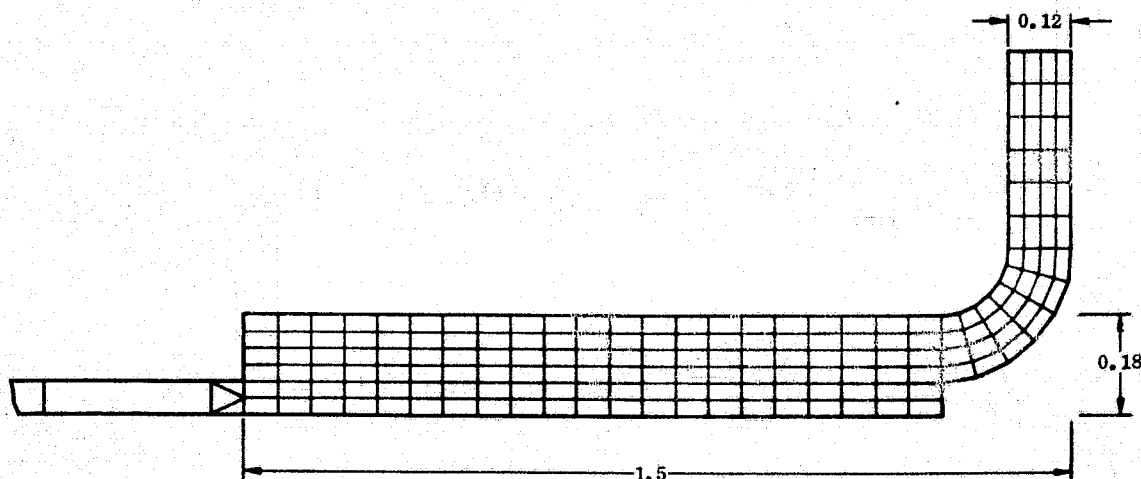


Figure 3.2-5. Symmetric Field Joint Finite Element Model

Forward Ring Dimensional Stability

Dimensional stability of the forward ring is critical as it supports the secondary mirror structure and affects the overall shell CTE. Fabrication considerations necessitated the use of pseudoisotropic laminates $[0/\pm 30/\pm 60/90]$ in the fabrication of the basic I-section ring. Thus, in order to bring the circumferential CTE to zero, additional laminates must be added to the caps of the ring (see Figure 3.2-6).

The minimization of the ring must take into consideration interaction of an effective shell length and the following constraints:

Shell Laminate	=	$[0/\pm 45.5/90]_s$, $t = .06$ in
Web Laminate	=	$[0/\pm 30/\pm 60/90]_{2s}$, $t = .12$ in
Web Flange	=	$[0/\pm 30/\pm 60/90]_s$, $t = .06$ in
I-Section Filler	=	Unidirectional

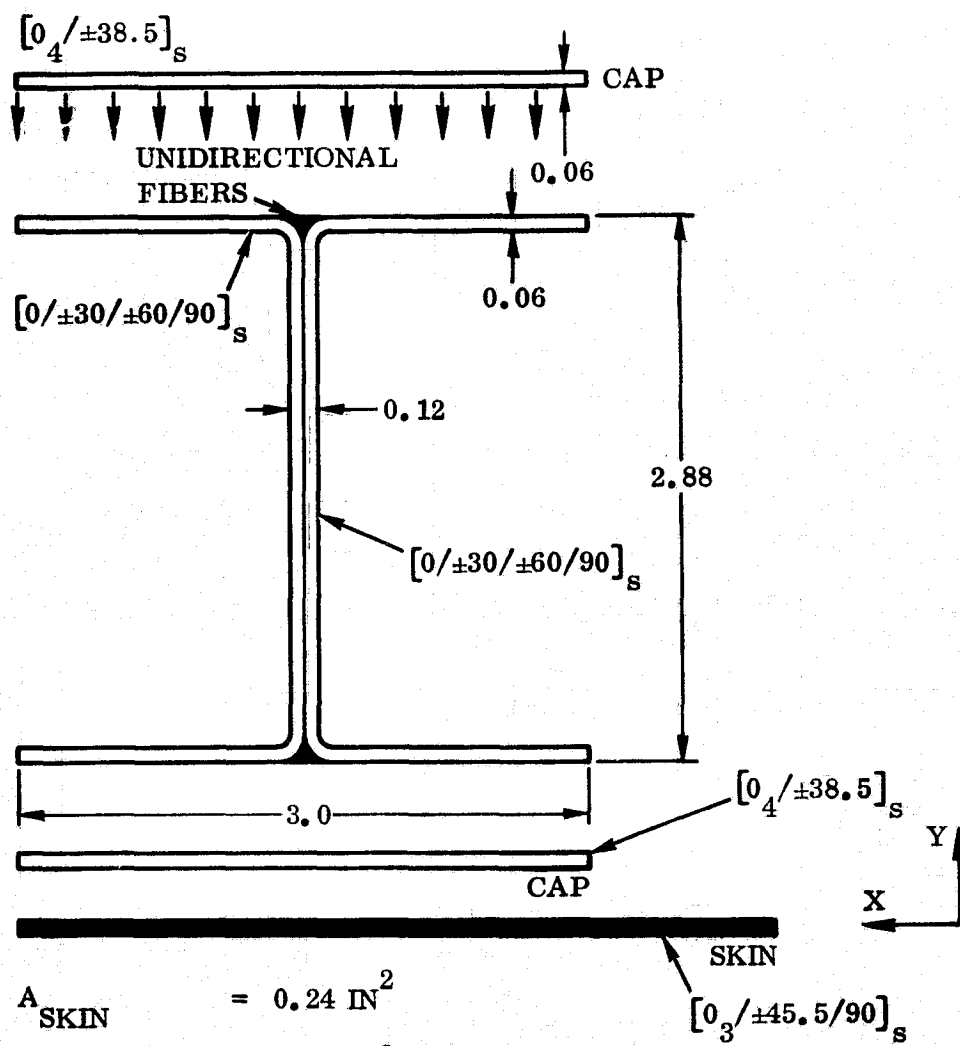
Consider the skin to be completely effective under the flanges. The remaining effective skin is determined by considering a cylinder with an end shear from Reference 3.2.6,

$$\delta_{\text{radial}} = \frac{V}{2D_L \lambda^3} \quad (5)$$

$$\text{where } \lambda = \sqrt[4]{\frac{E_H b t}{4R^2 D_L}} \quad (6)$$

$$\begin{aligned} D_L &= \text{longitudinal bending rigidity of the skin} \\ &= 465 \text{ lbs-in}^2 [0_3/\pm 5.5/90]_s \end{aligned}$$

$$\begin{aligned} E_H &= \text{Circumferential Youngs Modulus} \\ &= 7.882 \times 10^6 \text{ psi } [0_3/\pm 45.5/90]_s \end{aligned}$$



$$A_{\text{SKIN}} = 0.24 \text{ IN}^2$$

$$A_{\text{CAPS}} = 0.36 \text{ IN}^2$$

$$A_{0^\circ \text{ FIBERS}} \approx 0.03 \text{ IN}^2$$

$$A_{\text{I-SECTION}} = 0.6612 \text{ IN}^2$$

$$A_T = 1.29 \text{ IN}^2$$

$$A_T = 1.29 \text{ IN}^2$$

Figure 3.2-6. Forward Ring

$$R = 65.0 \text{ in}$$

$$t = .06 \text{ in}$$

$$b = 1.0 \text{ in}$$

$$\lambda = \frac{.495}{\text{in}}$$

$$\frac{V}{\epsilon} = 2D_L \lambda^3 \quad (7)$$

$$w = \text{effective shell length} = \frac{2D_L \lambda^3 R^2}{Et} = 1.01 \text{ in} \quad (8)$$

Thus, the total effective shell length is

$$w = 3.0 \text{ in} + 1.01 \text{ in} \sim 4.0 \text{ in} \quad (9)$$

$$E_T A_T \alpha_T \Delta T = E_1 A_1 \alpha_1 \Delta T + E_2 A_2 \alpha_2 \Delta T + E_3 A_3 \alpha_3 \Delta T + E_4 A_4 \alpha_4 \Delta T = 0 \quad (10)$$

where: 1 - refers to basic I ring
 2 - refers to cap laminates
 3 - refers to skin laminates
 4 - refers to unidirectional filler

$$A_1 = .6612 \text{ in}^2$$

$$A_2 = .36 \text{ in}^2$$

$$A_3 = .24 \text{ in}^2$$

$$A_4 = .03 \text{ in}^2$$

$$E_1 \text{ (pseudoisotropic)} = 10.558 \times 10^6 \text{ psi}$$

$$\alpha_1 \text{ (pseudoisotropic)} = .4178 \times 10^{-6} \epsilon/F^\circ$$

$$E_{3T} \text{ (skin)} = 7.882 \times 10^6 \text{ psi}$$

$$\alpha_{3T} \text{ (skin)} = 1.19 \times 10^{-6} \epsilon/F^\circ$$

$$E_4 \text{ (filler)} = 28.33 \times 10^6 \text{ psi}$$

$$\alpha_4(\text{filler}) = -.3 \times 10^{-6} \epsilon/\text{F}^\circ$$

$$E_2 \alpha_2 = \frac{-E_1 A_1 \alpha_1 - E_3 A_3 \alpha_3 - E_4 A_4 \alpha_4}{A_2} \quad (11)$$

$$= \frac{-(10,558)(.6612)(.4178) - (7,882)(.24)(1.19) - (28,33)(.03)(-.3)}{.36}$$

$$= \frac{-13.65 \text{ lb-}\epsilon}{\text{in}^2 \text{ -F}^\circ} \quad (12)$$

From Figure 3.2-7 either $[0_4/\pm 11.5]_s$ or $[0_4/\pm 38.5]_s$ will athermalize the ring. The forward ring, while athermalized circumferentially, will contribute $4.894 \times 10^{-8} \text{ in/F}^\circ$ to the longitudinal expansion of the half-scale shell. Thus, the effective CTE of the shell will become

$$\begin{aligned} \text{CTE} &= -.00539 \mu \text{ in/in-F}^\circ \\ &+ \frac{-3.55 \times 10^{-7} \text{ in/F}^\circ + .4894 \times 10^{-7} \text{ in/F}^\circ}{105.38 \text{ in}} \\ &= -.00829 \mu \text{ in/in-F}^\circ \quad (13) \end{aligned}$$

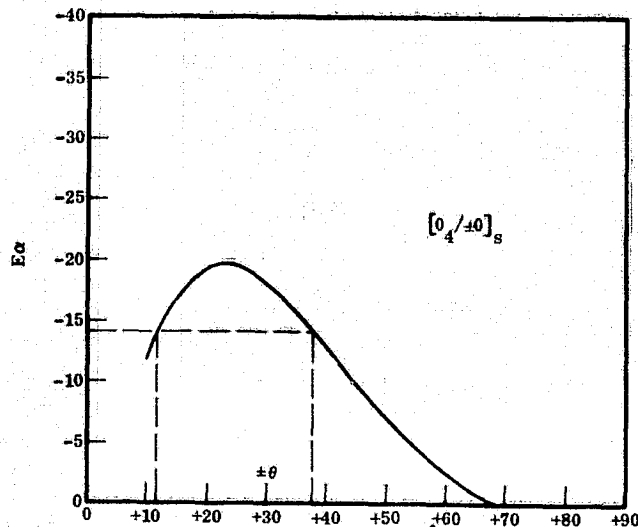


Figure 3.2-7. Forward Ring Athermalization Study

Intermediate Ring Laminates

The intermediate rings (Figure 3.2-8) are positioned at two stations consistent with the full-scale LST arrangement. The primary function of the intermediate rings is to maintain the shape of the shell to ensure overall stability. Each ring also provides the outer strap of a circumferential skin aplice. The skin splice arrangement is completed by the provision of an internal circumferential strap. The approach to the design of these rings is the same as the approach proposed for the LST to reduce costs. A T-section is used for the cross section. The proportions of the cross section are selected to allow the use of the same tooling as for the forward ring. The ply orientation is the same as for the shell, with the orientation such that the zero CTE directions of the ring cap and the shell coincide.

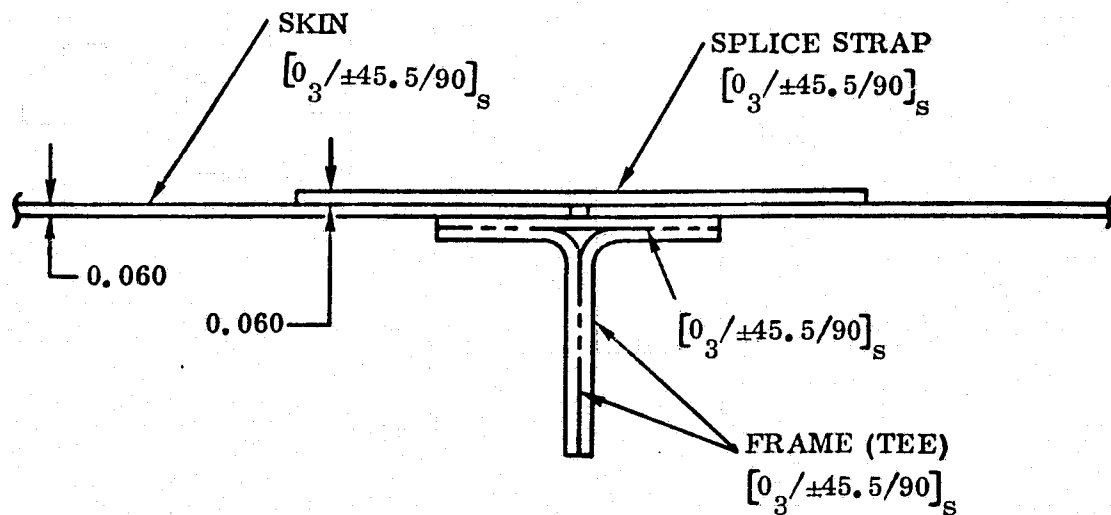


Figure 3.2-8. Cross Section, Intermediate Ring

The size of the ring segments and the location and arrangement of the splices are similar to those described for the secondary mirror support ring. The effect of through-the-thickness expansion of the tee is assumed negligible.

Field Splices and Attachment to LST Main Ring

To minimize costs the components used for these two items are identical. The detail arrangement of both is shown in Figure 3.2-9. The design is of course based on the more highly loaded attachment to the LST main ring. The peak loading in this case, however, is only 70.36 lb/in ultimate (see Equation 14). These rings are fabricated from $[0_3/\pm 45.5/90]_{2s}$ laminates and oriented such that the direction of zero CTE is coincident with the shell laminates. The dominant criterion for bolt selection arises from the requirement for non-magnetic properties. For the half-scale metering shell, A-286 CRES was selected as the bolt material.

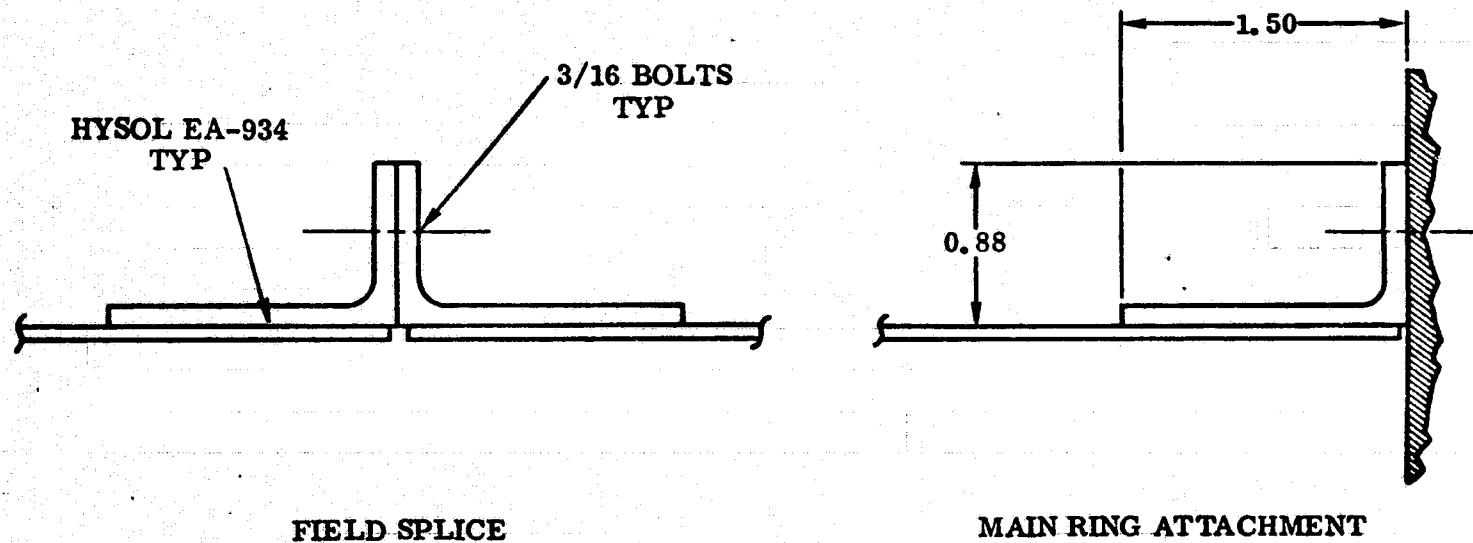


Figure 3.2-9. Field Splice and Attachment to LST Main Ring

Secondary Mirror Support Structure

This structure consists of a cylindrical hub on the optical axis of the telescope, supported from the forward ring of the shell by four radial legs. The hub consists of two concentric cylindrical skins attached at each end to a channel section frame to form a closed box section. The secondary mirror is attached via a system of alignment actuators to the forward face of the hub. Continuity of the bending structure across the hub is provided by torsion/bending in the annular box structure. The significant design criteria for the secondary mirror support structure are:

- a. The attainment of CTE 0 to minimize decenter and tilt due to non-uniform temperature distributions across the structure, and, to a lesser degree, despace due to temperature variations.
- b. Minimized projected frontal area to minimize obscuration.
- c. Adequate lateral stiffness in the legs for the first bending mode of the legs and for rotational response of the mass at the hub.

The last two criteria result in the selection of a solid-plank type cross-section for the legs to achieve the required stiffness with minimum frontal area. To meet the first criterion requires a ply orientation similar to the skin, which uses $[0_3/\pm 45.5/90]_S$. This is an excellent layup since, as illustrated by Figure 3.2-4, the CTE is relatively insensitive to manufacturing variations in the ply orientation. The thickness of the full-scale secondary mirror support leg will be 0.48 inch. This value was determined from dynamic stiffness requirements. Since the legs are not strength critical, it was decided, in contrast with the approach taken on the GEMS structure generally, to use half-scale thickness for the half-scale component. This approach effects a significant savings in material and layup costs of these thick components, while still simulating full-scale fabrication techniques and assuring the correct dimensional response to temperature variations.

A parameter study was conducted to determine the proper orientation of the $[0_3/\pm 45.5/90]_S$ laminate along the spider legs. The results of this study (Table 3-2.7) indicate that an orientation of approximately 4° - 20° from the lower edge of the leg will athermalize the structure, providing that the skin laminates in the mirror cage are oriented circumferentially. Figure 3.2-10 shows the spider leg laminate orientation.

The structure is sensitive to small variations in CTE. This is due to the tendency of the legs and cage to react as a mechanism. The effect of perturbations about zero CTE is shown in Figure 3.2-11.

Table 3-2.7. Effect of Zero CTE Laminate Orientation in Spider Legs on Secondary Mirror

	0°		4°		8°	
	Uniform Soak	Linear Gradient	Uniform Soak	Linear Gradient	Uniform Soak	Linear Gradient
Despace (μm)	0.985	-0.026	-0.0124	-0.0257	-0.949	-0.0248
Decenter (μm)	0.0005	-0.06	-0.0024	-0.0832	-0.0078	-0.0828
Tilt (μrad)	-0.0032	1.35	0.0162	0.975	0.0535	0.606

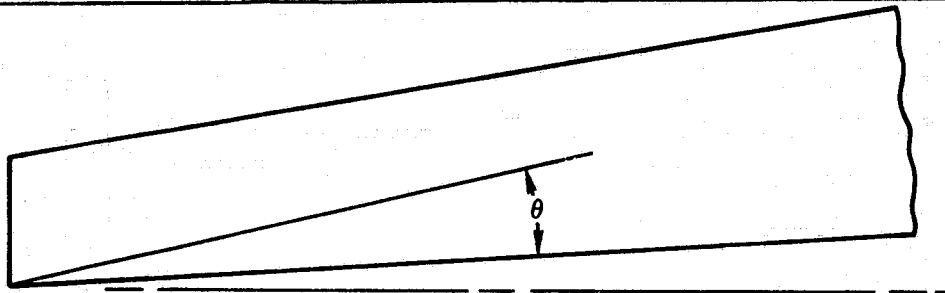


Figure 3.2-10. Spider Leg Laminate Orientation

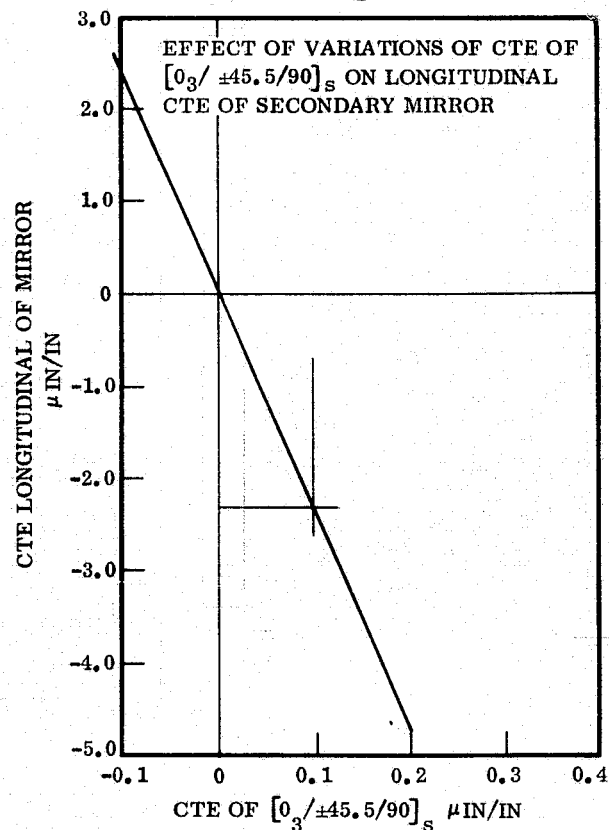


Figure 3.2-11. Effect of Variations of CTE of $[0_3/\pm 45.5/90]_S$ on Longitudinal CTE of Secondary Mirror

3.2.3 STRUCTURAL ANALYSIS

3.2.3.1 Shell Skin

Load Intensities

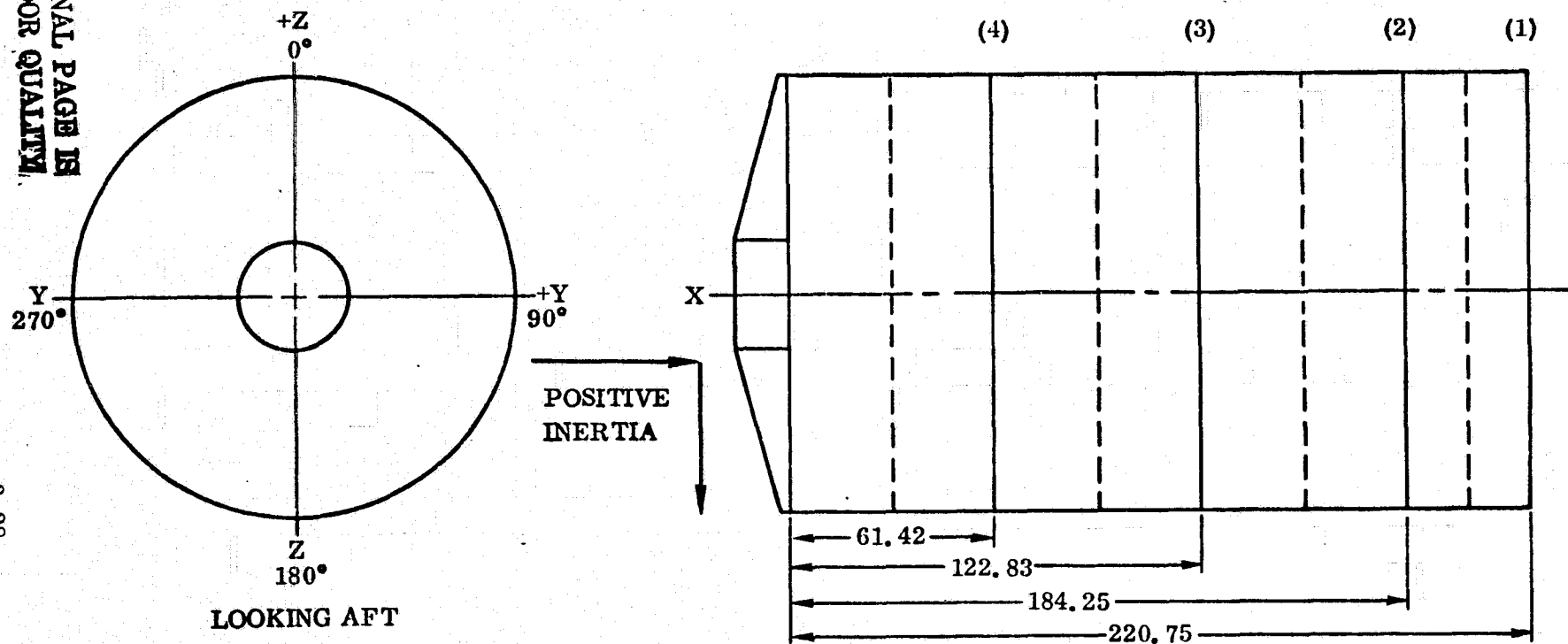
Load intensities for the full-scale shell have been derived by NASTRAN analysis for the potentially critical conditions. The results are shown in Table 3-2.8. Since the design of the shell will give equal strength around the circumference, the lower load intensities at the 90- and 270-degree positions are not presented. The load intensities in Table 3-2.8 are limit except for the crash condition, which is ultimate. From this data the following ultimate design load intensities are derived for the entry condition. Since the data in Table 3-2.8 was based on NASTRAN stress resultants at the center of the elements, a correction factor of 1.049 is necessary to determine the loads at the boundary. The maximum axial load condition is

$$N_{x_{\max}} = (1.049)(1.75)(\pm 38.33 \text{ lb/in}) = \pm 70.36 \text{ lb/in} \quad (14)$$

Skin Splices

The circumferential skin splices have been described in conjunction with the intermediate rings in Section 3.2.3. Three longitudinal splices occur at 120-degree arc intervals. The skins are butted and joined by internal and external splice strips bonded with room temperature curing Hysol EA-934. The splice straps and also the circumferential splice straps described in Section 3.2.3 use the same laminate $[0_3/\pm 45.5/90]_s$ as the basic skin. This design minimizes tooling and layup costs by allowing the straps to be layed up with the skin and subsequently cut from the cured panels. The splices contain much more material and surface continuity than adjacent areas and thus are not stress critical.

Table 3-2.8. Shell Load Intensities



Load Intensities (lb/in)

Location	1g Intensities		Crash		Landing ±1.5g X +2.5g Z	Entry ±0.25g X +3.0g Z	Orbit End Burn -3.3g X -0.5g Z
	X Axis	Z Axis	+9g X	+4.5g Z			
1-0	-1.64	12.64	-14.76	56.88	34.06	38.33	5.41
1-180	-1.64	-12.64	-14.76	-56.88	-34.06	-38.33	11.73
2-0	-1.54	10.81	-13.86	48.65	29.34	32.82	5.08
2-180	-1.54	-10.81	-13.86	-48.65	-29.34	-32.82	10.49
3-0	-1.41	7.67	-12.69	34.52	21.30	23.36	4.65
3-180	-1.41	-7.67	-12.69	-34.52	-21.30	-23.36	8.49
4-0	-1.26	4.52	-11.34	20.34	13.19	13.88	4.16
4-180	-1.26	-4.52	-11.34	-20.34	-13.19	-13.88	6.42

Metering Shell Local Stability

From (14) the peak compressive shell stress load at the base is

$$N_x = -70.36 \text{ lb/in} \quad (15)$$

The peak compressive shell load at the field joint is (Table 3-2.8)

$$N_x = (1.049)(1.75)(-32.82) = -60.25 \text{ lb/in} \quad (16)$$

These loads are both localized bending maximums. For the purpose of local stability analysis, assume the uniform loading to be the average of these loadings,

$$N_x = \frac{(-70.36 - 60.25)}{2} = -65.31 \text{ lb/in} \quad (17)$$

Using the stability equations of references (3.2.7 and 3.2.8), corrected for bending, and inputting the following material and geometric properties:

$$\begin{aligned} E_x &= 16.41 \times 10^6 \text{ psi} \\ E_y &= 7.88 \times 10^6 \text{ psi} \\ \nu_{xy} &= .298 \\ G_{xy} &= 2.987 \times 10^6 \\ R &= 65.0 \end{aligned} \quad (18)$$

$$t = .06$$

$$K_B = 1.8$$

$$N_{x_{cr}} = -63.36 \text{ lb/in}$$

compression

yields

$$N_{x_{cr} \text{ bending}} = K_B N_{x_{cr} \text{ compression}} = 114 \text{ lb/in} \quad (19)$$

$$M.S. = \frac{114}{65.31} - 1 = .746 \quad (20)$$

Shell Skin Peak Stresses

Based on the results of (14)

$$N_{x_{max}} = -70.36 \text{ lb/in} \quad (21)$$

This loading will produce the following maximum stress state in the laminate

$$\begin{aligned} \sigma_{11} &= -697.7 \\ \sigma_{22} &= -39.3 \text{ psi} \\ \tau_{12} &= -78.8 \text{ psi} \end{aligned} \quad (22)$$

$$M.S. = \text{large} \quad (23)$$

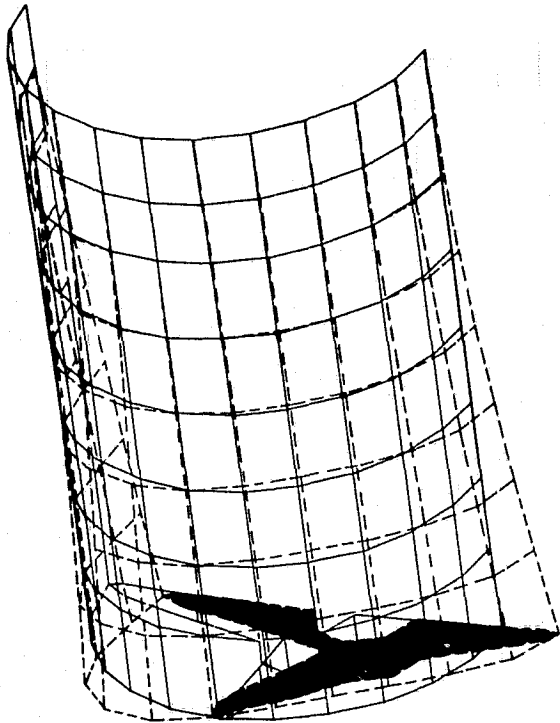


Figure 3.2-12. Cantilever Bending of Continuously Mounted Shell

Dynamic Analysis

Dynamic analysis of the full scale metering shell was performed on NASTRAN (Reference 3.2.14) to determine Mode 1 form and frequency. For a continuously mounted shell the first mode is cantilever bending (Figure 3.2-12). The natural frequency associated with this mode is 25.5 Hz.

3.2.3.2 Shell Rings

Forward Ring Lateral Stability

Analysis of a freely supported curved bar subjected to pure bending (Reference 3.2.3) indicates that

$$M_{cr} = \frac{EI + KG}{2R} \pm \left(\left(\frac{EI - KG}{2R} \right)^2 + \frac{EIKG\pi^2}{L^2} \right)^{1/2} \quad (24)$$

$$M_{cr} = -6,531 \text{ lb/in} \quad (25)$$

Based on the results of Reference 3.2.4, the maximum moment occurring at any point in the forward ring is

$$M = (1.75)(-2,978 \text{ lb-in}) = -5,212 \text{ lb-in ult. [entry]} \quad (26)$$

$$M.S. = .253 \quad (27)$$

This result is very conservative since the stabilizing effect of the shell has been ignored. The shell will add substantial support to the forward ring, as well as to the intermediate rings, thus eliminating this model of failure.

Forward Ring Flange Stability

The external ring flanges may be considered as plates simply support on three edges and free on the fourth. The instability stress is given by Reference 3.2.5.

$$\sigma_{x_{cr}} = G_{xy} \left(\frac{t}{b} \right)^2 + \frac{\pi^2 t^2 E_{xx}}{12L^2 (1-\nu_{xy} \nu_{yx})} \quad (28)$$

For long plates the second term is negligible. Thus,

$$\sigma_{x_{cr}} \approx G_{xy} \left(\frac{t}{b}\right)^2 \quad (29)$$

The flange is composed of two laminates. The lower laminate is pseudoisotropic with $G_{xy} = 4.78 \times 10^6$ psi. The cap laminate has a G_{xy} of 2.8×10^6 psi. Using this value as the lower bound and $t = .12$ inch and $b = 1.44$ inch

$$\sigma_{x_{cr}} = 19,444 \text{ psi} \quad (30)$$

From (26)

$$M_{-max} = -5,212 \text{ lb-in} \quad (31)$$

$$I = \frac{\sum EI}{\bar{E}}, \quad \bar{E} = \frac{\sum EA}{A_T} \quad (32)$$

$$I = \frac{3.474 \times 10^7 \text{ lb-in}^2}{15.805 \times 10^6 \text{ psi}} = 2.198 \text{ in}^4 \quad (33)$$

$$\bar{y} = 1.39 \text{ in}, y_o = 3.06 \text{ in} - 1.39 \text{ in} = 1.67 \text{ in} \quad (34)$$

$$\sigma_b = \frac{(-5,212 \text{ lb-in})(1.67 \text{ in})}{2.198 \text{ in}^4} = -3,960 \text{ psi} \quad (35)$$

$$\sigma_a = \frac{[(EA)_{cap} + (EA)_{flange}]}{\sum EA} \frac{P}{A_f} = \frac{.337(143 \text{ lb})}{.36 \text{ in}^2} = 134 \text{ psi} \quad (36)$$

$$\sigma_x = \sigma_b + \sigma_a = (-3,960 + 134) \text{ psi} = -3,826 \text{ psi} \quad (37)$$

$$M.S. = \text{large}$$

Interlaminar Tension - Forward Ring Flange

Normal-to-the-face loadings of circular ring sections induce transverse bending of the flanges. This bending may be conservatively approximated by an equivalent uniform loading, w , along the span of the frame flanges (Figure 3.2-13).

$$w = 2 \left(\frac{f_{ctb}}{Rbd\phi} \right) \sin \frac{d\phi}{2} = \frac{f_{ct}}{R} \quad (38)$$

$$M = \frac{wb^2}{2} \quad (39)$$

The transverse bending stress induced by the moment resulting from w is

$$f_B = \frac{Mc}{I} = \frac{wb^2}{2} \frac{6}{t_f^2} = \frac{3b^2 w}{t_f^2} = \frac{3b^2 f_c}{Rt_f} \quad (40)$$

The transverse shear load V (lb/in) $= wb = \frac{f_{ctb}}{R}$

Consider Figure 3.2-14. If it is assumed that the neutral plane of the transverse bending is the interface between the flange cap and the web flange, then the stress distribution in the flange will be as shown in Figure 3.2-15.

$$f_T = f_B/2 = \frac{3b^2 f_c}{2Rt_f} \quad (41)$$

$$f_{BT} = f_B/2 = \frac{3b^2 f_c}{2Rt_f} \quad (42)$$

$$f_s = \frac{V}{t_w/2} = \frac{2f_{ctb}}{Rt_w} \quad (43)$$

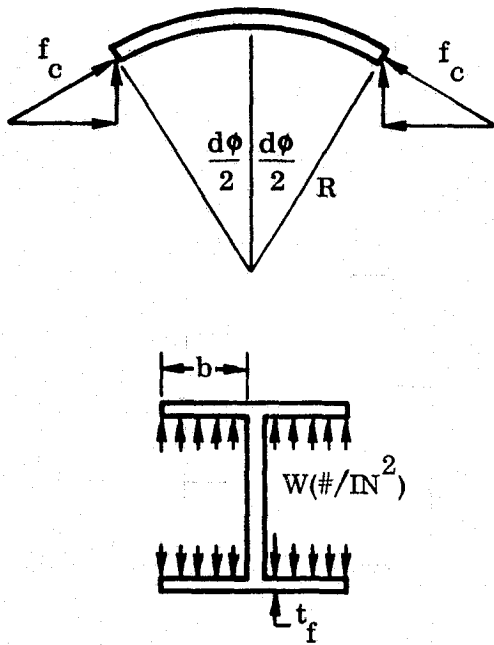


Figure 3.2-13. Resultant Loading of a Curved I Beam

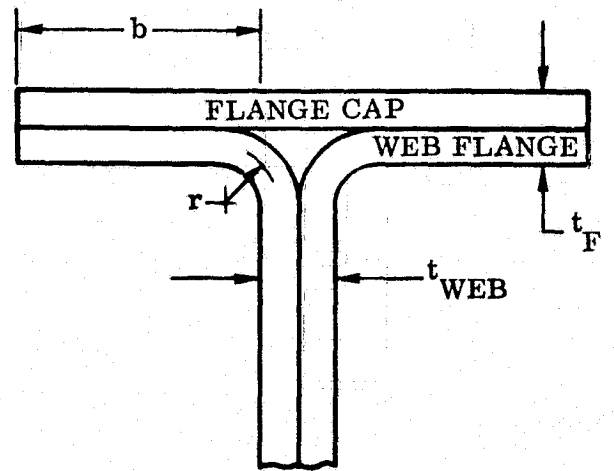


Figure 3.2-14. Detailed View of I Section Flange



Figure 3.2-15. Detailed View of Web Flange

These stresses will induce interlaminar normal stresses in the corner of the web flange. An exact solution for most individual laminates does not exist. However, an empirical formulation exists for certain representative laminates (see Appendix A). The $[\pm 45]_{ns}$ laminate has the most severe normal stress levels of those laminates for which data has been generated (Reference 3.2.9). Since interlaminar tension strength of epoxy composites is very low, it is reasonable to use the worst case stress formulation ($[\pm 45]_{ns}$) for the purposes of analysis. Thus, for $r/t = 1$ (r = inner radius of angle

$$\sigma_n = \sigma_{33} = 1.14 f_s + .175 f_{bt} - .656 f_T \quad (44)$$

$$= 1.14 \left(\frac{2f_c t b}{R t_w} \right) + .175 \left(\frac{3b^2 f_c}{2R t_f} \right) - .656 \left(\frac{3b^2 f_c}{2R t_f} \right) \quad (45)$$

$$= f_c \left(\frac{2.28 t b}{R t_w} - .481 \left(\frac{3b^2}{2R t_f} \right) \right) \quad (46)$$

$$= \frac{f_c t b^2}{R} \left(\frac{2.28}{b t_w} - .481 \left(\frac{3}{2 t_f^2} \right) \right) \quad (47)$$

For the case $t_f = t_w = t$

$$\sigma_{33} = \frac{f_c b^2}{R} \left(\frac{2.28}{b} - .7215 \frac{1}{t} \right) \quad (48)$$

To obtain an interlaminar tension field, f_c must be compressive. The maximum compressive stress is developed during shuttle liftoff (Reference 3.2.4).

$$M_{\max_{ult}} = (1.75)(2464) = -4311 \text{ lb-in} \quad (49)$$

$$P_{\max_{ult}} = (1.75)(-81) = -143 \text{ lb} \quad (50)$$

From Figure 3.2-6 the area properties of the forward ring with effective skin area are

$$\begin{aligned}
 A &= 1.2912 \text{ in}^2 \\
 I_{xx} &= 2.85 \text{ in}^4 \\
 \bar{y} &= 1.3919 \text{ in} \\
 y_o &= -1.6681 \\
 y_i &= +1.3919 \\
 E_{ef} &= 13.328 \times 10^6 \text{ psi}
 \end{aligned} \tag{51}$$

$$\epsilon_{\max} = \frac{M_{yo}}{E_{ef} I} = \frac{(-4311 \text{ lb-in})(-1.6681 \text{ in})}{(13.328 \times 10^6)(2.85 \text{ in}^4)} = -189.3 \mu \text{ in/in} \tag{52}$$

At the interface of the cap and the web flange

$$\epsilon = \frac{1.6081}{1.6681} \epsilon_{\max} = -182.49 \mu \text{ in/in} \tag{53}$$

At the lower edge of the upper web flange

$$\epsilon = \frac{1.5481}{1.6681} \epsilon_{\max} = -175.68 \mu \text{ in/in} \tag{54}$$

The average stress on the total flange due to the moment is

$$\begin{aligned}
 \sigma_{B_{avg}} &= - \frac{E_1 t_1 (175.68 \mu \text{ in/in} + 182.49 \mu \text{ in/in}) + E_2 t_2 (182.49 \mu \text{ in/in} + 189.3 \mu \text{ in/in})}{2(t_1 + t_2)} \\
 &= - \frac{(10.558 \times 10^6)(.06)(175.68 \mu \text{ in/in} + 182.49 \mu \text{ in/in}) + (20.8 \times 10^6)(.06)(182.49 \mu \text{ in/in} + 189.3 \mu \text{ in/in})}{.24} \\
 &= \underline{(182.49 \mu \text{ in/in} + 189.3 \mu \text{ in/in})} = -2878.7 \text{ psi}
 \end{aligned} \tag{55}$$

The average stress on the total flange due to the axial load is

$$\sigma_{A_{avg}} = \frac{P(E_1 t_1 + E_2 t_2)}{E_{ef} A_T (t_1 + t_2)} = \frac{-143((10.588 \times 10^6)(.06) + (20.8 \times 10^6)(.06))}{(13.328 \times 10^6)(1.2912)(.12)}$$

$$= -130.29 \text{ psi} \quad (56)$$

The worst case condition for interlaminar tension is that of maximum compression.

$$f_c = -2878.7 - 130.29 = -3009 \text{ psi} \quad (57)$$

$$\sigma_{33} = \frac{f_c b^2}{R} \left(\frac{2.28}{b} - \frac{.7215}{t} \right) = 427.2 \text{ psi} \quad (58)$$

where

$$\begin{aligned} b &= 1.5 - .06 = 1.44 \text{ inch} \\ R &= 65.0 \text{ inch} \\ t &= 0.12 \text{ inch} \end{aligned} \quad (59)$$

$$\sigma_{33} \text{ allowable} = 3,000 \text{ psi} \quad (60)$$

$$M.S. = \text{large} \quad (61)$$

3.2.3.3 Secondary Mirror Support. A NASTRAN structural model of the secondary mirror support structure was generated to facilitate an understanding of the complex interaction of the thermal expansions of its constitutive components (Figure 3.2-16).

The bar elements represent the spider leg-mirror cage support joint, the circular mirror cage rings, forward ring and dummy members which simulate the mirror attachments.

The CQUAD1 elements are general bending elements used to represent the spider legs and the mirror cage skin.

Critical Load Case

Two critical loading conditions have been determined from the NASTRAN analysis. The 9.0g longitudinal ultimate crash factor is critical for the mirror cage rings. The -3.0g condition for shuttle entry, producing -5.25g ultimate, is critical to the spider leg to metering shell attachment fittings.

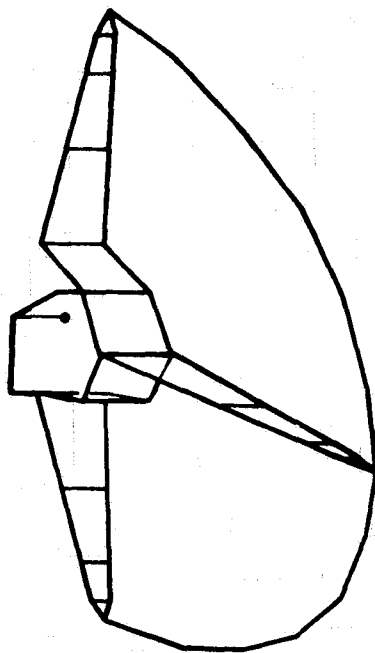
Hub Analysis

Ring Flange Stability

Stability of the channel ring flanges was considered in the worst case condition of complete reaction of the bending forces in the upper and lower channels. In actuality, some of this force will be reacted in shear around the closed cage structure. The force couple is the result of a 9.0g forward shift of the mirror structure for the ultimate crash condition. The point loads introduced by this loading are depicted in Figure 3.2-17.

The maximum positive moment occurs between load application points and is given by (Reference 3.2.6)

$$M_{\max}^+ = \frac{WR}{2} \left(\frac{1}{\sin \theta} - \frac{1}{\theta} \right) \quad (62)$$



STRUCTURAL COMPOSITION

32 BAR ELEMENTS

13 QUADRILATERAL PLATE ELEMENTS

3 TRIANGULAR PLATE ELEMENTS

Figure 3.2-16. Finite Element Model of Secondary Mirror Support Structure

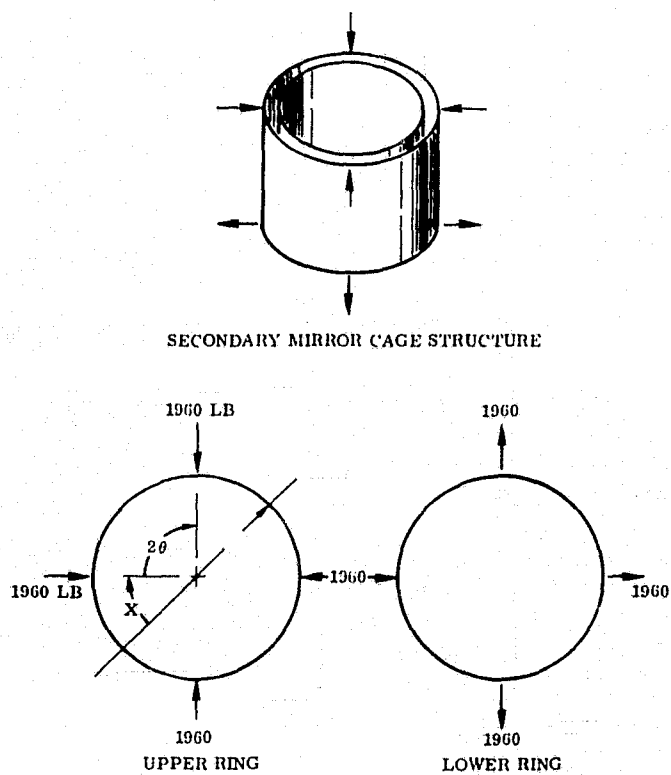


Figure 3.2-17. Point Loading of Secondary Mirror support Rings

where

W = point load (lb)

R = radius of the channel = 15.9 inch

2θ = angle between load points = 90°

$$M_{\max}^+ = .07 WR \quad (63)$$

$$T_{\max}^+ = \frac{W}{2\sin\theta} = .707W \quad (64)$$

The maximum negative moment occurs at the point of load application and is given by

$$M_{\max}^- = \frac{-WR}{2} \left(\frac{1}{\theta} - \cot\theta \right) = -.137 WR \quad (65)$$

The corresponding tensile load is

$$T = \frac{W}{2} \cot\theta = .5W \quad (66)$$

For the channel geometry depicted in Figure 3.2-18

$$\sigma_{\max} = \pm \left[\frac{Mc}{I} + \frac{P}{A} \right] = \pm \left[2.18 \frac{W}{\text{in}} , -7.03 \frac{W}{\text{in}} \right] \quad (67)$$

$$W = \pm 1960 \text{ lb}, \sigma_{\max} = \pm 17,993 \text{ psi} \quad (68)$$

The stability critical sections will be the flanges. From Reference 3.2.5,

$$\sigma_{\text{cr}} = G_{xy} \left(\frac{t}{bf} \right)^2 = 34,324 \text{ psi} \quad (69)$$

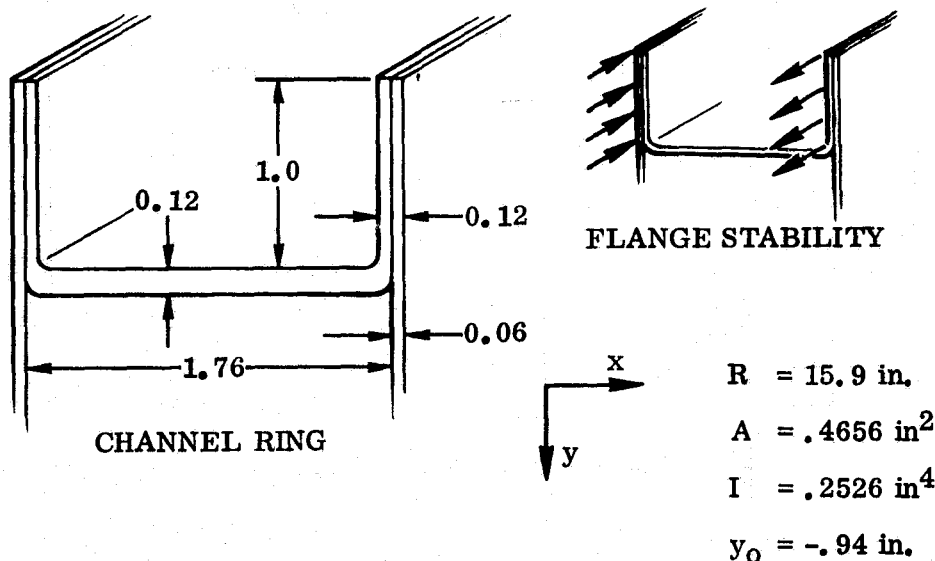


Figure 3.2-18. Secondary Mirror Support Ring

where

$$t = \text{flange thickness} = .12 \text{ in}$$

$$b_f = \text{flange width} = 1.12 \text{ in}$$

$$G_{xy} = \text{shear modulus of } [0_3/\pm 45.5/90]_s = 2.99 \times 10^6 \text{ psi}$$

Based on the results of (68), the average stress across the flange is:

$$\sigma_{\text{avg}} = \pm 16,979 \text{ psi} \quad (70)$$

$$M.S. = 1.02 \quad (71)$$

Ring Flange Transverse Bending

From (70), the maximum average flange stress will be

$$\sigma_{\text{max avg}} = \pm 16,979 \quad (72)$$

The transverse moment is given by

$$\frac{M}{in} = \frac{wb^2}{2} \quad (73)$$

$$w = \frac{\sigma_{max} \times t_f}{R} = 128.14 \text{ psi} \quad (74)$$

This transverse bending moment, in conjunction with the 16,979 psi circumferential flange stress will generate the following critical stress levels in one of the interior lamina.

$$\begin{aligned} \sigma_{11} &= 23,600 \text{ psi} \\ \sigma_{22} &= 2,685 \text{ psi} \\ \sigma_{12} &= -100 \text{ psi} \end{aligned} \quad (75)$$

Utilizing Hoffmans failure criteria

$$1 = \frac{\sigma_{11}^2 - \sigma_{11}\sigma_{22}}{f_{1tu}f_{1cu}} + \frac{\sigma_{22}^2}{f_{2tu}f_{2cu}} + \left(\frac{f_{1cu} - f_{1tu}}{f_{1cu}f_{1tu}} \right) \sigma_{11} + \left(\frac{f_{2cu} - f_{2tu}}{f_{2cu}f_{2tu}} \right) \sigma_{22} + \frac{\tau_{12}^2}{f_{12su}^2} \quad (76)$$

where

$$f_{1tu} = f_{1cu} = 100,000 \text{ psi}$$

$$f_{2tu} = 4000 \text{ psi} \quad (77)$$

$$f_{2cu} = 25,000 \text{ psi}$$

$$f_{12su} = 11,440 \text{ psi}$$

$$\begin{aligned} & \frac{(2.36 \times 10^4)^2 - (2.36 \times 10^4)(.2685 \times 10^4)}{10^{10}} + \frac{(.2685 \times 10^4)^2}{10^8} + \frac{2.1 \times 10^4(.2685 \times 10^4)}{10^8} + \left(\frac{-100}{1.144 \times 10^4} \right)^2 \\ &= .04936P^2 + .0721P^2 + .5639P + 7.6 \times 10^{-5}P^2 \end{aligned} \quad (78)$$

The stresses are linear functions of the circumferential stress and the transverse moment and, noting that the first, second, and fourth terms are quadratic in the stresses, we may write

$$.1215P^2 + .5639P - 1 = 0 \quad (79)$$

$$P = 1.369 \quad (80)$$

$$M.S. = \frac{P}{1} - 1 = .369 \quad (81)$$

From (48) the interlaminar tension stresses are given by

$$\sigma_{33} = \pm \frac{f_c b^2}{R} \left(\frac{2.28}{b} - \frac{.7215}{t} \right) \quad (82)$$

where

$$f_c = 16,979 \text{ psi}$$

$$t = .12 \text{ inch} \quad (83)$$

$$b = 1.0 \text{ inch}$$

$$R = 15.9 \text{ inch}$$

$$\sigma_{33} = \pm 3986 \text{ psi} \quad (84)$$

$$\sigma_{\text{allowable tension}} = 4000 \text{ psi} \quad (85)$$

$$M.S. = .0035 \quad (86)$$

Mirror Cage Shear Clips

From Reference 3.2.10, shear loading along the web of the clip (Figures 3.2-19 and 3.2-20) will induce the following critical stress level within the 12 ply laminate:

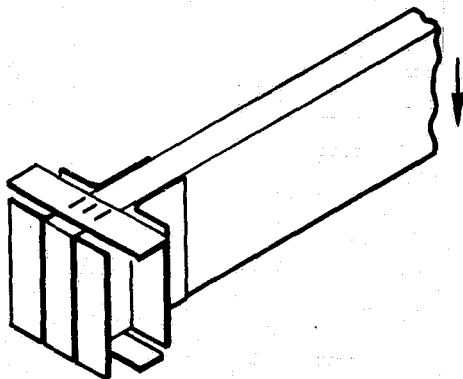


Figure 3.2-19. Spider Beam-Torque Box Shear Clips

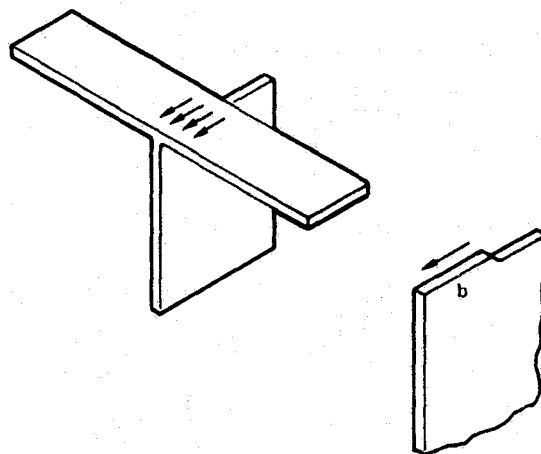


Figure 3.2-20. Shear Loading in T-Shear Clips

$$\begin{aligned}
 \sigma_{11} &= \pm 78.34 \frac{N_{xy}}{\text{in}} \\
 \sigma_{22} &= \pm 2.47 \frac{N_{xy}}{\text{in}} \\
 \tau_{12} &\approx \pm .084 \frac{N_{xy}}{\text{in}}
 \end{aligned} \tag{87}$$

Substitution of these values into the failure criteria (76) yields a quadratic equation in $N_{xy_{cr}}$.

$$N_{xy_{cr}}^2 + -7.4727 \times 10^2 N_{xy_{cr}} - 1.4406 \times 10^6 = 0 \tag{88}$$

$$N_{xy_{cr}} = 883.4 \text{ lb/in} \tag{89}$$

Based on the results of (68)

$$P = 1960 \text{ pounds} \tag{90}$$

Assuming a conservative parabolic peaking factor of 1.25 for the shear length of 1.82 inch

$$N_{xy} = (1.5)(1960 \text{ lb})/1.82 \text{ inch} = 1615 \text{ lb/in} \tag{91}$$

Doubling the thickness to .12 inch (24 plies) yields

$$M.S. = \frac{1767}{1615} - 1 = .094 \quad (92)$$

Peak Shear in the T-Shear Clip Bond

Consider the effective bond to comprise a circular region of radius a within the bond area (Figure 3.2-21).

$$\text{Shear Strain} = \gamma = a\beta \quad (93)$$

$$\text{where } \beta = \frac{2M}{G\pi a^4} \quad \text{Reference 3.2.6} \quad (94)$$

$$\tau_{\text{peak}} = \frac{2M}{\pi a^3} + \frac{V}{\pi a^2} \quad (95)$$



Figure 3.2-21. T-Shear Clip Effective Side Shear

Assume

$$a = 1.0 \text{ inch} \quad (96)$$

$$M = (1960 \text{ lb})(1.0 \text{ inch}) = 1960 \text{ lb-in}$$

$$V = 1,960 \text{ lb}$$

$$\tau_{\text{peak}} = 1,872 \text{ psi} \quad (97)$$

Reference 3.2.11 specifies a minimum average adhesive strength of 1,300 psi.
A conservative factor of 1.5 results in a shear peaking allowable of 1,950 psi.

$$M.S. = \frac{1950}{1872} - 1 = .042 \quad (98)$$

This value is very conservative since plasticity effects have been neglected.

3.2.3.4 Spider Leg Analysis

Normal Stresses in the Spider Leg-Metering Shell Joint

Consider Figure 3.2-22. For a 5.25g lateral shift the load distributions may be determined from statics, where

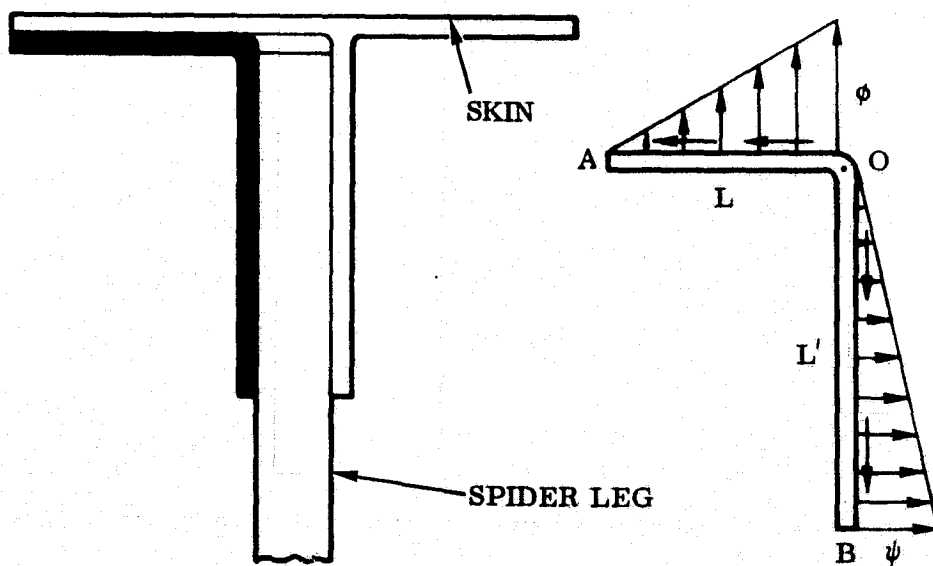


Figure 3.2-22. Spider Attach Flange

ϕ, ψ are peak stress levels

τ is the average shear stress

$$\tau = \frac{P}{bL'} \quad (99)$$

Moment of ϕ about A

$$M_{\phi A} = b \int_0^L \frac{\phi x^2}{L} dx = \frac{b\phi L^2}{3} \quad (100)$$

$$P = b \int_0^L \frac{\phi x}{L} dx = \frac{b\phi L}{2}, \quad \phi = \frac{2P}{bL} = \frac{2L'\tau}{L} \quad (101)$$

$$M_{\phi A} = \frac{2b\tau L' L}{3} \quad (102)$$

Moment of τ about A

$$M_{\tau A} = \tau b L' (L+t) \quad (103)$$

Moment of ψ about A

$$M_{\psi A} = \frac{b\psi}{L'} \int_t^{L'+t} (y^2 - t_y) dy = b\psi \left(\frac{L'^2}{3} + \frac{L't}{2} \right) \quad (104)$$

$$\Sigma_A M = 0 = M_{\phi A} + M_{\psi A} t - M_{\tau A} = 0 \quad (105)$$

$$\frac{2b\tau L'L}{3} + b\psi \left(\frac{L'^2}{3} + \frac{L't}{2} \right) - \tau bL'(L+t) = 0 \quad (106)$$

$$\psi = \tau \left(\frac{2L + 6t}{2L' + 3t} \right) \quad (107)$$

Given ψ , the resultant stresses at 0 can be determined and used to determine the interlaminar tension stress, ϕ , in the corner of the shear clip

Moment of ψ about 0

$$M_{\psi} = \frac{\psi L'^2}{2} = \frac{\tau(2L + 6t)}{(2L' + 3t)} \frac{L'^2}{3} \quad (108)$$

Moment of τ about 0

$$M_{\tau} = \frac{\tau L't}{2} \quad (109)$$

$$\Sigma_0 M = 0 = M_0 + M_{\psi} - M_{\tau} = 0 \quad (110)$$

$$M_0 = \frac{\tau L't}{2} - \frac{\tau L'^2}{3} \left(\frac{2L + 6t}{2L' + 3t} \right) \quad (111)$$

Given: $t = .12$ inch, $L' = 4.28$ inch, $L = 1.38$ inch

$b = 1.0$ inch and $P = 106.75$ lb/in

$$\frac{M_0}{in} = -2.13 \tau in^2 = -.5P = -53.38 \text{ lb/in/in} \quad (112)$$

$$\sigma_b = \frac{Mc}{I} = \pm \frac{(-53.38 \text{ lb-in})(.06 \text{ in})(.12)}{(1.0 \text{ in})(.12 \text{ in})^2} = \pm 22,242 \text{ psi} \quad (113)$$

$$\sigma_s = \frac{b \int_0^{L'} \frac{\psi x}{L'} = \frac{b\psi}{bLt} \frac{L'^2}{2} = \frac{\psi L'}{2t} \quad (114)$$

$$= \frac{L' \tau}{2t} \left(\frac{2L + 6t}{2L' + 3t} \right) = \frac{P}{2t} \left(\frac{2L + 6t}{2L' + 3t} \right) = \frac{1.63P}{2 \text{ in}} = 173.5 \text{ psi} \quad (115)$$

$$\sigma_t = \frac{\tau L'}{t} = \frac{P}{(1.0)t} = 890 \text{ psi} \quad (116)$$

From (44), $r/t = 1.0$

$$\sigma_{33} = 1.14(173.5 \text{ psi}) + .175(22,242 \text{ psi}) - .656(890 \text{ psi}) = 3,506 \text{ psi} \quad (117)$$

$$\sigma_{33}^{\text{allowable}} = 4,000 \text{ psi}$$

$$M.S. = .14 \quad (118)$$

Field Joint and Aft Attachment Flange

The flanges used for the field joint and the aft attachment flange have the same configuration. The bending moment will be greatest at the aft attachment flange. Thus, proper design of the aft flange will result in a conservative design for the field joint. The peak bending moment occurs for the case of entry (Reference 2.3.4).

The peak bending moment in the flange will occur at the edge of the bolt caps. From Figure 3.2-23, considering a .375 inch diameter bolt head, the peak moment will be

$$M_{\text{max}} = (.37 \text{ inch} - .1875 \text{ inch})P = .1825P\text{-in} \quad (119)$$

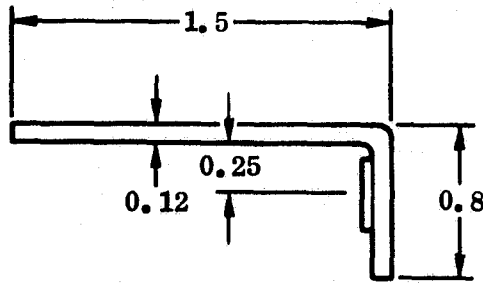


Figure 3.2-23. Field Joint Attach Flange

From (14), the maximum ultimate tensile load intensity is

$$N_{x \max} = \pm 70.36 \text{ lb/in} \quad (120)$$

For a 6 inch bolt spacing the maximum ultimate load per bolt in the region of peak bending will be

$$P_{\max} = 6.0 \text{ inch}(N_{x \max}) = 6.0 \text{ inch} (70.36 \text{ lb-in}) = 422 \text{ lb} \quad (121)$$

Assume that the load will distribute itself over at least a 2.0 inch width at the center of the flange. The maximum bending moment will then be

$$\frac{M_{\max}}{\text{in}} = \frac{P_{\max}}{2.0 \text{ in}} (.1825 \text{ in}) = 38.52 \text{ lb-in/in} \quad (122)$$

From Reference 3.2.10, a moment of 38.52 lb-in will generate the following peak natural axes stresses at different points within the laminate.

$$\sigma_{11} = \pm 72,878 \text{ psi}$$

$$\sigma_{22} = \pm 667 \text{ psi} \quad (123)$$

$$\tau_{12} = \pm 818.6 \text{ psi}$$

Taking a conservative approach, these values are assumed for one lamina and input to Hoffman's Failure Criteria.

$$\begin{aligned} & \left(\frac{\sigma_{11}^2 - \sigma_{11}\sigma_{22}}{F_{c1} F_{t1}} \right) F^2 + \frac{\sigma_{22}^2 F^2}{F_{c2} F_{t2}} + \left(\frac{F_{c1} - F_{t1}}{F_{c1} F_{t1}} \right) \sigma_{11} F \\ & + \left(\frac{F_{c2} - F_{t2}}{F_{c2} F_{t2}} \right) \sigma_{22} F + \frac{\tau_{12}^2}{F_{s12}^2} F^2 = 1 \end{aligned} \quad (124)$$

Given

$$F_{t1} = 100 \text{ ksi}$$

$$F_{t2} = 4.0 \text{ ksi} \quad (125)$$

$$F_{c1} = 100 \text{ ksi}$$

$$F_{c2} = 25.0 \text{ ksi}$$

$$F_{s12} = 11.44 \text{ ksi}$$

$$.5358F^2 + .1401F - 1 = 0 \quad (126)$$

$$F^2 + .2615 F - 1.866 = 0 \quad (127)$$

$$F = \frac{-.2615 \pm \sqrt{(.2615)^2 + 4(1.866)}}{2} = 1.2415 \quad (128)$$

$$MS = \frac{F}{1} - 1 = .2415 \quad (129)$$

Thus, for flange bending, a bolt spacing of 6.0 inch is adequate.

Interlaminar Tension Stresses in the Field Joint and Aft Attachment Flanges

Based on the results of (14)

$$N_{\theta_{\max}} = 70.36 \text{ lb-in} \quad (130)$$

From (119)

$$M = P(.1825 \text{ in}) \quad (131)$$

Again, assume that the load distributes itself over a 2.0 inch width at the corner of the flange. For a 2.0 inch width of flange

$$I = \frac{2(.12)^3}{12} = 2.88 \times 10^{-4} \text{ in}^4 \quad (132)$$

$$c = .06 \text{ inch} \quad (133)$$

$$f_b = \frac{Mc}{I} = \frac{(.1825 \text{ in})(.06 \text{ in})P}{2.88 \times 10^{-4} \text{ in}^4} = 38.02 \frac{P}{\text{in}^2} \quad (134)$$

$$\text{The shear stress} = f_s = \frac{P}{(.12 \text{ in})(2.0 \text{ in})} = 4.167 \frac{P}{\text{in}^2} \quad (135)$$

$$f_T = 0$$

From Appendix A, pg 6

$$\sigma_{33_{\max}} = 1.14 f_s + .175 f_b - .5751 f_T \quad (136)$$

$$= 1.14(4.167 \frac{P}{\text{in}^2}) + .175(38.02 \frac{P}{\text{in}^2}) - .656(0) = 11.4 \frac{P}{\text{in}^2} \quad (137)$$

$$\sigma_{33} \text{ allowable} = 4,000 \text{ psi} \quad (138)$$

$$\frac{P}{\text{bolt}} \text{ allowable} = \frac{4000}{11.4/\text{in}^2} \text{ psi} = 350.9 \text{ lb} \quad (139)$$

$$\text{Maximum bolt spacing} = \frac{350.9 \text{ lb}}{70.36 \text{ lb/in}} = 4.987 \text{ in} \quad (140)$$

This spacing need only occur in the region of maximum bending. The spacing at 90° from this region may be based on the condition for landing and braking (Reference 3.2.4).

$$N_x = 44.72 \text{ lb/in} \quad (141)$$

Minimum bolt spacing is

$$\frac{350.9 \text{ lb}}{44.72 \text{ lb/in}} = 7.85 \text{ in} \quad (142)$$

REFERENCES

- 3.2.1 GD/CA Report No. CASD-NAS73-015, "Graphite-Epoxy Metering Shell (GEMS)," Progress Report No. 2.
- 3.2.2 AFML-TR-74- , "Advanced Composite Missile and Space Design Data," G. E. Pynchon, June 1974.
- 3.2.3 Timoshenico and Gere, "Theory of Elastic Stability," 2nd Ed., p. 313.
- 3.2.4 NASTRAN Computer Run E0804F, "Metering Shell on Fixed Base," Oct. 3, 1973.
- 3.2.5 A. Holston Jr., AIAA Journal Vol 8, No. 7 p. 1352, July 1970.
- 3.2.6 Raymond J. Roark, "Formulas for Stress and Strain," 4th Ed.
- 3.2.7 Dow and Rosen, AIAA, Jan. 1965, pp 65-73.
- 3.2.8 NASA SP-8007, "Buckling of Thin-Walled Circular Cylinders," Aug. 1968.
- 3.2.9 Shaefer, W.H., Bender, R.E., Dunbar, D.R., et al, "Advanced Composite Wing and Empennage to Fuselage Attachment Fittings," General Dynamics Convair Division, AFML-TR-74-5.
- 3.2.10 SQ5 Computer Run E125055
- 3.2.11 MIL SPEC MMM-A-132 and GDCA Spec. 0-00096.

- 3.2.12 Dong, S. B., Sayegh, A. F., "Analysis of Laminated Curved Beams,"
Journal of the Engineering Mechanics Division, ASCE, August 1970.
- 3.2.13 Schaefer, W. H., Bender, R. E., Dunbar, D. R., et al, "Advanced
Composite Wing and Empennage to Fuselage Attachment Fittings,"
General Dynamics Convair Division, AFML-TR-74-5.
- 3.2.14 AFML-TR-74-5, "Advanced Composite Wing and Empennage to Fuselage
Attachment Fittings," Man. 1974.

SECTION 4

FABRICATION PROGRAM

4.1 COMPONENT FABRICATION

Manufacturing instructions were written for each type of Modmor I/X-30 graphite/epoxy parts. These instructions were based on established tooling and fabrication approaches. Figure 4.1 outlines the general manufacturing sequence used in the manufacturing of the graphite/epoxy metering shell (GEMS) assembly.

4.1.1 GENERAL LAYUP AND CURE PROCEDURES. The general layup and cure procedures used for the various Modmor I/X-30 graphite/epoxy parts is outlined below.

1. Tool Preparation - Cleaned molds and baked on release agent (30 to 60 minutes at 350F)
2. Layup Kit - Prepared complete kits of flat layups consisting of modules of two or three plies for multiple parts.
3. Preplying - Combined several or all the plies in part layup, either flat or on the shaped tool using vacuum bag pressure only.
4. Precompaction - Same as (3) except heat (160 \pm 10F) and vacuum bag pressure were used to prebleed resin and precompact flat module layups.
5. Cure Preparation - Prepared layup and tool assembly for autoclave cure using a minimum of two layers of Style 1534 glass cloth with vacuum bag seals. Except for the shell skins, bleeder was not used with the matched-die tooling approach. A minimum of two thermocouples were positioned on the tool surface to monitor cure temperature.
6. Post Cure - All flat laminates and complex shaped parts were post-cured in an air circulating oven or equivalent under atmospheric pressure only.

FABRICAT


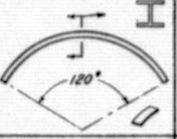
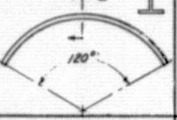
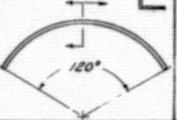
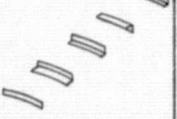

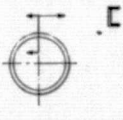
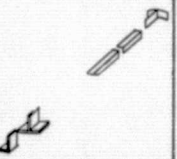
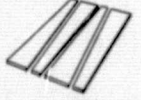
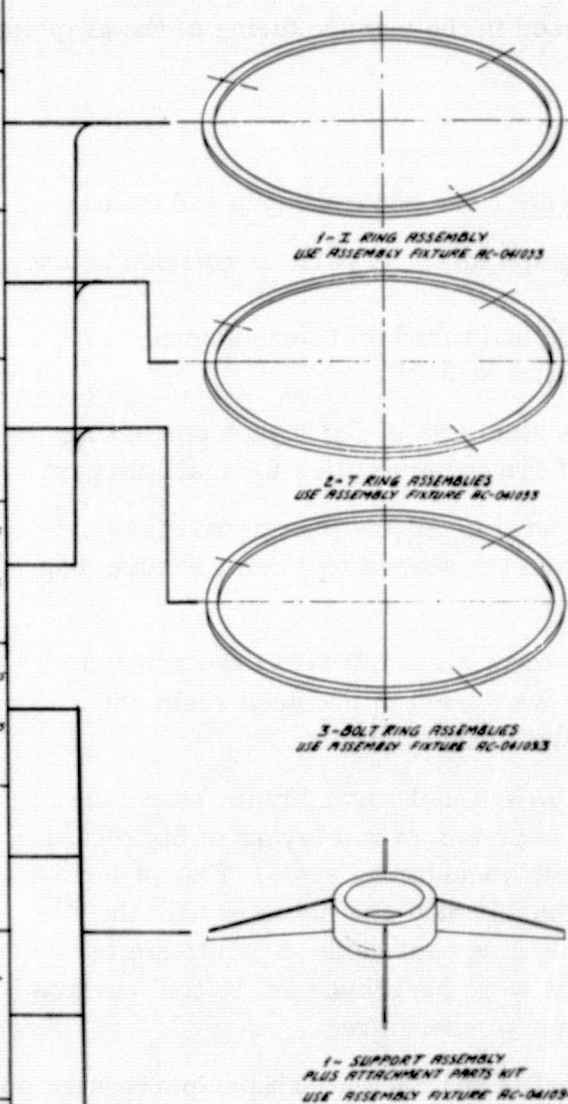
1 PRIORITY & TASK #	2 TASK TITLE	3	4 QUANTITY	5 PART NO & DESCRIPTION	6 FLAT LAYOUT	7 PRECOMPACT	8 EXTRACT	9
2	SHELL SKINS & SPLICE STRAPS	LONG SKINS & SPLICES  SHORT SKINS & SPLICES	3 3 3 3 6	72C0283-1 LONG SKIN PANEL -4 LONG LONGITUDINAL STRAPS -5 " " " -6 " " " -2 SHORT SKIN PANEL -7 " LONGITUDINAL STRAPS -8 " " " -6 CIRCUMFERENTIAL STRAPS	12 - 32 x 75 INCH 12 PLY IN 4 PLY MODULES	PRE-PLY		1 2 3 4 5 6
5	'I' RING SEGMENTS		3 3	72C0284-1 I RING SEGMENT 72C0279-3 I RING SPLICE STRAPS	FOR CHANNELS: 2 - 42 x 28 INCH 12 PLY IN 2 PLY MODULES FOR CAPS: 1 - 42 x 30 INCH 12 PLY IN 3 PLY MODULES	✓	36 KITS OF 2 PLY SEGMENTS FOR CHANNELS 24 KITS OF 3 PLY SEGMENTS FOR CAPS	1 2
4	'T' RING SEGMENTS		6	72C0284-2 T RING SEGMENT	FOR ANGLES: 4 - 40 x 33 INCH 12 PLY IN 2 PLY MODULES FOR CAP: 2 - 34 x 16 INCH 12 PLY IN 2 PLY MODULES	✓	72 KITS OF 2 PLY SEGMENTS FOR ANGLES 36 KITS OF 2 PLY SEGMENTS FOR CAP	1 2 3
1	BOLT RING SEGMENTS		9	72C0284-3 BOLT RING SEGMENT	1 - 27 x 70 INCH 24 PLY IN 2 PLY MODULES	✓	108 KITS OF 2 PLY SEGMENTS	1 2 3 4 5
3	RING SPLICE ANGLES		6 6 12 9 9	72C0279-1 I RING SPLICE ANGLE, INNER -2 " " " " OUTER -4 T RING " " -5 BOLT RING " " -6 " " " SPLICE STRAP	1 - 38 x 21 INCH 12 PLY IN 4 PLY MODULES	✓	39 - 4 PLY SEGMENTS FOR 33 ANGLES 27 - 4 PLY SEGMENTS FOR 9 STRAPS	1 2 3 4
7	HUB SKINS AND SPLICE STRAPS		2 4 2 2	72C0286-1 HUB INNER SKIN SEGMENT -2 HUB OUTER " " -3 LONG SPLICE STRAPS -4 SHORT " "	1 - 50 x 29 INCH 12 PLY IN 4 PLY MODULES	PRE-PLY	6 PIECES, 4 PLY FOR INNER SKIN SEGMENTS 6 PIECES, 4 PLY FOR OUTER SKIN SEGMENTS 3 PIECES, 4 PLY FOR SPLICE STRAPS	1 2 3
6	HUB RINGS		2 1	72C0287-1 HUB RING	1 - 33 x 18 INCH 12 PLY IN 2 PLY MODULES	✓	12 KITS OF 2 PLY SEGMENTS	1 2
8	SUPPORT TEES & ANGLES		8 8 8 4 4	72C0285-1 HUB TEES -2 HUB ATTACH ANGLES, SHORT -3 " " " LONG 72C0282-1 SPIDER ATTACH TEES -2 " " " ANGLES	1 - 36 x 24 INCH 12 PLY IN 6 PLY MODULES	✓	2 STRIPS, 6 PLY FOR HUB TEES 1 STRIP, 6 PLY " " " 2 STRIPS, 12 PLY FOR ANGLES (CHANNEL LAYOUT) 6 STRIPS, 6 PLY FOR SPIDER TEES 4 STRIPS, 6 PLY FOR SPIDER ANGLES.	1 2 3 4
9	SPIDER LEGS		4	72C0284-1 SPIDER LEGS	1 - 46 x 28.5 INCH 48 PLY IN 6 PLY MODULES	✓		1

Figure 4-1. GEMS Program Fabrication Sequence

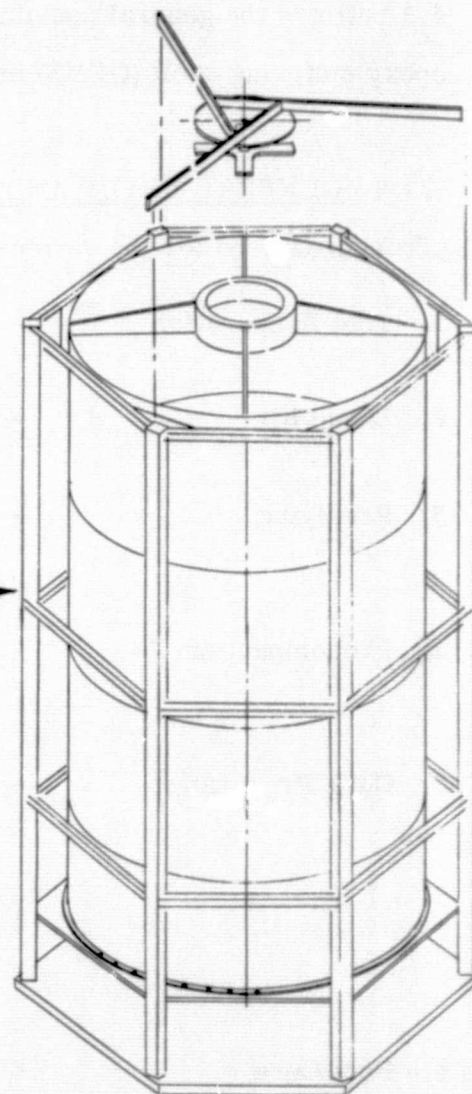
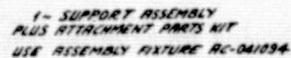
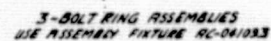
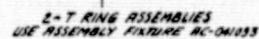
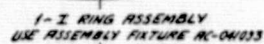
FOLDOUT FRAME

ORIGINAL PAGE 18
OF POOR QUALITY



11

3	14	15	16	17	EXTRACT & FINISH
				1	3-SKIN PANELS, SHORT 6- SPALCE STRAPS, +
				2	6- CIRCUM. SPALCE STRAPS 3- SKIN PANELS, LONG
				3	6- SPALCE STRAPS 3- SKIN PANELS, LONG
				4	6- SPALCE STRAPS + 3- SKIN PANELS +
				1	3- I RING SEGMENTS 3- SPALCE STRAPS
				1	3- "T" RING SEGMENTS
				2	3- " " " "
				1	3- BOLT RING SEGMENTS
				2	3- " " " "
				3	3- " " " "
				1	9- BOLT RING SPALCE ANGLES 3- " " " " STRAPS
				2	12- "T" RING SPALCE ANGLES
				3	12- "I" RING " " "
				1	2- HUB INNER SKIN SEGMENTS
				2	4- SPALCE STRAPS
				3	4- HUB OUTER SKIN SEGMENTS
				1	2- HUB RINGS
				1	8- HUB TEES
				2	8- ATTACH ANGLES, SHORT
				3	8- " " " " , LONG
				4	4- SPIDER TEES
				5	4- SPIDER ANGLES
				1	4- SPIDER LEGS



FINAL ASSEMBLY FIXTURE AC-04/106

4.1.2 TRIMMING AND MACHINING. A variety of hand tools and versatile lathe type machines were used to trim the detail Modmor I/X-30 graphite/epoxy parts for the GEMS assembly.

In nearly all cases, diamond coated cutting wheels, grinding wheels, and bits were used to either rough cut or final machine the various parts.

4.1.3 PROBLEM AREAS. Primary problem areas were directly related to the lack of "cohesive tackiness" between the layers of prepreg as they were being formed over tooling having sharp radii. The high moduli (55 to 59×10^6 psi) of the Modmor I graphite fiber may have been a contributing factor, but lack of tack in the wet prepreg was believed to be more significant. The "tackiness" problem made it impossible to layup the individual layers even though they consisted of two or more oriented plies that were vacuum bag preplied prior to layup. The affect of these material variables had a significant impact on the time required to make specific layups and resulted in each individual Modmor I/X-30 prepreg layer being temporarily wrapped with PVA tape as it was laid up to avoid spring-back over sharp radii. This lack of tack integrity also affected the handling of preplied or precompacted flat stacks of prepreg although to a lesser extent.

4.1.4 SHELL SKINS AND SPLICE STRAPS. The twelve (12) ply shell skins ($0/+45.5/0/-45.5/0/90$)_S and splice straps were first laid up, flat 75 x 32 inch, 4 ply at a time using an aluminum template to control the layup of the oriented plies as shown in Figure 4-2. Each form ply module was vacuum bagged at room temperature to consolidate the material and minimize movement of fibers during transfer to the aluminum male tool (see Figure 4-3). An outline of the general fabrication steps used to make each of the twelve (12) shell skin segments is as follows:



140934

Figure 4-2. Layup of Shell Skin 4-Ply Module



140571

Figure 4-3. Aluminum Skin Tool and 4-Ply Module

1. Cleaned mold and baked on two coats of Frekote 33.
2. Because of size of the skin layups, it required two people to lay up each individual layer and maintain proper fiber alignment and to transfer each 4-ply module to the aluminum tool. Figure 4.2 shows the layup on the tool. Each 4-ply module was preplied (vacuum bag).
3. Each 4 ply module was kept under vacuum bag pressure at room temperature after being transferred to the aluminum tool until completion of 12 ply layup.
4. Using an .040 inch thick, rolled aluminum caul plate, each 12 ply shell skin was cured in an autoclave using five ply of 181 style glass cloth as bleeder (see Figure 4-4). The cure schedule was:
 - a. Vacuum — 29 inches of Hg minimum
 - b. Pressure — 100 psig autoclave (applied at 250 \pm 10F)
 - c. Heat at 250 \pm 10F for 60 minutes, 3-5F/minute heatup rate plus 6 hours at 275 \pm 10F
cool to 160F, or lower, unbag and postcure (unrestrained)
16 hours at 275 \pm 10F
 - d. Lay out and trim individual parts using diamond coated routing tool

4.1.5 BOLT RING SEGMENTS. The nine (9) bolt ring segments were fabricated on steel tooling. Each segment was a 120 degree segment and 24 ply thick. Cure was done in an autoclave. Flat two-ply modules were laid up and precompacted to yield kits used in the layup of the bolt rings. The module sequence when laid up on the tool is as shown in Figure 4-5.

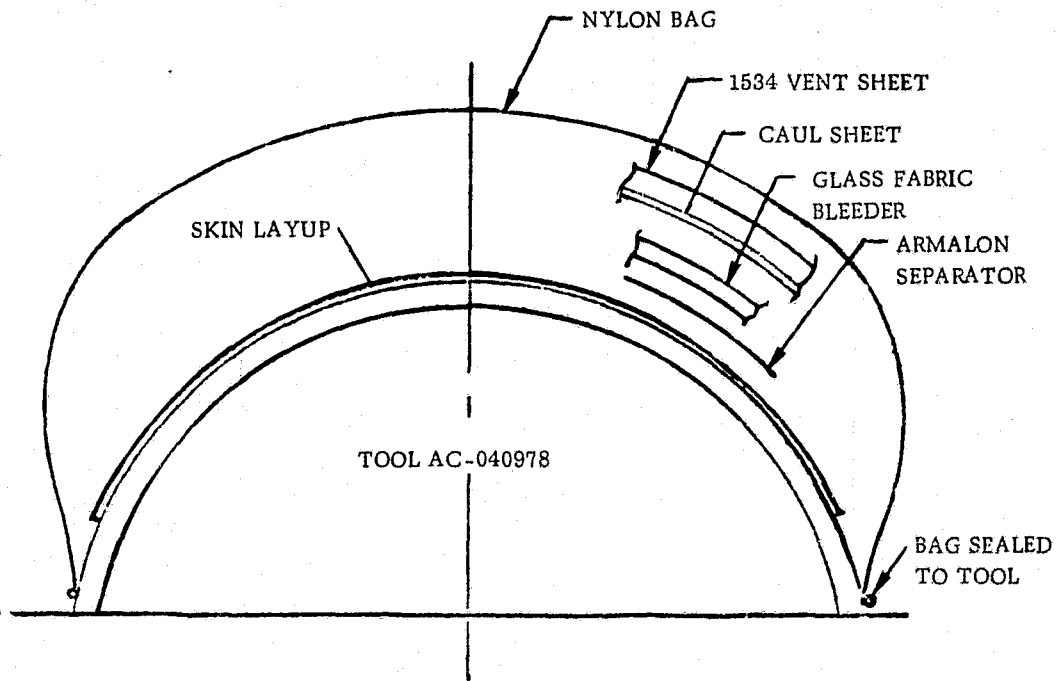


Figure 4-4. Illustration of Shell Skin Prepared for Cure

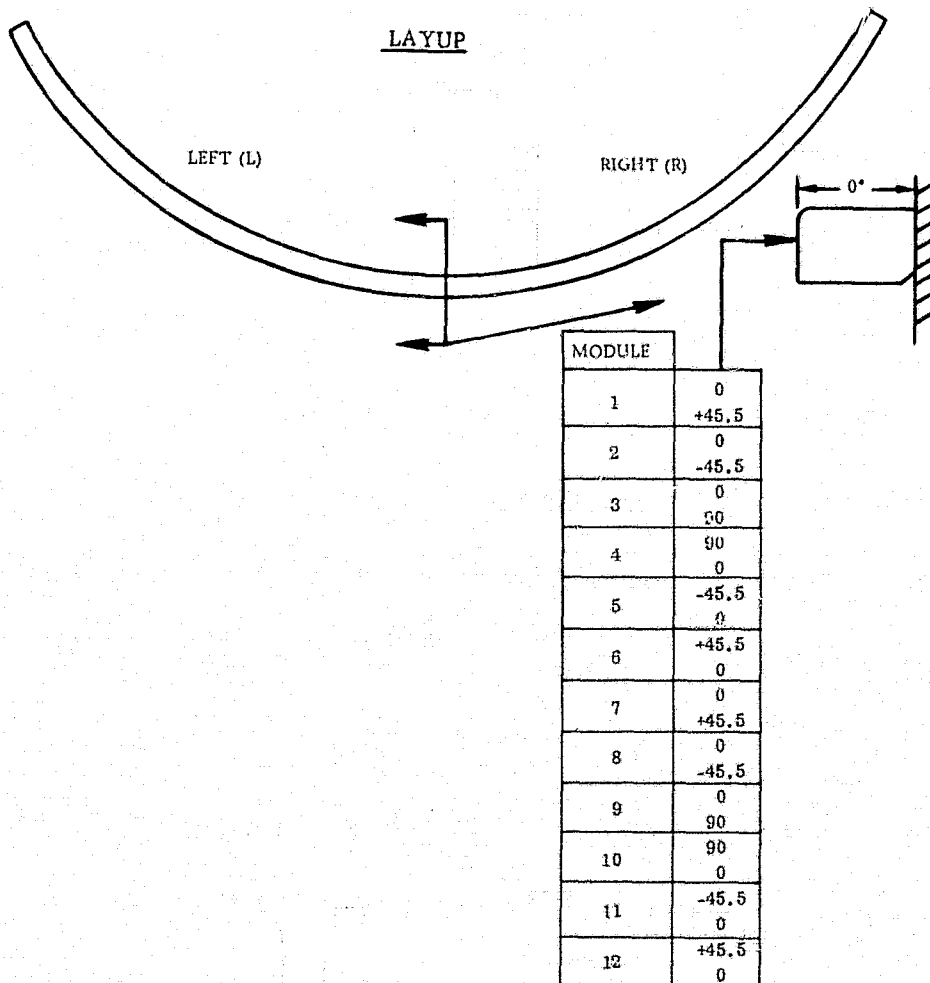


Figure 4-5. Layup of Bolt Ring Segment

A summary of the fabrication procedure for the bolt ring segments is presented here.

1. The steel tool and caulplates were cleaned and working surfaces conditioned with Frekote 33.
2. Two-ply modules were precompacted, $160 \pm 10F$, 15-20 minutes vacuum plus 50 psig.
3. Pieces of 2-ply modules were cut to patterns and positioned on the tool using a continuous overwrap of PVA to hold the layup in place.
4. The layup was vacuum bagged, as necessary, to assist in forming the prepreg to the tool.
5. After plying a total of 12 modules or 24 plies on the tool, the Modmor I/X-30 angle bolt ring layup was bagged (see Figure 4-6) for autoclave cure with the PVA wrap over last layer left intact. No bleeder was used since each two ply module.

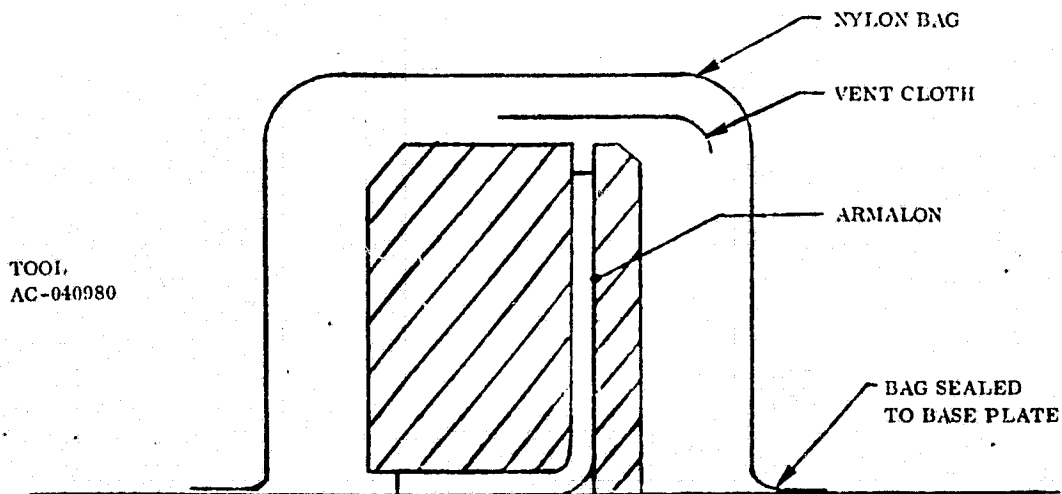
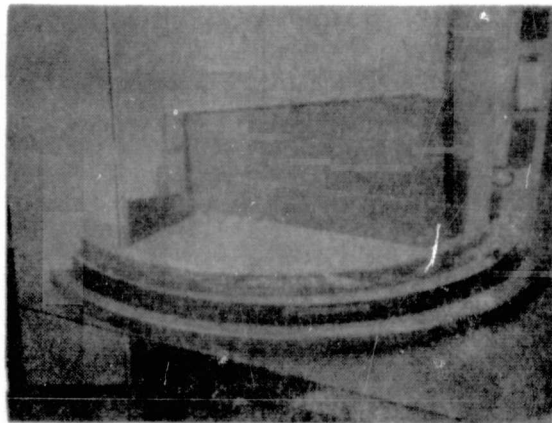


Figure 4-6. Bolt Ring Bagged for Autoclave Cure

6. Each bolt ring was cured while under full vacuum plus 100 psig (applied at 240F), heated to $250 \pm 10\text{F}$ and after being held for 60 minutes heated to $275 \pm 10\text{F}$ for 6 hours.
7. The temperature of the part was below 160F when the all-pressure was released.
8. All of the bolt rings were postcured 16 hours at $275 \pm 10\text{F}$.

A photograph showing cured bolt rings and bolt ring tooling is given in Figure 4-7.



14-0570

Figure 4-7. Cured Bolt Rings and Tooling

4.1.6 "T" RING SEGMENTS. The six (6) "T" ring segments were fabricated in 120° segments using steel tooling. The 24-ply inverted "T" consisted of flat, two-ply modules laid up on each half of the steel tooling and a cap section tying

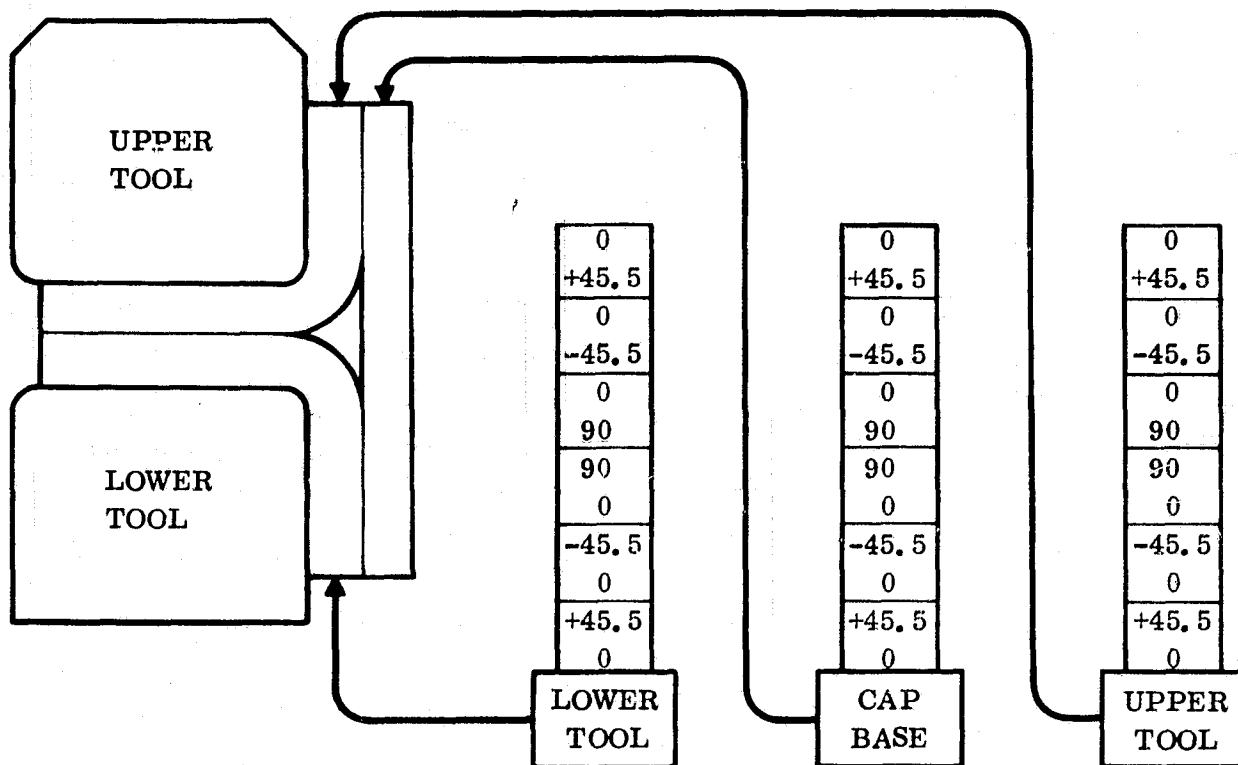


Figure 4-8. "T" Ring Segment Layup

A summary of the fabrication procedure for the inverted "T" ring segments is presented here.

1. The steel tools and caul plates were cleaned and working surfaces conditioned with Frekote 33.
2. Layup 36-two-ply modules and precompact in six stacks, six modules each, at $160 \pm 10^\circ\text{F}$, 15-20 minutes, vacuum bag plus 50 spig autoclave pressure.
3. Two-ply modules were cut and laid up on tool using a PVA overwrap to hold them in place, layups were vacuummed, as necessary, to set the formed pieces in place.

4. After laying up the six, 2-ply modules on each tool half (web-flange areas), the two sections were brought together and the cap base located in place.
5. Each inverted "T" ring segment was bagged for autoclave cure (Figure 4-9) and cured while under full vacuum plus 100 psig (applied at 240F), heated to $250 \pm 10\text{F}$ and after being held for 60 minutes heated to $275 \pm 10\text{F}$ for 6 hours.
6. The temperature of the part was reduced to below 160F prior to release of all pressure.
7. All of the "T" rings were then postcured for 16 hours at $275 \pm 10\text{F}$. Each was final trimmed using diamond coated cutting wheels.

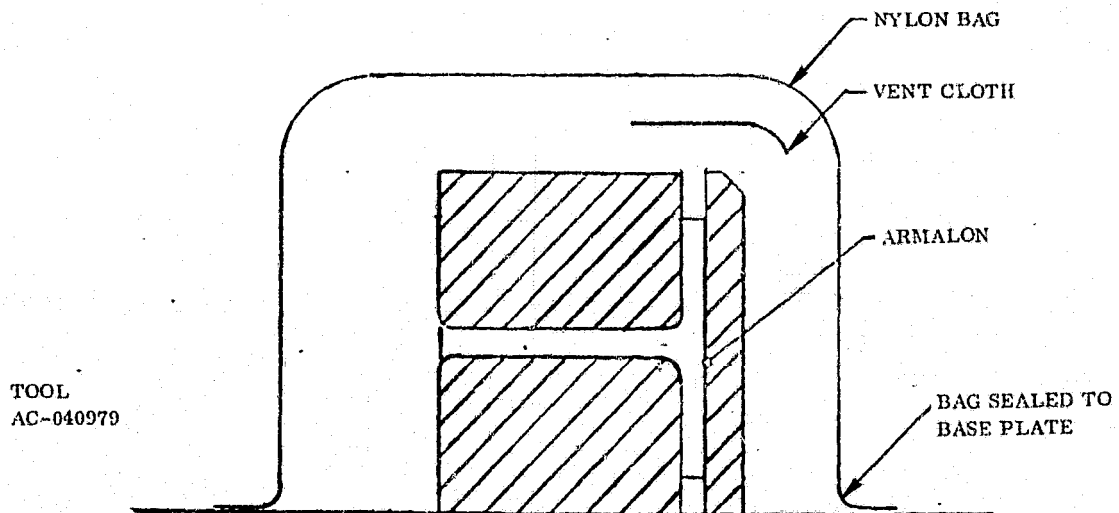


Figure 4-9. Inverted "T" Ring Bagged for Autoclave Cure

4.1.7 "I" RING SEGMENTS. Three I-ring segments were fabricated as 120° segments using basically the same procedure as used for the bolt ring and inverted "T" ring. However, the degree of difficulty was greater for the "I" ring because of shape configuration, particularly the forming of the web-flange areas.

A series of flat modules consisting of 2 and 3 plies were laid up and precompacted in an autoclave using vacuum plus 50 psig, 160 ±10F heat, and 15-20 minutes time interval. The layup configuration is given in Figure 4-10. A summary of the fabrication procedure used for the I-ring segments is presented here.

1. Steel tooling was cleaned and Frekote 33 release agent applied and baked on at 300F.
2. Layup flat 12 two-ply modules and 4 three-ply modules and autoclave precompact (160 ±10F, 15-20 minutes, vacuum plus 50 psig).
3. From each precompacted module make kits.
4. For each of three ring segments, strips for web-flange areas were cut 6 inch long and butt spliced on tool. Cap layups were continuous pieces.
5. During layup PVA tape was used to maintain proper fiber orientation and configuration and vacuum bag pressure as necessary.
6. Each assembly was bagged for autoclave cure (Figure 4-11 and cured as follows:
Vacuum - 29 in. Hg (min)
Pressure - 100 psig (applied at 240F)

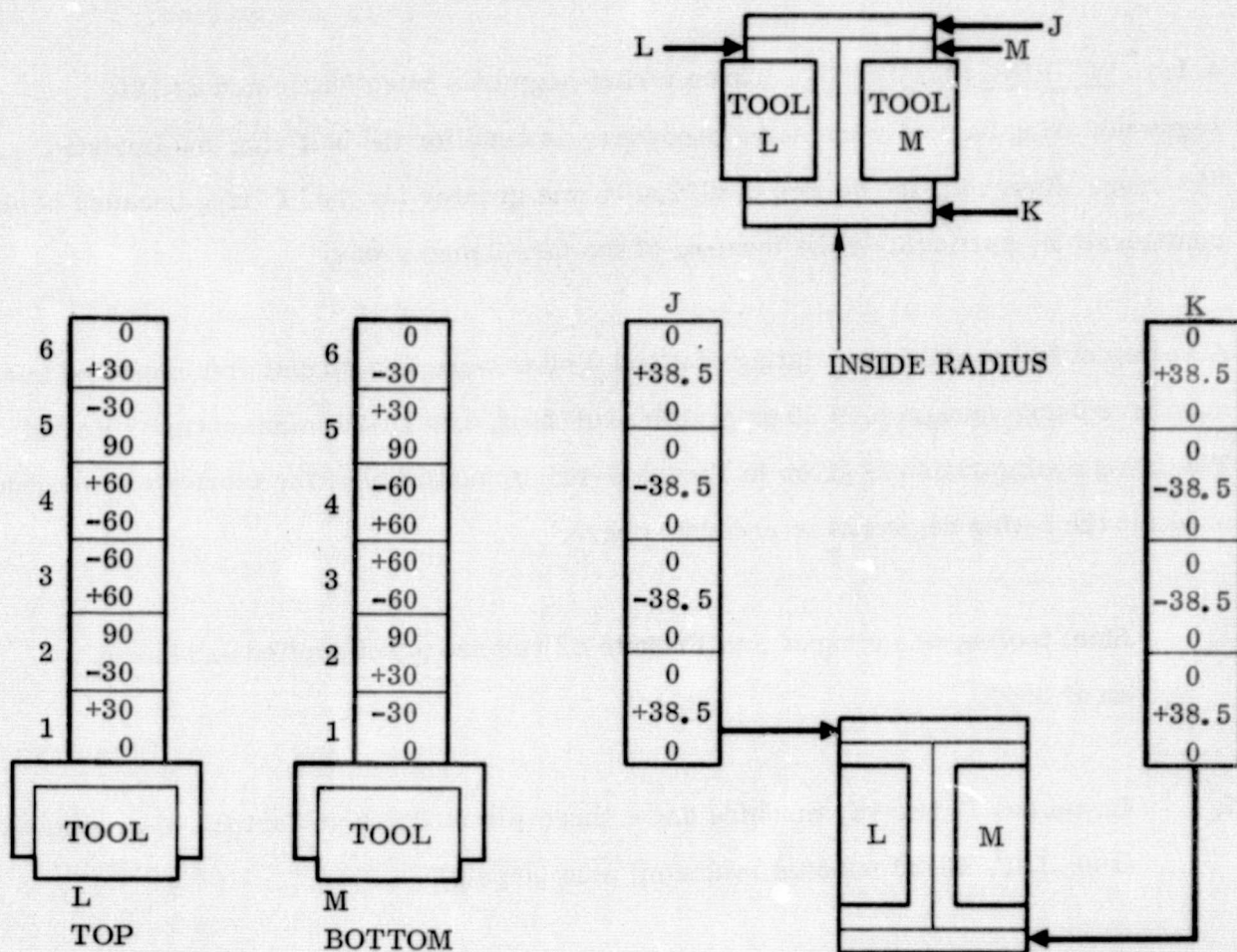


Figure 4-10. Layup Configuration for the I-Ring Segments

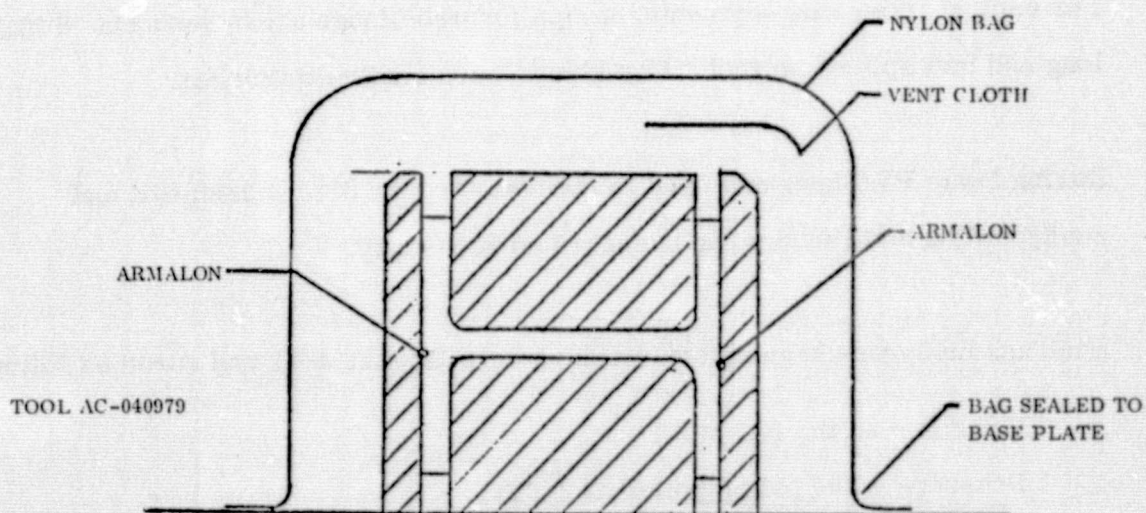
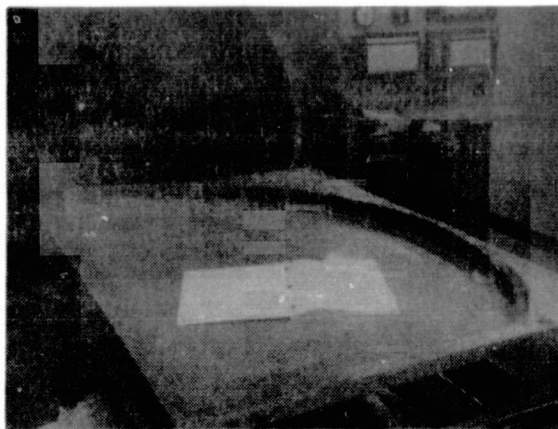


Figure 4-11. I-Ring Segments Bagged for Autoclave Cure

Heat at $250 \pm 10^\circ\text{F}$ for 60 minutes, $3\text{--}5^\circ\text{F/minute}$ heat-up rate
plus 6 hours at $275 \pm 10^\circ\text{F}$
Cool to 160°F , or lower, unbag and postcure (unrestrained) 16
hours at $275 \pm 10^\circ\text{F}$



14-0569

Figure 4-12. Cured Splice Angles on Steel Tool

4.1.8 RING SPLICE ANGLES AND STRAPS. Forty-five (45) assorted splice angles fabricated using steel tooling similar to the bolt ring tooling and flat caul plates. The splice angles were made as multiple items (total of 12) on one tool and consisted of two, 6-ply modules that were autoclave-heat precompacted prior to layup. Each splice angle was approximately 4.5 inches long. A series of cured splice angles unbagged after autoclave cure are shown in Figure 4-12. Also, a flat panel approximately 4.5- x 10-inch was laid up and cured in an autoclave.

The basic layup kits were obtained for the splice angles, splice straps from the 21- x 38-inch flat layup shown in Figure 4-13. The various parts were laid up and bagged for cure as illustrated in Figures 4-14, 4-15, and 4-16 using the standard 275°F cure schedule for the X-30 resin matrix.

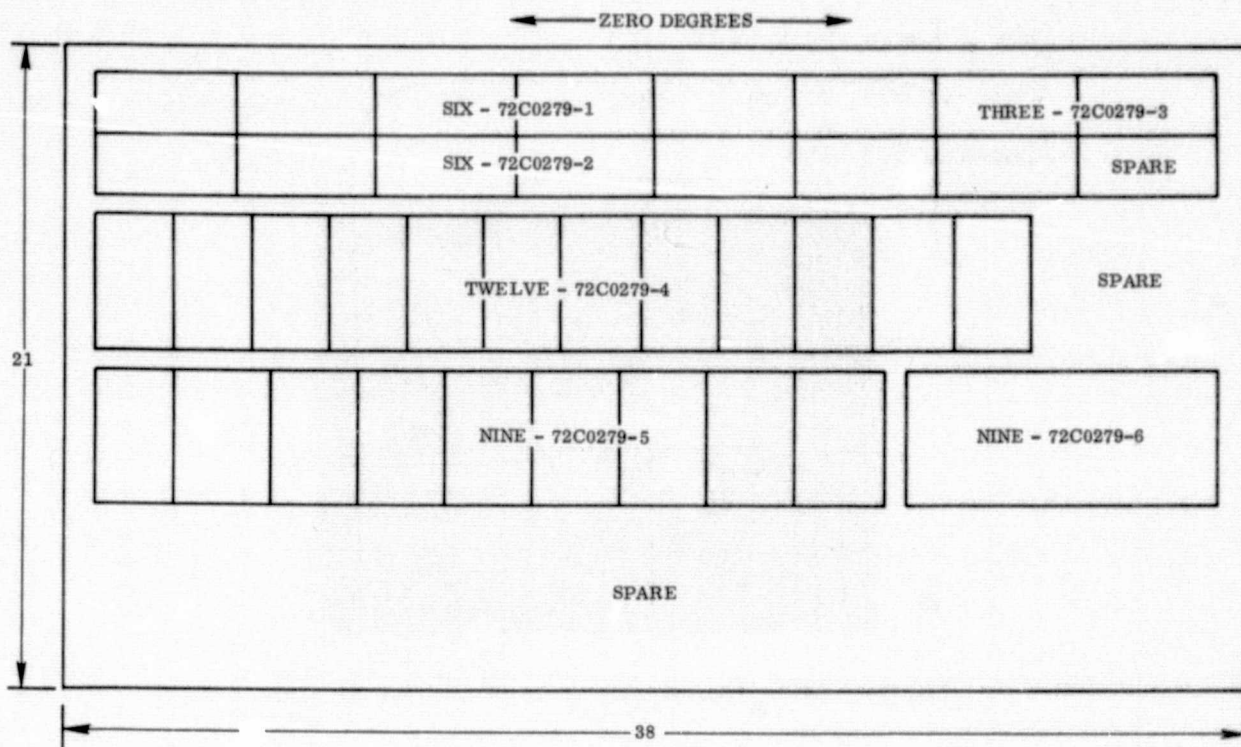


Figure 4-13. Flat Layup and Kit Extraction

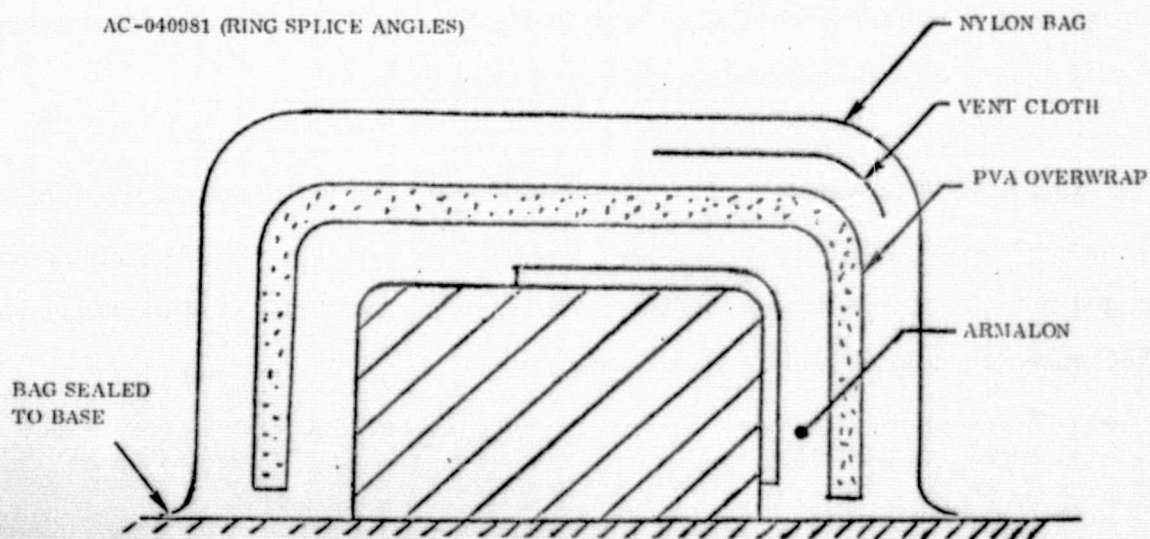


Figure 4-14. Splice Angles

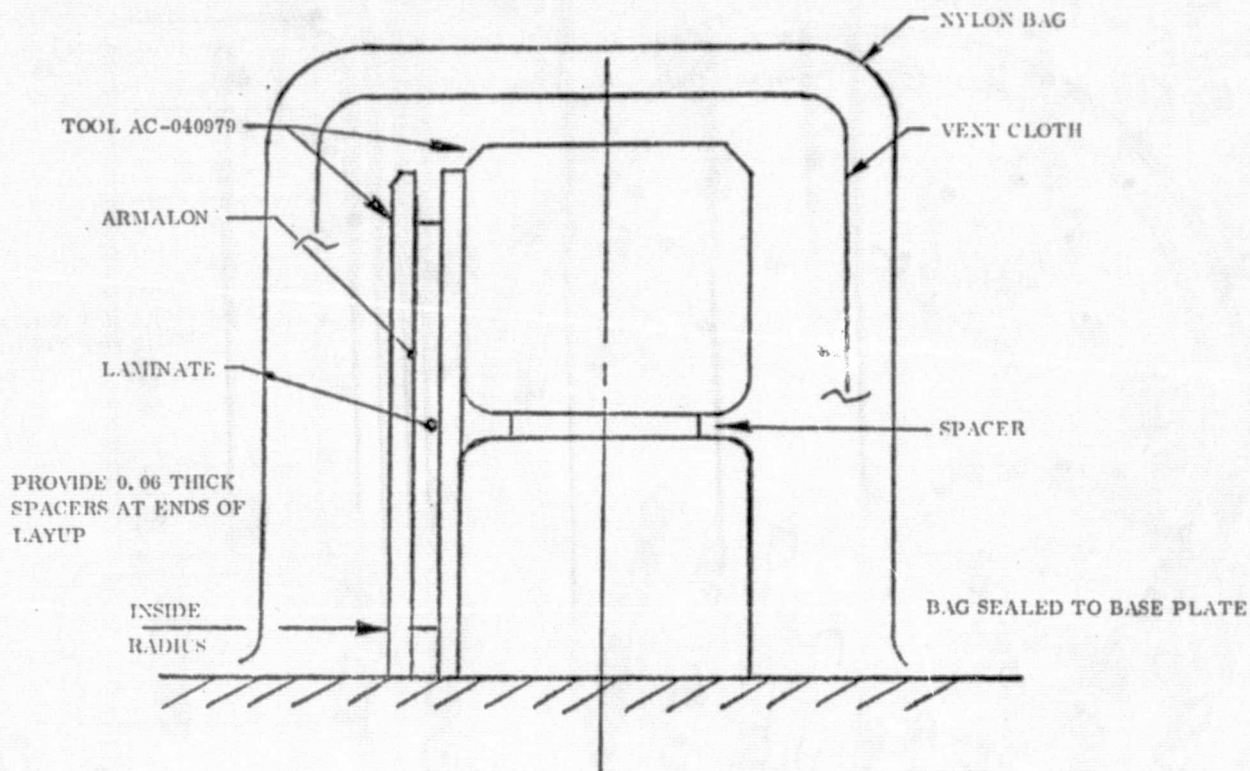


Figure 4-15. Splice Straps

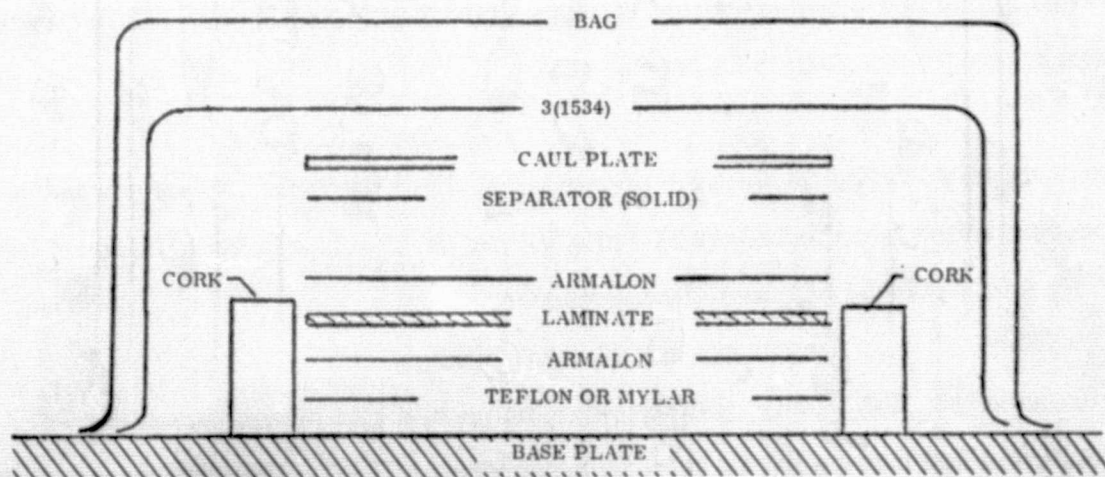


Figure 4-16. Flat Panel

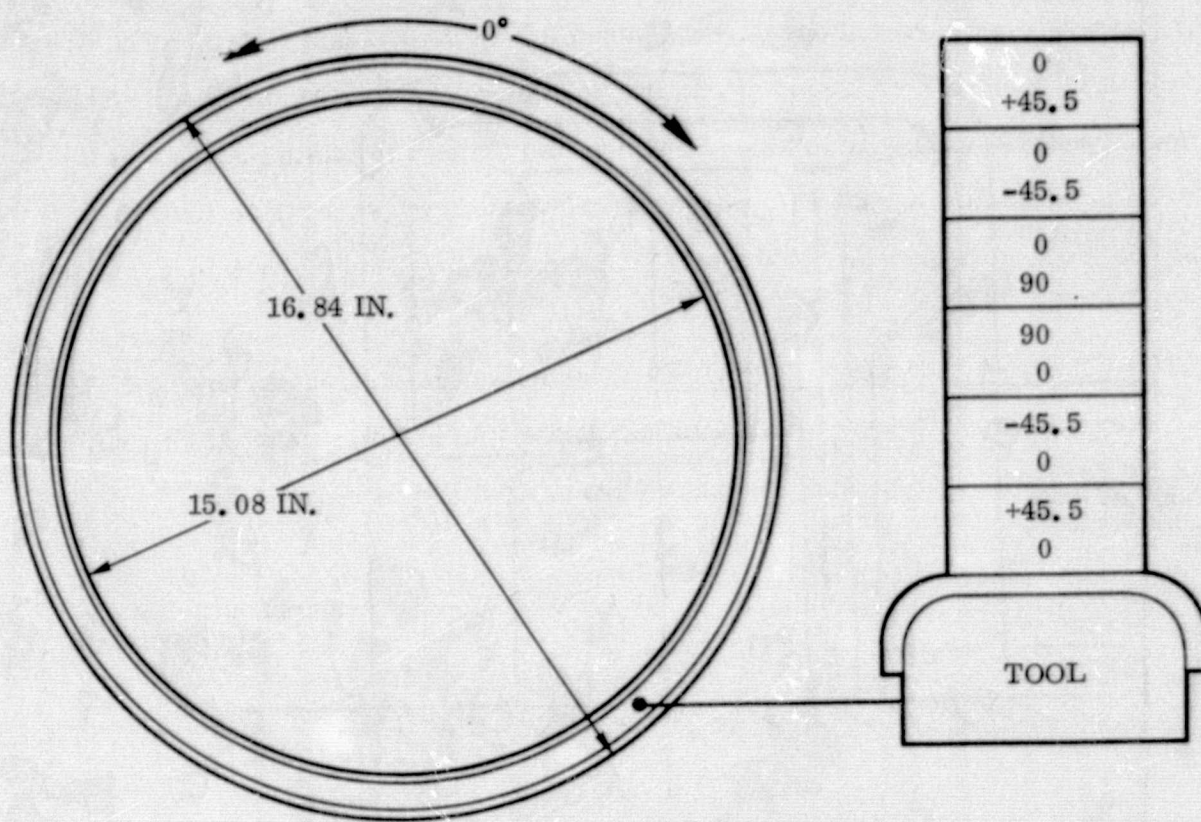


Figure 4-17. Hub Channel Ring Layup

4.1.9 HUB CHANNEL RINGS. Two identical Modmor I/X-30 graphite/epoxy hub channel rings were fabricated using steel tooling and a glass fabric reinforced TRV overpress. Orientation was $[0/+45.5/0/-45.5/0/90]_s$.

Kits were made up using six flat two-ply modules, 33- x 18-inch. The 2-ply modules were precompacted in an autoclave at $160 \pm 10^\circ\text{F}$ for 15-20 minutes under vacuum bag (25 in. Hg min.) plus 50 psig autoclave pressure.

The precompacted, flat, 2-ply modules were cut up into kits of approximately 20° segment strips and laid up on the steel tool (see Figure 4-17). Vacuum bag pressure was used to prepreg the layups, but the PVA overwrap was still used primarily to maintain the layup in place.

The standard 275F cure and postcure was used for the X-30 resin matrix. The first hub channel ring was damaged in attempting to remove it from the steel tool. This difficulty was due primarily to lack of any draft on the tool to minimize friction between tool and cured graphite/epoxy part. Several thumb screw type fixtures had to be made to remove the Modmor I/X-30 parts from the steel tool.

4.1.10 HUB SKINS AND SPLICE STRAPS. This task consisted of fabricating 2 inner skin segments, 4 outer skin segments, and 4 splice straps using Modmor I/X-30 graphite/epoxy prepreg. The basic fabrication steps were:

1. Prepare tools by cleaning and applying Frekote 33 release agent.
2. Layup flat, 6, two-ply modules approximately 50 x 29 inches.
3. Cut the six modules to make 180° inner skin segments, one layup for splice straps, and two 180° outer skin segments.
4. Layup and bag segments for autoclave cure (Figure 4-18) using 5 ply of 7781 style glass cloth as bleeder.
5. Run standard 275F cure and postcure for X-30 epoxy resin.
6. Trim each segment to drawing dimensions using diamond coated cutting tools.

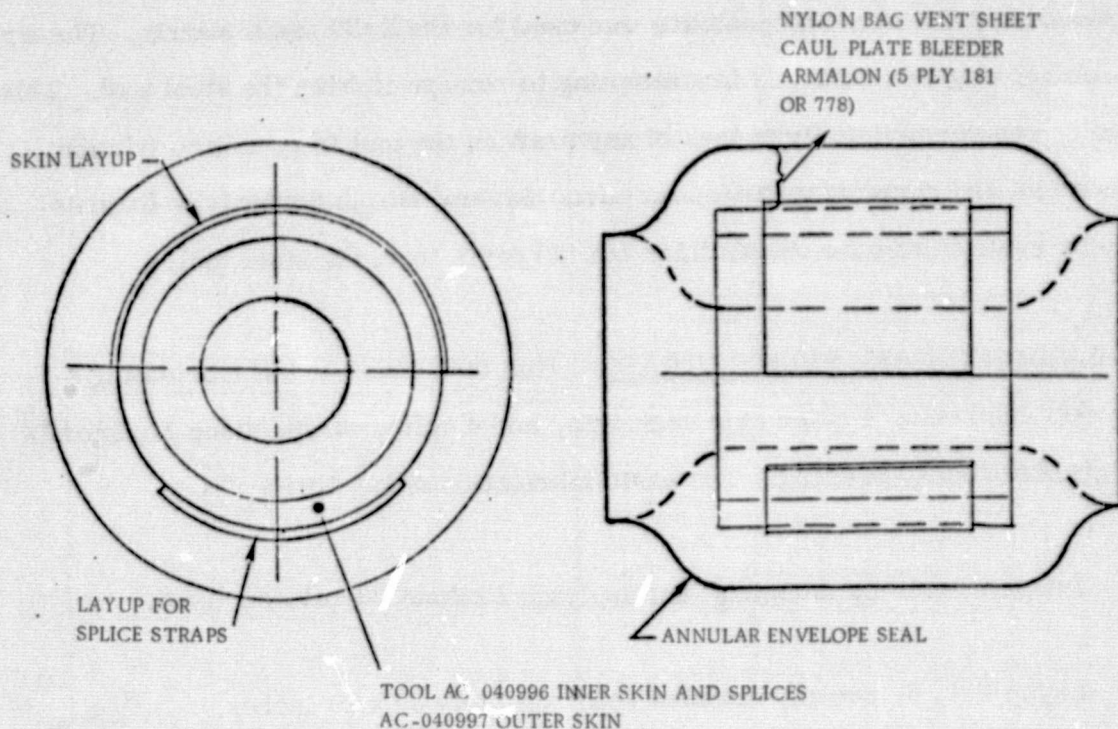


Figure 4-18. Bagging Schematic for Hub Skins and Splice Straps

4.1.11 SUPPORT TEES AND ANGLES. This task consisted of the fabrication of 32 assorted angles and tees using Modmor I/X-30 graphite/epoxy prepreg tapes. The basic fabrication steps are as follows.

1. Prepare tool.
2. Layup flat, 2, six-ply modules 24 x 36 inches (see Figure 4-19).
3. Precompact each module in an autoclave at $160 \pm 10^{\circ}\text{F}$ for 15-20 minutes under vacuum bag (29 in. Hg) plus 50 psig pressure using 2 plies of 120 style glass cloth as bleeder.
4. Cut the modules to form kits required to lay up the different angles and tees.

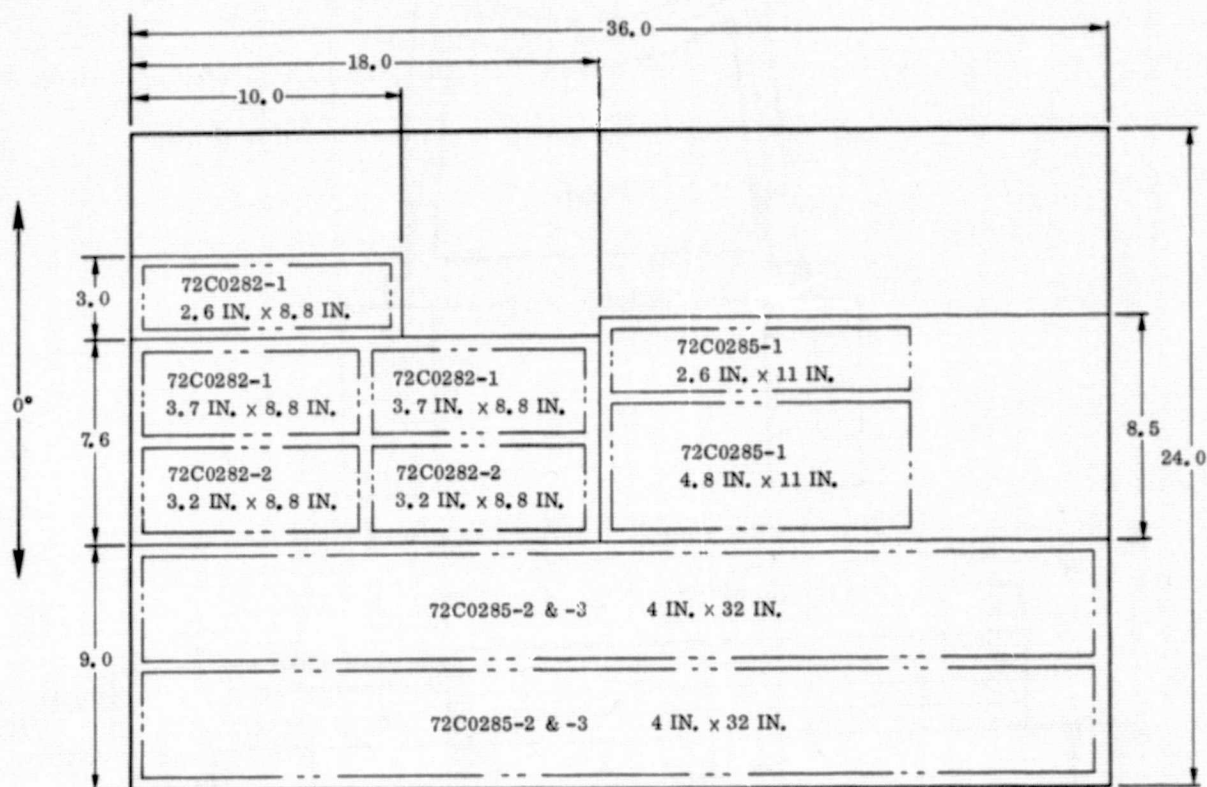


Figure 4-19. Layup Module for Angles and Tee's

5. Layup each part and bag for autoclave cure using PVA overwrap but no bleeder (Figures 4-19, 4-20, 4-21, and 4-22).
6. Cure each part using standard 275F cure and postcure.
7. Trim parts to net dimensions.

4.1.12 SPIDER LEGS. This task consisted of the fabrication of 4 identical spider legs using Modmor I/X-30 graphite/epoxy prepreg tapes. The basic fabrication steps were as follows:

1. Prepare flat, picture-frame type aluminum tool.
2. Layup 4, flat, six-ply modules approximately 48 x 28.6 inches.

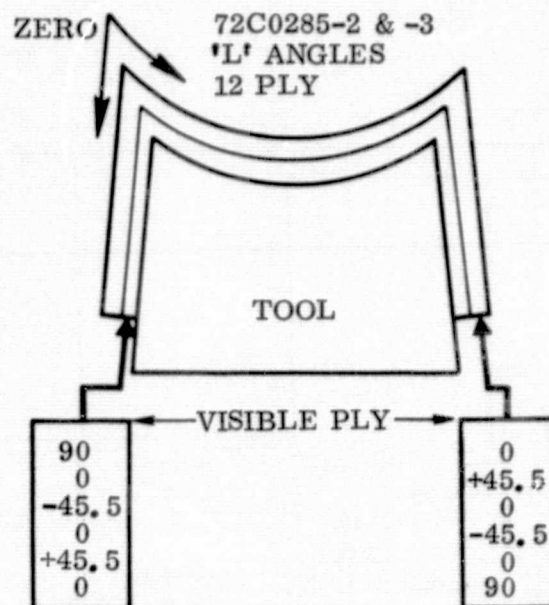


Figure 4-20. Modmor I/X-30 Angles Layup

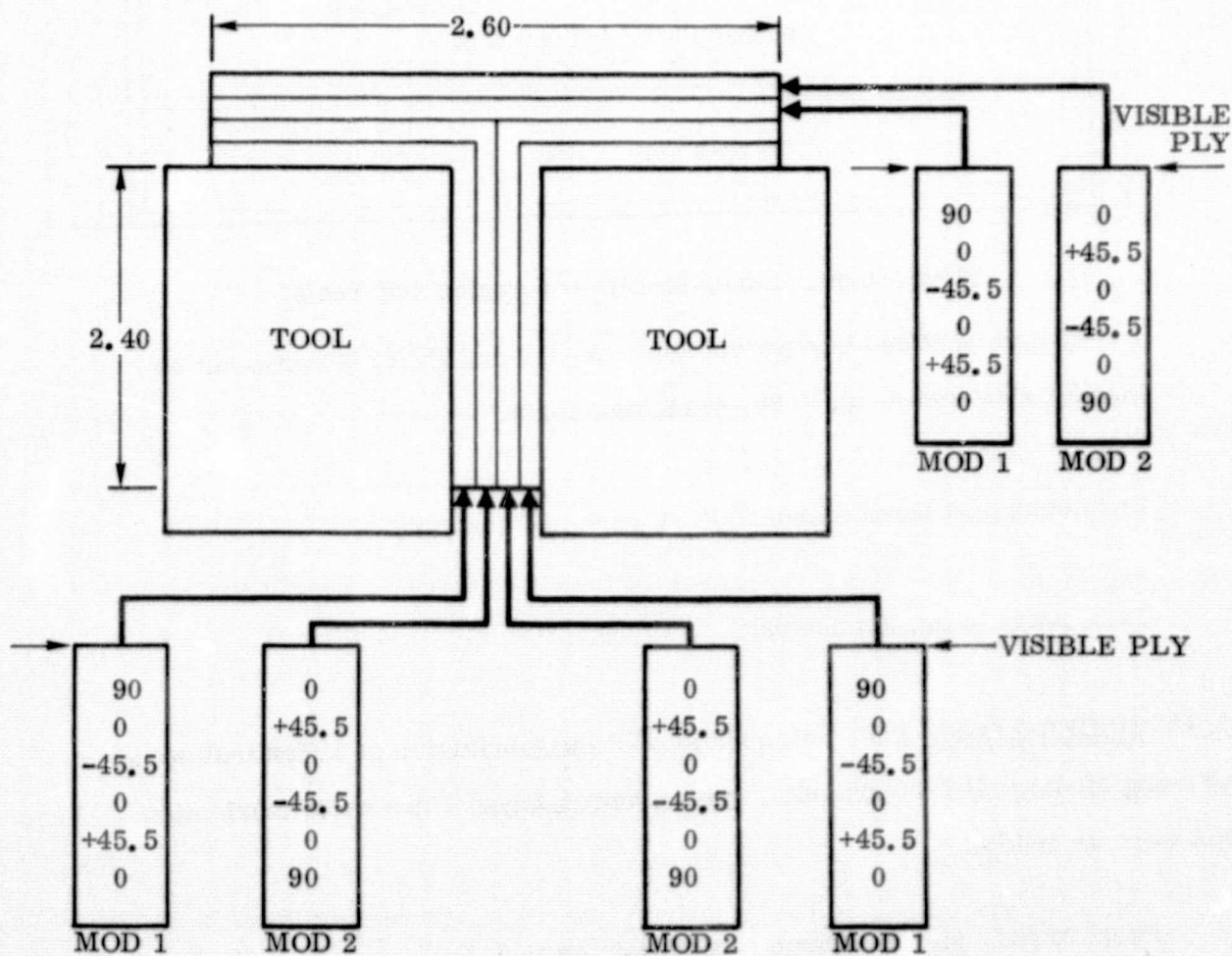


Figure 4-21. Modmor I/X-30, 24-Ply T

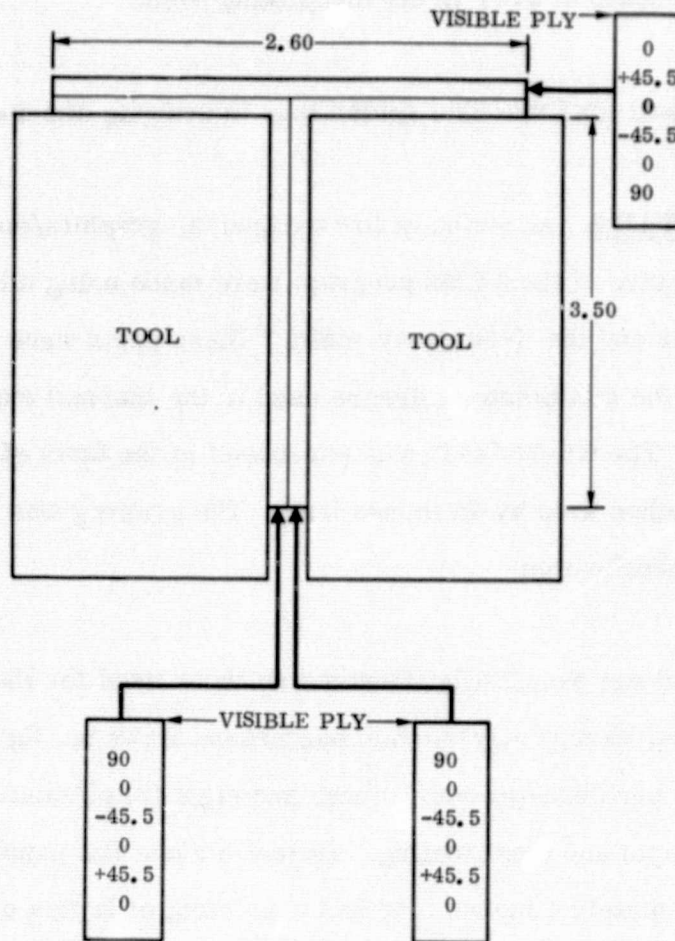


Figure 4-22. Modmor I/X-30 T Angle Layup

3. Precompact each module in an autoclave using vacuum (29 in. Hg min.) plus 50 psig autoclave at 160 \pm 10F for 15-20 minutes.
4. Cut from each module two 20 x 26 inch rectangular with the 26-inch side aligned 40-20 ft. to the 0° ply orientation.
5. Lay up the resulting 8 modules in tool using 4 plies of 7781 style glass cloth as a bleeder/vent combination and bag for cure.
6. Run standard autoclave cure, vacuum bag (29 in. Hg minute) plus 100 psig (applied at 240F) at 2-3° F/minute heatup rate to 250F for 60 minutes to 275F for 6 hours.

7. Postcure 16 hours at 275F in air circulating oven.
8. Rough trim and final machine spider legs to drawing dimensions.

4.1.13 OTHER DETAILS. A series of low expansion, graphite/epoxy parts for stable support structure of the GEMS program were made using ultra high modulus GY-70 graphite fiber and the X-30 epoxy resin. These parts were used to provide stable supports for the dilatometer mirrors used in the thermal expansion measurement of the GEMS. The GY-70/X-30 was purchased in the form of prepreg flat sheets, approximately 12 inches wide by 45 inches long. The prepreg was bought to a Convair material specification.

The layup procedure was essentially the same as those used for the Modmor I/X-30 graphite/epoxy parts, except only vacuum bag pressure (29 in. Hg min.) was used during the 160 ±10F prebleed-precompaction; and eight (8) plies at a time were laid up using both aluminum and steel tooling. Except for one flat panel these parts were angles approximately 4 inches long and consisting of layups oriented $[0/+45/90/-45]_{s(x)}$ with symmetrical multiples (x) ranging from 1 to 3 of the basic eight ply module. The parts were cured, were bagged and cured in an autoclave using the same cure cycle used for the Modmor I/X-30 graphite/epoxy parts.

4.2 SUBASSEMBLIES

There are seven Modmor I/X-30 subassemblies for the GEMS structure. They are:

1. Three Bolt Rings
2. Two "T" Rings
3. One "I" Ring
4. One Secondary Mirror Support

The 120° ring segments and the associated splice angles and straps were final trimmed using diamond coated cutting tools. The ring frames were then subassembled into complete rings in a common bench-top type subassembly fixture. Particularly noteworthy during this and subsequent assembly operations was the excellent fit-up of all the detail parts. Hysol EA-934 room temperature curing epoxy adhesive was used to join the 120° ring segments. A minimum of twelve hours was allowed for cure prior to removal of any subassembly from a fixture. The bonding of the details to make the secondary mirror support subassembly is shown in Figure 4-23.

4.3 FINAL ASSEMBLIES

Upon completion of trim and bonding operations the graphite/epoxy components and subassemblies were assembled using the relatively simple fixture shown in Figure 4-24.

The completed ring assemblies were installed in the final assembly fixture with six locators per ring to assure concentricity and station plane location. Following this,

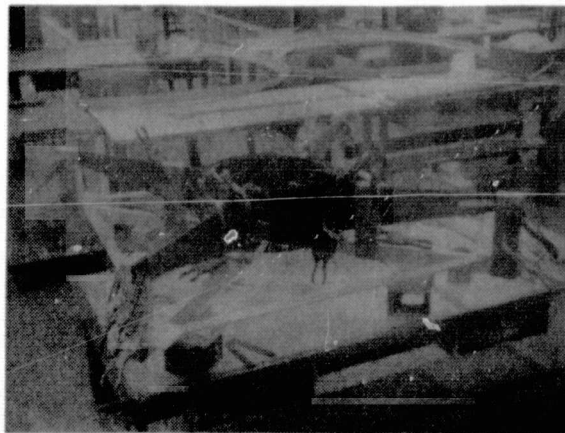


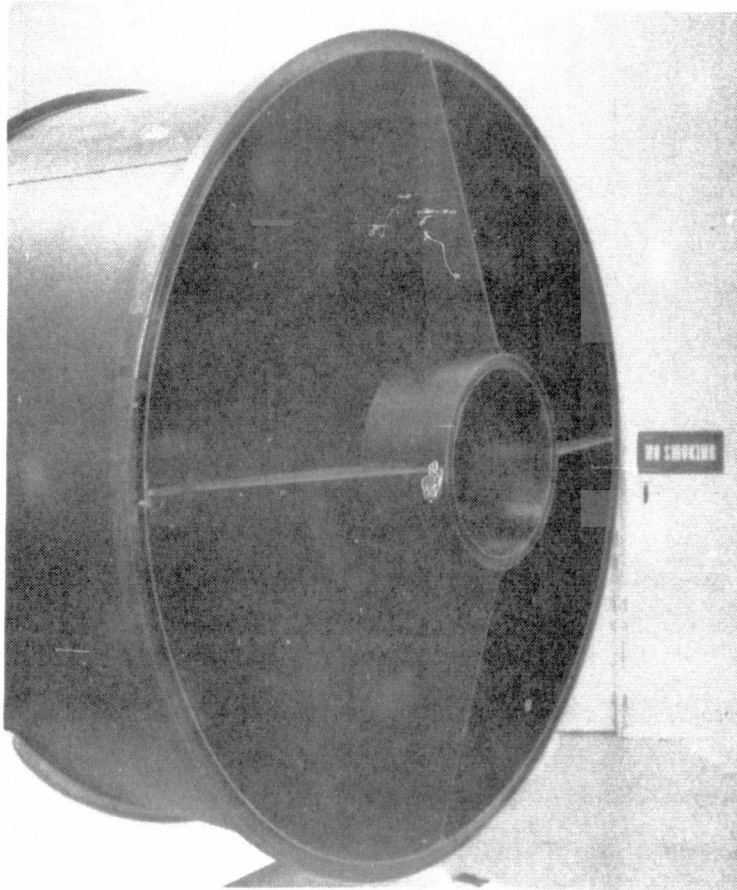
Figure 4-23. GEMS Secondary Mirror Support Subassembly



14-1987

Figure 4-24. Final Assembly Fixture

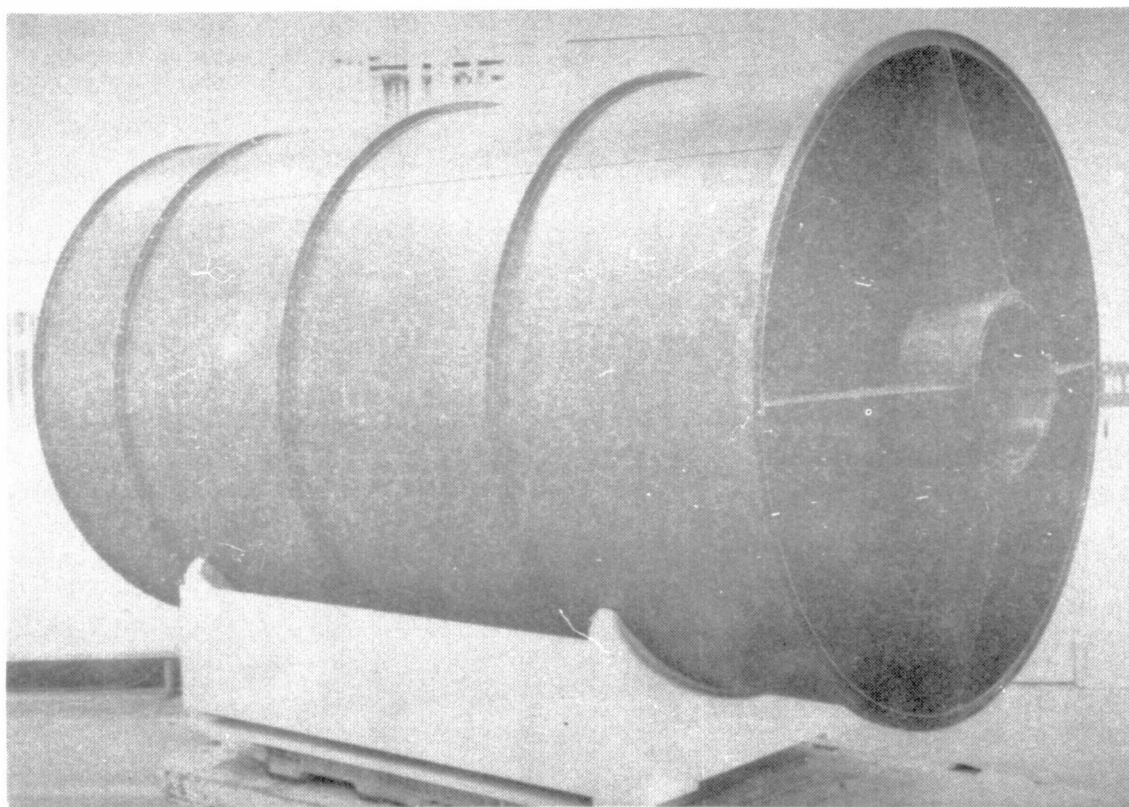
the 120° skin segments and the associated circumferential splice straps were installed using an inflatable hose to apply bonding pressure. This operation proved to be very simple, since the 1.52 mm (0.06 inch) thick skins were very compliant and precision fit of the skin edges was not required with the strap type splice. The secondary mirror support spider subassembly was then attached to the GEMS shell structure (see Figure 4-25), maintaining the concentricity, parallelism, and spacing requirements of the hub relative to the base of the shell. The attachment of each spider leg to the forward I-ring was designed to be tolerant of slight local misalignments to allow accurate alignment of the hub. A view of the completed assembly is shown in Figure 4-26.



14-2146

Figure 4-25. Secondary Mirror Spider Support
Banded In-Place

ORIGINAL PAGE IS
OF POOR QUALITY



14 2147

Figure 4-26. GEMS Assembly Before Instrumentation

SECTION 5

TEST PROGRAM

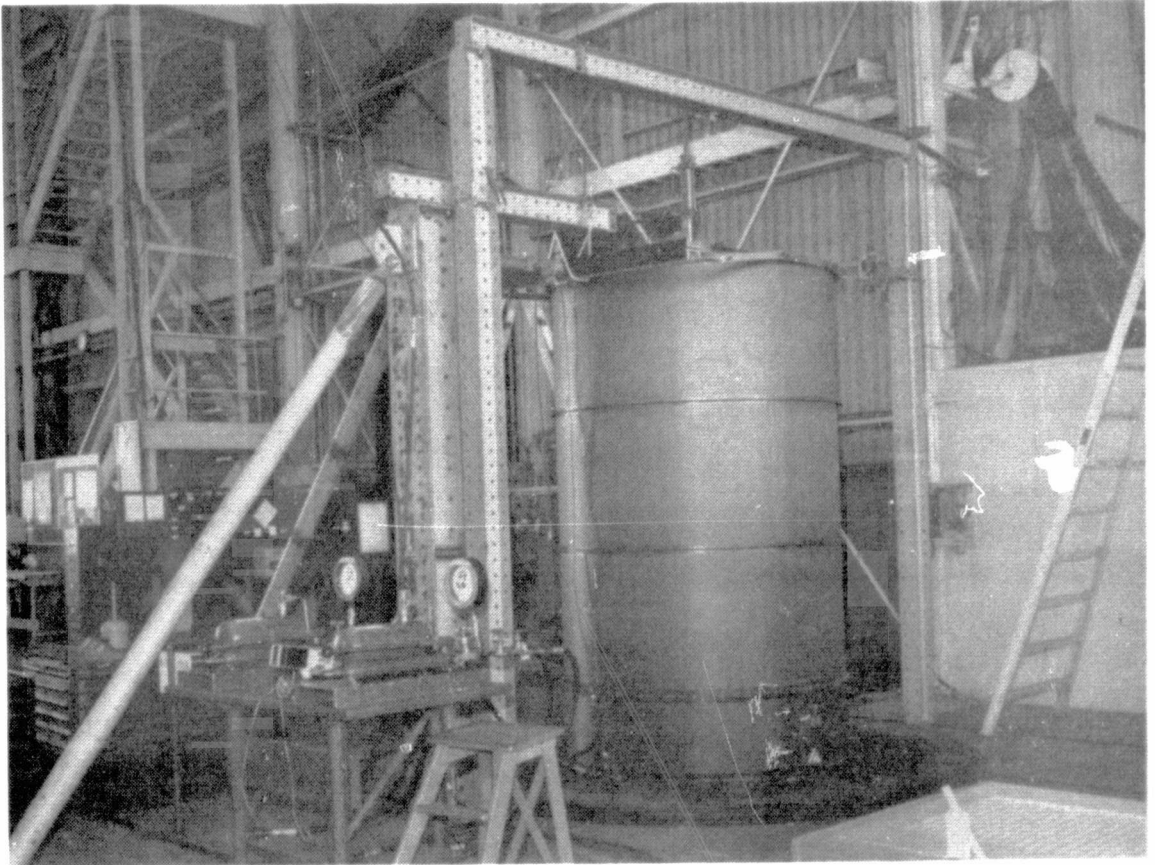
5.1 STATIC TEST

5.1.1 SUMMARY. Two static tests were satisfactorily performed on the graphite/epoxy metering shell (GEMS) assembly (72C0280). An axial load of 180 pounds was applied in the forward direction to the secondary mirror support structure assembly. A side load of 1,100 pounds was applied in the 180° direction to the most forward frame. These conditions respectively induced the limit load on the secondary mirror support and the limit load intensities in the shell skin and the aft attachment flange. Limit load was not exceeded to assure preservation of the specimen for thermal expansion testing. Each test condition was run 5 times, and test data for each run are presented herein.

5.1.2 TEST SPECIMEN. The test specimen was the graphite/epoxy metering shell assembly (72C0280) which was 2.949 M (116.1 inches) long and 1.643 M (64.68 inches) in diameter. The assembly consisted of a thin cylinder with 5 frames (72C0283) along its length and a secondary mirror support structure assembly (72C0281) at the forward end. Detail descriptions of the test specimen and its fabrication are presented in Sections 3.0 and 5.0.

5.1.3 TEST SETUP

5.1.3.1 Test Fixture. The test specimen was bolted to a 1.5-inch thick steel baseplate which was bolted to the 3-foot thick concrete floor of the test laboratory building (Figure 5.1-1). The 3/16 diameter bolts attaching the specimen to the baseplate were torqued to 20 inch-pounds plus running torque. The 180-pound axial load was reacted by the trussed roof of the test laboratory building. The 1,100-pound side load was reacted by a vertical column which was braced in two directions. The dead weight of the



14-2374

Figure 5.1-1. Test Setup

ORIGINAL PAGE IS
OF POOR QUALITY

side-load hydraulic cylinder, load cell, and whiffle tree beams was relieved by elastic shock cord as shown in Figure 5.1-2.

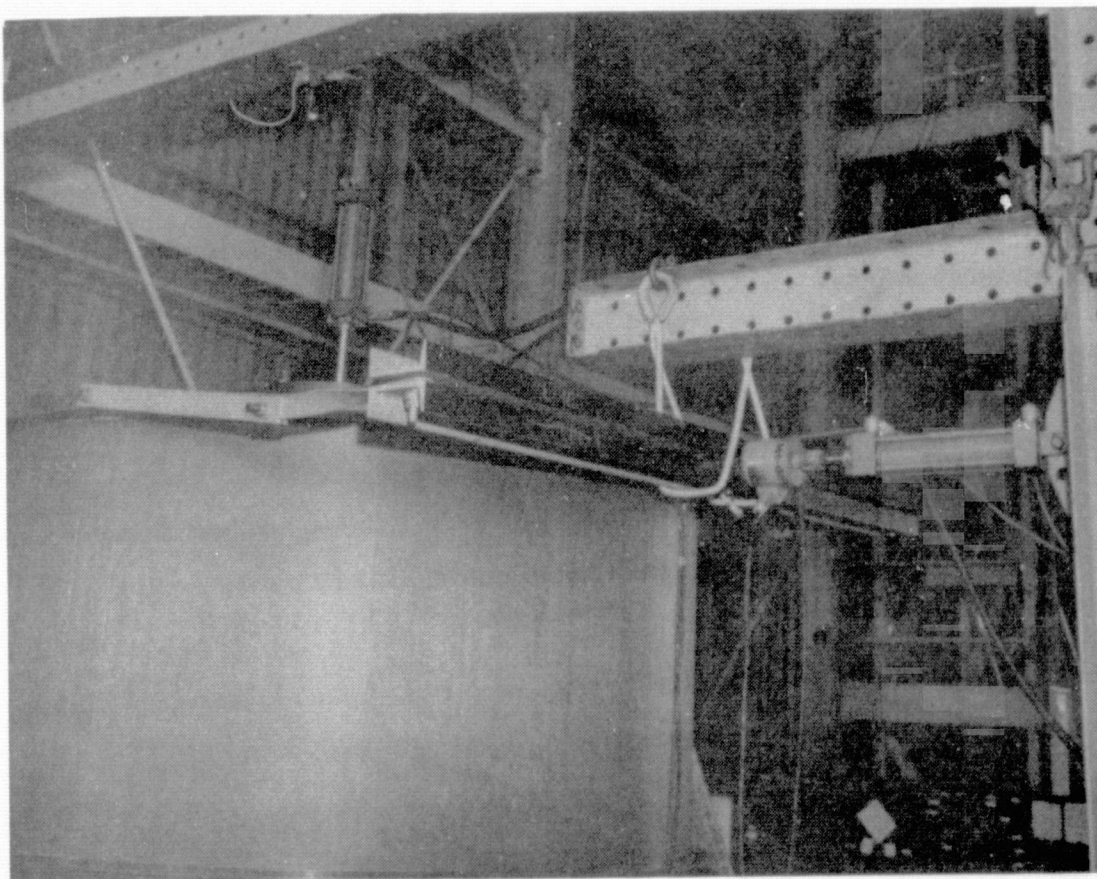
A flat steel plate applied the 180-pound axial load uniformly to the circular hub of the secondary mirror support structure assembly. A thin aluminum strap was wrapped half way around the specimen at the forward frame (from 270° , through 0° , to 90°). The two ends of the strap were beamed together, and the 1,100-pound side load was applied in tension to the beam (see Figure 5.1-2). Thin aluminum strap segments were used as fillers between the frame and strap between the frame splices. All of these straps were held in place with double-faced tape.

5.1.3.2 Instrumentation. The test specimen was instrumented with 3 rosette and 16 axial strain gages. The locations of these gages are shown in Figure 5.1-3. Two deflection transducers were installed to measure the axial deflection of the secondary mirror support structure hub and the side deflection of the forward frame.

A strain gaged load cell was attached to the piston rod of each hydraulic cylinder. The output of the load cell was calibrated in pounds of load.

5.1.3.3 Loading System. Pressure was applied to each hydraulic cylinder by a portable hydraulic hand pump. Pressure was increased until the proper load was indicated by the load cell.

5.1.3.4 Data Recording System. Strain data were recorded on a high speed data acquisition system which had a computer section to convert the raw data into engineering units. Tabulated strain data in microinches per inch were furnished by a medium speed printer.



14-2373

Figure 5.1-2. Loading Cylinder Installations

ORIGINAL PAGE IS
OF POOR QUALITY

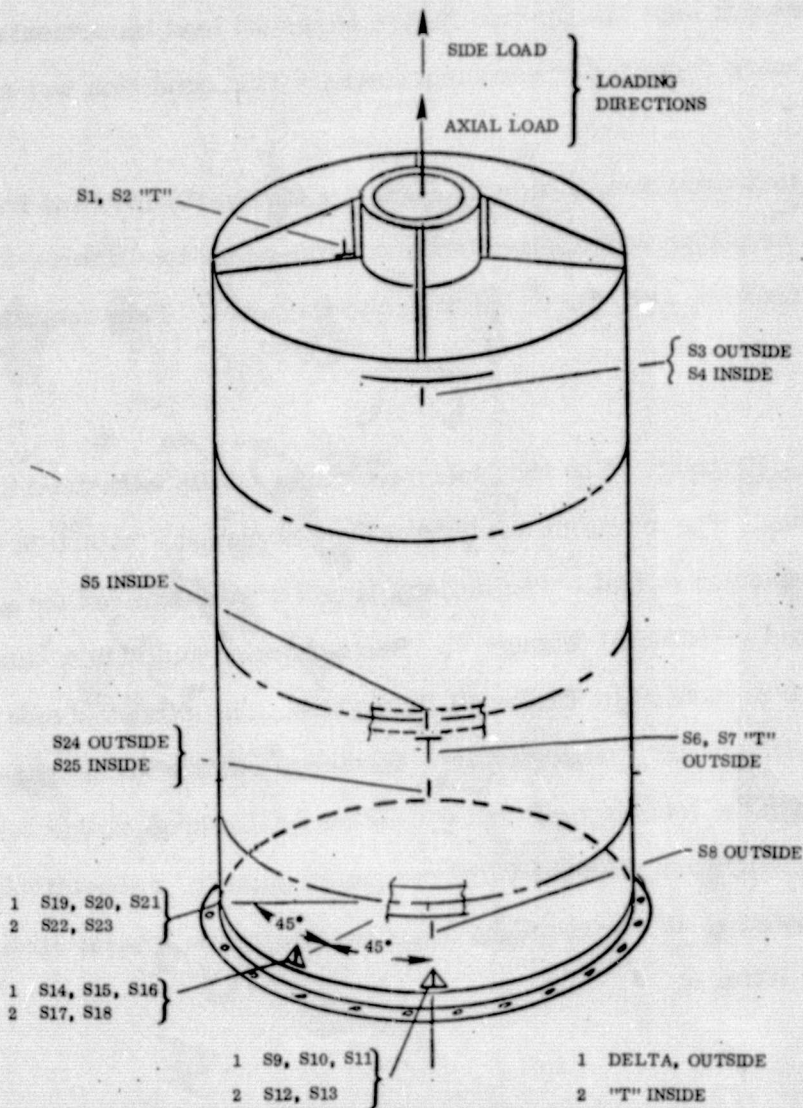


Figure 5.1-3. GEMS Strain Gage Locations

ORIGINAL PAGE IS
OF POOR QUALITY.

5.1.4 TEST CONDITIONS AND PROCEDURES. The first test condition, a forward axial load was applied uniformly to the hub of the secondary mirror support structure assembly. The axial load was applied in five 36-pound load increments to 180 pounds, and strain data were recorded at each increment. This condition was applied 5 times.

For the second test condition, a side load was applied to the forward frame of the GEMS assembly. The side load was applied in eleven 100-pound load increments to 1,100 pounds, and strain data were recorded at each increment. This condition was applied 5 times.

5.1.5 TEST RESULTS. The test specimen successfully withstood the axial and side load test runs. There was no evidence of any structural failure in the test specimen or the graphite/epoxy material. The deflection and strain data for the axial load test runs are presented in Tables I through V. The deflection and strain data for the side load test runs are presented in Tables VI through X. The axial and side deflections are identified as D1 and D2, respectively. The three rosette strain gages are designated by the letter R with the letters A, B and C to identify the three elements. The A and C elements were oriented longitudinally and circumferentially, respectively. The B element was oriented at 45° between the other two elements. Axial strain gages are designated by the letter S.

Tables I-V. Deflection and Strain Data for the Axial Load Test Runs

Table I

AXI L 36 LBS DATE: 10 / 14 / 74 TIME: 7 : 36 : 5

FILE: 4 RECORD: 3 CHANNELS 386 THROUGH 413

CHAN				
386	-2. D1	+ . D2	+ .	-13. S1
390	+ . S2	-21. S3	+6. S4	+ . S5
394	+2. S6	-4. S7	-6. S8	-7. R9A
398	+ . R10B	+7. R11C	-6. S12	-2. S13
402	+ . R14A	+4. R15B	+2. R16C	-4. S17
406	-2. S18	+4. R19A	+ . R20B	+2. R21C
410	+ . S22	+9. S23	-4. S24	+ . S25

AXIAL 72 LBS DATE: 10 / 14 / 74 TIME: 7 : 36 : 45

FILE: 4 RECORD: 4 CHANNELS 386 THROUGH 413

CHAN				
386	-4. D1	+ . D2	+ .	-23. S1
390	+ . S2	-11. S3	+20. S4	-2. S5
394	-4. S6	+ . S7	-4. S8	-2. R9A
398	-2. R10B	+4. R11C	-2. S12	-2. S13
402	+4. R14A	+2. R15B	+2. R16C	-4. S17
406	+ . S18	+2. R19A	+16. R20B	+ . R21C
410	+2. S22	+16. S23	+2. S24	+2. S25

AXIAL 108 LBS DATE: 10 / 14 / 74 TIME: 7 : 37 : 35

FILE: 4 RECORD: 5 CHANNELS 386 THROUGH 413

CHAN				
386	-7. D1	- . D2	+ .	-34. S1
390	+2. S2	-18. S3	+30. S4	+ . S5
394	+ . S6	-2. S7	+2. S8	-7. R9A
398	+ . R10B	+7. R11C	+16. S12	-2. S13
402	+9. R14A	+ . R15B	+2. R16C	-4. S17
406	+ . S18	+ . R19A	-2. R20B	-2. R21C
410	+2. S22	+16. S23	+ . S24	+4. S25

Tables I-V. Deflection and Strain Data for the Axial Load Test Runs

Table I

AXIAL 36 LBS DATE: 10 / 14 / 74 TIME: 7 : 36 : 5

FILE: 4 RECORD: 3 CHANNELS 386 THROUGH 413

CHAN				
386	-2. D1	+ . D2	+ .	-13. S1
390	+ . S2	-21. S3	+6. S4	+ . S5
394	+2. S6	-4. S7	-6. S8	-7. R9A
398	+ . R10B	+7. R11C	-6. S12	-2. S13
402	+ . R14A	+4. R15B	+2. R16C	-4. S17
406	-2. S18	+4. R19A	+ . R20B	+2. R21C
410	+ . S22	+9. S23	-4. S24	+ . S25

AXIAL 72 LBS DATE: 10 / 14 / 74 TIME: 7 : 36 : 45

FILE: 4 RECORD: 4 CHANNELS 386 THROUGH 413

CHAN				
386	-4. D1	+ . D2	+ .	-23. S1
390	+ . S2	-11. S3	+20. S4	-2. S5
394	-4. S6	+ . S7	-4. S8	-2. R9A
398	-2. R10B	+4. R11C	-2. S12	-2. S13
402	+4. R14A	+2. R15B	+2. R16C	-4. S17
406	+ . S18	+2. R19A	+16. R20B	+ . R21C
410	+2. S22	+16. S23	+2. S24	+2. S25

AXIAL 108 LBS DATE: 10 / 14 / 74 TIME: 7 : 37 : 35

FILE: 4 RECORD: 5 CHANNELS 386 THROUGH 413

CHAN				
386	-7. D1	- . D2	+ .	-34. S1
390	+2. S2	-18. S3	+30. S4	+ . S5
394	+ . S6	-2. S7	+2. S8	-7. R9A
398	+ . R10B	+7. R11C	+16. S12	-2. S13
402	+9. R14A	+ . R15B	+2. R16C	-4. S17
406	+ . S18	+ . R19A	-2. R20B	-2. R21C
410	+2. S22	+16. S23	+ . S24	+4. S25

Table I, Contd

AXIAL 144 LBS DATE: 10 / 14 / 74 TIME: 7 : 38 : 10

FILE: 4 RECORD: 6 CHANNELS 386 THROUGH 413

CHAN				
386	-9. D1	- . D2	+.	-41. S1
390	+2. S2	-18. S3	+41. S4	+2. S5
394	+. S6	-2. S7	+9. S8	+25. R9A
398	+. R10B	+7. R11C	-9. S12	+. S13
402	+4. R14A	+2. R15B	+7. R16C	-6. S17
406	-2. S18	+2. R19A	-2. R20B	+. R21C
410	+2. S22	+2. S23	+. S24	+6. S25

AXIAL 180 LBS DATE: 10 / 14 / 74 TIME: 7 : 38 : 45

FILE: 4 RECORD: 7 CHANNELS 386 THROUGH 413

CHAN				
386	-12. D1	- . D2	+.	-55. S1
390	+. S2	-30. S3	+53. S4	+. S5
394	-2. S6	-2. S7	-27. S8	-7. R9A
398	-2. R10B	+4. R11C	-6. S12	-4. S13
402	+2. R14A	+7. R15B	+2. R16C	-6. S17
406	+. S18	+4. R19A	+. R20B	-2. R21C
410	+. S22	+4. S23	-2. S24	+4. S25

ORIGINAL PAGE IS
OF POOR QUALITY

Table II

AXIAL ZERO DATE: 10 / 14 / 74 TIME: 7 : 39 : 37

FILE: 4 RECORD: 8 CHANNELS 386 THROUGH 413

CHAN				
386	-2. D1	+ . D2	+ .	+2. S1
390	+4. S2	+2. S3	-2. S4	+ . S5
394	-4. S6	+4. S7	-27. S8	-4. R9A
398	+ . R10B	+4. R11C	-2. S12	-2. S13
402	-2. R14A	+ . R15B	+2. R16C	-4. S17
406	+ . S18	+2. R19A	+11. R20B	+ . R21C
410	+ . S22	+6. S23	-2. S24	+13. S25

AXIAL 36 LBS R2 DATE: 10 / 14 / 74 TIME: 7 : 41 : 56

FILE: 4 RECORD: 9 CHANNELS 386 THROUGH 413

CHAN				
386	-3. D1	+ . D2	+ .	-9. S1
390	+2. S2	-4. S3	+6. S4	+2. S5
394	+ . S6	+2. S7	-2. S8	+7. R9A
398	-4. R10B	+2. R11C	-6. S12	+ . S13
402	+ . R14A	-2. R15B	+ . R16C	-4. S17
406	+ . S18	+2. R19A	-2. R20B	+2. R21C
410	+ . S22	+16. S23	-13. S24	+4. S25

AXIAL 72 LBS R2 DATE: 10 / 14 / 74 TIME: 7 : 42 : 38

FILE: 4 RECORD: 10 CHANNELS 386 THROUGH 413

CHAN				
386	-4. D1	+ . D2	+ .	-20. S1
390	+ . S2	-23. S3	+20. S4	-2. S5
394	+ . S6	-2. S7	+2. S8	+ . R9A
398	+ . R10B	+4. R11C	-4. S12	+ . S13
402	+4. R14A	+4. R15B	+2. R16C	-4. S17
406	+ . S18	+2. R19A	+23. R20B	+4. R21C
410	-6. S22	+16. S23	-18. S24	+4. S25

Table II, Contd

AXIAL 108 LBS R2 DATE: 10 / 14 / 74 TIME: 7 : 43 : 21

FILE: 4 RECORD: 11 CHANNELS 386 THROUGH 413

CHAN				
386	-7. D1	- . D2	+ .	-37. S1
390	+2. S2	-23. S3	+30. S4	-4. S5
394	+2. S6	+ . S7	+6. S8	-7. R9A
398	-7. R10B	+7. R11C	+9. S12	-2. S13
402	+2. R14A	+11. R15B	+4. R16C	-4. S17
406	+ . S18	+4. R19A	+16. R20B	+4. R21C
410	+ . S22	+13. S23	-2. S24	+2. S25

AXIAL 144 LBS R2 DATE: 10 / 14 / 74 TIME: 7 : 44 : 12

FILE: 4 RECORD: 12 CHANNELS 386 THROUGH 413

CHAN				
386	-9. D1	- . D2	+ .	-41. S1
390	+ . S2	-23. S3	+37. S4	+ . S5
394	+2. S6	-2. S7	+9. S8	-9. R9A
398	-9. R10B	+4. R11C	+13. S12	-2. S13
402	+2. R14A	-7. R15B	+2. R16C	-2. S17
406	-2. S18	+7. R19A	-2. R20B	+4. R21C
410	+ . S22	+2. S23	-9. S24	+ . S25

AXIAL 180 LBS R2 DATE: 10 / 14 / 74 TIME: 7 : 44 : 44

FILE: 4 RECORD: 13 CHANNELS 386 THROUGH 413

CHAN				
386	-12. D1	- . D2	+ .	-55. S1
390	+2. S2	-32. S3	+51. S4	-2. S5
394	+ . S6	-2. S7	+2. S8	-2. R9A
398	-4. R10B	+2. R11C	+4. S12	+ . S13
402	-4. R14A	+4. R15B	+4. R16C	-9. S17
406	-4. S18	+2. R19A	+25. R20B	+4. R21C
410	-2. S22	+20. S23	+ . S24	-16. S25

Table III

AXIAL ZERO DATE: 10 / 14 / 74 TIME: 7 : 45 : 10

FILE: 4 RECORD: 14 CHANNELS 386 THROUGH 413

CHAN				
386	-2. D1	+ . D2	+ .	+2. S1
390	-9. S2	+ . S3	-4. S4	+ . S5
394	-9. S6	-2. S7	-2. S8	+18. R9A
398	+ . R10B	+ . R11C	-6. S12	+ . S13
402	-4. R14A	+2. R15B	+ . R16C	+ . S17
406	+ . S18	+2. R19A	+16. R20B	+2. R21C
410	+2. S22	+11. S23	-6. S24	+ . S25

AXIAL 36 LBS R3 DATE: 10 / 14 / 74 TIME: 7 : 45 : 57

FILE: 4 RECORD: 15 CHANNELS 386 THROUGH 413

CHAN				
386	-2. D1	- . D2	+ .	-9. S1
390	+ . S2	-11. S3	+11. S4	-2. S5
394	-2. S6	-2. S7	-29. S8	-9. R9A
398	+ . R10B	+4. R11C	-9. S12	-6. S13
402	+ . R14A	+11. R15B	+ . R16C	+2. S17
406	+ . S18	+2. R19A	+30. R20B	+2. R21C
410	-2. S22	+16. S23	-2. S24	+ . S25

AXIAL 72 LBS R3 DATE: 10 / 14 / 74 TIME: 7 : 46 : 24

FILE: 4 RECORD: 16 CHANNELS 386 THROUGH 413

CHAN				
386	-5. D1	+ . D2	+ .	-18. S1
390	+4. S2	-11. S3	+20. S4	+2. S5
394	+ . S6	+11. S7	+4. S8	-11. R9A
398	-7. R10B	-2. R11C	-6. S12	-4. S13
402	+ . R14A	+2. R15B	+2. R16C	-4. S17
406	+ . S18	+2. R19A	+ . R20B	+2. R21C
410	+ . S22	+9. S23	-4. S24	+ . S25

Table III, Contd

AXIAL 108 LBS R3 DATE: 10 / 14 / 74 TIME: 7 : 47 : 6

FILE: 4 RECORD: 17 CHANNELS 386 THROUGH 413

CHAN

386	-7. D1	- . D2	+ .	-32. S1
390	+2. S2	-11. S3	+32. S4	+ . S5
394	+ . S6	-2. S7	+4. S8	+42. R9A
398	+2. R10B	+2. R11C	-6. S12	+ . S13
402	-6. R14A	+2. R15B	+7. R16C	-6. S17
406	-2. S18	+2. R19A	-2. R20B	-2. R21C
410	+2. S22	+6. S23	-2. S24	+2. S25

AXIAL 144 LBS R3 DATE: 10 / 14 / 74 TIME: 7 : 47 : 39

FILE: 4 RECORD: 18 CHANNELS 386 THROUGH 413

CHAN

386	-10. D1	+ . D2	+ .	-46. S1
390	+2. S2	-23. S3	+41. S4	+ . S5
394	+ . S6	-2. S7	-9. S8	+ . R9A
398	+ . R10B	+2. R11C	+2. S12	+2. S13
402	+ . R14A	-2. R15B	+2. R16C	-4. S17
406	-2. S18	+2. R19A	+7. R20B	+ . R21C
6 410	+ . S22	+2. S23	-4. S24	-11. S25

AXIAL 180 LBS R3 DATE: 10 / 14 / 74 TIME: 7 : 48 : 6

FILE: 4 RECORD: 19 CHANNELS 386 THROUGH 413

CHAN

386	-12. D1	- . D2	+ .	-55. S1
390	+ . S2	-35. S3	+46. S4	-2. S5
394	+4. S6	-6. S7	-23. S8	-14. R9A
398	-9. R10B	+2. R11C	-6. S12	-4. S13
402	-2. R14A	+14. R15B	+4. R16C	-4. S17
406	-4. S18	+7. R19A	+ . R20B	+7. R21C
6 410	-4. S22	+16. S23	-4. S24	+2. S25

ORIGINAL PAGE IS
OF POOR QUALITY

Table IV

AXIAL ZERO DATE: 10 / 14 / 74 TIME: 7 : 49 : 2

FILE: 4 RECORD: 20 CHANNELS 386 THROUGH 413 -

CHAN

386	-2. D1	+. D2	+. S4	+2. S1
390	+2. S2	+. S3	+. S4	+. S5
394	+. S6	+11. S7	+2. S8	+42. R9A
398	+. R10B	+2. R11C	-2. S12	+2. S13
402	-2. R14A	+2. R15B	+2. R16C	-4. S17
406	-2. S18	+2. R19A	+2. R20B	+2. R21C
410	-2. S22	+11. S23	-4. S24	-9. S25

AXIAL 36 LBS R4 DATE: 10 / 14 / 74 TIME: 7 : 49 : 38

FILE: 4 RECORD: 21 CHANNELS 386 THROUGH 413

CHAN

386	-2. D1	-. D2	+. S4	-11. S1
390	+2. S2	-4. S3	+11. S4	+. S5
394	-9. S6	+9. S7	+2. S8	+35. R9A
398	+. R10B	-2. R11C	-11. S12	-2. S13
402	-6. R14A	+2. R15B	+. R16C	-6. S17
406	-6. S18	+2. R19A	-4. R20B	+11. R21C
410	+2. S22	+13. S23	-16. S24	-13. S25

AXIAL 72 LBS R4 DATE: 10 / 14 / 74 TIME: 7 : 50 : 20

FILE: 4 RECORD: 22 CHANNELS 386 THROUGH 413

CHAN

386	-4. D1	-. D2	+. S4	-25. S1
390	+2. S2	-14. S3	+20. S4	-2. S5
394	-2. S6	-2. S7	+. S8	-9. R9A
398	+. R10B	+4. R11C	+9. S12	-2. S13
402	+13. R14A	+. R15B	+2. R16C	-6. S17
406	+. S18	+. R19A	-4. R20B	+2. R21C
410	+. S22	+9. S23	+4. S24	+2. S25

Table IV, Contd

AXIAL 108 LBS R4 DATE: 10 / 14 / 74 TIME: 7 : 50 : 54

FILE: 4 RECORD: 23 CHANNELS 386 THROUGH 413

CHAN				
386	-7. D1	+ . D2	+ .	-30. S1
390	-7. S2	-18. S3	+32. S4	+ . S5
394	+ . S6	-4. S7	+4. S8	-11. R9A
398	-4. R10B	+ . R11C	-4. S12	-2. S13
402	+2. R14A	+ . R15B	+4. R16C	-4. S17
406	+ . S18	+4. R19A	+7. R20B	+ . R21C
410	-2. S22	+13. S23	-2. S24	+ . S25

AXIAL 144 LBS R4 DATE: 10 / 14 / 74 TIME: 7 : 51 : 22

FILE: 4 RECORD: 24 CHANNELS 386 THROUGH 413

CHAN				
386	-9. D1	- . D2	+ .	-46. S1
390	+2. S2	-21. S3	+39. S4	+ . S5
394	+ . S6	+4. S7	-13. S8	+32. R9A
398	+ . R10B	+ . R11C	-9. S12	+2. S13
402	-6. R14A	+4. R15B	+2. R16C	-6. S17
406	-4. S18	+2. R19A	+32. R20B	+4. R21C
410	-2. S22	+18. S23	+ . S24	-16. S25

AXIAL 180 LBS R4 DATE: 10 / 14 / 74 TIME: 7 : 51 : 49

FILE: 4 RECORD: 25 CHANNELS 386 THROUGH 413

CHAN				
386	-12. D1	+ . D2	+ .	-58. S1
390	+ . S2	-32. S3	+41. S4	+ . S5
394	+6. S6	-4. S7	-27. S8	-14. R9A
398	+2. R10B	+2. R11C	-11. S12	+ . S13
402	+2. R14A	+4. R15B	+4. R16C	-4. S17
406	+2. S18	+4. R19A	+4. R20B	+2. R21C
410	+ . S22	+16. S23	-9. S24	+2. S25

Table V

AXIAL ZERO DATE: 10 / 14 / 74 TIME: 7 : 52 : 27

FILE: 4 RECORD: 26 CHANNELS 386 THROUGH 413

CHAN

386	-2. D1	-2. D2	+. .	-2. S1
390	+. S2	-2. S3	+. S4	+. S5
394	+. S6	+. S7	-6. S8	-2. R9A
398	-4. R10B	+4. R11C	-6. S12	-2. S13
402	+. R14A	+4. R15B	-2. R16C	-6. S17
406	-2. S18	+2. R19A	-4. R20B	-4. R21C
410	+. S22	+13. S23	+2. S24	+. S25

AXIAL 36 LBS R5 DATE: 10 / 14 / 74 TIME: 7 : 53 : 0

FILE: 4 RECORD: 27 CHANNELS 386 THROUGH 413

CHAN

386	-2. D1	-2. D2	+. .	-11. S1
390	+2. S2	-21. S3	+11. S4	+. S5
394	-2. S6	-20. S7	+. S8	+42. R9A
398	+. R10B	-2. R11C	-11. S12	+. S13
402	-9. R14A	+. R15B	+4. R16C	-4. S17
406	+. S18	+2. R19A	+20. R20B	+. R21C
410	-2. S22	+16. S23	-2. S24	-11. S25

AXIAL 72 LBS R5 DATE: 10 / 14 / 74 TIME: 7 : 53 : 36

FILE: 4 RECORD: 28 CHANNELS 386 THROUGH 413

CHAN

386	-5. D1	+. D2	+. .	-20. S1
390	-9. S2	-23. S3	+16. S4	+. S5
394	+. S6	+. S7	+. S8	-7. R9A
398	+. R10B	+2. R11C	-2. S12	+. S13
402	+. R14A	+2. R15B	+2. R16C	-2. S17
406	-2. S18	+2. R19A	-4. R20B	+4. R21C
410	-6. S22	+16. S23	-2. S24	+6. S25

Table V, Contd

AXIAL 108 LBS R5 DATE: 10 / 14 / 74 TIME: 7 : 54 : 3

FILE: 4 RECORD: 29 CHANNELS 386 THROUGH 413

CHAN				
386	-7. D1	- . D2	+ .	-34. S1
390	+2. S2	-16. S3	+30. S4	+ . S5
394	-6. S6	-4. S7	-6. S8	-14. R9A
398	+ . R10B	+ . R11C	-11. S12	+2. S13
402	+ . R14A	+18. R15B	+2. R16C	-6. S17
406	-2. S18	+2. R19A	+30. R20B	+4. R21C
410	+ . S22	+18. S23	-4. S24	+4. S25

AXIAL 144 LBS R5 DATE: 10 / 14 / 74 TIME: 7 : 54 : 30

FILE: 4 RECORD: 30 CHANNELS 386 THROUGH 413

CHAN				
386	-9. D1	+ . D2	+ .	-46. S1
390	+2. S2	-39. S3	+39. S4	+ . S5
394	-4. S6	-2. S7	+13. S8	+16. R9A
398	+ . R10B	-4. R11C	-11. S12	+2. S13
402	-2. R14A	+4. R15B	+4. R16C	-6. S17
406	+ . S18	+2. R19A	+4. R20B	+4. R21C
410	-2. S22	+16. S23	-9. S24	+ . S25

AXIAL 180 LBS R5 DATE: 10 / 14 / 74 TIME: 7 : 55 : 21

FILE: 4 RECORD: 31 CHANNELS 386 THROUGH 413

CHAN				
386	-12. D1	+ . D2	+ .	-58. S1
390	+4. S2	-46. S3	+48. S4	+ . S5
394	+ . S6	-4. S7	+6. S8	-11. R9A
398	+2. R10B	+2. R11C	-6. S12	+ . S13
402	+2. R14A	+7. R15B	+7. R16C	-4. S17
406	+ . S18	+4. R19A	+7. R20B	+2. R21C
410	-2. S22	+16. S23	-4. S24	+2. S25

ORIGINAL PAGE IS
OF POOR QUALITY

Table V, Contd

AXIAL FINAL ZERO DATE: 10 / 14 / 74 TIME: 7 : 56 : 16

FILE: 4 RECORD: 32 CHANNELS 386 THROUGH 413

CHAN				
386	-2. D1	-2. D2	+2. S1	
390	-2. S2	+2. S3	-2. S5	
394	+2. S6	+2. S7	+11. R9A	
398	+2. R10B	+2. R11C	-2. S13	
402	-2. R14A	+2. R15B	-4. S17	
406	-2. S18	+2. R19A	-2. R21C	
410	+2. S22	+2. S23	+2. S25	
		+2. S24		

Tables VI-X. Deflection and Strain Data for the Side Load Test Runs

Table VI

SIDE LD 100# R1 DATE: 10 / 14 / 74 TIME: 8 : 8 : 23

FILE: 5 RECORD: 3 CHANNELS 386 THROUGH 413

CHAN				
386	-• D1	+3• D2	+•	+2• S1
390	+2• S2	-11• S3	+6• S4	+• S5
394	+• S6	+4• S7	+4• S8	+7• R9A
398	+2• R10B	+7• R11C	-20• S12	+6• S13
402	+6• R14A	+2• R15B	+11• R16C	-13• S17
406	+4• S18	+7• R19A	+4• R20B	+7• R21C
410	+2• S22	-6• S23	+6• S24	-32• S25

SIDE LD 200# R1 DATE: 10 / 14 / 74 TIME: 8 : 9 : 10

FILE: 5 RECORD: 4 CHANNELS 386 THROUGH 413

CHAN				
386	+• D1	+9• D2	+•	+2• S1
390	+7• S2	-21• S3	+6• S4	+• S5
394	-2• S6	+6• S7	+13• S8	+16• R9A
398	+7• R10B	+14• R11C	-23• S12	+16• S13
402	+20• R14A	+21• R15B	+21• R16C	-18• S17
406	+6• S18	-4• R19A	+4• R20B	+9• R21C
410	+• S22	+4• S23	+9• S24	-16• S25

SIDE LD 300# R1 DATE: 10 / 14 / 74 TIME: 8 : 9 : 58

FILE: 5 RECORD: 5 CHANNELS 386 THROUGH 413

CHAN				
386	-• D1	+14• D2	+•	+4• S1
390	+7• S2	-18• S3	+16• S4	+2• S5
394	+2• S6	+11• S7	+43• S8	+18• R9A
398	+11• R10B	+14• R11C	-25• S12	+20• S13
402	+30• R14A	+42• R15B	+32• R16C	-20• S17
406	+11• S18	-4• R19A	+25• R20B	+7• R21C
410	+2• S22	+2• S23	+13• S24	-44• S25

ORIGINAL PAGE IS
OF POOR QUALITY

Table VI, Contd

SIDE LD 400# R1 DATE: 10 / 14 / 74 TIME: 8 : 10 : 37

FILE: 5 RECORD: 6 CHANNELS 386 THROUGH 413

CHAN

386	- . D1	+19. D2	+ .	+2. S1
390	+4. S2	-25. S3	+18. S4	+2. S5
394	-2. S6	-6. S7	+52. S8	+14. R9A
398	+16. R10B	+28. R11C	-25. S12	+30. S13
402	+41. R14A	+60. R15B	+42. R16C	-32. S17
406	+11. S18	-4. R19A	+18. R20B	+7. R21C
410	+ . S22	+2. S23	+23. S24	-55. S25

SIDE LD 500# R1 DATE: 10 / 14 / 74 TIME: 8 : 11 : 17

FILE: 5 RECORD: 7 CHANNELS 386 THROUGH 413

CHAN

386	- . D1	+25. D2	+ .	+4. S1
390	+2. S2	-25. S3	+25. S4	+4. S5
394	-4. S6	-4. S7	+71. S8	+30. R9A
398	+18. R10B	+35. R11C	-25. S12	+34. S13
402	+51. R14A	+60. R15B	+56. R16C	-39. S17
406	+18. S18	-4. R19A	+16. R20B	+7. R21C
410	-2. S22	+2. S23	+27. S24	-64. S25

SIDE LD 600# R1 DATE: 10 / 14 / 74 TIME: 8 : 11 : 51

FILE: 5 RECORD: 8 CHANNELS 386 THROUGH 413

CHAN

386	- . D1	+30. D2	+ .	+ . S1
390	+2. S2	-37. S3	+27. S4	+4. S5
394	+2. S6	+4. S7	+82. S8	+37. R9A
398	+18. R10B	+42. R11C	-18. S12	+39. S13
402	+58. R14A	+74. R15B	+63. R16C	-48. S17
406	+20. S18	-7. R19A	+44. R20B	+7. R21C
410	-6. S22	+6. S23	+32. S24	-74. S25

Table VI, Contd

SIDE LD 700# R1 DATE: 10 / 14 / 74 TIME: 8 : 12 : 29

FILE: 5 RECORD: 9 CHANNELS 386 THROUGH 413

CHAN

386	- . D1	+37. D2	+. .	+2. S1
390	+. S2	-37. S3	+34. S4	+4. S5
394	-4. S6	-9. S7	+92. S8	+32. R9A
398	+28. R10B	+51. R11C	-43. S12	+53. S13
402	+72. R14A	+88. R15B	+72. R16C	-51. S17
406	+27. S18	-4. R19A	+14. R20B	+7. R21C
410	+. S22	+4. S23	+32. S24	-106. S25

SIDE LD 800# R1 DATE: 10 / 14 / 74 TIME: 8 : 13 : 3

FILE: 5 RECORD: 10 CHANNELS 386 THROUGH 413

CHAN

386	- . D1	+42. D2	+. .	+4. S1
390	+7. S2	-39. S3	+39. S4	+6. S5
394	+4. S6	-2. S7	+103. S8	+51. R9A
398	+28. R10B	+56. R11C	-43. S12	+55. S13
402	+81. R14A	+100. R15B	+86. R16C	-60. S17
406	+32. S18	-7. R19A	+23. R20B	+2. R21C
410	-6. S22	+4. S23	+37. S24	-108. S25

SIDE LD 900# R1 DATE: 10 / 14 / 74 TIME: 8 : 13 : 43

FILE: 5 RECORD: 11 CHANNELS 386 THROUGH 413

CHAN

386	- . D1	+47. D2	+. .	+. S1
390	+2. S2	-44. S3	+48. S4	+4. S5
394	+6. S6	-4. S7	+133. S8	+56. R9A
398	+35. R10B	+65. R11C	-32. S12	+64. S13
402	+93. R14A	+121. R15B	+91. R16C	-67. S17
406	+34. S18	-7. R19A	+11. R20B	+7. R21C
410	-4. S22	+6. S23	+34. S24	-118. S25

Table VI, Contd

SIDE LD 1000# R1 DATE: 10 / 14 / 74 TIME: 8 : 14 : 24

FILE: 5 RECORD: 12 CHANNELS 386 THROUGH 413

CHAN				
386	- . D1	+54. D2	+ .	+2. S1
390	+2. S2	-56. S3	+55. S4	+6. S5
394	+4. S6	-6. S7	+156. S8	+88. R9A
398	+39. R10B	+74. R11C	-62. S12	+69. S13
402	+104. R14A	+128. R15B	+107. R16C	-76. S17
406	+37. S18	-7. R19A	+21. R20B	+4. R21C
410	+ . S22	+ . S23	+50. S24	-139. S25

SIDE LD 1100# R1 DATE: 10 / 14 / 74 TIME: 8 : 14 : 54

FILE: 5 RECORD: 13 CHANNELS 386 THROUGH 413

CHAN				
386	- . D1	+60. D2	+ .	-2. S1
390	+7. S2	-56. S3	+60. S4	+6. S5
394	+4. S6	-13. S7	+174. S8	+56. R9A
398	+46. R10B	+84. R11C	-60. S12	+83. S13
402	+109. R14A	+142. R15B	+114. R16C	-81. S17
406	+48. S18	-7. R19A	+25. R20B	+7. R21C
410	+ . S22	+4. S23	+50. S24	-152. S25

Table VII

SIDE LD ZERO DATE: 10 / 14 / 74 TIME: 8 : 16 : 3

FILE: 5 RECORD: 14 CHANNELS 386 THROUGH 413

CHAN				
386	- . D1	+3. D2	+ .	+2. S1
390	+7. S2	-7. S3	+2. S4	+ . S5
394	+6. S6	+6. S7	-2. S8	+32. R9A
398	+ . R10B	-2. R11C	-13. S12	+ . S13
402	-9. R14A	-9. R15B	+ . R16C	-9. S17
406	+6. S18	-4. R19A	+9. R20B	+7. R21C
410	+ . S22	+6. S23	-2. S24	+ . S25

SIDE LD 100# R2 DATE: 10 / 14 / 74 TIME: 8 : 16 : 52

FILE: 5 RECORD: 15 CHANNELS 386 THROUGH 413

CHAN				
386	- . D1	+4. D2	+ .	+2. S1
390	-2. S2	-14. S3	+6. S4	+ . S5
394	-2. S6	+2. S7	+ . S8	+2. R9A
398	+2. R10B	+4. R11C	-23. S12	+9. S13
402	-2. R14A	+2. R15B	+9. R16C	-18. S17
406	+6. S18	-9. R19A	+2. R20B	+9. R21C
410	+ . S22	+2. S23	+6. S24	-27. S25

SIDE LD 200# R2 DATE: 10 / 14 / 74 TIME: 8 : 17 : 53

FILE: 5 RECORD: 16 CHANNELS 386 THROUGH 413

CHAN				
386	- . D1	+10. D2	+ .	-2. S1
390	+4. S2	-21. S3	+6. S4	+ . S5
394	+ . S6	+ . S7	+27. S8	+42. R9A
398	+7. R10B	+9. R11C	-30. S12	+13. S13
402	+2. R14A	+16. R15B	+16. R16C	-25. S17
406	+11. S18	-9. R19A	+28. R20B	+9. R21C
410	+ . S22	-4. S23	+11. S24	-27. S25

ORIGINAL PAGE IS
OF POOR QUALITY

Table VII, Contd

SIDE LD 300# R2 DATE: 10 / 14 / 74 TIME: 8 : 20 : 32

FILE: 5 RECORD: 17 CHANNELS 386 THROUGH 413

CHAN

386	+• D1	+16• D2	+•	+• S1
390	+2• S2	-30• S3	+13• S4	+• S5
394	-2• S6	+• S7	+39• S8	+18• R9A
398	+9• R10B	+18• R11C	-39• S12	+20• S13
402	+25• R14A	+37• R15B	+30• R16C	-25• S17
406	+16• S18	-4• R19A	+4• R20B	+• R21C
410	+• S22	+• S23	+20• S24	-44• S25

SIDE LD 400# R2 DATE: 10 / 14 / 74 TIME: 8 : 21 : 24

FILE: 5 RECORD: 18 CHANNELS 386 THROUGH 413

CHAN

386	+• D1	+20• D2	+•	+2• S1
390	+• S2	-28• S3	+23• S4	+2• S5
394	+2• S6	+• S7	+55• S8	+25• R9A
398	+14• R10B	+25• R11C	-36• S12	+27• S13
402	+37• R14A	+42• R15B	+39• R16C	-34• S17
406	+18• S18	-9• R19A	+35• R20B	+9• R21C
410	+• S22	+4• S23	+20• S24	-48• S25

SIDE LD 500# R2 DATE: 10 / 14 / 74 TIME: 8 : 22 : 16

FILE: 5 RECORD: 19 CHANNELS 386 THROUGH 413

CHAN

386	+• D1	+25• D2	+•	+2• S1
390	+2• S2	-35• S3	+25• S4	+4• S5
394	+2• S6	+2• S7	+71• S8	+30• R9A
398	+18• R10B	+35• R11C	-39• S12	+41• S13
402	+55• R14A	+56• R15B	+51• R16C	-46• S17
406	+23• S18	-9• R19A	+44• R20B	+7• R21C
410	-6• S22	+6• S23	+23• S24	-67• S25

Table VII, Contd

SIDE LD 600# R2 DATE: 10 / 14 / 74 TIME: 8 : 22 : 53

FILE: 5 RECORD: 20 CHANNELS 386 THROUGH 413

CHAN				
386	- . D1	+31. D2	+ .	+ . S1
390	+4. S2	-35. S3	+32. S4	+4. S5
394	+2. S6	-2. S7	+87. S8	+35. R9A
398	+23. R10B	+44. R11C	-46. S12	+44. S13
402	+58. R14A	+67. R15B	+67. R16C	-48. S17
406	+27. S18	-11. R19A	+11. R20B	+9. R21C
410	+ . S22	+6. S23	+34. S24	-101. S25

SIDE LD 700# R2 DATE: 10 / 14 / 74 TIME: 8 : 23 : 28

FILE: 5 RECORD: 21 CHANNELS 386 THROUGH 413

CHAN				
386	- . D1	+37. D2	+ .	+2. S1
390	+2. S2	-37. S3	+37. S4	+4. S5
394	+2. S6	-2. S7	+103. S8	+42. R9A
398	+25. R10B	+49. R11C	-53. S12	+46. S13
402	+74. R14A	+79. R15B	+72. R16C	-55. S17
406	+32. S18	-9. R19A	+11. R20B	+7. R21C
410	+ . S22	-11. S23	+39. S24	-97. S25

SIDE LD 800# R2 DATE: 10 / 14 / 74 TIME: 8 : 24 : 4

FILE: 5 RECORD: 22 CHANNELS 386 THROUGH 413

CHAN				
386	- . D1	+42. D2	+ .	+2. S1
390	-2. S2	-42. S3	+41. S4	+6. S5
394	+2. S6	-6. S7	+117. S8	+42. R9A
398	+30. R10B	+56. R11C	-60. S12	+60. S13
402	+74. R14A	+105. R15B	+81. R16C	-64. S17
406	+37. S18	-7. R19A	+14. R20B	+7. R21C
410	-6. S22	+6. S23	+43. S24	-104. S25

Table VII, Contd

SIDE LD 900# R2 DATE: 10 / 14 / 74 TIME: 8 : 24 : 35

FILE: 5 RECORD: 23 CHANNELS 386 THROUGH 413

CHAN				
386	- . D1	+48. D2	+ .	+2. S1
390	+2. S2	-49. S3	+44. S4	+4. S5
394	+2. S6	-6. S7	+124. S8	+74. R9A
398	+30. R10B	+63. R11C	-43. S12	+62. S13
402	+102. R14A	+109. R15B	+91. R16C	-71. S17
406	+39. S18	-9. R19A	+18. R20B	+11. R21C
410	+ . S22	-11. S23	+50. S24	-125. S25

SIDE LD 1000# R2 DATE: 10 / 14 / 74 TIME: 8 : 25 : 6

FILE: 5 RECORD: 24 CHANNELS 386 THROUGH 413

CHAN				
386	- . D1	+54. D2	+ .	+2. S1
390	+2. S2	-49. S3	+55. S4	+6. S5
394	+6. S6	-6. S7	+156. S8	+51. R9A
398	+44. R10B	+72. R11C	-66. S12	+69. S13
402	+111. R14A	+123. R15B	+107. R16C	-74. S17
406	+39. S18	-7. R19A	+21. R20B	+ . R21C
410	+ . S22	-6. S23	+53. S24	-139. S25

SIDE LD 1100# R2 DATE: 10 / 14 / 74 TIME: 8 : 25 : 44

FILE: 5 RECORD: 25 CHANNELS 386 THROUGH 413

CHAN				
386	+ . D1	+60. D2	+ .	+2. S1
390	+ . S2	-53. S3	+62. S4	+6. S5
394	+ . S6	-11. S7	+163. S8	+53. R9A
398	+46. R10B	+79. R11C	-73. S12	+81. S13
402	+107. R14A	+142. R15B	+114. R16C	-76. S17
406	+53. S18	-7. R19A	+25. R20B	+4. R21C
410	+ . S22	+4. S23	+50. S24	-152. S25

Table VIII

SIDE LD ZERO DATE: 10 / 14 / 74 TIME: 8 : 26 : 25

FILE: 5 RECORD: 26 CHANNELS 386 THROUGH 413

CHAN				
386	+• D1	+4• D2	+•	+• S1
390	+2• S2	-30• S3	-2• S4	-2• S5
> 394	-2• S6	+• S7	-25• S8	-4• R9A
> 398	-7• R10B	+• R11C	-23• S12	+• S13
402	-11• R14A	-9• R15B	-2• R16C	-9• S17
406	+9• S18	-7• R19A	+18• R20B	+4• R21C
410	+• S22	+• S23	-2• S24	-4• S25

SIDE LD 100# R3 DATE: 10 / 14 / 74 TIME: 8 : 27 : 4

FILE: 5 RECORD: 27 CHANNELS 386 THROUGH 413

CHAN				
386	-• D1	+6• D2	+•	+4• S1
390	+2• S2	-16• S3	+4• S4	+2• S5
394	-2• S6	+• S7	-4• S8	+23• R9A
398	+4• R10B	+4• R11C	-30• S12	+6• S13
402	+• R14A	+• R15B	+9• R16C	-16• S17
406	+11• S18	-4• R19A	+25• R20B	+7• R21C
6 410	+• S22	+6• S23	+11• S24	-16• S25

SIDE LD 200# R3 DATE: 10 / 14 / 74 TIME: 8 : 27 : 35

FILE: 5 RECORD: 28 CHANNELS 386 THROUGH 413

CHAN				
386	-• D1	+10• D2	+•	+4• S1
390	+4• S2	-18• S3	+9• S4	+• S5
> 394	+• S6	+• S7	+23• S8	+23• R9A
398	+7• R10B	+11• R11C	-30• S12	+13• S13
402	+16• R14A	+14• R15B	+18• R16C	-25• S17
406	+18• S18	-7• R19A	+23• R20B	+7• R21C
410	-6• S22	+6• S23	+• S24	-27• S25

ORIGINAL PAGE IS
OF POOR QUALITY

Table VIII, Contd

SIDE LD 300# R3 DATE: 10 / 14 / 74 TIME: 8 : 28 : 18

FILE: 5 RECORD: 29 CHANNELS 386 THROUGH 413

CHAN				
386	- . D1	+15. D2	+ .	+2. S1
390	+4. S2	-23. S3	+13. S4	+ . S5
394	+ . S6	+ . S7	+41. S8	+2. R9A
398	+11. R10B	+11. R11C	-34. S12	+20. S13
402	+18. R14A	+28. R15B	+28. R16C	-30. S17
406	+20. S18	-9. R19A	+39. R20B	+7. R21C
410	+ . S22	+9. S23	+18. S24	-37. S25

SIDE LD 400# R3 DATE: 10 / 14 / 74 TIME: 8 : 28 : 57

FILE: 5 RECORD: 30 CHANNELS 386 THROUGH 413

CHAN				
386	+ . D1	+21. D2	+ .	+4. S1
390	+2. S2	-30. S3	+20. S4	-2. S5
394	+2. S6	+6. S7	+62. S8	+30. R9A
398	+16. R10B	+25. R11C	-36. S12	+27. S13
402	+44. R14A	+39. R15B	+42. R16C	-37. S17
406	+18. S18	-7. R19A	+9. R20B	+7. R21C
410	-4. S22	+4. S23	+18. S24	-60. S25

SIDE LD 500# R3 DATE: 10 / 14 / 74 TIME: 8 : 29 : 33

FILE: 5 RECORD: 31 CHANNELS 386 THROUGH 413

CHAN				
386	+ . D1	+27. D2	+ .	+ . S1
390	+2. S2	-37. S3	+18. S4	+2. S5
394	-4. S6	-4. S7	+78. S8	+18. R9A
398	+18. R10B	+30. R11C	-43. S12	+34. S13
402	+44. R14A	+53. R15B	+53. R16C	-41. S17
406	+25. S18	-7. R19A	+14. R20B	+7. R21C
410	+ . S22	+2. S23	+25. S24	-85. S25

Table VIII, Contd

SIDE LD 600# R3 DATE: 10 / 14 / 74 TIME: 8 : 30 : 9

FILE: 5 RECORD: 32 CHANNELS 386 THROUGH 413

CHAN				
386	+• D1	+31• D2	+•	+2• S1
390	+7• S2	-35• S3	+30• S4	+4• S5
394	+2• S6	+6• S7	+89• S8	+28• R9A
398	+23• R10B	+39• R11C	-34• S12	+41• S13
402	+55• R14A	+67• R15B	+65• R16C	-48• S17
406	+32• S18	-9• R19A	+14• R20B	+7• R21C
410	+• S22	+6• S23	+37• S24	-88• S25

SIDE LD 700# R3 DATE: 10 / 14 / 74 TIME: 8 : 30 : 41

FILE: 5 RECORD: 33 CHANNELS 386 THROUGH 413

CHAN				
386	+• D1	+38• D2	+•	+4• S1
390	+7• S2	-39• S3	+39• S4	+4• S5
394	+• S6	-2• S7	+92• S8	+37• R9A
398	+25• R10B	+51• R11C	-50• S12	+48• S13
402	+67• R14A	+84• R15B	+72• R16C	-53• S17
406	+34• S18	-9• R19A	+18• R20B	+7• R21C
410	+• S22	+6• S23	+37• S24	-108• S25

SIDE LD 800# R3 DATE: 10 / 14 / 74 TIME: 8 : 31 : 14

FILE: 5 RECORD: 34 CHANNELS 386 THROUGH 413

CHAN				
386	-• D1	+43• D2	+•	+• S1
390	+2• S2	-46• S3	+41• S4	+6• S5
394	+2• S6	-2• S7	+117• S8	+37• R9A
398	+32• R10B	+58• R11C	-55• S12	+53• S13
402	+79• R14A	+95• R15B	+84• R16C	-57• S17
406	+37• S18	-4• R19A	+14• R20B	+4• R21C
410	+• S22	+6• S23	+46• S24	-111• S25

Table VIII, Contd

SIDE LD 900# R3 DATE: 10 / 14 / 74 TIME: 8 : 32 : 4

FILE: 5 RECORD: 35 CHANNELS 386 THROUGH 413

CHAN				
386	- . D1	+48. D2	+ .	+2. S1
390	-2. S2	-51. S3	+44. S4	+6. S5
394	+4. S6	-6. S7	+108. S8	+32. R9A
398	+37. R10B	+67. R11C	-66. S12	+57. S13
402	+95. R14A	+114. R15B	+95. R16C	-67. S17
406	+44. S18	-7. R19A	+21. R20B	+7. R21C
410	+ . S22	-2. S23	+43. S24	-125. S25

SIDE LD 1000# R3 DATE: 10 / 14 / 74 TIME: 8 : 32 : 48

FILE: 5 RECORD: 36 CHANNELS 386 THROUGH 413

CHAN				
386	+ . D1	+54. D2	+ .	+2. S1
390	+2. S2	-53. S3	+53. S4	+6. S5
394	+4. S6	+ . S7	+138. S8	+53. R9A
398	+42. R10B	+72. R11C	-64. S12	+74. S13
402	+97. R14A	+126. R15B	+100. R16C	-71. S17
406	+46. S18	-9. R19A	+42. R20B	+7. R21C
410	-6. S22	+4. S23	+50. S24	-134. S25

SIDE LD 1100# R3 DATE: 10 / 14 / 74 TIME: 8 : 33 : 53

FILE: 5 RECORD: 37 CHANNELS 386 THROUGH 413

CHAN				
386	- . D1	+61. D2	+ .	+2. S1
390	+ . S2	-58. S3	+60. S4	+6. S5
394	+6. S6	-4. S7	+172. S8	+79. R9A
398	+46. R10B	+74. R11C	-71. S12	+81. S13
402	+107. R14A	+144. R15B	+114. R16C	-78. S17
406	+55. S18	-7. R19A	+44. R20B	+9. R21C
410	-6. S22	+6. S23	+57. S24	-155. S25

Table IX

SIDE LD ZERO DATE: 10 / 14 / 74 TIME: 8 : 34 : 45

FILE: 5 RECORD: 38 CHANNELS 386 THROUGH 413

CHAN				
386	+• D1	+4• D2	+•	+• S1
390	+• S2	-16• S3	-2• S4	-2• S5
394	+• S6	-4• S7	-36• S8	-25• R9A
398	-2• R10B	+2• R11C	-13• S12	+2• S13
402	-13• R14A	-11• R15B	-2• R16C	-6• S17
406	+9• S18	-4• R19A	+7• R20B	+9• R21C
410	+• S22	+2• S23	-4• S24	-4• S25

SIDE LD 100# R4 DATE: 10 / 14 / 74 TIME: 8 : 35 : 26

FILE: 5 RECORD: 39 CHANNELS 386 THROUGH 413

CHAN				
386	+• D1	+5• D2	+•	+• S1
390	+2• S2	-21• S3	+4• S4	+2• S5
394	+2• S6	-2• S7	+11• S8	-14• R9A
398	+2• R10B	+4• R11C	-20• S12	+9• S13
402	+• R14A	+• R15B	+9• R16C	-13• S17
406	+16• S18	-7• R19A	+14• R20B	+7• R21C
410	-6• S22	-9• S23	+4• S24	-6• S25

SIDE LD 200# R4 DATE: 10 / 14 / 74 TIME: 8 : 35 : 59

FILE: 5 RECORD: 40 CHANNELS 386 THROUGH 413

CHAN				
386	+• D1	+10• D2	+•	+• S1
390	+• S2	-18• S3	+6• S4	+2• S5
394	+• S6	-2• S7	+27• S8	+14• R9A
398	+7• R10B	+14• R11C	-27• S12	+16• S13
402	+13• R14A	+7• R15B	+18• R16C	-20• S17
406	+16• S18	-7• R19A	+2• R20B	+4• R21C
410	+• S22	-9• S23	+13• S24	-48• S25

Table IX, Contd

SIDE LD 300# R4 DATE: 10 / 14 / 74 TIME: 8 : 36 : 34

FILE: 5 RECORD: 41 CHANNELS 386 THROUGH 413

CHAN				
386	- . D1	+15. D2	+ .	+ . S1
390	+4. S2	-18. S3	+16. S4	+2. S5
394	+ . S6	+2. S7	+41. S8	-7. R9A
398	+7. R10B	+16. R11C	-25. S12	+20. S13
402	+23. R14A	+23. R15B	+28. R16C	-32. S17
406	+18. S18	-11. R19A	+2. R20B	+7. R21C
410	+2. S22	-6. S23	+23. S24	-44. S25

SIDE LD 400# R4 DATE: 10 / 14 / 74 TIME: 8 : 37 : 14

FILE: 5 RECORD: 42 CHANNELS 386 THROUGH 413

CHAN				
386	+ . D1	+21. D2	+ .	+4. S1
390	+2. S2	-23. S3	+20. S4	+ . S5
394	+ . S6	-2. S7	+59. S8	+37. R9A
398	+14. R10B	+25. R11C	-39. S12	+27. S13
402	+20. R14A	+42. R15B	+39. R16C	-37. S17
406	+20. S18	-9. R19A	+7. R20B	+14. R21C
410	+ . S22	+6. S23	+13. S24	-60. S25

SIDE LD 500# R4 DATE: 10 / 14 / 74 TIME: 8 : 37 : 47

FILE: 5 RECORD: 43 CHANNELS 386 THROUGH 413

CHAN				
386	- . D1	+27. D2	+ .	+ . S1
390	+4. S2	-32. S3	+25. S4	+4. S5
394	-6. S6	-6. S7	+75. S8	-2. R9A
398	+18. R10B	+35. R11C	-48. S12	+37. S13
402	+41. R14A	+56. R15B	+51. R16C	-41. S17
406	+27. S18	-9. R19A	+11. R20B	+9. R21C
410	+2. S22	+6. S23	+30. S24	-71. S25

Table IX, Contd

SIDE LD 600# R4 DATE: 10 / 14 / 74 TIME: 8 : 38 : 18

FILE: 5 RECORD: 44 CHANNELS 386 THROUGH 413

CHAN				
386	-• D1	+32• D2	+•	+2• S1
390	-2• S2	-30• S3	+32• S4	+4• S5
394	+• S6	+• S7	+92• S8	+58• R9A
398	+23• R10B	+32• R11C	-57• S12	+46• S13
402	+43• R14A	+70• R15B	+67• R16C	-51• S17
406	+25• S18	-7• R19A	+11• R20B	+7• R21C
410	+2• S22	+6• S23	+32• S24	-83• S25

SIDE LD 700# R4 DATE: 10 / 14 / 74 TIME: 8 : 38 : 51

FILE: 5 RECORD: 45 CHANNELS 386 THROUGH 413

CHAN				
386	-• D1	+38• D2	+•	+• S1
390	+2• S2	-32• S3	+37• S4	+6• S5
394	+2• S6	-4• S7	+108• S8	+67• R9A
398	+25• R10B	+46• R11C	-66• S12	+50• S13
402	+58• R14A	+84• R15B	+77• R16C	-51• S17
406	+34• S18	-7• R19A	+21• R20B	+7• R21C
410	-2• S22	+2• S23	+37• S24	-99• S25

SIDE LD 800# R4 DATE: 10 / 14 / 74 TIME: 8 : 39 : 23

FILE: 5 RECORD: 46 CHANNELS 386 THROUGH 413

CHAN				
386	+• D1	+43• D2	+•	+4• S1
390	-9• S2	-44• S3	+44• S4	+6• S5
394	-2• S6	-4• S7	+126• S8	+16• R9A
398	+28• R10B	+56• R11C	-55• S12	+57• S13
402	+72• R14A	+95• R15B	+84• R16C	-57• S17
406	+39• S18	-7• R19A	+21• R20B	+7• R21C
410	+• S22	+• S23	+41• S24	-106• S25

ORIGINAL PAGE IS
OF POOR QUALITY

Table IX, Contd

SIDE LD 900# R4 DATE: 10 / 14 / 74 TIME: 8 : 39 : 58

FILE: 5 RECORD: 47 CHANNELS 386 THROUGH 413

CHAN

386	- . D1	+48. D2	+ .	+4. S1
390	+2. S2	-56. S3	+51. S4	+6. S5
394	+4. S6	+ . S7	+138. S8	+39. R9A
398	+35. R10B	+65. R11C	-57. S12	+64. S13
402	+86. R14A	+109. R15B	+91. R16C	-69. S17
406	+41. S18	-9. R19A	+16. R20B	+7. R21C
410	+4. S22	+6. S23	+39. S24	-122. S25

SIDE LD 1000# R4 DATE: 10 / 14 / 74 TIME: 8 : 40 : 32

FILE: 5 RECORD: 48 CHANNELS 386 THROUGH 413

CHAN

386	- . D1	+54. D2	+ .	+2. S1
390	+2. S2	-53. S3	+55. S4	+6. S5
394	+2. S6	-4. S7	+140. S8	+32. R9A
398	+35. R10B	+67. R11C	-69. S12	+71. S13
402	+95. R14A	+137. R15B	+100. R16C	-71. S17
406	+46. S18	-7. R19A	+16. R20B	+7. R21C
410	+2. S22	+6. S23	+46. S24	-132. S25

SIDE LD 1100# R4 DATE: 10 / 14 / 74 TIME: 8 : 41 : 14

FILE: 5 RECORD: 49 CHANNELS 386 THROUGH 413

CHAN

386	+ . D1	+60. D2	+ .	-2. S1
390	+4. S2	-51. S3	+62. S4	+6. S5
394	+4. S6	+4. S7	+177. S8	+79. R9A
398	+46. R10B	+79. R11C	-69. S12	+78. S13
402	+121. R14A	+135. R15B	+119. R16C	-78. S17
406	+53. S18	-7. R19A	+23. R20B	+9. R21C
410	-2. S22	+6. S23	+50. S24	-162. S25

ORIGINAL PAGE IS
OF POOR QUALITY

Table X

SIDE LD ZERO DATE: 10 / 14 / 74 TIME: 8 : 42 : 3

FILE: 5 RECORD: 50 CHANNELS 386 THROUGH 413

CHAN

386	- . D1	+4. D2	+ .	+4. S1
390	+2. S2	-11. S3	+2. S4	+ . S5
394	-4. S6	-2. S7	-4. S8	-28. R9A
398	-2. R10B	+ . R11C	-18. S12	+2. S13
402	-13. R14A	-11. R15B	-2. R16C	+2. S17
406	+11. S18	-4. R19A	+21. R20B	+9. R21C
410	-6. S22	+6. S23	-11. S24	+ . S25

SIDE LD 100# R5 DATE: 10 / 14 / 74 TIME: 8 : 42 : 54

FILE: 5 RECORD: 51 CHANNELS 386 THROUGH 413

CHAN

386	- . D1	+7. D2	+ .	+ . S1
390	+4. S2	-30. S3	+6. S4	-4. S5
394	+ . S6	+2. S7	+16. S8	-30. R9A
398	+4. R10B	+4. R11C	-4. S12	+6. S13
402	-4. R14A	-4. R15B	+11. R16C	-16. S17
406	+13. S18	-2. R19A	+2. R20B	+16. R21C
410	+2. S22	+2. S23	+6. S24	-16. S25

SIDE LD 200# R5 DATE: 10 / 14 / 74 TIME: 8 : 43 : 29

FILE: 5 RECORD: 52 CHANNELS 386 THROUGH 413

CHAN

386	- . D1	+11. D2	+ .	+2. S1
390	+7. S2	-23. S3	+9. S4	+ . S5
394	+ . S6	-2. S7	+9. S8	-16. R9A
398	+4. R10B	+14. R11C	-23. S12	+13. S13
402	+6. R14A	+18. R15B	+18. R16C	-20. S17
406	+18. S18	-9. R19A	+14. R20B	+11. R21C
410	-2. S22	+6. S23	+11. S24	-27. S25

Table X, Contd

SIDE LD 340# R5 DATE: 10 / 14 / 74 TIME: 8 : 44 : 8

FILE: 5 RECORD: 53 CHANNELS 386 THROUGH 413

CHAN				
386	+• D1	+15• D2	+•	+• S1
390	+2• S2	-32• S3	+13• S4	+• S5
394	+• S6	-6• S7	+41• S8	-23• R9A
398	+9• R10B	+14• R11C	-43• S12	+25• S13
402	+16• R14A	+35• R15B	+30• R16C	-50• S17
406	+18• S18	-9• R19A	+21• R20B	+9• R21C
410	-4• S22	16• S23	+18• S24	-46• S25

SIDE LD 400# R5 DATE: 10 / 14 / 74 TIME: 8 : 44 : 38

FILE: 5 RECORD: 54 CHANNELS 386 THROUGH 413

CHAN				
386	+• D1	+22• D2	+•	+4• S1
390	-4• S2	-30• S3	+18• S4	+2• S5
394	-6• S6	-4• S7	+55• S8	-18• R9A
398	+16• R10B	+23• R11C	-50• S12	+27• S13
402	+25• R14A	+39• R15B	+44• R16C	-34• S17
406	+25• S18	-7• R19A	+9• R20B	+7• R21C
410	-2• S22	+4• S23	+23• S24	-67• S25

SIDE LD 500# R5 DATE: 10 / 14 / 74 TIME: 9 : 45 : 22

FILE: 5 RECORD: 55 CHANNELS 386 THROUGH 413

CHAN				
386	-• D1	+27• D2	+•	+2• S1
390	+2• S2	-25• S3	+25• S4	+2• S5
394	+• S6	-4• S7	+71• S8	-4• R9A
398	+21• R10B	+28• R11C	-50• S12	+37• S13
402	+37• R14A	+53• R15B	+49• R16C	-41• S17
406	+32• S18	-11• R19A	+37• R20B	+7• R21C
410	-2• S22	+9• S23	+30• S24	-88• S25

Table X, Contd

SIDE LD 600# R5 DATE: 10 / 14 / 74 TIME: 8 : 45 : 54

FILE: 5 RECORD: 56 CHANNELS 386 THROUGH 413

CHAN

386	- . D1	+32. D2	+ .	+4. S1
390	-11. S2	-37. S3	+30. S4	+4. S5
394	-6. S6	-6. S7	+94. S8	+32. R9A
398	+23. R10B	+37. R11C	-55. S12	+39. S13
402	+48. R14A	+65. R15B	+65. R16C	+44. S17
406	+32. S18	-9. R19A	+14. R20B	+7. R21C
410	-2. S22	+4. S23	+32. S24	-92. S25

SIDE LD 700# R5 DATE: 10 / 14 / 74 TIME: 8 : 46 : 31

FILE: 5 RECORD: 57 CHANNELS 386 THROUGH 413

CHAN

386	+ . D1	+38. D2	+ .	+2. S1
390	+2. S2	-42. S3	+37. S4	+4. S5
394	+2. S6	+2. S7	+108. S8	+16. R9A
398	+28. R10B	+46. R11C	-36. S12	+55. S13
402	+60. R14A	+74. R15B	+72. R16C	-48. S17
406	+37. S18	-7. R19A	+11. R20B	+7. R21C
410	+2. S22	+6. S23	+37. S24	-94. S25

SIDE LD 800# R5 DATE: 10 / 14 / 74 TIME: 8 : 47 : 2

FILE: 5 RECORD: 58 CHANNELS 386 THROUGH 413

CHAN

386	- . D1	+43. D2	+ .	-4. S1
390	+7. S2	-35. S3	+41. S4	+2. S5
394	+4. S6	+ . S7	+128. S8	+14. R9A
398	+35. R10B	+58. R11C	-48. S12	+55. S13
402	+74. R14A	+86. R15B	+84. R16C	-60. S17
406	+39. S18	-7. R19A	+16. R20B	+9. R21C
410	+2. S22	+4. S23	+43. S24	-120. S25

Table X, Contd

SIDE LD 900# R5 DATE: 10 / 14 / 74 TIME: 8 : 47 : 32

FILE: 5 RECORD: 59 CHANNELS 386 THROUGH 413

CHAN				
386	+• D1	+48• D2	+•	+• S1
390	+2• S2	-63• S3	+48• S4	+6• S5
394	+4• S6	-6• S7	+142• S8	+21• R9A
398	+37• R10B	+55• R11C	-60• S12	+64• S13
402	+83• R14A	+112• R15B	+93• R16C	-62• S17
406	+44• S18	-7• R19A	+35• R20B	+9• R21C
410	-2• S22	+6• S23	+60• S24	-125• S25

SIDE LD 1000# R5 DATE: 10 / 14 / 74 TIME: 8 : 49 : 7

FILE: 5 RECORD: 60 CHANNELS 386 THROUGH 413

CHAN				
386	-• D1	+54• D2	+•	+2• S1
390	+4• S2	-56• S3	+55• S4	+9• S5
394	+4• S6	-4• S7	+154• S8	+25• R9A
398	+42• R10B	+67• R11C	-71• S12	+74• S13
402	+90• R14A	+126• R15B	+100• R16C	-71• S17
406	+44• S18	-9• R19A	+51• R20B	+9• R21C
410	+• S22	-4• S23	+55• S24	-157• S25

SIDE LD 1100# R5 DATE: 10 / 14 / 74 TIME: 8 : 48 : 42

FILE: 5 RECORD: 61 CHANNELS 386 THROUGH 413

CHAN				
386	+• D1	+61• D2	+•	+2• S1
390	-2• S2	-58• S3	+62• S4	+9• S5
394	+4• S6	-13• S7	+172• S8	+30• R9A
398	+46• R10B	+79• R11C	-60• S12	+74• S13
402	+102• R14A	+137• R15B	+114• R16C	-76• S17
406	+53• S18	-7• R19A	+30• R20B	+7• R21C
410	+• S22	+• S23	+55• S24	-152• S25

ORIGINAL PAGE IS
OF POOR QUALITY.

Table X, Contd

SIDE LD FINAL ZE DATE: 10 / 14 / 74 TIME: 8 : 49 : 32

FILE: 5 RECORD: 62 CHANNELS 386 THROUGH 413

CHAN				
386	- . D1	+4 . D2	+ .	+4 . S1
390	+7 . S2	-14 . S3	+2 . S4	+ . S5
394	-4 . S6	-2 . S7	+ . S8	+14 . R9A
398	+ . R10B	+ . R11C	-32 . S12	+2 . S13
402	-18 . R14A	-9 . R15B	+2 . R16C	-6 . S17
406	+11 . S18	-4 . R19A	+4 . R20B	+7 . R21C
410	-2 . S22	+4 . S23	-2 . S24	-2 . S25

5.1.6 CORRELATION OF STRAIN GAUGE RESULTS WITH ANALYTICAL

PREDICTIONS. Strain gauge results obtained from the GEMS Static tests are converted to local stress resultants and compared with analytical predictions in this section. The stresses corresponding to the maximum test loads levels are derived using the following stress strain relations.

1. Axial Stress (at locations having axial and transverse gauges)

$$\sigma_x = \frac{E_x}{1 - \mu_{xy}\mu_{yx}} (\epsilon_x - \epsilon_y \mu_{yx}) \quad (1)$$

At locations having axial gauges only, the true stress can only be determined if no lateral constraints (e.g., an adjacent ring) exist. For this case the stress is given by

$$\sigma_x = E_x \epsilon_x \quad (1A)$$

When back to back gauges exist the stresses at the inner and outer faces are determined using equations (1) or (1A) as applicable and the average axial stress given by $\sigma_{avg} = 0.5(\sigma_i + \sigma_o)$ computed.

2. Shear Stress

Shear stresses are evaluated at locations having a 45° rosette.

The shear stress is given by

$$\tau_{xy} = G(\gamma_{xy}) = G(\epsilon_x + \epsilon_y - 2\epsilon_2)$$

The average elastic constants, for the $[0/\pm 45.5/90]_s$ Modmor I/X-30 laminate used in the analysis are given below

$$E_x = 16.412 \text{ msi}$$

$$E_y = 7.882 \text{ msi}$$

$$\mu_{xy} = 0.298$$

$$G_{xy} = 2.987 \text{ msi}$$

Measured and predicted stresses at gauge locations at the base of the shell for the 1,100 pound side load condition, and in the spider arm for the 180 pound axial load condition are given in Table 5-1. Due to the erratic behavior of the gauges at low stress levels no correlation was possible for the 180 pound loading at other locations.

Table 5-1. Summary of Predicted and Measured Stresses

Location	Loading	Gauge Nos.	Predicted psi	Measured psi	Remarks
Shell at End Ring $\theta = 0^\circ$	1,100 lb Side Load	24-25	-609	-837	See Note 1
Shell at End Ring $\theta = 45^\circ$	1,100 lb Side Load	14-18	431	439	
Shell at End Ring $\theta = 90^\circ$	1,100 lb Side Load	19-23	180 (shear)	-149.4 (shear)	
Shell at End Ring $\theta = 90^\circ$	1,100 lb Side Load	19-23	0	0	
Shell at End Ring $\theta = 180^\circ$	1,100 lb Side Load	9-13	609	536	See Note 2
Spider Arm	180 lb Axial	1-2	-930	-903	

Notes: 1 Based on the average of back to back axial gauges. Due to the proximity of the end ring lateral restraint exists which is not accounted for due to the absence of lateral gauges.

2 The gauges at this location exhibited erratic behavior, the measured stress of 536 psi is based on a linear extrapolation of the measured strain of 1,000 lb load for gauge no. 9.

5.2 DYNAMIC TEST

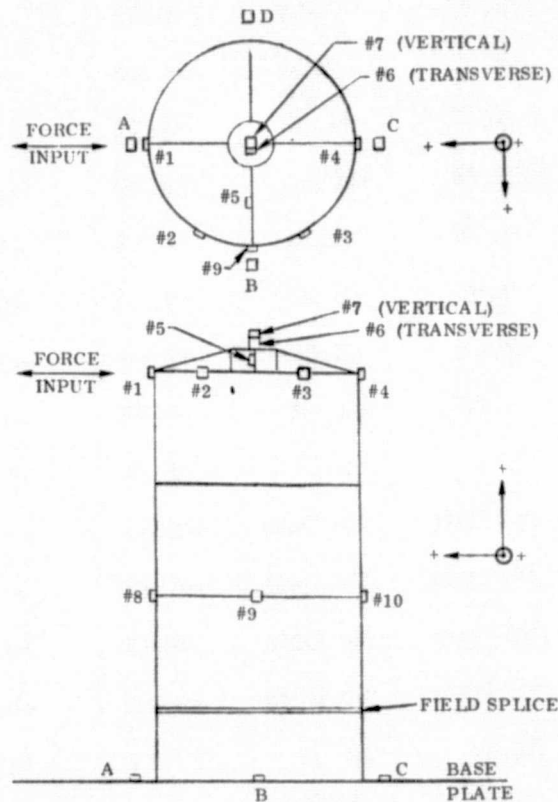
5.2.1 TEST SETUP AND CONDITIONS. The test specimen was secured to the baseplate of the static test fixture and instrumented with 10 accelerometers. A mass of 112 pounds was attached to the secondary mirror support to simulate the secondary mirror. A Ling V50 (50 lb-force) electrodynamic exciter was attached to the top of the specimen in the lateral direction. Low force input (0.25 pounds to 0.75 pounds) sweeps from 5 Hz to 125 Hz were made to determine resonant frequencies and steady state responses of the accelerometers were recorded. Amplitude decay was then performed to determine the structure damping coefficient at each of the resonant frequencies. The field splice bolts were then measured for their existing torque value and 15 inch-pound additional torque was applied to each bolt. The above testing was repeated.

The secondary mirror simulation mass was then reduced from 112 pounds to 58 pounds. The above testing was again repeated.

5.2.2 INSTRUMENTATION. Figure 5.2-1 shows the location of the accelerometers and the "sign convention" to be used when determining mode shapes from the response data in Table 5-2.

5.2.3 TEST RESULTS. The Modal Data (accelerometer response) for each of the configurations is tabulated in Table 5-2. Locations A, B, C and D are baseplate measurements in the vertical direction.

The Damping Coefficients determined for each of the configurations are tabulated in Table 5-3.



Accelerometer locations and
Accelerometer sign convention

Figure 5.2-1. Accelerometer Locations and
Accelerometer Sign Convention

ORIGINAL PAGE IS
OF POOR QUALITY

Table 5-2. Modal Data

Accel. Location	Relative Amplitude				
1	+6.08	+7.55	+4.45	+8.53	+4.13
2	+0.65	-2.13	+0.71	-2.17	-0.45
3	+0.92	-0.96	+0.92	-0.76	-0.14
4	+5.44	+6.45	+4.12	+7.57	+3.58
5	+29.70	-12.50	+28.20	-9.69	-0.75
6	+1.78	-4.74	+1.92	-4.77	-0.72
7	-0.60	-0.30	-0.49	-0.46	-0.14
8	+2.40	+3.00	+1.68	+3.38	+1.52
9	+0.70	-1.51	+0.74	-1.48	-0.37
10	+2.42	+2.77	+1.78	+3.29	+1.75
A	No Data	No Data	-0.48	-1.01	-0.52
B	No Data	No Data	-0.18	+0.36	+0.09
C	No Data	No Data	-0.46	+0.82	+0.45
D	No Data	No Data	+0.16	-0.43	-0.12
Frequency, Hz	22.34	22.88	22.39	22.96	29.40
Simulated Mass	112#	112#	112#	112#	58#
Field Splice Bolt Torque	20 in-lb	20 in-lb	35 in-lb	35 in-lb	35 in-lb

Note: 1. All readings were taken with 0.5 pounds excitation force.

2. The torque as listed is the "net" torque above the bolt "running" torque.

Table 5-3. Damping Coefficient

Simulated Mass Pounds	Field Splice Bolt Torque - In-Lb	Frequency Hz	Force Input Pounds	Damping Zeta
112	20	22.36	0.25	0.0025
112	20	22.34	0.50	0.0031
112	20	22.34	0.75	0.0028
112	20	22.92	0.25	0.0036
112	20	22.88	0.50	0.0035
112	20	22.85	0.75	0.0034
112	35	22.38	0.50	0.0030
112	35	22.98	0.5	0.0039
58	35	29.36	0.25	0.013
58	35	29.32	0.50	0.010
58	35	29.30	0.75	0.012

Note: The torque as listed is the "net" torque above the bolt "running" torque.

5.2.4 ANALYSIS OF RESULTS. Upon reducing the test data, it was found that significant base motion occurred. Fortunately, accelerometers mounted on the baseplate recorded the amplitude. This analysis accounts for the base motion by correcting the measured frequency of the fundamental mode. The procedure is outlined below.

If the GEMS and the baseplate are considered to be two springs in series, then the static deflection at the shaker location due to the shaker force input would be given by

$$\delta = P \left(\frac{1}{K_G} + \frac{1}{K_B} \right)$$

where P is the applied force, K_G is the GEMS stiffness and K_B is the baseplate stiffness.

In terms of the GEMS and baseplate deflections,

$$\delta = \delta_G = \delta_B$$

The deflection due to the GEMS is therefore

$$\delta_G = \frac{P}{K_G} = \delta - \delta_B$$

or the GEMS stiffness is

$$K_G = \frac{1}{\delta - \delta_B}$$

Neglecting baseplate mass effects, the GEMS fundamental frequency with a rigid baseplate is given by

$$\omega = \omega_M \sqrt{\frac{K_G}{K_G + K_B}}$$

where ω_M is the measured frequency. Rewriting this equation in terms of deflections yields

$$\omega = \omega_M \sqrt{\frac{\delta}{\delta - \delta_B}}$$

Section 5.2.3 lists deflections and frequencies obtained from the GEMS vibration test. For the 58 pound secondary mirror, the modal frequency was 29.5 Hz and the average deflection at the shaker location was +3.86 inches (normalized). Baseplate deflections in the plane of the shaker were +0.45 and -0.52. The baseplate accelerometers were located equidistant from the GEMS, 70 inches apart. The angular rotation of the GEMS due to baseplate motion was therefore

$$\theta = \frac{0.52 + 0.45}{70} = 0.0139 \text{ RAD.}$$

The deflection at the shaker located 112 inches above the baseplate was therefore

$$\delta_B = (112)(0.0139) = 1.55 \text{ inches}$$

Using the previously derived equation, the corrected frequency is

$$\omega = 29.4 \sqrt{\frac{3.86}{3.86 - 1.55}} = 38.0 \text{ Hz}$$

This result is obtained from the test with the 58 pound (quarter scale) mass for the secondary mirror, a condition which is consistent with the mass of the GEMS structure which is also one quarter scale. The value of 38 Hz would indicate a fixed base resonant frequency of $38/\sqrt{4} = 19$ Hz for a full scale metering shell. This could be significantly improved by an increase in the number of bolts the field splice and the attachment flange.

5.3 THERMAL VACUUM TEST

5.3.1 TEST DESCRIPTION

5.3.1.1 Objectives. The objective of this test was to demonstrate the dimensional stability of the GEMS assembly in a varying thermal environment.

Initially the intent was to measure despace, tilt, and decenter of the secondary mirror support relative to a reference plane in the vicinity of the LST primary mirror location. Prior to the test, some uncertainty arose with respect to the feasibility of measuring the extremely low thermal strains in the thermal vacuum test chamber conditions. In view of this situation, it was decided in concurrence with MSFC, to concentrate on despace measurements only. This is the most critical mode for the LST and is the one which can be most directly measured. Limiting the measurement to despace would facilitate the resolution of problems anticipated with the measurement system.

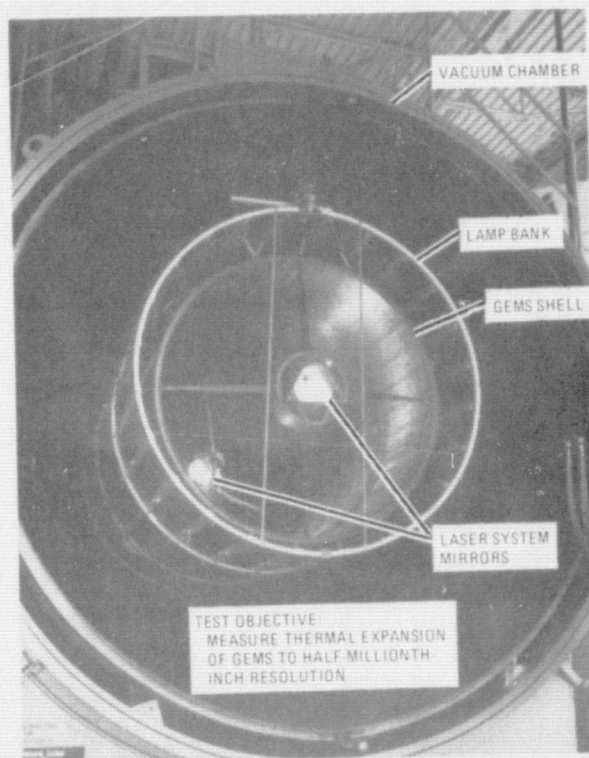
5.3.1.2 Test Set-Up. The GEMS was suspended in a horizontal position in the vacuum chamber, as shown in Figure 5.3-1. The suspension system consisted of a statically determinate system of stainless steel cables designed to prevent the transmission of thermal and mechanical strains from the chamber wall.

Surrounding the shell of the GEMS was an annular array of heat lamps attached to an annular fixture suspended separately from the GEMS. The lamp array consisted of five annular banks placed end-to-end and each consisting of 24 equally spaced lamps.

Specimen temperature could be reduced to -100°F by the application of LN_2 in the cold wall of the vacuum chamber. During the tests, the specimen temperature could be varied between -100°F and -20°F by use of the lamp bank. The lamps were designed to allow the imposition of a uniform temperature change in the shell of the specimen, a stepped longitudinal temperature gradient, or a stepped circumferential temperature gradient.

An optically flat window was provided in the vacuum chamber wall in line with centerline of the GEMS assembly. The Hewlett-Packard laser/sensor unit and the associated optics were mounted on a platform outside the chamber to shoot through this window. A flat mirror for the measurement system was attached at each end of the GEMS centered on the centerline of the GEMS. One mirror registered on the forward edge of the secondary mirror support hub, the other in the plane of the aft attachment flange. Dimensional stable graphite-epoxy supports supported these mirrors from the GEMS structure. To further minimize distortion on the long span of the aft support, this structure was insulated with multilayer aluminized mylar insulation.

The response of the 53 thermocouples distributed over the GEMS and the aft stable support were recorded on magnetic tape. This type of recording was also used for the dimensional readings from the Hewlett-Packard dilatometer.



14-3149

Figure 5.3-1 GEMS in Thermal Vacuum Test

ORIGINAL PAGE IS
OF POOR QUALITY

5.3.2 INSTRUMENTATION

5.3.2.1 Thermocouples. The GEMS was instrumented with 53 thermocouples as shown in Figure 5.3.2-1 plus 5 additional thermocouple which were used to control the power input into the heating lamps. The thermocouples on the secondary mirror support hub were on the outside surface of this double cylinder. Those on the shell were bonded to inside surface of this portion of the structure. The aft spider was wrapped with a multilayer of aluminized mylar insulation to reduce the temperature changes in this mirror support structure.

5.3.2.2 Laser System. The Hewlett-Packard model 5526A laser measurement system with plane mirror dilatometer optics was used to measure despace between the secondary mirror support and the aft spider. This system has a basic resolution of 0.013 micrometers (0.5 microinches). This despace measurement geometry is shown in Figures 5.3.2-2 and 5.3.2-3. The plane mirrors are shown in position indexed against the mirror support structures. The laser system requires that these plane mirrors be parallel within about 30 arc seconds for proper optical alignment. This was attained by lightly sanding the indexing points of the aft spider at the metering shell attachment points. A second requirement, for the laser system to respond only to the dimensional

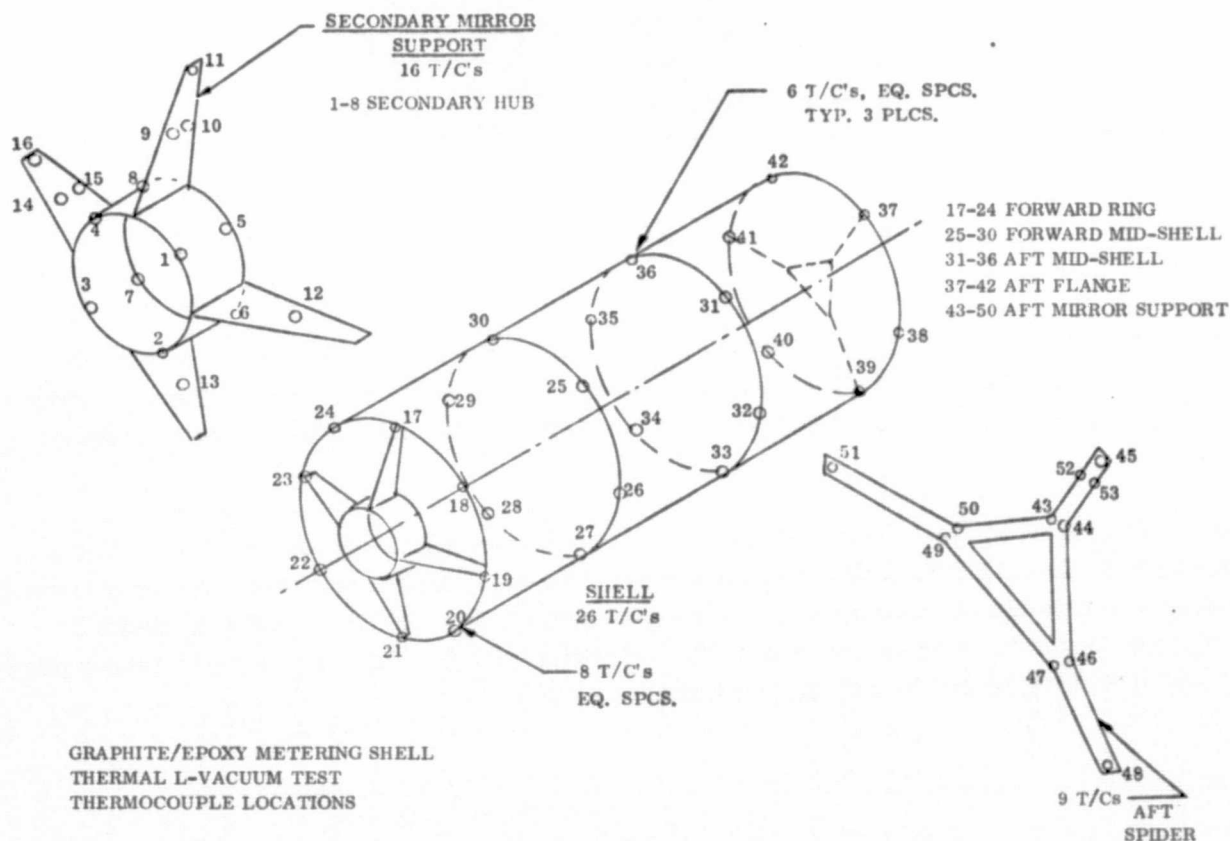


Figure 5.3.2-1. Thermocouple Locations

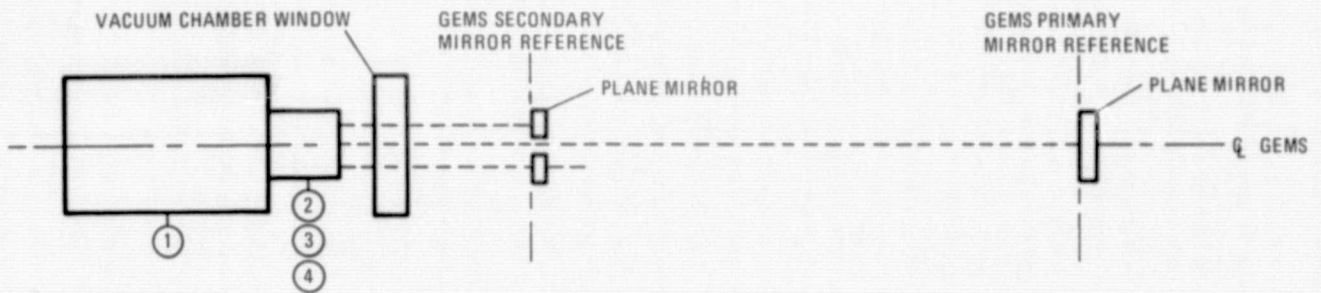
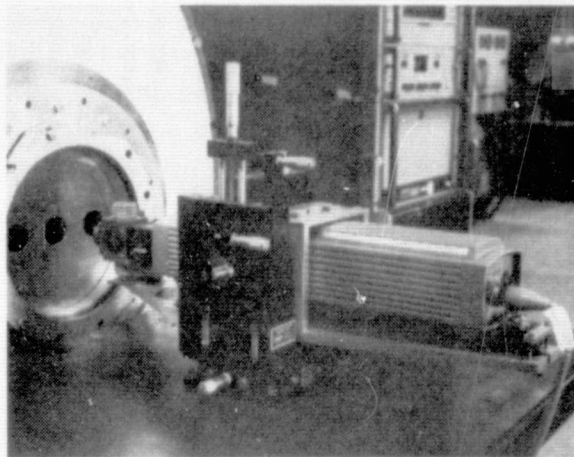


Figure 5.3.2-2. Schematic of Hewlett-Packard Laser Measurement System



14-3911

Figure 5.3.2-3. Laser/Optical Assembly

changes of the two mirrors, is that the pressure variations in the vacuum chamber should be less than 10^{-4} torr. This was achieved, as is documented in the following section, by pumping the chamber below this pressure during all of the measurement cycles.

All of the thermocouple data and one laser output was stored on magnetic tape via a Hewlett-Packard Model 2019A data system. The data, thus recorded, was in a format suitable for computer processing. This processing included transforming thermocouple voltages to temperatures and the averaging of the temperatures on various parts of the structure to aid in the analysis of the results.

5.3.3 TEST HISTORY. The vacuum chamber pumping procedure was as follows. The initial pumping was done by three to six 280 cfm mechanical vacuum pumps (roughing pumps). Next, a ring jet booster diffusion pump (booster pump) was used while being backed by one or two roughing pumps. There are two LN₂ cold traps (LN₂ traps) between the booster pump and the main diffusion pumps (diffusion pumps). The diffusion pumps are always open to the chamber and all pumping was done through them. The diffusion pumps are backed by the booster pump and pump the chamber through an optically black louvre arrangement (chevron) that is chilled by LN₂. This provides a cold trap between the diffusion pumps and the chamber and must be full while the diffusion pumps are hot. It also acts as a section of the LN₂ chilled, optically black shroud that lines the inside of chamber. This shroud (coldwall) is a corrugated sheet of stainless steel welded to a smooth sheet of stainless steel. A pump circulates LN₂ through the chevron and the corrugations of the coldwall.

Shutdown was initiated by turning off the diffusion pumps. The LN₂ was blown out of the cold wall with hot GN₂ while the chevron was kept full. After the diffusion pumps were cool (1-1 1/2 hours), the LN₂ was blown out of the chevron with hot GN₂. At this time the chamber was blanked off (no pumping). The LN₂ traps were allowed to run dry. The lamps were run as long as possible and temperature cycles were stopped at the high temperature of the cycle to prevent over-chilling the specimen before the LN₂ was removed from the coldwall and chevron.

25 November 1974, Monday

At the start of the shift, the chamber pressure was atmospheric and the specimen average temperature was 63° F. The moisture desorption cycle was started. At 1530 the pumping was switched back to the roughing pumps. The LN₂ traps were kept full overnight.

26 November 1974, Tuesday

At the start of the shift, the chamber pressure was 32μ and the specimen average temperature was 56° F.

10 December 1974, Tuesday

At the start of the shift, the chamber pressure was 32μ and the specimen average temperature was 51° F. At 0740 the pumping was switched to the booster pump. By 1025 the pressure was 20μ and the chevron was filled. At 1230 the diffusion pumps were pumping and the pressure was 1.6×10^{-6} torr. By 1300 the coldwall was full and the pressure had reached 6×10^{-7} torr. The pressure remained below 1×10^{-6} torr until shutdown at 2124.

The first half of the first uniform temperature cycle was started at 1800. The laser signal was lost due to a deposit on the mirrors, probably water condensation. The GEMS temperature was raised to +75° F, but the mirror temperatures remained at

-20°F. At 2020, the LN₂ was blown out of the coldwall in an attempt to raise the mirror temperatures.

11 December 1974, Wednesday

At the start of the shift the chamber pressure was 290 μ and the specimen average temperature was 46°F. At 0915 the roughing pumps were started. The LN₂ traps were filled at 0924. By 0932 the pressure was 200 μ and the pumping was switched to the booster pump. At 0959 the chevron was filled. By 1052 the diffusion pumps were pumping and the pressure was 4.6×10^{-6} torr. The pressure remained below 1×10^{-5} until shutdown at 2103.

The lamps were turned on and the GEMS temperature was raised to +100°F. At 1228 hot GN₂ was started flowing through the coldwall, but the chevron was kept full. At 1817 the power to the center lamp ring was shut off because a transformer in the controller burned out.

12 December 1974, Thursday

At the start of the shift the chamber pressure was 500 μ and the specimen average temperature was 58°F. At 0755 the pressure was 125 μ and pumping was switched to the booster pump. At 0800 the pressure was 30 μ and the chevron was filled. By 0850 the diffusion pumps were pumping and the pressure was 5.4×10^{-5} torr. The coldwall was filled. By 0904 the pressure had reached 2×10^{-6} and remained below 2.5×10^{-5} torr until shutdown at 2130.

The end lamp rings were turned on at 0935 to maintain specimen temperature while the third controller was repaired. The transformer supplied 120 vac to the control unit and 2.5 vac to two vacuum tubes. The 120 vac was supplied from a wall socket and two transformers were used to convert this to 2.5 vac for the tubes.

13 December 1974, Friday

At the start of the shift the chamber pressure was 2 torr and the specimen average temperature was 54°F.

At 0725 the roughing pumps were started. The LN₂ traps were filled and by 0810 the pressure was 500 μ . At this time the pumping was switched to the booster pump. At 1227 the pressure was 6×10^{-4} torr and the chevron was filled. By 1320 the diffusion pumps were pumping and the pressure was 3×10^{-6} torr. The pressure remained below this until shutdown at 2126.

At 1400 the end lamp rings were turned on. By 1622 the repairs to the center controller were complete and it was turned on. The coldwall was filled.

The second half of the first uniform temperature cycle (UTC) was completed. The second UTC and the first half of the third UTC were also run.

16 December 1974, Monday

At the start of the shift the chamber pressure was 4 torr and the specimen average temperature was +29°F.

At 0710 the roughing pumps were started. The LN₂ traps were filled and at 0815 the pressure was 350μ. Pumping was switched to the booster pump and by 0817 the pressure was 80μ. The chevron was filled at that time. By 1041 the diffusion pumps were pumping and the coldwall was filled. The pressure was 4×10^{-7} torr and remained below 5×10^{-7} torr until shutdown at 2129.

The third uniform temperature cycle was completed, as were the fourth through ninth. The first half of the tenth UTC was run.

17 December 1974, Tuesday

At the start of the shift the chamber pressure was 300μ and the specimen average temperature was -4°F.

The roughing pumps were started at 0715. At 0800 the pressure was 125μ. The pumping was switched to the booster pump and the chevron was filled. At 0922 the diffusion pumps were pumping and the coldwall was full. The pressure was 2.8×10^{-6} torr. By 1001 the pressure was 3.8×10^{-7} torr and remained below 6.2×10^{-7} torr until shutdown at 2031.

The tenth UTC was completed. The 11th through 17th UTC were run. During the second half of the 18th UTC the vacuum jacket on the LN₂ dewar ruptured. As the dewar could no longer be pressurized, LN₂ circulation through the chevron and coldwall could not be maintained. Shutdown was started immediately.

18 December 1974, Wednesday

At the start of the shift the chamber pressure was 400μ and the specimen average temperature was +46°F.

At 0754 the roughing pumps were started. The LN₂ dewar was bypassed by plumbing an LN₂ trailer into the system. The LN₂ had to be run into the chevron and coldwall at 15 to 20 minute intervals using ullage pressure as the LN₂ pump could not be used.

At 1522 the pressure was 200μ. The pumping was switched to the booster pump and the chevron was filled. By 1627 the diffusion pumps were pumping and the coldwall was full. The pressure was 5.3×10^{-7} torr and remained below 5.4×10^{-7} torr until shutdown at 2125. Half of the nineteenth UTC was run.

19 December 1974, Thursday

At the start of the shift the chamber pressure was 250μ and the specimen average temperature was $+26^{\circ}\text{F}$.

At 0705 the roughing pumps were started. The LN_2 traps were filled. At 0735 the pumping was switched to the booster pump. The pressure was 100μ . By 1010 the pressure was 7.8×10^{-4} torr and pumping was switched back to the roughing pumps. At 1240 the pressure was 100μ and pumping was switched to the booster pump and the chevron was filled. By 1327 the diffusion pumps were pumping and the pressure was 5.6×10^{-6} torr. The coldwall was filled and by 1429 the pressure was 4×10^{-7} torr. The pressure remained below 6.6×10^{-7} torr until shutdown at 2112.

The 19th UTC was completed and two forward shell temperature cycles were run.

20 December 1974, Friday

At the start of the shift the chamber pressure was 400μ and the specimen average temperature was $+7^{\circ}\text{F}$.

At 0710 the roughing pumps were started. The LN_2 traps were filled. At 1740 the pressure was 175μ and pumping was switched to the booster pump. The chevron was filled. At 0908 the pressure was 2.2×10^{-6} torr, the diffusion pumps were pumping, and the coldwall was filled. By 1019 the pressure was 4×10^{-7} torr and was kept below 6.2×10^{-7} torr until shutdown at 1941. Following shutdown, the chamber was backfilled with dry GN_2 and left for the Christmas holiday.

Four aft shell temperature cycles and two mid-shell temperature cycles were run prior to shutdown.

30 December 1974, Monday

At the start of the shift the chamber pressure was atmospheric (with GN_2) and the specimen average temperature was 48°F .

The roughing pumps were started at 0933. The LN_2 traps were filled and by 1039 the pressure was 200μ . The pumping was switched to the booster pump and at 1052 the pressure was 26μ . The chevron was filled. At 1131 the coldwall was filled. By 1137 the diffusion pumps were pumping and the pressure was 8.6×10^{-6} torr. At 1415 the pressure was 4.4×10^{-7} torr and was kept below this level until shutdown at 1517.

One-half of a UTC was run. This concluded the thermal vacuum testing of the GEMS.

5.3.4 TEST RESULTS. The GEMS was tested under four thermal loading conditions as listed in Figure 5.3.4-1. Heat was supplied by a concentric lamp bank surrounding the structure and the vacuum chamber cold wall, at -320F, provided a radiative heat sink for cooling. The temperatures were uniform in the circumferential direction for all test conditions. Thermal cycling was between the temperatures of -28.9C (-20F) and -73.3C (-100F) (nominal) and in those tests in which only a portion of the structure was cycled; the remaining portions were held at (-28.9C) -20F. The temperatures attained on the secondary mirror support, particularly on the hub assembly were lower than the shell temperatures due to the greater distance to the lamps. The aft spider temperature changed very little during each testing period of about 10 hours, due to the multilayer insulation around it.

In the uniform temperature cycles the entire shell was cycled between (-20F) and -73.3C (-100F). The aft spider temperature was nearly constant at 51.1C (-60F) with a slight downward trend during each test day. The secondary mirror support hub cycled between about -62.2C (-80F) and -73.3C (-100F).

In the forward shell cycles, the forward ring saw the full temperature range of (-20F) to (-100F) while the aft mid shell and aft flange were held at a constant -28.9 (-20F).

The aft shell cycles were just the reverse of the forward shell cycles with the forward ring held at a constant -28.9C (-20F) while the aft flange was cycled between -28.9C (-20F) and -73.3C (-100F).

In the midshell cycles the forward ring and aft flange were held at -28.9C (-20F) while the center of the shell was cycled between -28.9C (-20F) and 65.5C (-85F). The center would get no colder than this with the ends held at -28.9C (-20F).

In the following paragraphs typical data are presented for each type of thermal cycle and the results are discussed. In each case the data consists of one change in overall length of the GEMS and the associated structural temperature changes plotted as a function of elapsed time. The temperature data consists of a plot of the shell average temperature and also plots of the average temperatures for various parts of the structure, such as the forward and aft shell rings, secondary support hub, etc. Table 5.3.4-1 identifies the groups of thermocouples, each of has been averaged for this purpose.

Also shown in all of the data plots is the times at which power was changed to the lamp banks. "OFF" indicates power off to start a cooling half cycle and "INC" indicates increased power to initiate a heating half cycle.

5.3.4.1 Uniform Temperature Cycles. The GEMS was cycled a total of 20 times with the shell temperature varied between -28.9C (-20F) and -73.3C (-100F). This thermal testing provides the basis for evaluating the overall stability performance of the structure. The design criterion for this condition was adopted, for consistency,

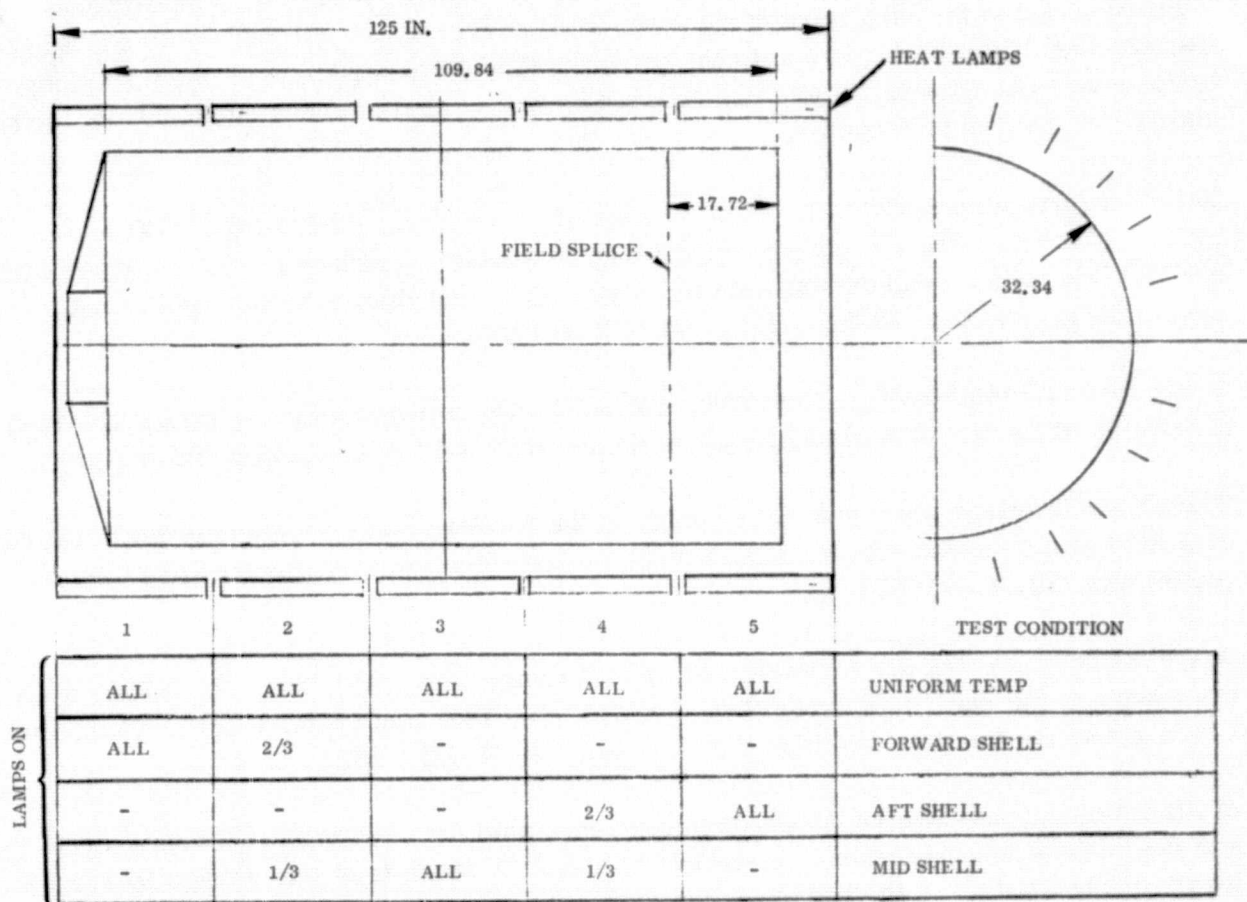


Figure 5.3.4-1. GEMS Test Conditions

ORIGINAL PAGE IS
OF POOR QUALITY

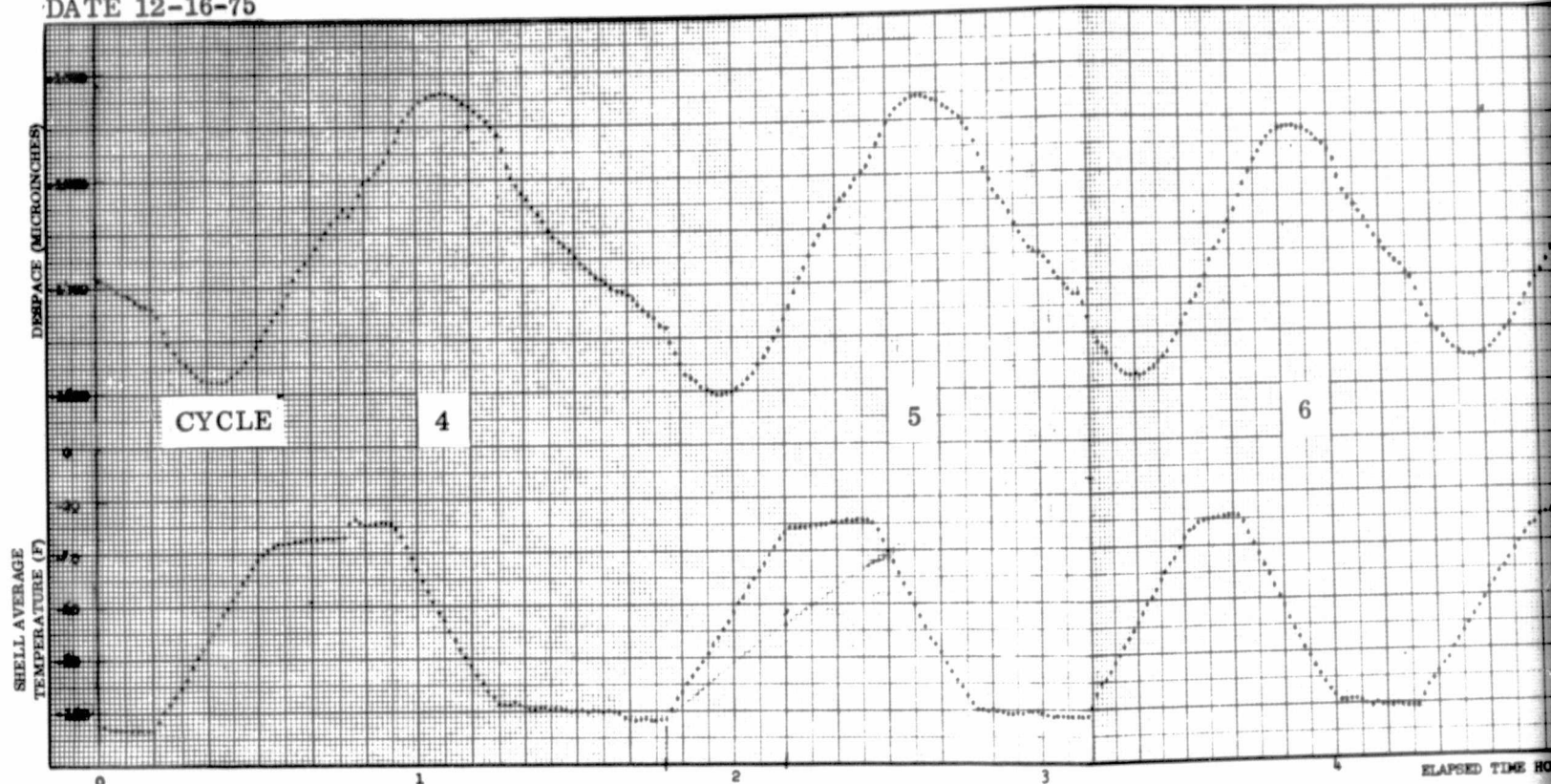
Table 5.3.4.-1. Thermocouple Groups - Thermocouple
Locations by Number are shown in Figure 5.3.2-1.

<u>Thermocouples</u>	<u>Substructures</u>
17-42	Shell Average
17-24	Forward Ring
25-30	Fwd. Mid Shell
31-36	Aft Mid Shell
37-42	Aft Ring
1-8	Secondary Hub
9, 12-15	Hub Legs
49, 50	Aft Mirror Support

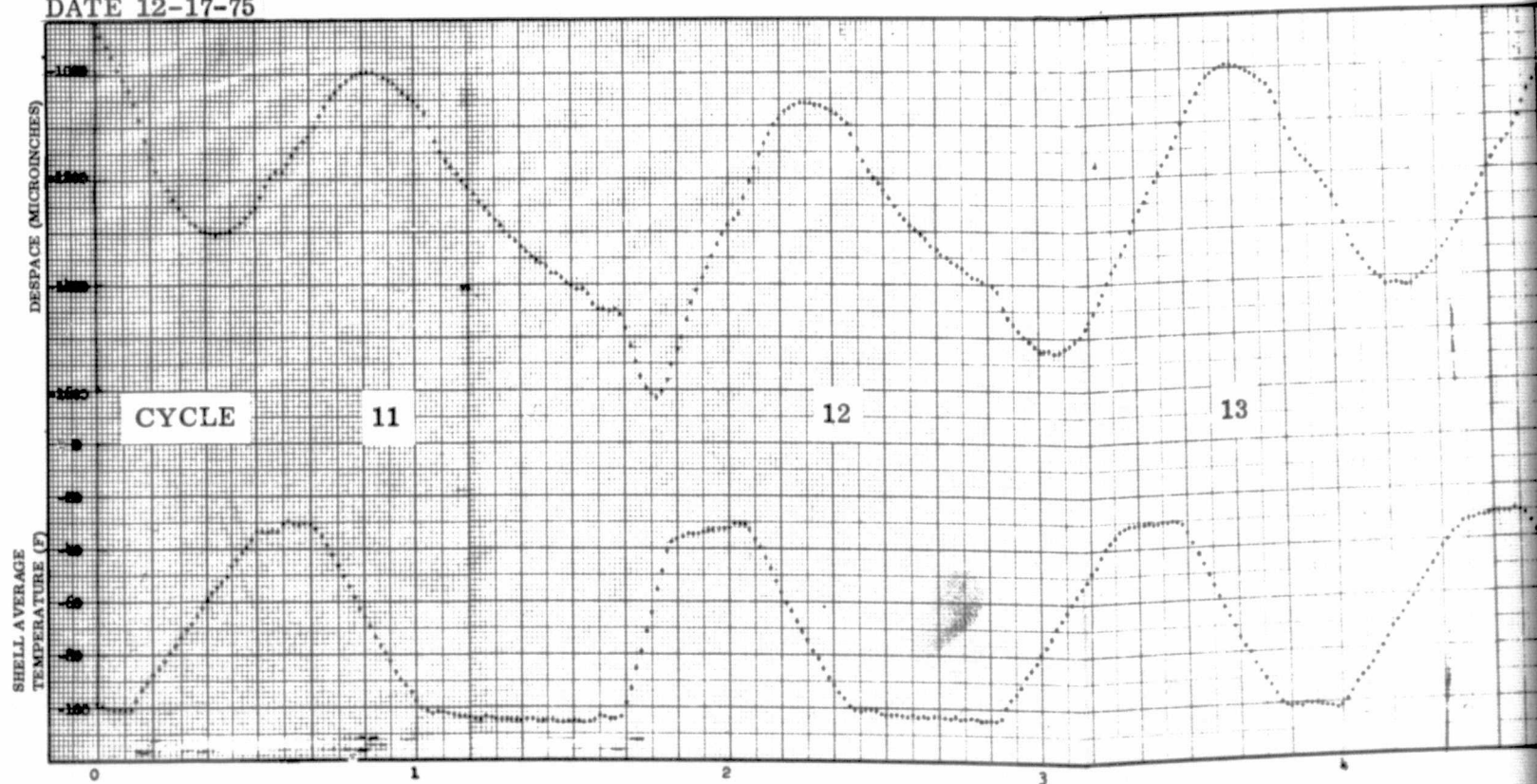
from RFQ 8-3-50-32713-RDD, Design, Fabrication, and Test of a Graphite Epoxy Metering Truss Structure. The requirements there-in were adopted because they represent the most stringent design goals we were aware of for the full scale LST. The full scale LST despace requirement from this document is ± 2 micrometers (± 80 microinches) for a 5.55 C (10F) uniform temperature change. The GOAL adopted for the half scale GEMS was therefore ± 1.0 Micrometers ± 40 microinches for a 5.55C (10F) temperature change.

In Figures 5.3.4-2 and 5.3.4-3 we present the despace data and the average shell temperatures for the uniform temperatures cycles 4 through 17. The shell responded very quickly to the changing temperatures of the lamp bank. The despace changes were very consistent with respect to the magnitude of the despace change and shape of the despace curve in relationship to the thermal cycles. The despace cycles lag the thermal cycles by about 14 minutes under these test conditions. There is a definite inflection point in the despace curve each time the temperature is increased from (-100F). The same effect is apparent during the initial part of the cooling half cycles to a lesser extent. In Figures 5.3.4-4 and 5.3.4-5 the complete data for groups of thermocouples is plotted for the 12th and 13th thermal cycles. From these figures it is evident that all of the thermocouples responded in unison except for the aft spider which was well insulated and changed temperature very little over the interval of a thermal cycle. Since all parts of the structure to which thermocouples were attached responded in phase with the shell temperature, the lag in the thermal expansion must therefore be attributed to the thermal response of structural elements for which the temperatures were not measured. These are probably elements which have a substantial heat capacity in comparison with the thin shell skin, or elements which, like the inner cylinder of the secondary mirror support hub, were in the shadow of the lamps and partially shielded from a direct view of the cold wall. An additional indication that this type of phenomenon is involved is the net positive CTE

DATE 12-16-75



DATE 12-17-75



FOLDOUT FRAME

5-60

ORIGINAL PAGE IS
OF POOR QUALITY

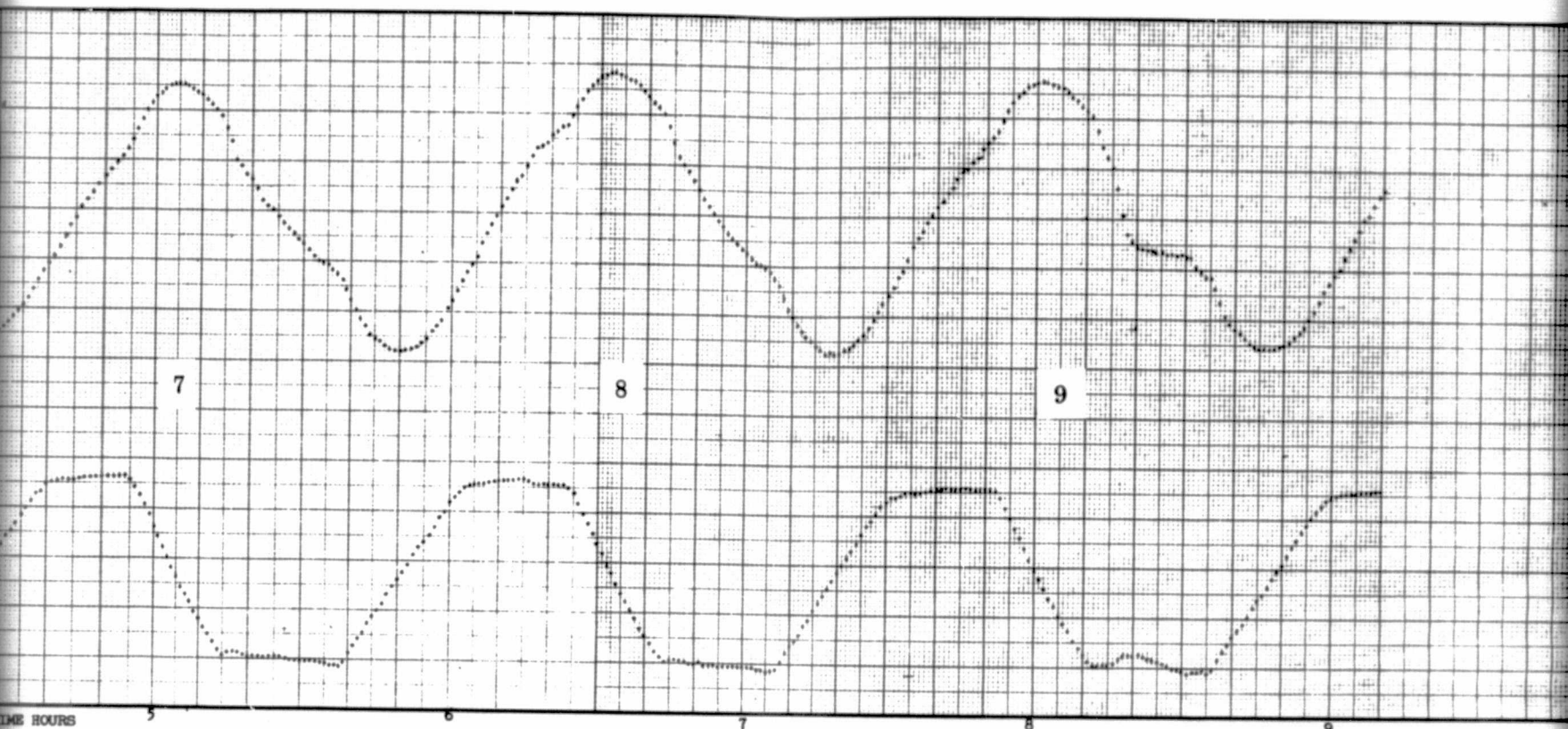


Figure 5.3.4-2. GEMS Uniform Temperature Cycle

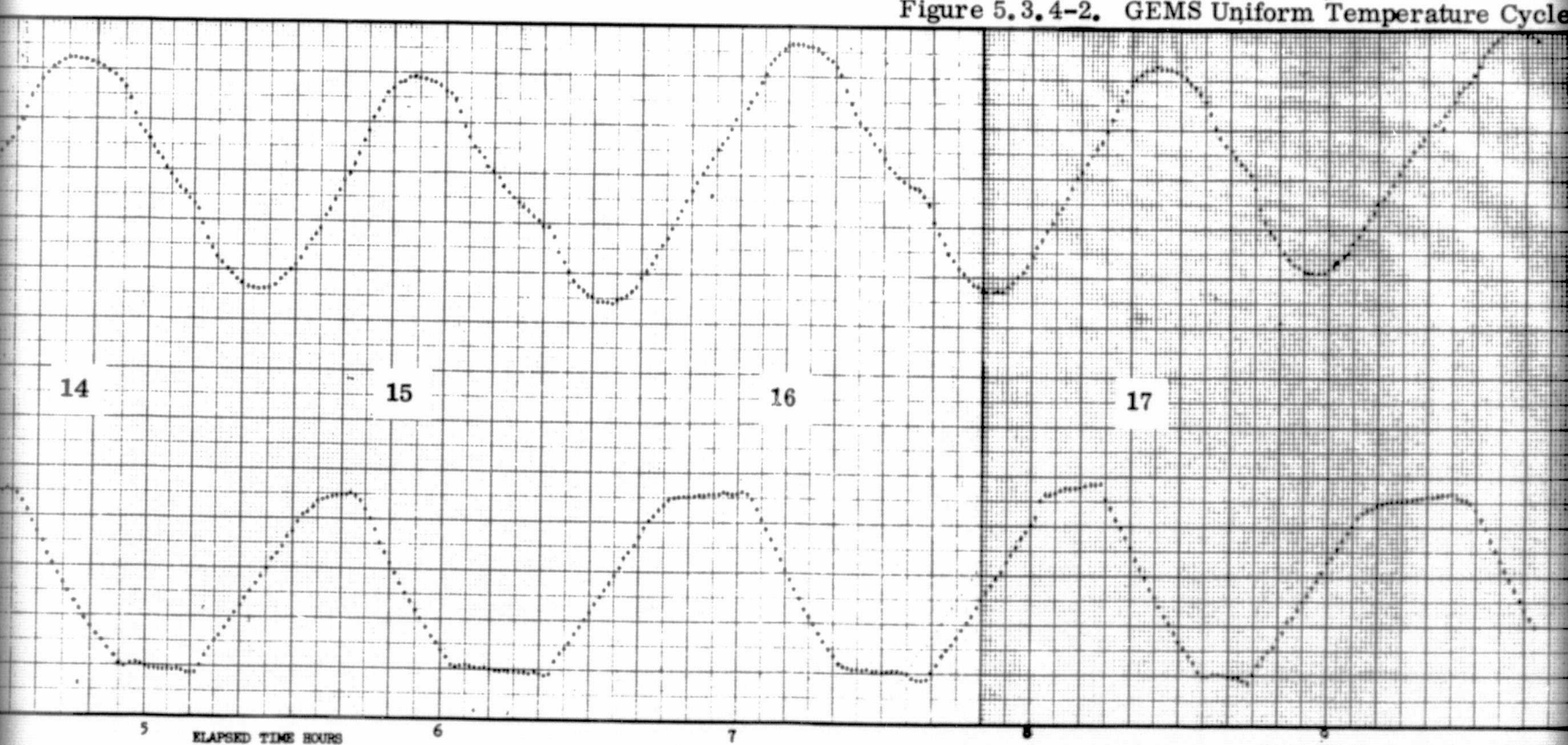


Figure 5.3.4-3. GEMS

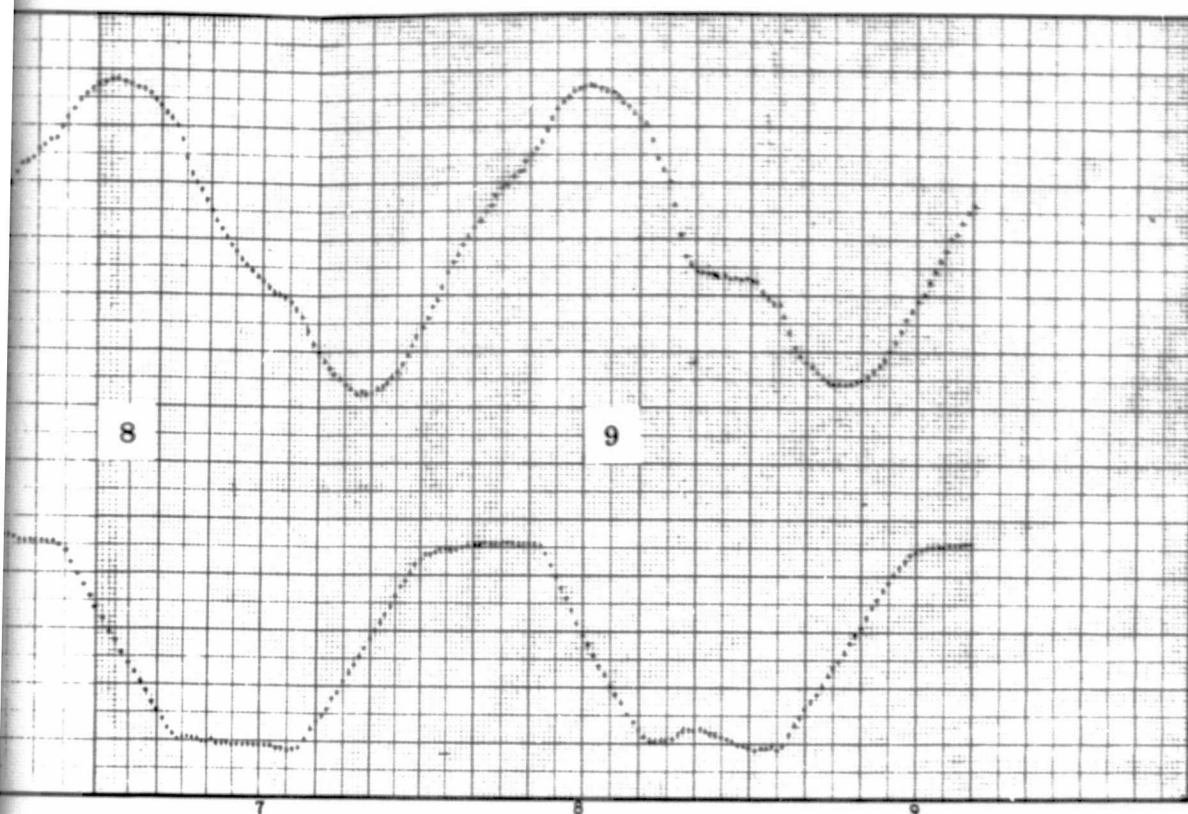


Figure 5.3.4-2. GEMS Uniform Temperature Cycles

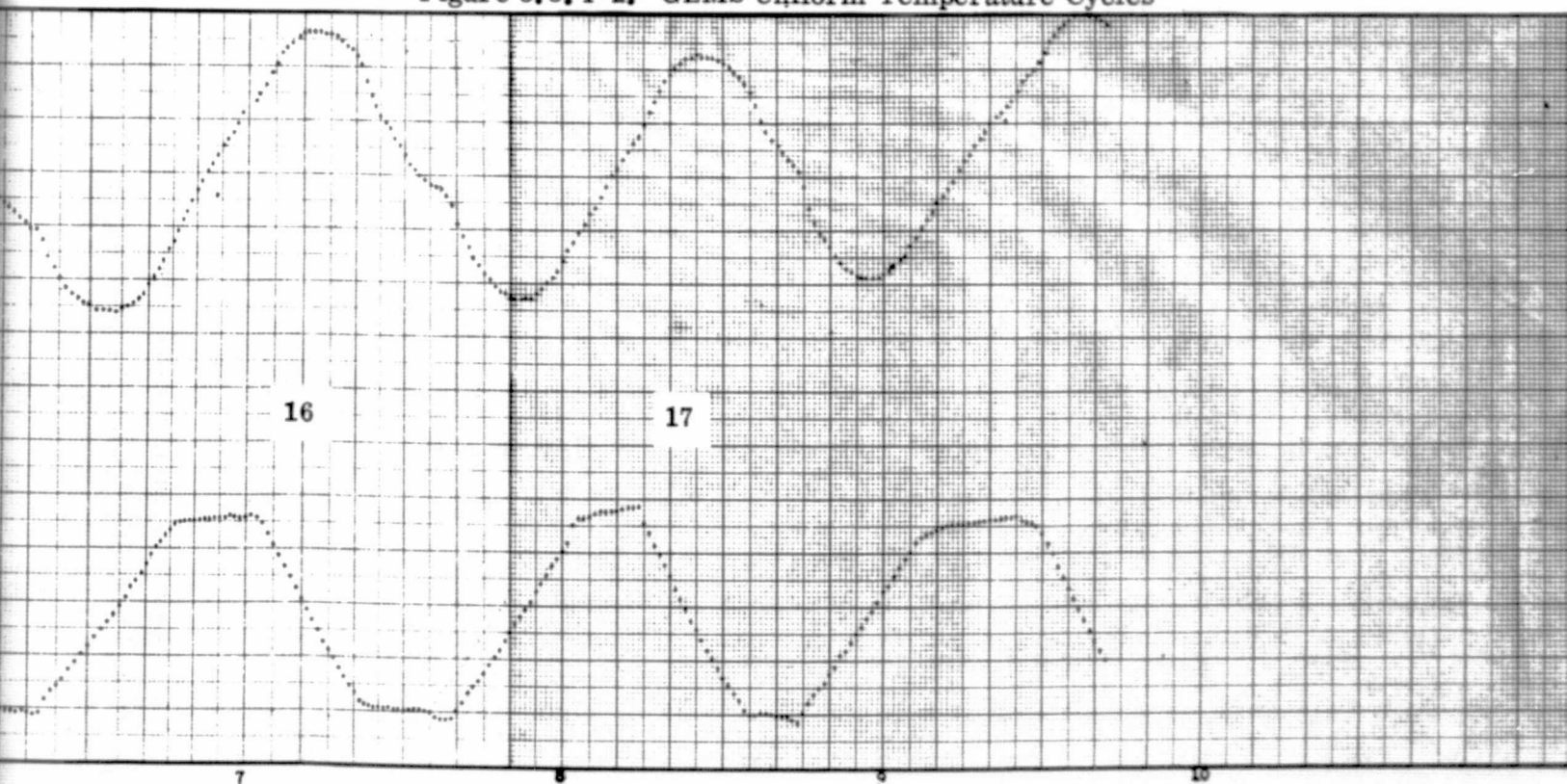


Figure 5.3.4-3. GEMS Uniform Temperature Cycles

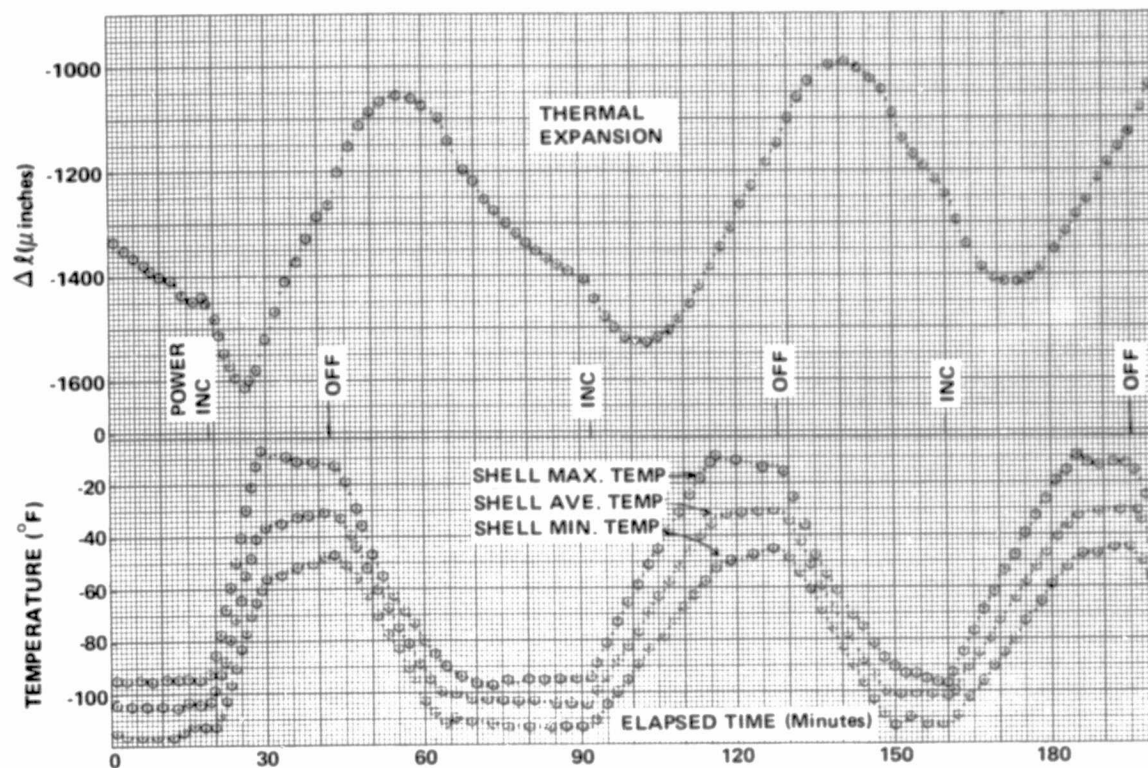


Figure 5.3.4-4. Uniform Temperature Cycles

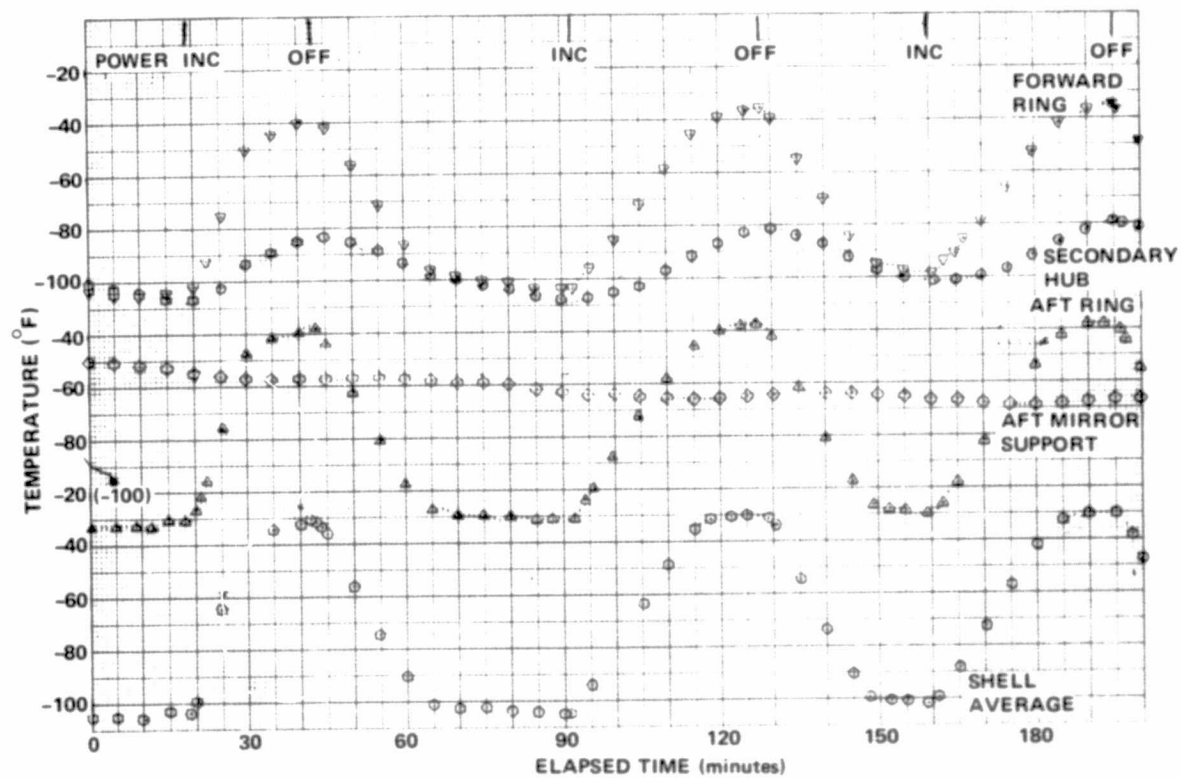


Figure 5.3.4-5. Uniform Temperature Cycles

measured in these thermal cycles. The shell skin is expected, on the basis of coupon tests, to have a negative CTE that would result in a negative despace of about 40 microinches per 5.55C (10F) temperature change. The graphical data presented in this section indicates that the despace is positive, and in the 17th cycle has a magnitude of 59 microinches per 5.55C (10F) temperature change.

There was, in addition, a definite trend for the despace change to get smaller as the thermal cycling progressed. This trend is evident in Table 5.3.4-2 where the despace change is given for each of the thermal cycles.

Table 5.3.4-2. Despace, Uniform Temperature Cycles.

Thermal Cycle	Despace	
	$\mu\text{in}/10\text{F}$	$\mu\text{m}/5.5\text{C}$
4	74	1.88
5	72	1.83
6	60	1.52
7	68	1.73
8		
9	73	1.85
10	72	1.83
11	69	1.75
12	71	1.80
13	65	1.65
14	61	1.55
15	60	1.52
16	67	1.70
17	60	1.52

This characteristic lowering of the CTE with repeated thermal cycling had previously been seen during coupon tests. It appears that the thermal cycling induces localized stress relieving within the graphite epoxy which results in a lowering of the CTE. The effect is complete in one or two cycles at -320F and takes place at a slower rate at higher temperatures. It has not been positively observed at temperatures above -59.4C (-75F). The lower temperature of -73.3 (-100F) in the GEMS tests seems to take a large number of cycles and even though there has been an appreciable improvement in the thermal performance after 17 cycles, the process still does not seem to be complete and quite possibly the despace change would be reduced further with additional thermal cycles.

5.3.4.2 Forward Shell Cycles. The GEMS was subjected to two thermal cycles in which, as is shown in Figure 5.3.4-1; the forward part of the shell and the secondary mirror support was cycled while the remainder of the structure was held at 28.9C (-20F). The forward ring (thermocouples 17-24 in Figure 5.3.2-1) actually was the portion of the shell which saw the full temperature range while the secondary hub and the forward midshell were subjected to a smaller temperature range. The remainder of the structure was held at a constant 28.9C (-20F). The data for a representative portion of these cycles is shown in Figures 5.3.4-6 and 5.3.4-7. The despace curve closely resembles the uniform temperature cycle despace curve - there is a lag in the despace curve with respect to the thermal curves and the inflection points in the despace data at high heating and cooling rates are even more pronounced. It again would appear that some portion of the secondary mirror support, where thermocouples were not located, was still changing temperature when all of the thermocouples indicated thermal equilibrium.

The thermal changes of the forward ring, secondary hub, and forward midshell are listed in Table 5.3.4-3 with the maximum despace changes for each half thermal cycle.

Table 5.3.4-3. Forward Shell Cycle Deltas

ΔT (F)			Δ Despace (μ in)
Forward Ring	Forward Midshell	Secondary Hub	
76	52	42	620
-73	-50	-38	-642
73	48	36	580

5.3.4.3 Midshell Cycles. In the midshell cycles the two mirror support spiders and the shell end rings were held at -28.9C (-20F) and the center of the shell was cycled between -28.9C (-20F) and -59.4C (-75F). The center of the shell would go no lower than -59.4C (-75F,) with all heat input in this area reduced to zero, due to the thermal conductivity and heat input into the forward and aft ends of the shell. The temperatures at the aft and forward midshell locations when these conditions were between -28.9C (-20F) and -42.7C (-45F). The thermocouple and despace data is presented in Figures 5.3.4-8 and 5.3.4-9. Not shown is the temperature at the shell midpoint. The only thermocouple at this location was one used to control the lamp bank in this area and the temperature was measured only at the ends of each half cycle to check the performance of the controller. The temperature at this location was -28.9C (-20F) at the end of each half "hot" cycle and -59.4C (-75F) at the end of each half "cold" cycle.

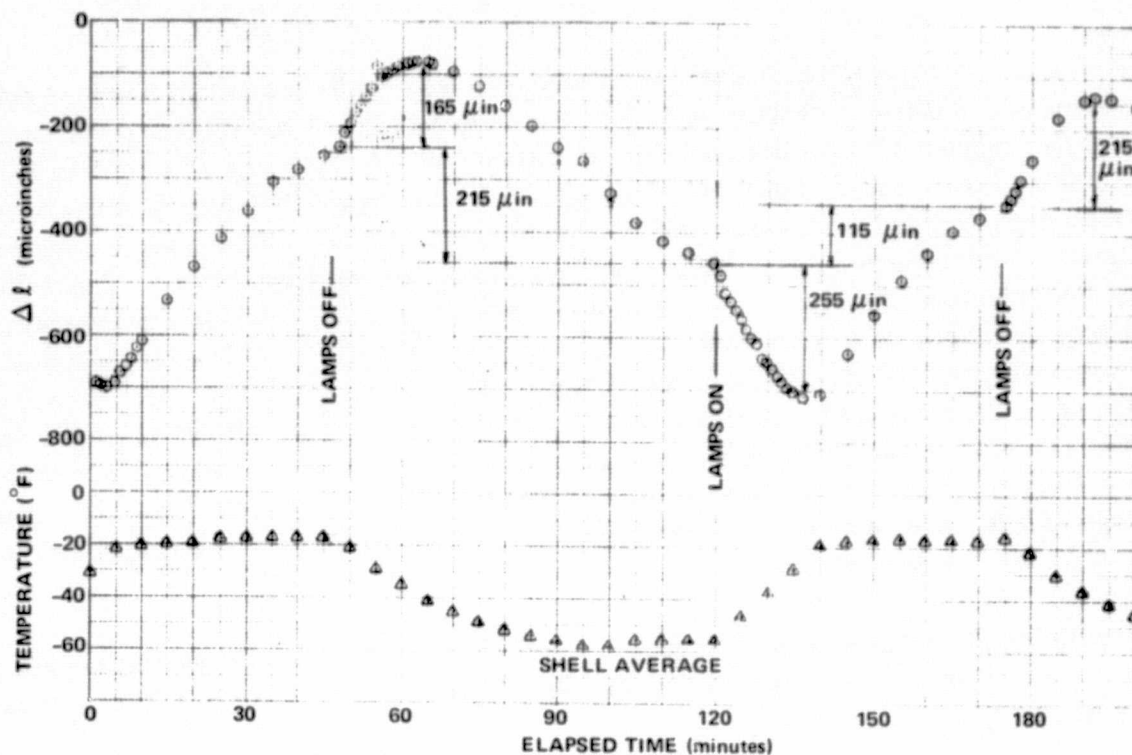


Figure 5.3.4-6. Forward Shell Cycles

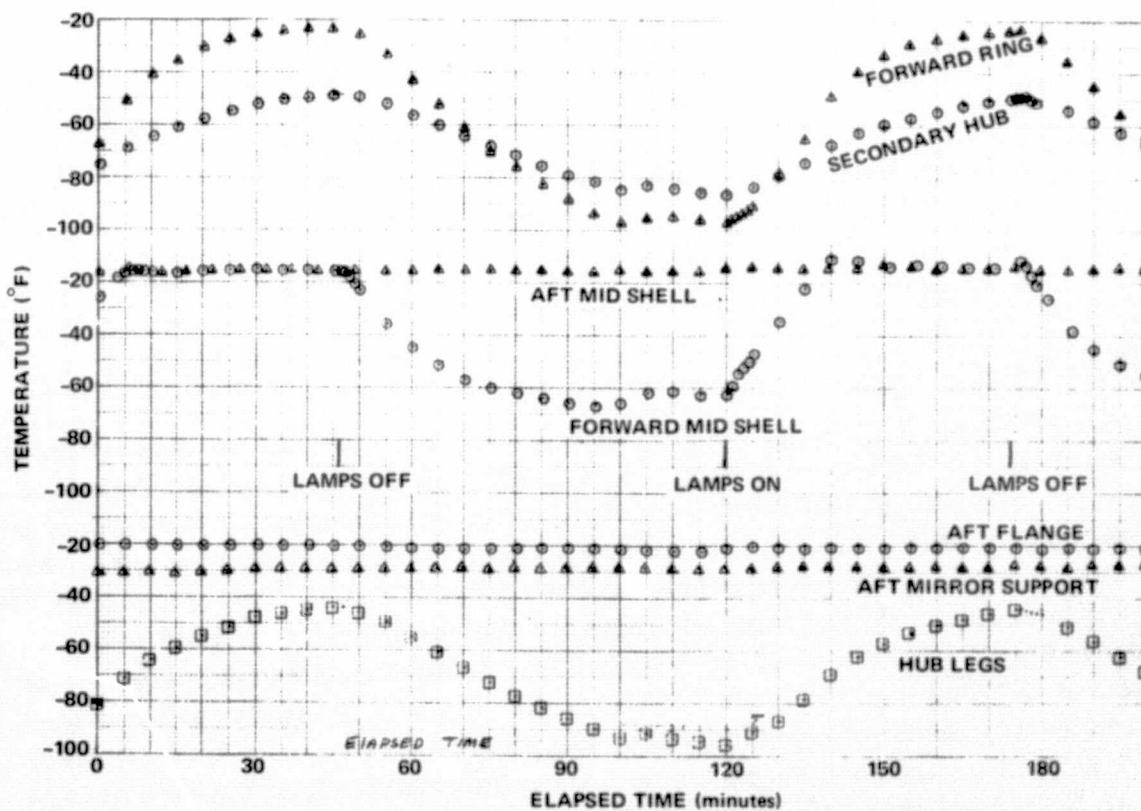


Figure 5.3.4-7. Forward Shell Cycles

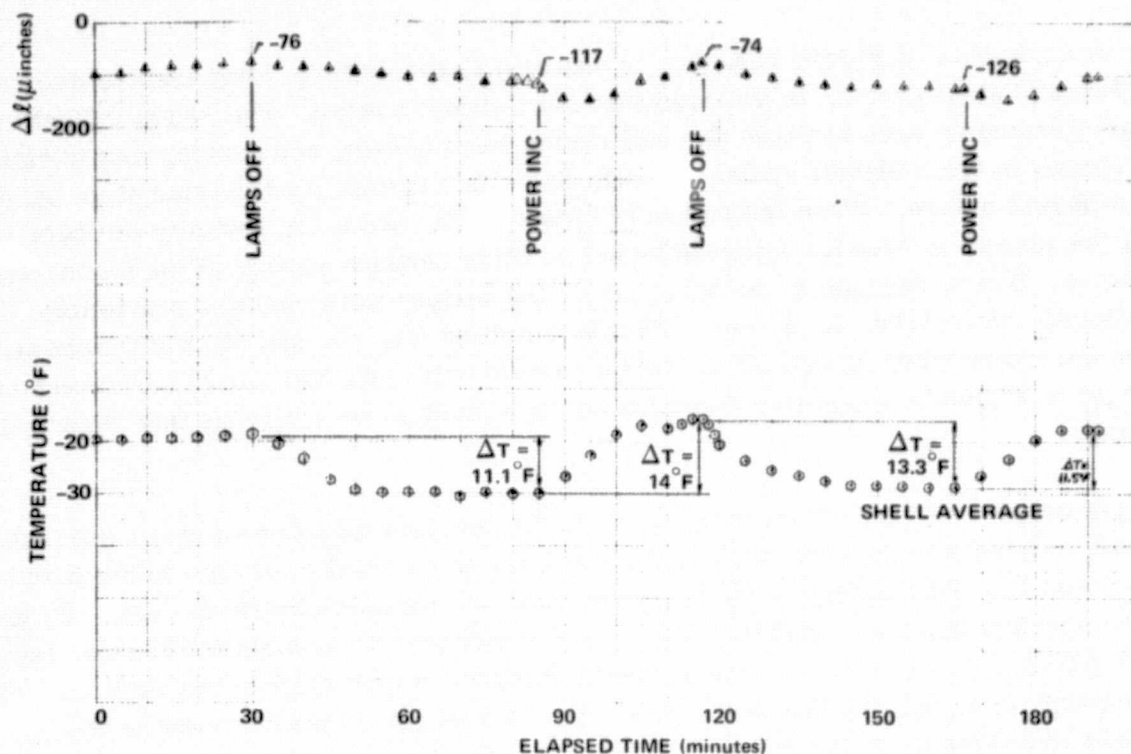


Figure 5.3.4-8. Midshell Cycles

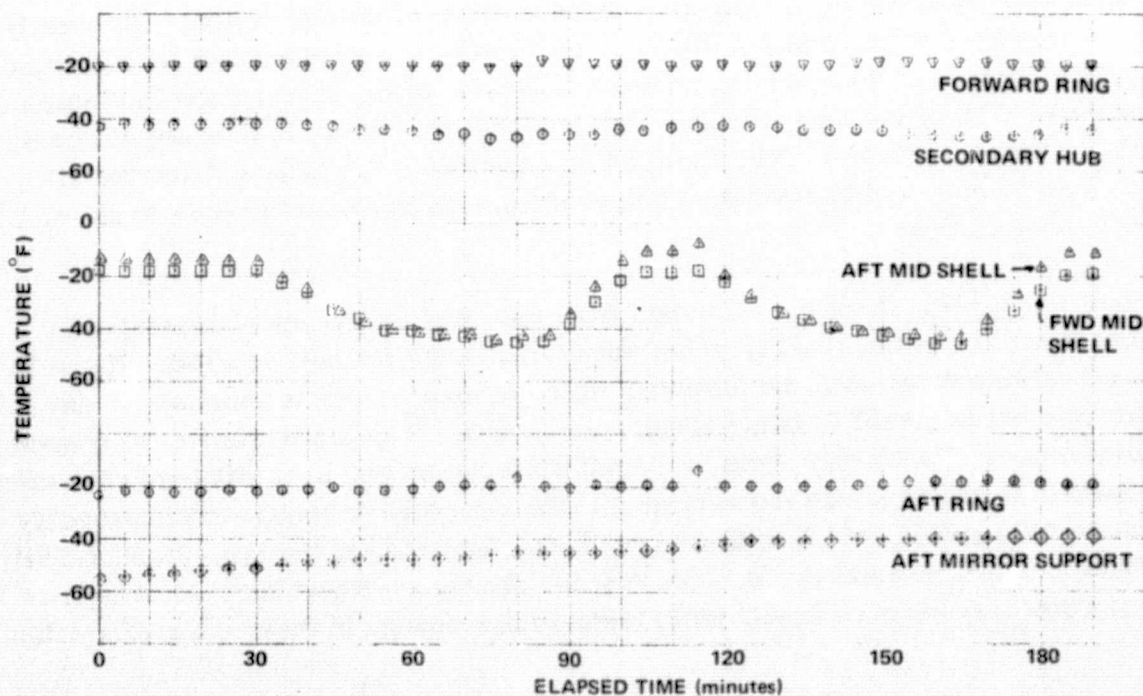


Figure 5.3.4-9. Midshell Cycles

The despace data of Figure 5.3.4-8, in contrast to the uniform temperature cycles and the forward shell cycles, is in phase with the thermal cycles. The sharp inflection points previously seen in these thermal cycles when heating and cooling was initiated are absent in the midshell cycles although there is a transitory behavior of an apparent different nature. When the power is turned on the structure initially exhibits a negative change in despace followed by net positive despace change at the higher temperature. These changes in despace, under the temperature changes previously mentioned, were 1.04, 1.09, and 1.32 micrometers (41, 43, and 52 microinches). When the lamps were turned off to start a cooling half cycle the initial movement in despace was also in a negative direction but at a much slower rate as that seen upon cooling.

The net response of the structure appears to be the superposition of three separate effects. These are: (a) distortion of the shell due to thermal gradients in the thickness direction, (b) the negative CTE of the shell and its quick thermal response, and (c) the positive thermal expansion of the field splice and its associated thermal lag due to greater mass. The distortion due to transverse gradients in the shell will always result in a negative despace change since the despace measurement is the straight line distance along the shell which has been warped into a non-cylindrical surface. The initial dimensional change upon the application of heating or cooling is dominated by this distortion and the negative CTE of the shell, therefore upon heating these two effects are in the same direction resulting in a more pronounced negative change in despace. Upon cooling, the negative CTE of the shell is in the positive direction thereby reducing the negative despace effect of the distortion. Ultimately, the system comes to thermal equilibrium, the transverse gradient and its accompanying distortion were gone and the positive expansion of the field splice dominates the negative CTE of the shell resulting in a net positive change in despace of about 0.89 mincrometers/5.55C. The field splice 44.45CM (17.5 inches) from the aft ring, could be expected to have seen a temperature change of from -20F to about -32F in these cycles.

5.3.4.4 Aft Shell Cycles. The data from the aft shell cycles is presented in Figures 5.3.4-10 and 5.3.4-11. Here we see that when the heat is applied there is about a 5 minute delay until the minimum of the despace curve is reached. Upon cooling this lag is smaller, being about 3-4 minutes. This lag is similar to response at the beginning of each half cycle in the midshell cycles and is attributed to the effects discussed in connection with those results. The net positive coefficient is probably due to the field splice, which in these cycles was subjected to the full -28.9C (-20F) to -73.3C (-100F) thermal cycle. The despace change averaged 1.14 micrometers (45 microinches) for each 5.55C (10F) temperature change in these aft shell cycles.

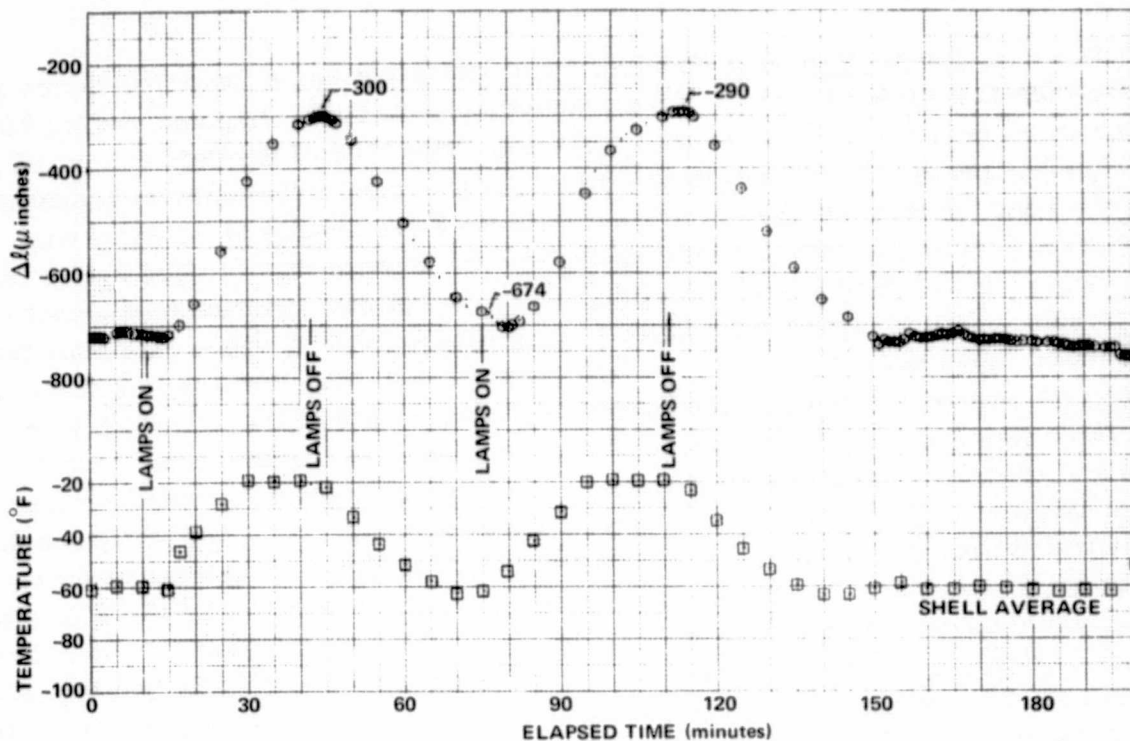


Figure 5.3.4-10. Aft Shell Cycles

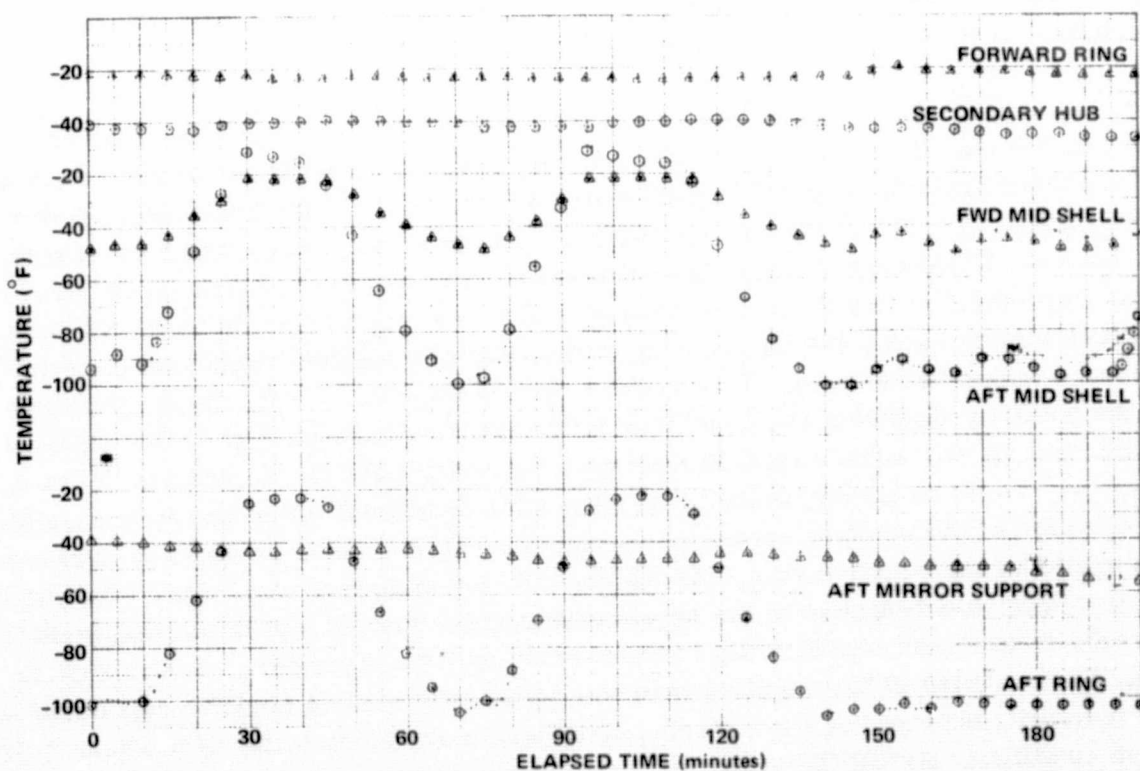


Figure 5.3.4-11. Aft Shell Cycles

5.3.4.5 Summary of Test Results. The interpretation of the midshell and aft shell thermal cycles in terms of the gradients (due to the heating and cooling rates), the known negative CTE of the shell and the positive CTE of the field splice and possibly other parts of the structure now allows us to return to the uniform temperature cycles and the forward shell cycles and examine those results in the same way. The despace data for the forward shell cycles and the uniform temperature cycles both indicate that complete thermal equilibrium was not attained at each temperature extreme. This is indicated by the continuing change in the despace data after the thermocouples had leveled out at a fixed temperature. The time lag is attributed to the high heating and cooling rates at the beginning of each half cycle which introduces a transitory dimensional change which is a function of the heating rate. The effect is not completely understood, however, the following observations can be made from the uniform temperature cycles. From Figures 5.3.4-2, -3 -4 and -5 we see that the transitory dimensional change is more sharply peaked for the higher heating rates. The effect, upon heating, results in a despace change of from (-3.18 to -4.45 micrometers) (-125 to -175 microinches) and (3.18 to 5.08 micrometers) (125 to 200 microinches) during cooling. This same transitory behavior is even more apparent in the forward shell cycles, Figures 5.3.4-6 and 5.3.4-7. The heating and cooling rates in these cycles are lower than those in the uniform temperature cycles, particularly at the forward ring. This may indicate that the principal source of this effect is in the region of the secondary mirror support structure/forward ring and in the uniform temperature cycles some compensation or reduction of the effect is made by the positive coefficient of the field splice/aft ring.

The rates of temperature change during these tests were much greater than are expected during the LST mission (Reference 1 and 2). From these studies the expected maximum rate of change of temperature in the shell will be 0.43C (0.77F) per hour, which is 1/200 of the test heating and cooling rates. The transitory effects seen in the test, which depend upon the heating rate, are therefore, much more pronounced than they would be in a flight environment. Due to conductivity effects at the lower radiant heating rates, the thermal lag of the heavier, positive expansion elements would probably be reduced. This would have two effects. First, the temperature of the positive expansion elements may more closely approach that of the negative shell, and, if so, would result in a relatively greater positive expansion. This however, would be accompanied by an extremely beneficial effect due to the temperature cycles of the positive expansion elements being in phase, or close to in phase with the cycles of the negative skin. As Figure 5.3.4-6 clearly shows, due to the out-of-phase effect, the response of the negative skin after "lamps off" in the test condition, actually contributes significantly to the overall positive expansion. In contrast to this, the response of the negative skin will reduce the overall positive expansion if the thermal responses of the metering components are close to being in phase in the flight condition. As will be shown in the following section, this conclusion regarding

the thermal lag of the more massive sections is supported by a thermal analysis of a ring section subjected to a heat flux of the same magnitude as the test heat flux.

A comment is also in order regarding the moisture desorption and the uniform temperature cycles for which data is not presented in this report (UTC's 1-2 1/2 and 17 1/2-20). The data from the moisture desorption and the first two and one-half uniform temperature cycles is fragmentary and of questionable value due to the chamber being opened several times for the correction of problems at the beginning of the test. (See the test history for 25 November to 13 December.) The last two and one-half cycles were interrupted by the failure of the LN₂ cold wall system on 17 December and are not presented for the same reason. The remaining thermal cycles for which data is presented were obtained without interruption or loss of laser signal.

REFERENCES

1. Structures and Materials for LST, General Dynamics Convair Report LST-72T-056, J. D. Forest, et al, December 1972.
2. Thermal Analysis of Secondary Mirror Spider, Extended Sun Shield and Light Baffle, General Dynamics Convair Report LST-73T-096, R. L. Pleasant, September 1973.

5.3.5 STRUCTURAL ANALYSIS. The GEMS was analyzed, using finite element computer programs, to predict the thermal response of the structure. The initial analysis was performed prior to the thermal vacuum testing of the structure. The results of this analysis were in fair agreement with the experimental results. Subsequent to the tests, more detailed analysis was made of the various substructures (splices, rings, etc.) to improve the correlation of the analytic and experimental results thereby yielding a more complete understanding of the structure.

5.3.5.1 Initial Analysis. The initial analysis used NASTRAN, a finite element program. The structure was modeled using bars and membranes with the aft ring rigidly constrained. The shell properties, expansion coefficients and modulus, were determined during the testing of tag ends from the shell panels. This data comprised the input for the shell model program. The elements of this model are shown in Figure 5.3.5-1 where the x direction is along the optical axis of the GEMS.

The second sub-structure of the analysis was the secondary support structure/forward ring combination. Laminate properties for this sub-structure were derived from lamination theory which provided the computer program input for this analysis. The forward ring was modeled as a single element, and the elements of the secondary mirror support structure are shown in Figure 5.3.5-2.

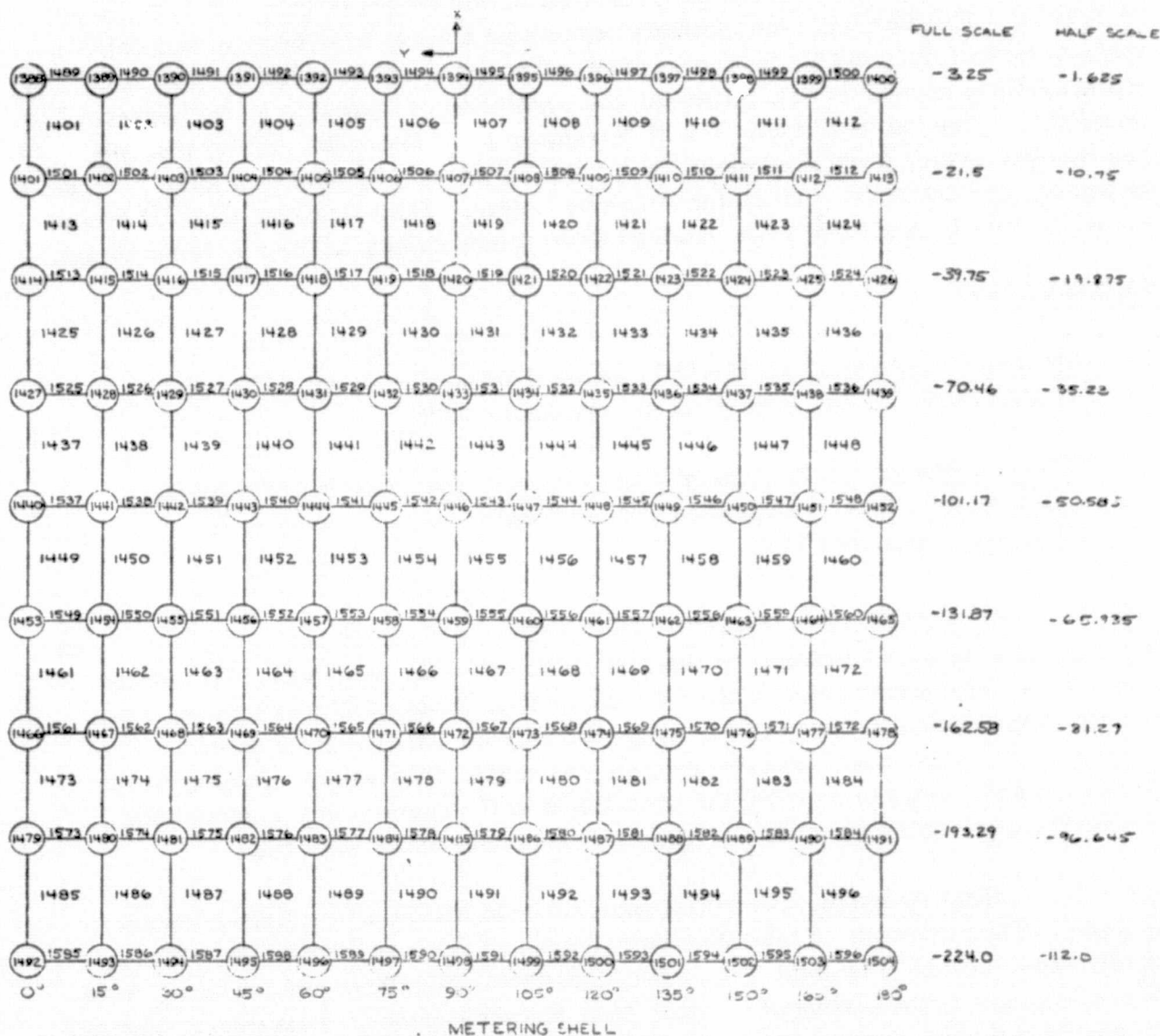


Figure 5.3.5-1. Shell Model Program Elements

ORIGINAL PAGE IS
OF POOR QUALITY

INPUT COORDINATE SYSTEM

Z

The resultant expansion of GEMS, based on this analysis, was predicted to be (0.60 micrometers) (+23.8 microinches) for a temperature increase of 5.55C (10F). This compares with 1.5 micrometers (59 microinches) per 5.55C (10F) measured in the uniform temperature tests. The program was rerun to determine the contribution of the secondary support structure/forward ring combination alone (as shown in Figure 5.3.5-2). The ring was given 3 longitudinal supports. The results indicated that this sub-structure contributed only 0.066 micrometers (2.62 microinches) despace for each 5.55C (10F) of temperature change.

Based on these results and the experimental measurements it was decided that more detailed analysis was needed. Rather than remodel the entire structure, it was more convenient and meaningful to develop finite element models for various sub-structures such as the shell splices, the front ring, front ring/secondary mirror support joint, the field splice and the aft mirror spider. These results are presented in the following paragraphs.

5.3.5.2 Front Ring/Secondary Mirror Support Joint. This joint is shown in Figure 5.3.5-3. The analysis took into account the high transverse CTE of the attachment between the spider legs and the shell. This coefficient is $+0.82 \mu\text{m/mC}$ ($+18 \mu \text{ in/in } ^\circ\text{F}$). The support legs have a coefficient of zero. The result of this transverse coefficient in the 5 mm (0.20) inches of the joints is a positive contribution to despace of 0.29 micrometers (11.55 microinches) per 5.55C (10F) change in temperature. This strong coupling of joint expansion to despace is much larger than was initially predicted for the entire forward ring/secondary support structure sub-structure.

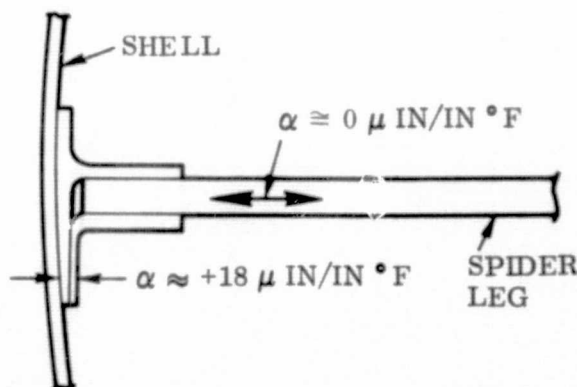


Figure 5.3.5-3. Front Ring/Secondary Mirror Support Joint

5.3.5.3 Forward Ring. The forward ring was analyzed separately to determine its overall contribution to the shell despace. The dimensions and finite elements of this ring are shown in Figure 5.3.5-4. The ring was modeled using SOLIDSAP, axi-symmetric elements and the appropriate properties of the shell and the ring sections. Included in this ring analysis was the effect of the 3 circumferential splices in the ring. The net contribution of the forward ring was predicted to be 0.134 micrometers (+ 5.28) microinches per 5.55C (10F) temperature change.

5.3.5.4 Intermediate Splice Substructures. The intermediate splices on the shell were modeled as shown in Figure 5.3.5-5 which shows half of the splice. This axi-symmetric SOLIDSAP model was constrained at the adhesive line between each half of the splice. The adhesive was also accounted for in the model. This model predicted a positive despace contribution of 0.031 micrometers (1.21 microinches) for each 5.55C (10F) increment in temperature.

5.3.5.5 Shell Substructure. The basic shell properties were experimentally determined and these results provided the input for shell substructure contribution. Since segments of the shell were included with each of the ring and flange models, to allow for the coupling of these components with the shell, the net shell length is shorter than the overall GEMS. Figure 5.3.5-6 shows the dimensions of the bare shell substructure segments. These shell segments yield a despace of -0.69 micrometers (-27.1 microinches) for each 5.55C (10F) temperature change.

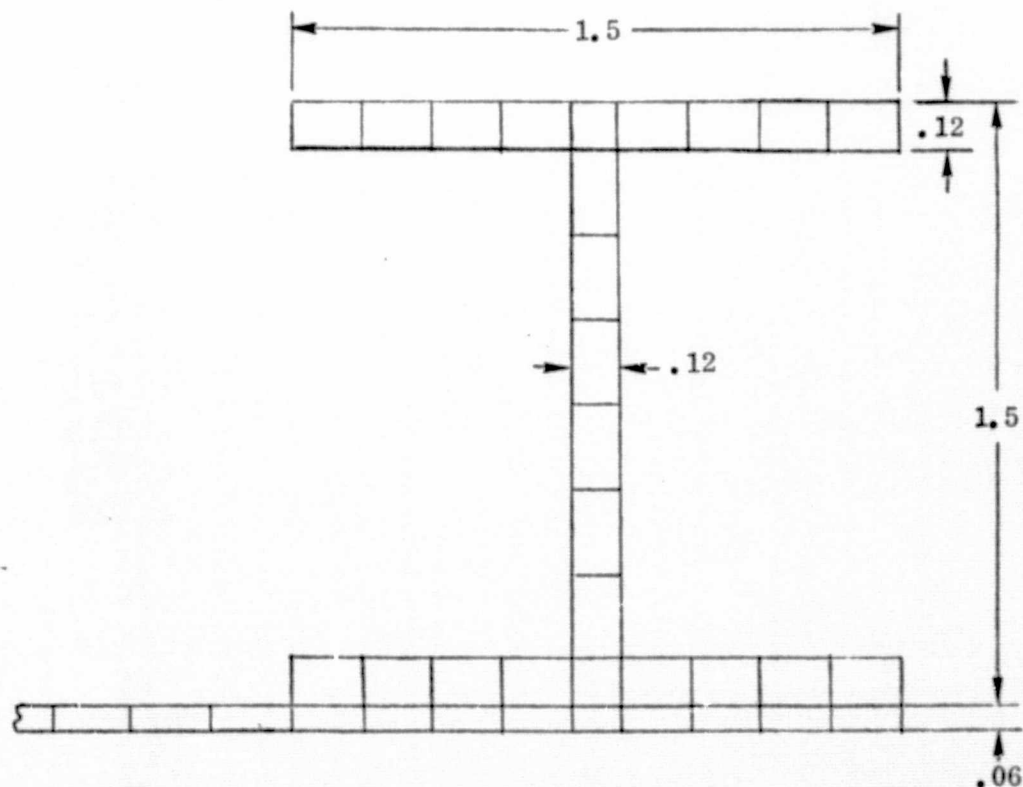


Figure 5.3.5-4. Forward Ring Model

ORIGINAL PAGE IS
OF POOR QUALITY

5-74

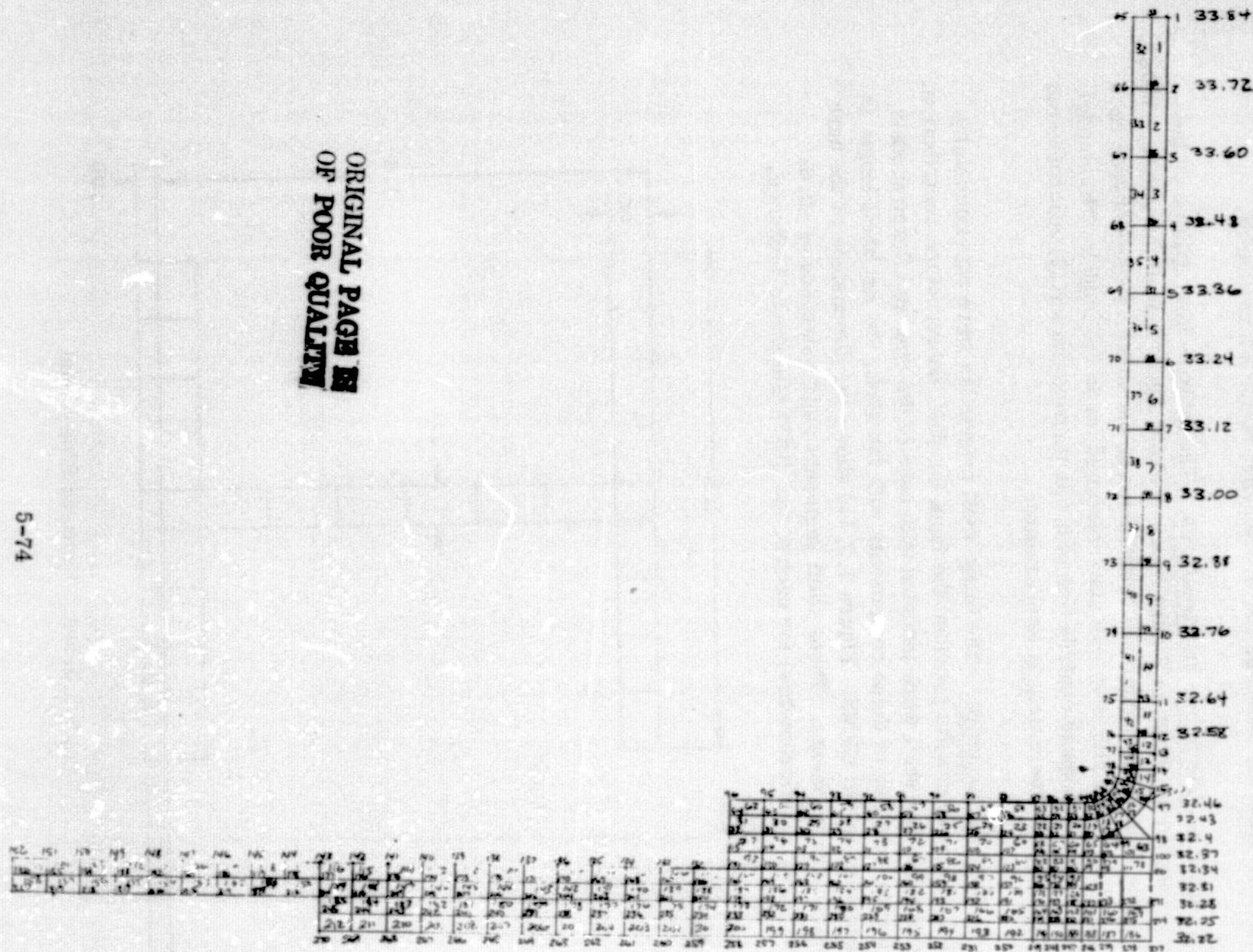


Figure 5.3.5-5. Intermediate Splice Model

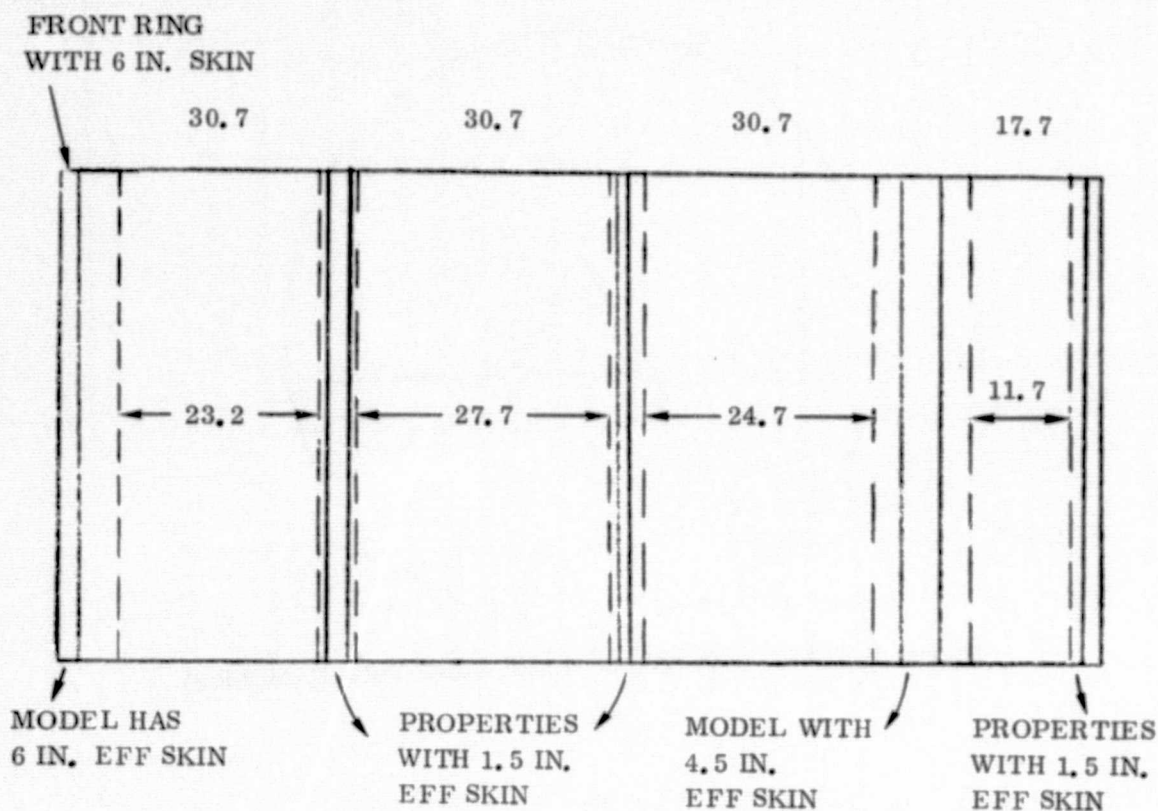


Figure 5.3.5-6. Shell Segments

5.3.5.6 Aft Mirror Support/Aft Ring Substructure. The aft mirror support and aft ring were modeled as a substructural element. The ring was modeled as CBARS and the spider legs were analyzed as CQDMEM elements of SOLIDSAP as in Figures 5.3.5-7 and 5.3.5-8. The model was constrained against rotation and translation at 3 locations. The material properties of the members were determined from lamination theory. Since the aft mirror support was well insulated in the tests and therefore, did not change temperature significantly, compared to the ring. The individual contributions of these members was calculated. It was found that the aft mirror support yields a despace of 0.013 micrometers (0.53 microinches) per each 5.55C (10F) temperature increase and the contribution of the aft ring was 0.176 micrometers (6.92 microinches) per each 10F temperature change.

5.3.5.7 Field Splice. The field splice was the most difficult substructure to model in a finite element program. The difficulty is due to the widely spaced bolts which are through the splice and provide the constraint conditions in the model. The thermal properties of the bolts, that is the high positive CTE of the bolts, and the through the thickness properties of the flange result in constraints which are temperature dependent. It was not possible to completely model the system in the time span available. However, a number (4) of simpler models were devised as shown in Figures 5.3.5-9 and 5.3.5-10 which allowed us to bracket the effective thermal coefficient for the flange. From these results we estimate that the flange contribution is +1.02 micrometers (+40 microinches) for each 5.55C (10F) temperature increase.

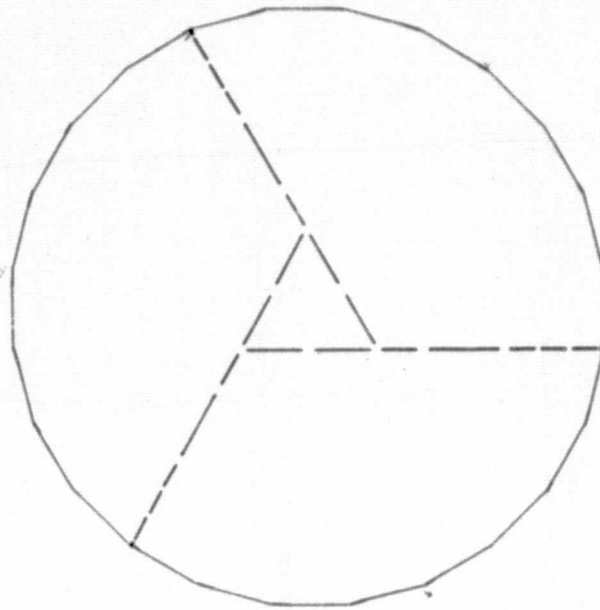


Figure 5.3.5-7. Aft Spider Model Axial View (Graphics)

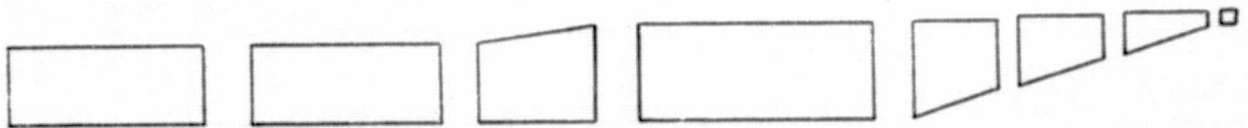


Figure 5.3.5-8. Aft Spider Leg (Graphics)

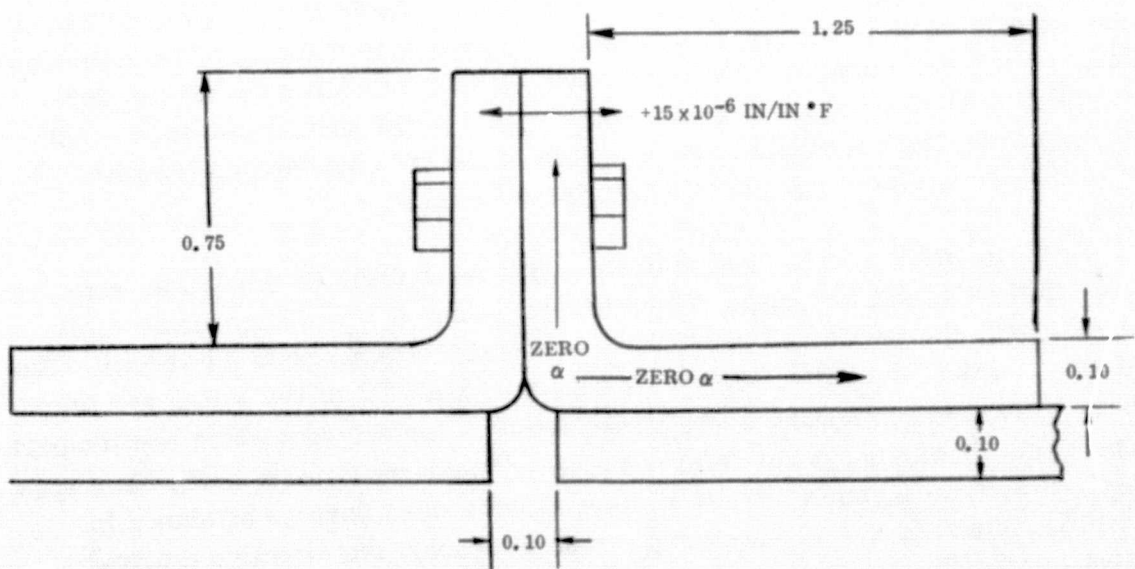


Figure 5.3.5-9. Field Splice

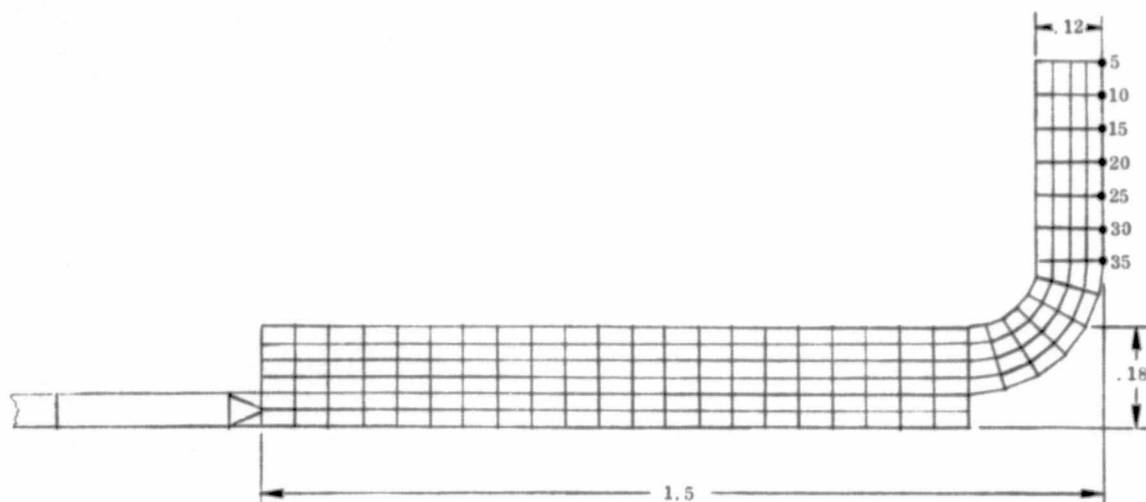


Figure 5.3.5-10. Field Splice Model

5.3.5.8 Analytic Despace. Using the preceding results for the subassemblies in a series combination the analytical despace for the entire GEMS was calculated. Each subassembly contributes a despace which was written in terms of a unit temperature change. The subassembly temperatures for each of the 4 types of experimental thermal cycles was input (from the experimental results) to the computer program, with each subassembly thermal coefficient, in an attempt to reproduce the experimental despace measurements. The results of this analysis is shown in Figures 5.3.5-11 through 5.3.5-14 for each type of thermal cycle. The results are in fairly good agreement with two exceptions: first, the experimentally observed time lag of the despace with respect to temperature was not analytically observed, and the large transitory behavior in the forward shell cycles was not reproduced. Actually the prediction of the forward shell cycles was not as good as desired, neglecting the transitory effects. The results do indicate that the transitory effects in the forward shell cycles are probably due to thermal gradients in this substructure since the theory does not account for gradients (which were not measured anyway) in the elements and the agreement is poorest during the high heating and cooling portions of the thermal cycles. This conclusion was enhanced by the last computer run in which the experimentally measured despace was reproduced by a computer program in which the difference between the experimental and theoretical results was minimized by allowing the CTE of the various subelements to be a variable. The computer program assigned CTE's to the various subelements which minimized this difference. The minimization was very good, as shown in Figure 5.3.5-15, where portions of the 4 types of thermal cycles are shown. The theoretical curves and the experiment curves are in virtual agreement throughout the high heating/cooling segments. The computer selected CTE's to achieve this match, however, were entirely unreasonable. The conclusion is that since a match cannot be achieved without gradients and reasonable CTE's the actual cause is gradients and non-equilibrium temperatures at parts of the structure not instrumented with thermocouples. The results further indicate that the most significant gradients and non-equilibrium conditions are located in secondary support/forward ring subassembly and the field splice.

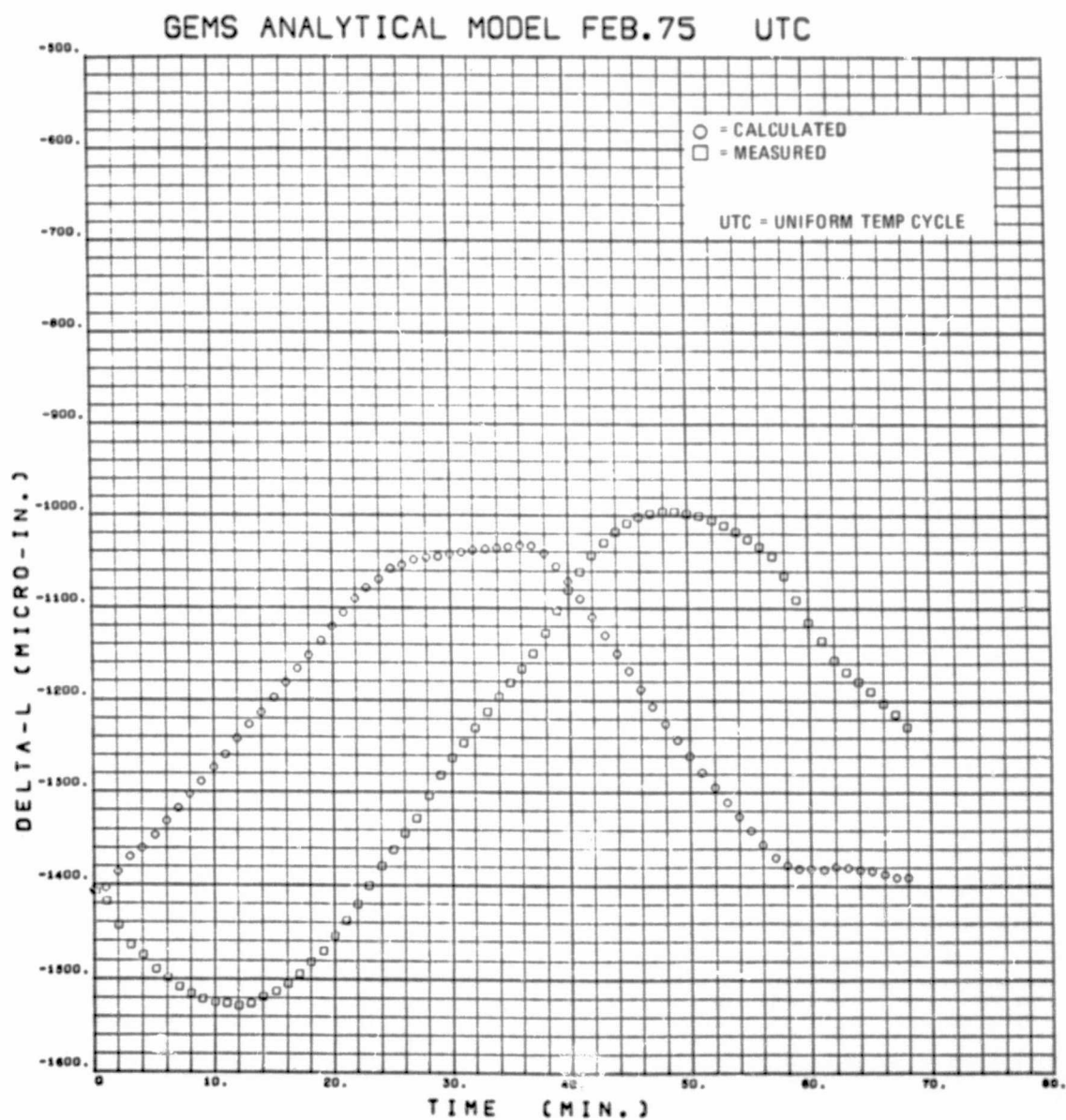


Figure 5.3.5-11. GEMS Analytical Model UTC

GEMS ANALYTICAL MODEL FEB.75 SPTC

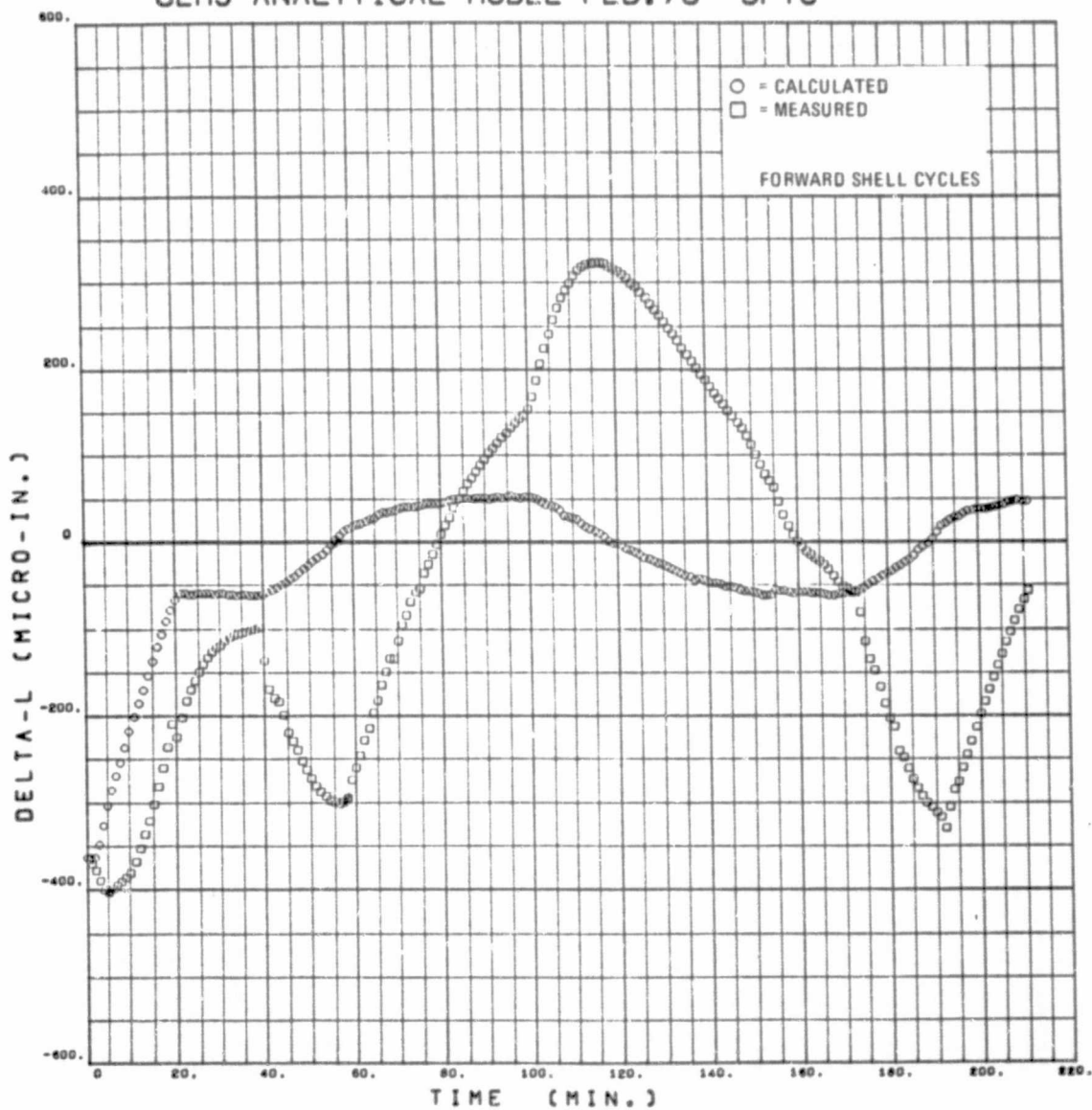


Figure 5.3.5-12. GEMS Analytical Model SPTC

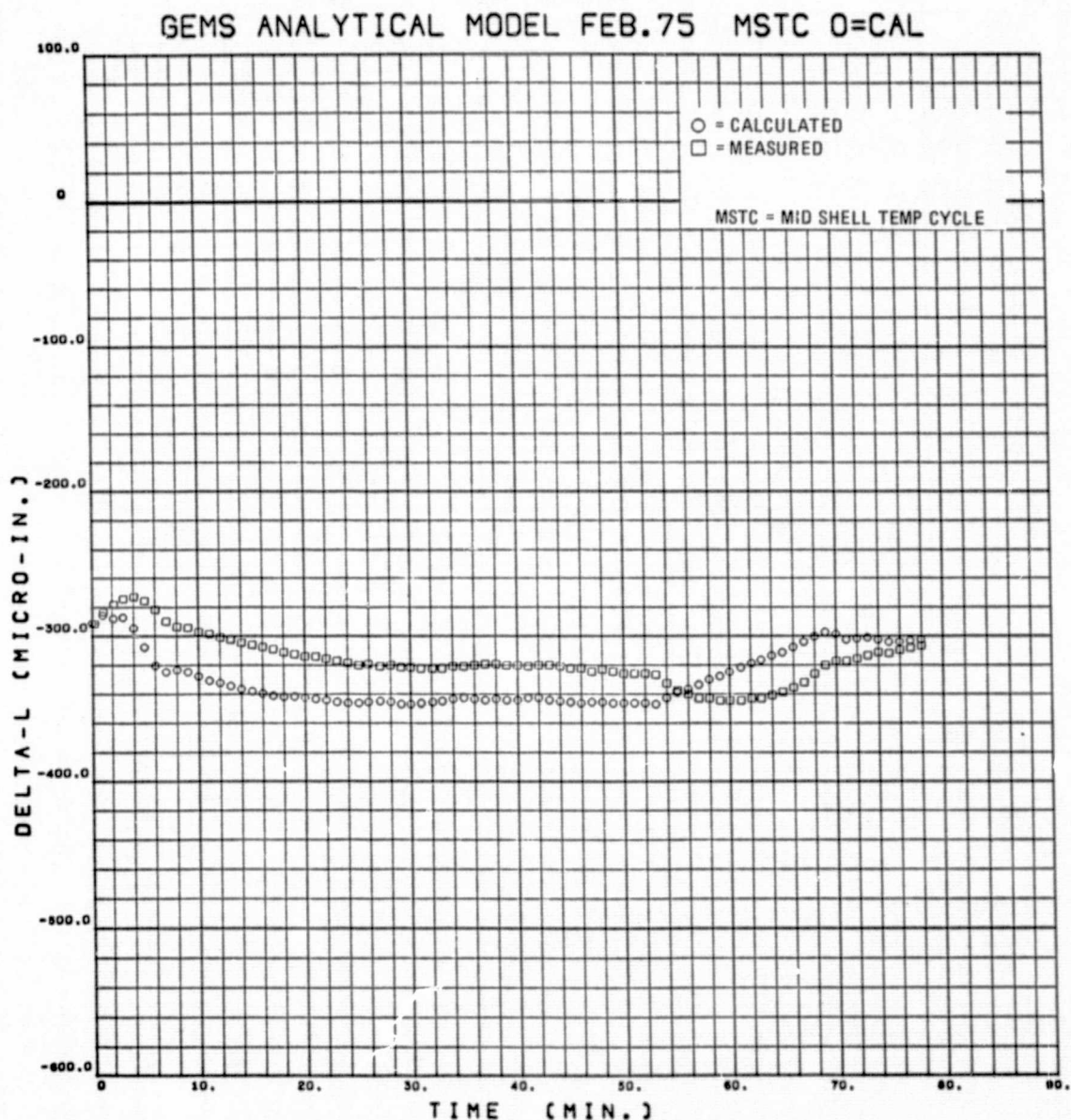


Figure 5.3.5-13. GEMS Analytical Model MSTC 0 = CAL

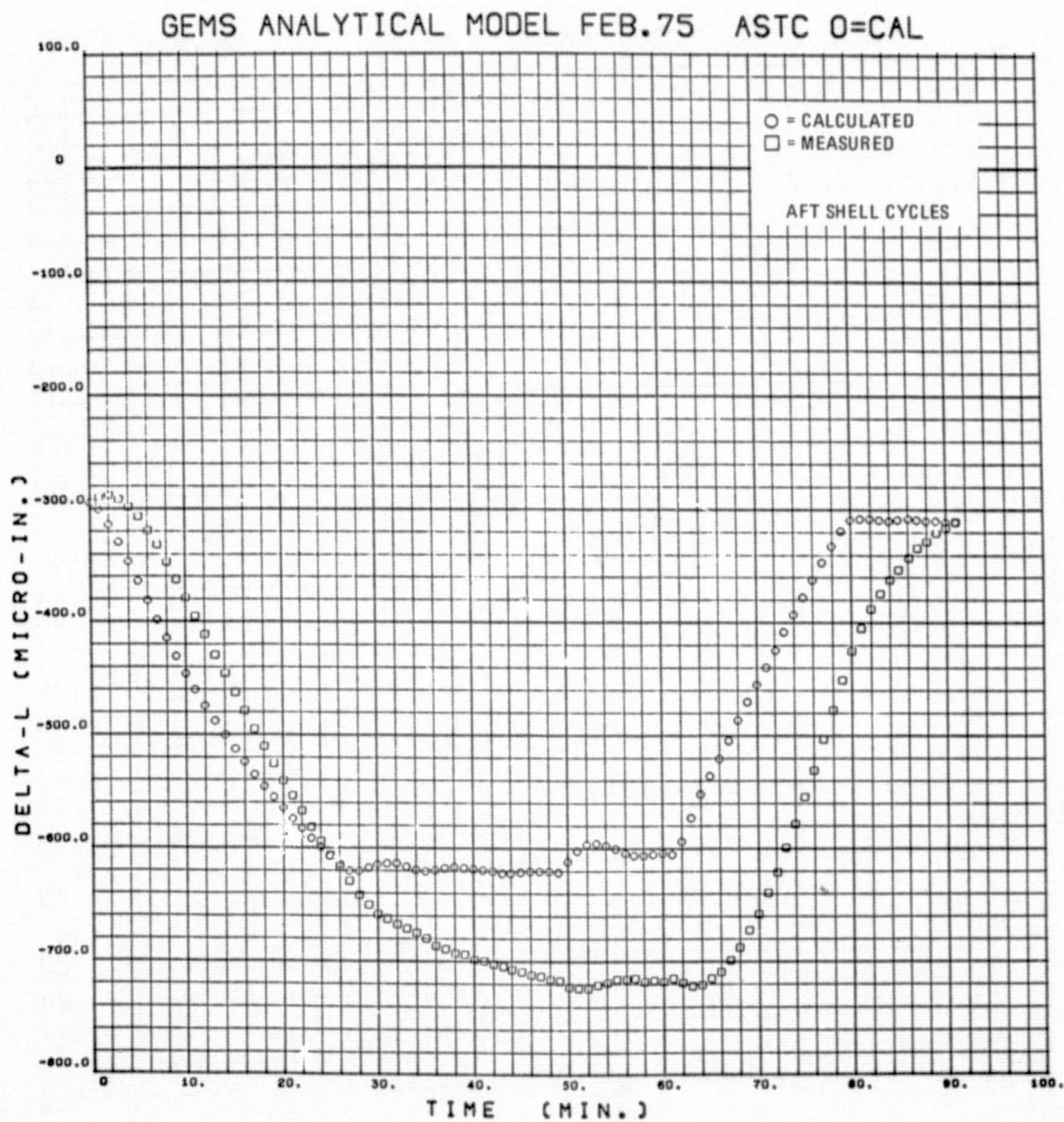


Figure 5.3.5-14. GEMS Analytical Model ASTC 0 = CAL

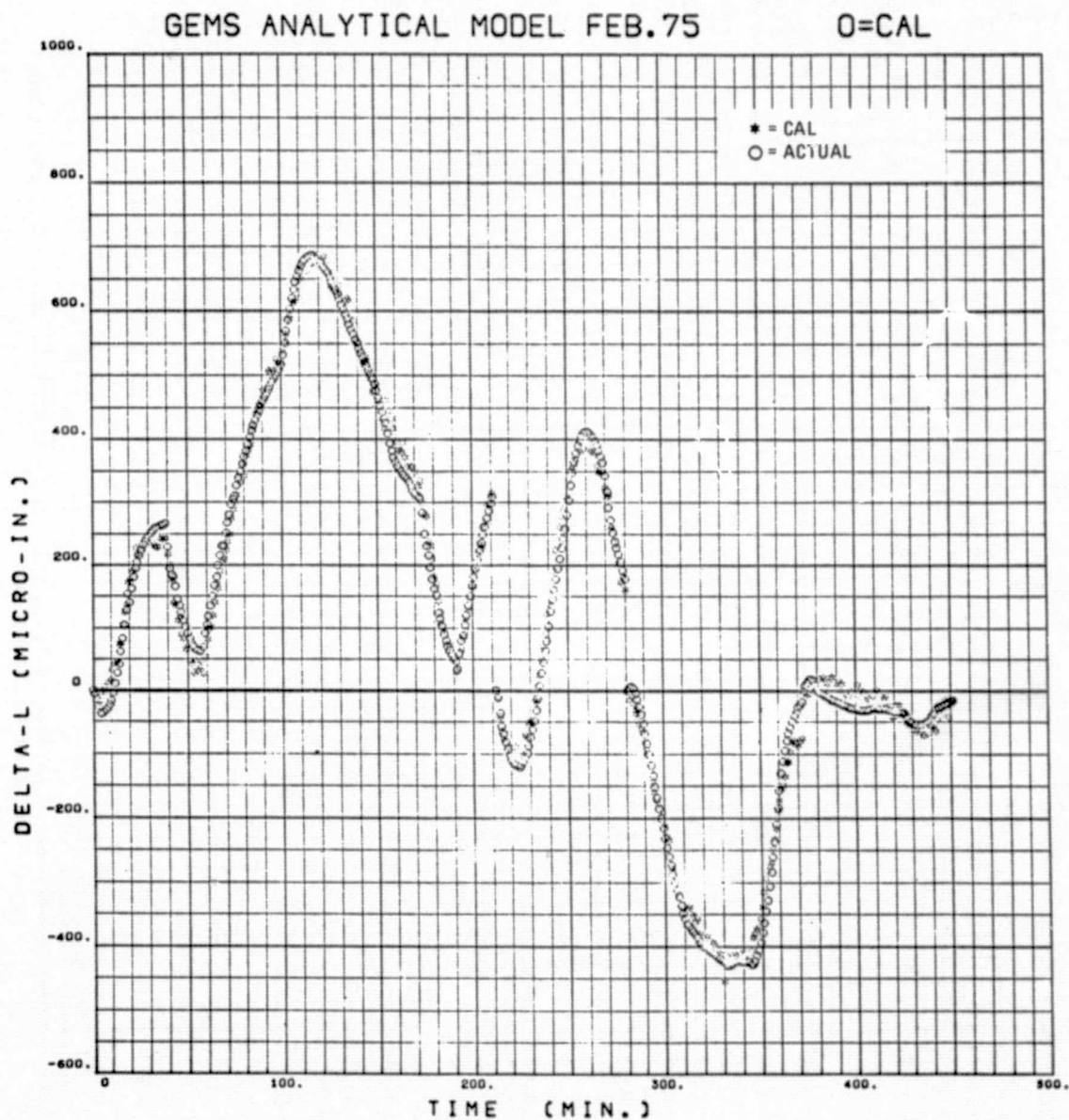


Figure 5.3.5-15. GEMS Analytical Model Optimization * = CAL

5.3.5.9 Summation of Theoretical Results. Using the theoretically derived contributions of the various components to the total despace gives:

	<u>Micrometers/5.55C</u>
Secondary Mirror Support	0.290
Intermediate Splices	0.124
Field Splice	1.020
Aft Ring	0.167
Shell	<u>0.690</u>
	2.29

The negative expansion shell is additive here, since as previously noted, the test data indicated that this was the case due to the response of the skin and the other elements being out-of-phase. The theoretical result correlates fairly well with the measured value of 1.52 micrometers/5.55C. Some reduction is to be expected in the test since some of the elements listed probably did not experience the full test temperature range. On the basis of the theoretical value for despace, if in the low heating rate condition applicable to the LST flight case, the response of the skin is in phase with the other elements, the response of the negative skin will be subtractive and the despace will be:

$$2.29 - (2 \times 0.69) = 0.91 \text{ microinches/5.55C.}$$

5.3.5.10 Field Splice Thermal Model. The field splice and shell were modeled to determine the temperature profile of each under various heat loads. The analysis was intended to determine the thermal lag of the splice with respect to the shell under both test and flight heat loads.

The model consisted of a 12-inch by 33-inch section of 0.060-inch-thick shell with the field splice modeled in the center running in the 12-inch direction. The model was adiabatically constrained at the boundary and the measured temperature-dependent, thermal conductivity, specific heat, and surface emittance were input into the model program.

The thermal vacuum test heat fluxes were adjusted in the model program to reproduce the observed skin temperature profile, and the temperature of the center of the splice was calculated. The results of this analysis are presented in Figure 5.3.5-16. There is significant thermal lag in the splice, creating an out-of-phase-condition between the negative expansion skin and positive expansion splice similar to that indicated by the test despace data.

During LST flight conditions the rate of change of the skin temperature will be approximately one two-hundredth the test rate of change. To conservatively approximate the

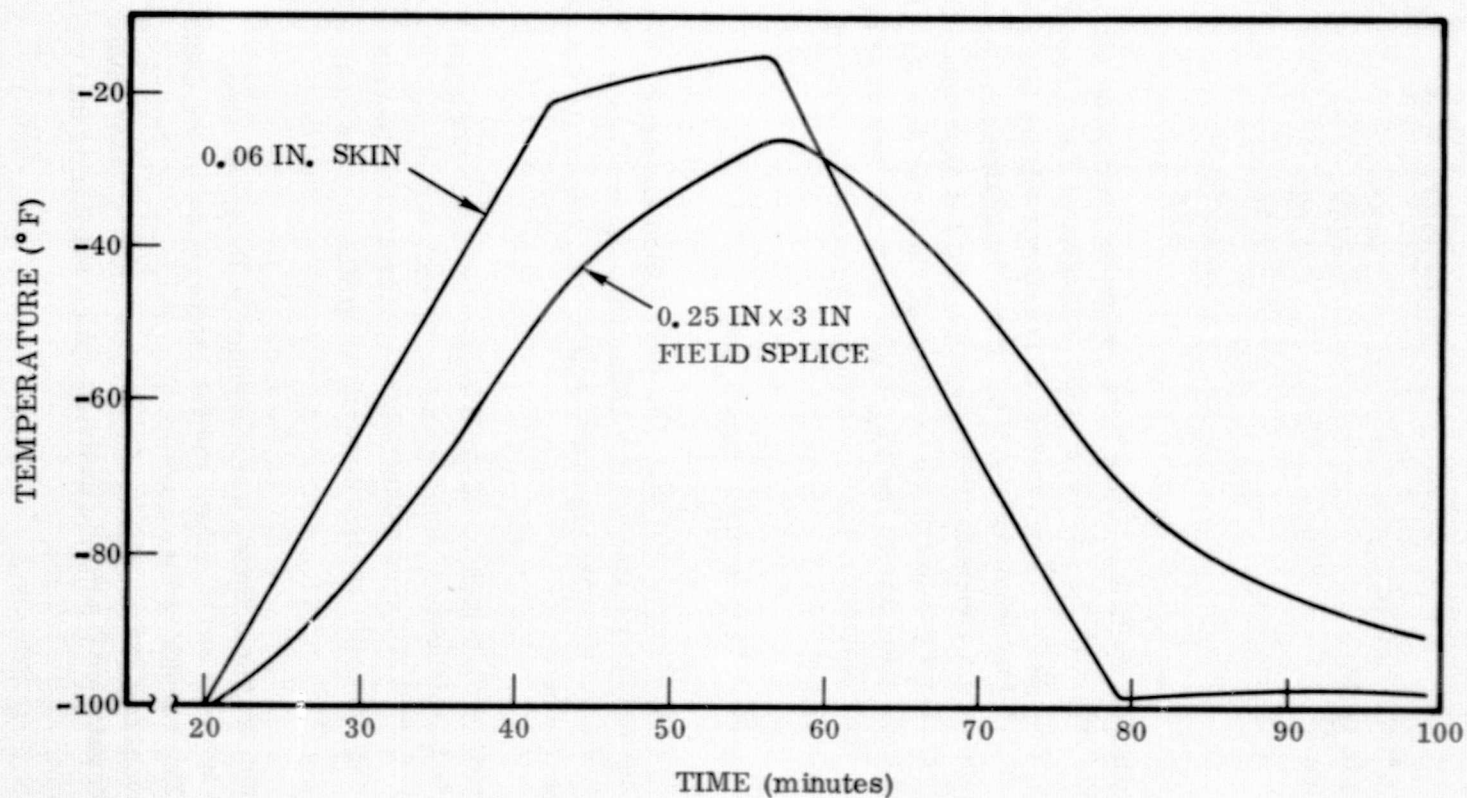


Figure 5.3.5-16. Graphite/Epoxy Section Temperature Response to Thermal Vacuum Test Heating

flight conditions, the model was subjected to a heat flux, which resulted in a skin rate of temperature change of $2.1^{\circ}\text{F}/\text{hour}$, which is three times the expected flight rate of change. The resultant temperature of the splice is shown in Figure 5.3.5-17. The skin temperature gradually rises 0.3°F above the ring temperature and maintains this difference for the remainder of the exposure to this heat input. This indicates that the skin and the field splice will respond in phase to the low heating rates of the flight environment.

We therefore conclude that the test environment was much more severe than necessary, particularly the high heating rates to produce thermal cycles of 80°F temperature changes in 40-minute intervals. The resultant temperature gradients are much too large to represent a flight environment, and they introduce larger dimensional changes than would be induced if the GEMS were cycled at a lower rate or if the dimensional changes were measured with the structure in complete thermal equilibrium at the temperature extremes. The analysis and test results indicate that the GEMS despace would approach and possibly be less than $1\text{ micrometer}/5.55^{\circ}\text{C}$ in the actual flight condition.

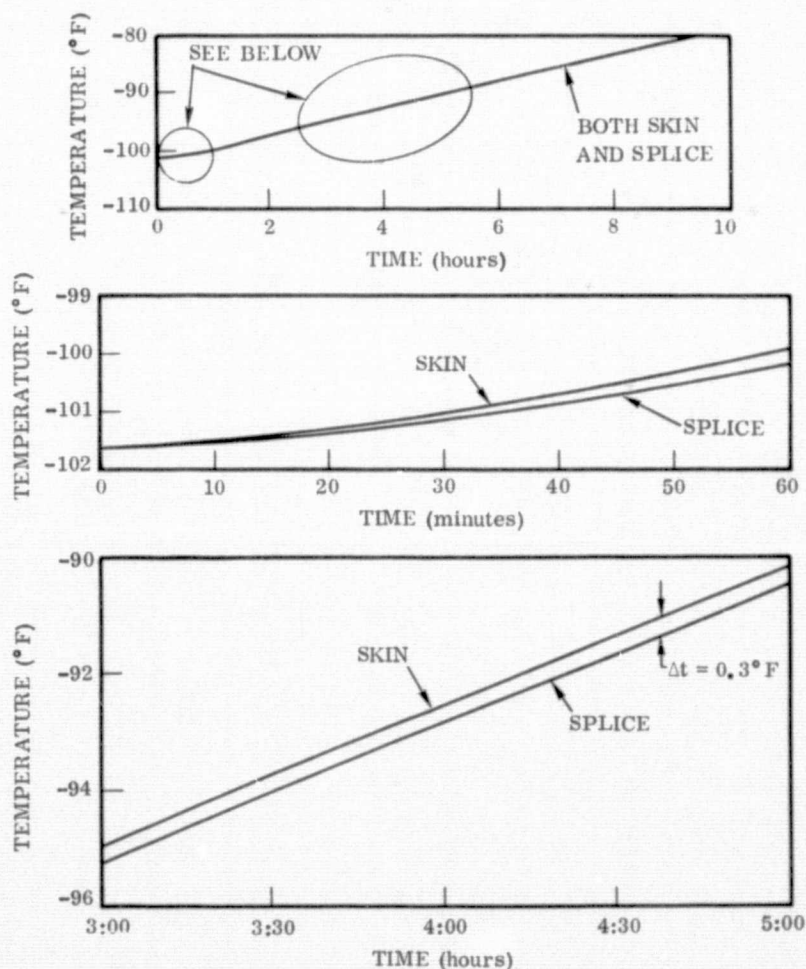


Figure 5.3.5-17. Graphite/Epoxy Section Temperature Response to Predicted Flight Heating Conditions

SECTION 6

CONCLUSIONS AND RECOMMENDATIONS

6.1 CONCLUSIONS

The following conclusions may be made:

- . The measured performance of the GEM closely approached the goal of ± 1.0 micrometers/5.55C.
- . Some improvement would probably have been attained by additional thermal cycling, or by precycling the GEMS components before assembly.
- . Significant improvement in the measured values would probably have been obtained by testing at flight heating rates since this would cause compensating positive and negative expansion elements to respond in-phase.
- . The Hewlett-Packard Plane Mirror Dilatometer is satisfactory for the measurement of submicrometer strains in large structures.
- . The stiffness of the shell type metering structure amply exceeds the 15 Hz requirement specified in the LST Phase A report.
- . The shell type structure and the proposed secondary mirror support arrangement can be designed to the strength requirements of the LST.
- . The low cost fabrication techniques and the associated tooling concepts can be adapted directly to the full-scale LST metering structure.

6.2 RECOMMENDATIONS

The following recommendations are made:

1. Perform additional thermal expansion tests at heating rates more closely consistent with the flight case.
2. Investigate the effect on performance of additional thermal cycles.
3. Perform dynamic tests in the vacuum chamber to investigate low amplitude responses and damping characteristics.

4. Perform design and analytical studies of the dimensional stability of secondary mirror support configurations.
5. Eliminate or redesign the field splice. For test purposes the effect of the field splice can be eliminated by removing the aft section of the GEMS and then using the plane of the field splice as the measurement reference plane.